FEASIBILITY STUDY OF

USING OPTICAL MOIRÉ INTERFEROMETRY TECHNIQUE FOR

FINE-GRAIN SURFACE RELIEF IN HERITAGE RECORDING

A Dissertation

by

SAMER AL-RATROUT

Submitted to the Office of Graduate Studies of
Texas A&M University
in partial fulfillment of the requirements for the degree of

DOCTOR OF PHILOSOPHY

August 2005

Major Subject: Architecture

FEASIBILITY STUDY OF

USING OPTICAL MOIRÉ INTERFEROMETRY TECHNIQUE FOR

FINE-GRAIN SURFACE RELIEF IN HERITAGE RECORDING

A Dissertation

by

SAMER AL-RATROUT

Submitted to the Office of Graduate Studies of
Texas A&M University
in partial fulfillment of the requirements for the degree of

DOCTOR OF PHILOSOPHY

Approved by:

Chair of Committee,	Robert Warden
Committee Members,	David Woodcock
	Donald H. House
	Richard Burt
Head of Department,	Phillip J. Tabb

August 2005

Major Subject: Architecture

ABSTRACT

Feasibility Study of Using Optical Moiré Interferometry Technique for Fine-Grain Surface Relief in Heritage Recording. (August 2005)
Samer Al-Ratrout, B.S., University of Jordan;
M.S., University of Jordan
Chair of Advisory Committee: Prof. Robert Warden

In order to prepare for the prospective need for heritage 3D recording, the main objective of this research was to investigate a new depth measuring method that can reduce identified limitations of current point-to-point measuring approaches. The limitations were time-money consumption, intrusiveness, accuracy assumption and efficiency.

In many disciplines other than heritage recording, optical moiré interferometry techniques (OMIT) are well developed as a measuring method and are considered fast, non-intrusive, accurate, and efficient. Based on these considerations, this research hypothesized that OMIT, as a measuring method, is feasible with respect to time-consumption and accuracy in acquiring depth measurement for fine-grain surface relief for historic recording.

To test this hypothesis, a feasibility investigation was carried in which OMIT was used for surface relief topographic recording. This goal was approached by performing a comparison study between the OMIT measuring method as the investigated method and the hand measuring method as the control method. For each method, the comparison required performing eight experimental samplings of relief recording for a pre-designed physical model surface.

The data collected from the hand measuring samples were the depth measurements of predefined points on the model surface and the time-consumption for both measuring and data preparing processes. The data collected from the OMIT measuring samples were moiré dark fringes generated

on the model surface and the time-consumption for both moiré generating and data preparing processes. For measurement accuracy evaluation, the collected depth data were prepared in the form of topographic contour drawings.

For the OMIT feasibility evaluation, a comparison was carried out to examine the resulting topographic contour drawings for depth measurement accuracy level and measuring process time-consumption.

In conclusion, the OMIT method showed higher depth measurement accuracy levels and lower process time-consumption than the hand method. The OMIT method also demonstrated less intrusiveness and more efficiency. This superiority validates the feasibility of using fine-grain surface relief for heritage recording purposes.

Finally, the observed advantages of the OMIT method were presented to establish potentials for future developments and investigations. The observed limitations of the method were also pointed out to establish trends for recommendations and further studies.

DEDICATION

"سبحانك لاعلم لنا إلا ما علمتنا
إنك أنت العليم الحكيم"

“Glory to Thee, of knowledge we have none, save what Thou hast taught us, in truth it is Thou who art perfect in knowledge and wisdom.”

To

My mother, my wife, my sisters and my children

Abdulmunim, Mohammad and Zaid

ACKNOWLEDGMENTS

I would like to thank my family for supporting me through the years of my studies. I would especially like to express my appreciation to my mother for her infinite belief in me and to my wife, Iman, for her endless support and dedication.

I would like to thank Prof. Robert Warden for generously offering his knowledge and time and for making his distinguished experience in historic recording available to me.

I would also like to thank Dr. Donald House for his knowledgeable guidance through the wonders of the digital imaging world and for his encouragement that gave me confidence to touch the limits.

I would also like to thank Dr. Richard Burt for his sharp remarks in photogrammetry and statistics and for his suggestions and guidance through the world of measurement precision and accuracy.

I would like to thank Prof. Thomas Regan, Dean of the Department of Architecture, for his support and concern and for motivating me to reach a better best.

I will forever be grateful to Dr. David Woodcock, Director of the Historic Resources Imaging Laboratory, for introducing me to the world of heritage appreciation. I am grateful to him for offering the HRIL resources for my experiments. His endless support as a mentor and as a colleague was a source of inspiration to me in my studies and my life.

TABLE OF CONTENTS

CHAPTER Page

LIST OF TABLES

LIST OF FIGURES

FIGURE Page

FIGURE Page

FIGURE Page

FIGURE Page

FIGURE Page

CHAPTER I

INTRODUCTION

I.1. BACKGROUND

Modern technologies offer novel powerful tools and media for heritage recording that were not available in the recent past. These technologies make it possible to enhance the quantity and the quality of recording information for heritage documentation purposes.

Future trends in heritage recording involve generating 3D virtual records of heritage structures within digital environments. These environments can handle precise measurement records and offer these records in a form of 3D virtual models.

In order to utilize these digital environments, the translation process of heritage structures from real forms to virtual existence requires highly detailed records of objects. The major challenge in this process is to generate enough measurements to virtually reconstruct the recorded elements to precisely reflect the real forms.

Surface relief is a basic piece needed to fill the gap between traditional records and virtual 3D records of historic structures. Detailed measurement records of surface relief generate the basic fabric for creating larger virtual shapes by stitching those surfaces to fill in between edges and boundary lines.

Traditional recording techniques such as hand measuring, total station surveying, and photogrammetry can hardly fulfill the contemporary requirements of very-accurate 3D recording. Those techniques utilize a point-to-point measurement principal approach to offer measurements of boundaries, basic relief profiles, special identified texture marks, edged recesses and cracks.

This dissertation follows the style and format of Applied Optics.

For surfaces relief, these techniques involve methods that provide measurement records based on point-to-point linear measurement information. These methods rely on referring every measurement to two visible reference marks that are usually hard to spot on fine-grain organic surfaces. To accurately reflect changes in the relief, those reference marks need to be scattered in a way which reflects the changes on the surface.

In that scope, curved surfaces with fine-grain relief are considered a real challenge to the traditional recording techniques. These surfaces are like portions of interior facades of caves, natural elements surfaces, parts of stone works, portions of ornament works, statues with curved surfaces, and other heritage objects with smooth, curved surfaces. These fine-grain curved surfaces are common in heritage structures due to the use of primitive creation and construction methods and sometimes due to deterioration effects resulting from time and the forces of nature. In recent years, some of the newly constructed structures have followed design trends that utilize old and new materials in creating organic forms and shapes to produce facades with these kind of curved fine-grain surfaces. Usually, these surfaces lack reference marks and require a substantial number of artificial marking targets to be attached to the surfaces for measurement purpose.

Future demands for 3D digital documentation of fine-grain surface relief place heavy loads on those traditional recording techniques, raising concerns of inaccuracy and time-consumption.

As a state-of-the-art technology, Laser scanners are currently preferred for this kind of 3D digital documentation, but they are too expensive and raise concerns of producing massive and sometimes disturbed data.

For 3D recording of fine-grain surface relief the need for new techniques is justified by the necessity to solve key limitations and satisfy key needs related to heritage traditional 3D recording techniques.

Before now, the principles providing integral measurement information of surface relief have not been assimilated into the heritage recording field. The integral measurement information principals offer full-field quantitative measurements with minimal reliance on reference marks.

Optical moiré interferometry techniques (OMIT) are unique in that they incorporate the integral measurement principle. The OMIT are fast and relatively inexpensive, but are undeveloped with respect to heritage recording.

To approach the future, this study will introduce OMIT to the traditional recording field. For heritage recording purposes, the study will test the feasibility of using the OMIT for recording the change in relief depth of fine-grain surfaces on the basis of time-consumption and accuracy assumption.

I.2. Statement of the problem

The purpose of this research is to improve the recording of surface contours of fragile objects with curved fine-grain surfaces by reducing some of the limitations associated with the current depth measuring techniques by investigating new supporting methods.

When extracting depth measurements, limitations of time-money consumption, intrusiveness, accuracy assumption, and efficiency have a serious impact on the recording process. These limitations are associated mainly with point-to-point information principles used by traditional techniques.

The limitation of time-money consumption is related mainly to the amount of effort invested in extracting depth measurement from point-to-point information using traditional tools.

The limitation of accuracy assumption is also related to these point-to-point information principles. The assumption of flatness between measured points reduces depth measurement accuracy in the areas between those points. Increasing the number of measured points usually reduces this problem but this approach raise the time-money consumption problem again.

Another significant limitation is the risk of damaging the measured object while attaching targets to the surface because of the need to gather more measured points to reflect the change in the relief of the surface.

OMIT as a measurement method has been well developed with respect to many disciplines other than heritage recording.[1,2] The traditional need for accurate surface relief measurements of large heritage elements was not critical in the recent past. The 2D drawings limited the space potentials of the final record forms. These limited space potentials were the main reason for not amplifying the collected measurement data. While at the same time, highly detailed relief measurements were essential when recording objects in many other disciplines. In those disciplines, the OMIT were employed and proved fast,

accurate, non-intrusive, and relatively inexpensive, revealing surface relief measurements in one set of information.

I.3. Research hypotheses

Based on the well established potentials of the OMIT to satisfy heritage prospect needs for 3D recording, the main hypothesis of this research is that, on time-consumption base, the OMIT measuring process can be feasible in accurately obtaining quantitative depth measurement for fine-grain surface relief.

The two main concerns in this hypothesis are depth measurement accuracy and process time-consumption when employing the OMIT as measuring method for heritage recording.

The research hypothesis of depth measurement accuracy assumes that if the ratio between depth measurement error average of the hand measuring method and the depth measurement error average of the targeted OMIT measuring method is one, then depth measurement accuracy level for both methods is the same. The greater the ratio is above one the higher accuracy the OMIT method has. The lower the ratio is below one the lower accuracy the OMIT method has.

The research hypothesis of time-consumption assumes that if the ratio between process time average of the hand measuring method and the process time average of the targeted OMIT method is one, then time-consumption for both methods is the same. The greater the ratio is above one the less time-consuming the OMIT method is. The lower the ratio is below one the more time-consuming the OMIT method is.

Generally, the hypotheses of good research should meet the recognized criteria of constructed validity, testability and relevancy to the investigated problem.[3]

The aforementioned main hypothesis of this research was based on the assumption that the use of hand method and the OMIT method for depth

measurement of fine-grain surface relief has a constructed validity. The validity for hand method is supported by well-established practices in heritage recording. The validity for OMIT method is supported by previous research and well-established practices in many other disciplines.

The second base of the research main hypothesis assumed that for heritage structures, the use of the hand method and the OMIT method for contour recording of surface relief is testable. This testability is based on the ability to collect and analyze depth data acquired from physical models using available equipment like non-metric digital camera, off-the-shelf LCD projector and a personal computer.

The third base for the research main hypothesis assumes that for the targeted accuracy of one-eighth of an inch, comparing the two methods for time-consumption needed for data acquisition and data treatment is relevant to testing the feasibility of those methods.

I.4. Theoretical framework

This study assumes a post-positivist view of the world with a critical realistic approach. According to this view, the world is received as a container of three worlds. The first world is the physical world of bodies and their physical and physiological states, events and forces. The second world is the psychological world of experiences and unconscious mental events. The third world is the intellectual world containing human mental products [4,5]

Studying the feasibility of using the OMIT for surface relief in heritage recording is a study related to this three-world approach. It considers the physical world in the physical existence of the surface and the measuring instruments. It also considers the psychological world in the perception of surface relief measurement and measuring process time. Finally it considers the intellectual world through the mental reasoning and judgment on processes comparison result.

Within those worlds there is no authority on the ultimate truth. [5] This study variables in those worlds are believed to exist physically. The knowledge about their existence is based on the human interaction procedures within the three worlds. Those procedures are the physical perception of their existence, the mental reasoning about their nature and characteristics, and finally the mental judgment on the validity of that perception.[6] For this relative truth, the knowledge about the variables is only probable and not certain. It is a knowledge mixed with perception errors, prejudgment, and expectation. The facts confirming the variables physical existence make that existence only probable. [7,5]

The adapted approach in this experimental study is the scientific approach. The scientific problem solving approach and common sense reasoning are essentially the same process of trial and error. [4,8] As humans, the common sense approach for determining a surface relief depth is established using the senses of sighting, touching and sometimes hearing. Humans seek to build relative relations between surface formations. They do that depending on trial and error reasoning of previous sensory experiences. The adapted scientific approach is appropriate for performing the study investigations because, like the common sense approach, the scientific approach uses sensing tools, gathers evidence, and implements procedures to assure that observations are supportable. Those three categories established the main investigation aspects in this study: the measurement tools are the sensing tools; the generated data is the gathered evidence; and the process evaluation and data interpretation and analysis are the support to the concluded results. By implementing this scientific approach, objectivity in this investigation can be approached, but absolute objectivity cannot be achieved. [4]

In the critical realistic approach of this view of the world, the scientific approach to attain solutions can be achieved through attempts to criticize and falsify. With this approach, when moving toward truth with the absence of negative instances, confidence begins to grow in the assumptions. [8,9] Criticizing

and falsifying attempts were established in this study through critical examination of the measuring procedures and instruments, and through comparing approaches of different methods' outputs.

In this study, the involvement of computer software used to generate the true model will satisfy the need to use triangulation across the output of the imperfect measuring tools. This triangulation is necessary to provide a more accurate representation of the surface relief formation in reality. Repeated tests usually show where data conflicts lie. [4]

As a dualist/objectivist, the epistemological stance in this study assumes that knowledge exists as an external phenomenon outside the observer, and the observer should maintain a distance while studying that phenomenon. In standing apart from the situation the objectivity of the observer can be achieved by involving the internal and external evidence. [10,11] According to this stance, to accomplish internal evidence, the conclusions of the study should be maintained unbiased by personal effects.[12] This was achieved in this study by confirming building the conclusion outputs of the depth measurement accuracy based entirely on unbiased data inputs. The adaptation of study conclusions by others for similar situation will accomplish external evidence in this stance perspective.[11,13] This was established in this study by reviewing other disciplines literature to determine the validity of moiré method for measuring the change in surface relief depth. This validity formed the basis for developing a methods comparison procedure for concluding feasibility of using moiré method for objects with fine-grain surfaces in heritage recording.

I.5. Organization of this document

This first chapter introduced the investigated problem and established the research hypotheses and the theoretical framework.

Based on this introduction, Chapter II presents the previous literature and work in the research area in relation to the limitations of heritage recording

techniques. The second chapter also introduces moiré topography as a proposed recording technique and presented the previous literature related to history, application, physics, geometry, mathematics and the deficiencies of this method.

After introducing the moiré method in Chapter II, Chapter III explains the research methodology to be followed for investigating the feasibility of using moiré method for heritage recording. The third chapter presents the pilot study explaining the experimental variables, the investigated methods' instrumentation, the experimental samples, and the acquired data treatments.

Chapter IV provides details related to performing the experiments, establishing the true model and generating time and measurement data. The chapter also discusses and analyzes contour generating methods and the encountered problems.

In Chapter V, the resulting contours accuracies from Chapter IV are evaluated and compared. The time-consumptions of the compared methods are interpreted and compared and conclusions are derived from analyzing the data results.

Finally, based on the data analysis conclusions, Chapter VI summarizes the experiments in this research and concludes by evaluating the feasibility of the investigated OMIT method. The established advantages and limitations of the method are presented. Finally, recommendations for using the OMIT and suggested trends for future studies are also presented.

CHAPTER II

LITERATURE REVIEW

This chapter introduces the previous work in the area of the limitations of the contemporary heritage recording techniques. The chapter also discusses potentials of moiré topography as a recording technique. The literature related to history, application, physics, geometry, mathematics and the deficiencies of moiré are also presented.

II.1. Introduction

Heritage documentation is needed on different scales of precision. Performing reconstruction to preserve structures needs precise documentation.[14]

Traditional recording techniques, such as hand measuring, total station surveying, and photogrammetry can hardly fulfill the requirements when very accurate records of historic structures are required.[14,15] When curved and fragile heritage features are precisely recorded, the main difficulty is associated with the need for measuring a considerable number of reference points on the feature's fragile surfaces. The physical constrains of approaching the surface of the recorded object needs also to be considered.[16]

Future demands for 3D digital documentation place heavy loads on the traditional techniques. These techniques are generally too inaccurate, or too time-consuming.[17,18] Laser scanners are currently preferred for 3D digital documentation but they are too expensive and they produce massive and sometimes disturbed data.[18]

II.2. Limitations in heritage recording techniques

Contour recording of surface relief is one type of 3D recording approach used to document heritage elements.[1]

In heritage recording, the demand for new techniques in contour recording is supported by the requisite to solve two key problems and satisfy two key needs associated with the contemporary contour recording techniques. [18,19]

The first key problem is time-money consumption that occurs in relation to the used measurement method. When using manual recording as a contour measurement method, considerable time and labor are required to produce even the minimum of essential measurements.[20,21] Using equipment like total-station requires training. With this equipment, interpretation of the collected data can be very time-consuming.[22,23] State-of-the-art equipment like laser-scanners are expensive to obtain and maintain. Software solutions for obtaining information from photos face problems with special cases, such as recording the relief of a fine-grain surface.[24]

The second key problem associated with contour recording techniques is the assumption of accuracy. Technologies and methods used for recording heritage structures must be accurate enough for the required needs.[18,19] The measured data are usually distances between groups of two identified points. These measured distances assume a flat surface between the measured points. Measurement accuracy will be affected by the reliability of this assumption. Current technologies and methods attempt to meet the accuracy requirements through collecting more measurements of closer point groups. With these attempts, the traditional technologies and methods fail to meet the need for efficiency in managing tools, cost and labor time.[25]

For heritage recording, there is a need for more efficient tools for recording relief contours of irregular surfaces. Ancient heritage sites lack regularity due to erosion and non-standardization of construction.[19] This requires great time and expense to create accurate contour records using the current technology and methods.

There is also a need for remote-non-intrusive techniques when handling fragile or unapproachable elements. The recoding process needs non-intrusive

techniques to prevent the deterioration of fragile ancient heritage. Unapproachable objects require remote close-range recording techniques.[26]

II.3. The OMIT as a contour recording technique

Traditional contour recording technologies, associated with point-to-point measurement principals, tend to represent an object's surface based on point-to-point information. Some of the principals used are optical triangulation, stereoscopy and photogrammetry. [27]

The involvement of principles yielding integral surface information has not yet been introduced to heritage recording field. The OMIT is unique because it incorporates the principle of integral measurement. [27]

Since 1970, OMIT has been used to make measurements for topographic mapping of the human body without physical contact.[28] This involvement in medical photogrammetry revealed that OMIT requires simple equipment and provides geometric information with accuracy within several tenths of a millimeter.[1] Research confirms that the OMIT is fast and relatively inexpensive, but is undeveloped with respect to historic structures.[2]

Previous research also confirms that OMIT as a recording technique is characterized by unique qualities. Those qualities are: the full field measurements, high sensitivity of in-plane instrument displacements, insensitivity to out-of-plane instrument displacements, tiny zone measurements using high resolution instruments, high contrast and visibility of fringes, compatibility with both large and small displacements and object sizes and being a real time technique.[29]

Investigating OMIT for optical non-destructive testing and inspection in his study titled "Moiré in science and engineering", Sciammarella C. concluded that the effect of OMIT makes it feasible to remotely measure the changes experienced by surface deformation.[2]

In another study titled “Moiré interferometry” published in 2000, the authors Post D., Han, B. and Ifju, G. stated that

> “*Whereas moiré interferometry and microscopic moiré interferometry are currently used in many fields of engineering and science, we anticipate that they will be used much more extensively in the same fields, and applications will extend into many additional fields. The unique combination of capabilities – whole-field measurements, very high sensitivity, very high special resolution, excellent signal-to-noise ratio, extensive range, etc. – will be put to use for measurements and explorations, as engineering tools and research tools, in widely diverse applications. They include applications not yet imagined!*” [29]

On the other hand, to achieve more practical OMIT, many investigations have been made to solve the physical problems of the techniques without involving mathematical calculations.[30]

Other studies in cultural heritage recording predicted that OMIT has the potential to be used for fast and accurate recording of fragile archaeological elements.[31]

II.3.1. Definitions of terms

As an optical phenomenon, moiré can be visualized when two closely identical grating of lines are superimposed, as illustrated in Fig. 1. By viewing these gratings against light background, dark fields called “moiré fringes” are observed. The dark fringes are caused by blocking light when the opaque areas in one pattern overlap the transparent or the opaque areas of the other. On the other hand, light areas between fringes results from overlapping the transparent parts of the two gratings.[32] The small differences in spaces between lines or the orientation of the two patterns will affect the shape and spacing of the fringes.[33,34]

As a relief measurement method, the base for moiré technique is the comparison of two states of identical line-gratings. The first state is the initial state (reference or unloaded line-grating), and the second state is the modified state (loaded line-gating associated with surface deformation of the object). The changes in the grating appearance from one state to the other reflect the perpendicular displacements experienced by the surfaces with respect to a reference plane.

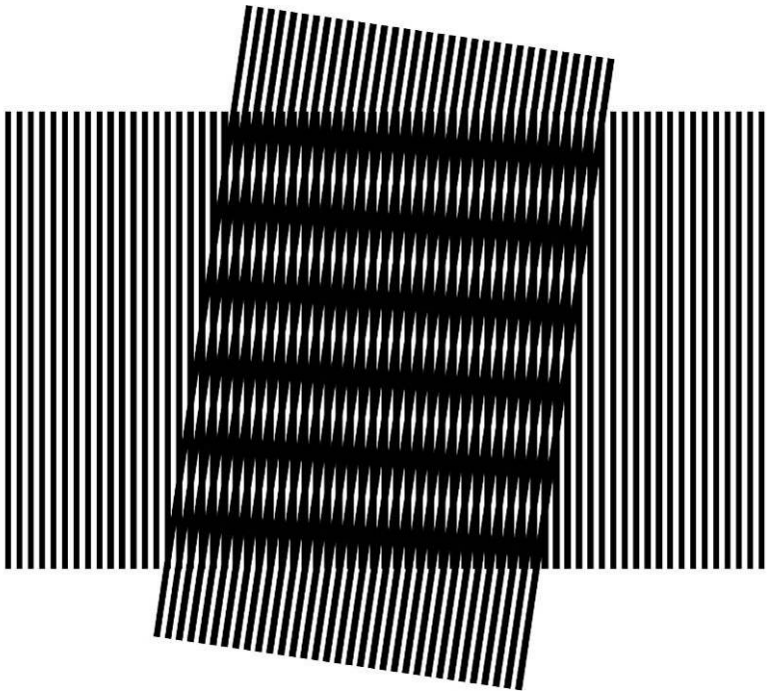

Fig. 1. Moiré dark fringes formation by relative rotation of two grids.

In practice, the process of the OMIT is performed in many arrangements and means to produce the required results. One of those arrangements, which will be used in this study, is the deformed grating technique. This technique is performed by projecting the reference grating in the form of light pattern on the object's surface to produce the loaded grating. With no physical contact with the object surface, superimposing both images of reference and loaded grating from

the same point of view will produce the topographic shadow fields that are called “moiré fringes”

II.3.2. History of moiré

The word moiré indicates the watered or wavy appearance. The term evolved from the ancient French word “mouaire”, which was derived originally from the English word “mohair” which refer to the name of the wavy fleece of the Angola Goat.[35]

As an optical phenomenon, moiré was noted in the scientific literature more than a century ago. It was in Lord Rayleigh writings in 1874 when it was initially referred to as “bar patterns”.[34] Terms like Brewster bands, Haidenger rings, Newton rings, waterlines, and interference fringes have all been introduced since then to describe these optical patterns.[35]

The word “moiré” survived translation into English when it was introduced for the first time as a metaphor in a scientific French article by Multo (1925) as “des franges de moiré” to refer literally to these watered fringes.[35]

II.3.3. The physics of moiré topography for 3D objects

As explained in section (II.3.1), optical Moiré as a phenomenon generates dark fringes and clear fringes as a result of superimposing two or more patterns.[34] The deformations of the projected pattern are usually associated with surface relief deformation. In this case, dark fringes which represent the surface topography can be generated by superimposing the images of the deformed pattern and the original projected pattern.

As shown in Fig. 2, when superimposed, the intersection of the deformed pattern lines with the original pattern lines produces low light intensities (low light reflections and high light absorption) in the form of continuous stripes. Those resulting stripes have larger area percentage than any dark stripes found in the deformed and original patterns separately. This happens as a result of

overlapping the dark colored areas in the superimposed patterns. This arrangement maximizes the percentage of the dark areas in the superimposed regions resulting in low light intensity.

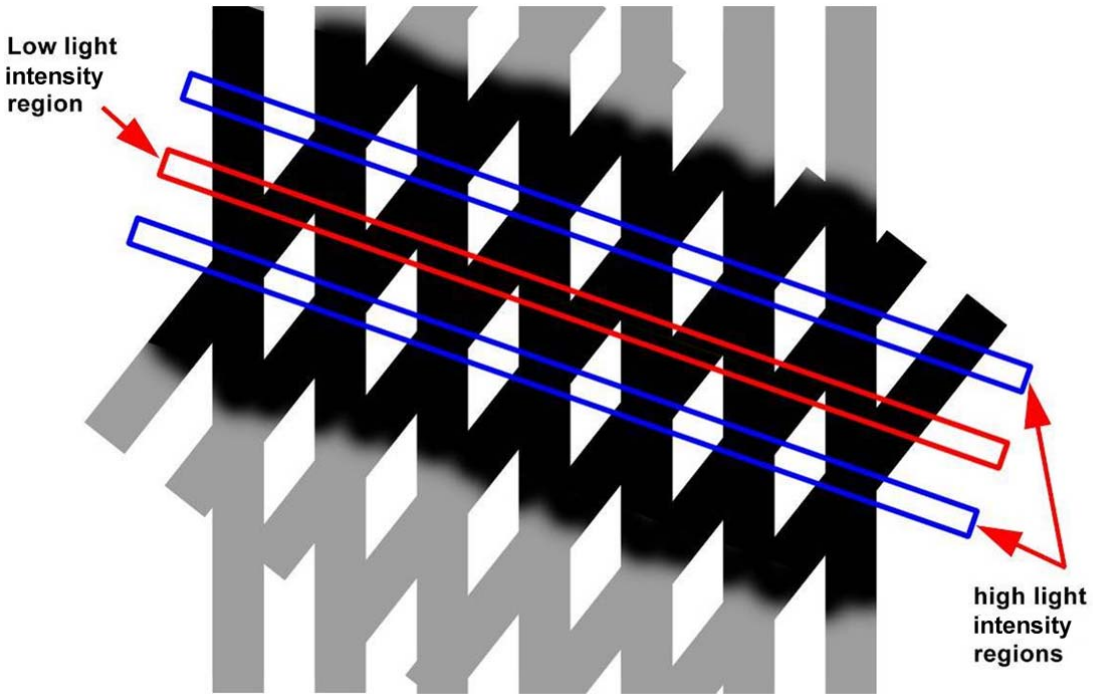

Fig. 2. The optical phenomenon causing the formation of moiré fringes.

The light colored areas overlapping in the superimposed patterns also produce continuous stripes, in this case with high light intensity (high light reflection and low light absorption). This happened as a result of stacking the adjacent light color diamond shaped areas. These diamond shaped areas are the result of light colored areas overlapping. These stripes with high light frequency are the regions that have the minimum dark colored area percentage and the maximum light colored area percentage. The minimum dark colored areas are the result of stacking the overlapped portions of the input dark lines to minimize the percentage of the resulting dark area.

The visual illusion resulting from the presence of the low light intensity stripe between two high light intensity stripes can be visually perceived as a continuous dark region. This dark region is known as the dark fringe.

In case of point-light-source projections or parallel projections, the deformation of a projected pattern in its simplest form is always an enlargement deformation with an amount relative to the projection angle. The larger the angle is the more the stretching factor will be. Superimposing the stretched line pattern on the original line pattern, or vise versa, will generate visually the third line pattern. This third pattern is the moiré dark fringes. These fringes are the result of line combinations which are derived from the two input patterns. These combinations are lines overlapping and lines separating, as shown in Fig. 3.

In these visual combinations, the fringes locations hold a record of lines overlapping and separation places. These places reflect the relative changes that the original line pattern went though to reach the deformed pattern form. From these relative places, information about the projection angle can be retrieved in relation to the reference plane. Depth information can also be quantified in relation to that reference plane.

Physically speaking, in its simplest form, each fringe happens once every time the original pattern is stretched with the amount of one pitch unit of the original grid. An example is projecting an original grid (of a one inch pitch distance between straight lines) into a reference plane containing an inclined flat surface with an inclination of 2 inches every 10 inches (20% inclination). Looking toward the reference plane with the inclined surface from an angled viewpoint of 45°, the resulting deformed grid on the inclined surface will be a stretched version of the original grid projection on the reference plane.

From the 45° angle viewpoint, while the inclined surface stretches the ten inch area received on its surface (11 grid lines), the stretched area will cover an area of 12 inches (13 grid lines) of the area received by the reference plane. When the 11 line-stretched-grid is superimposed on the 13 grid lines on the

reference plane, the result will be overlapped lines generating two moiré dark fringes.

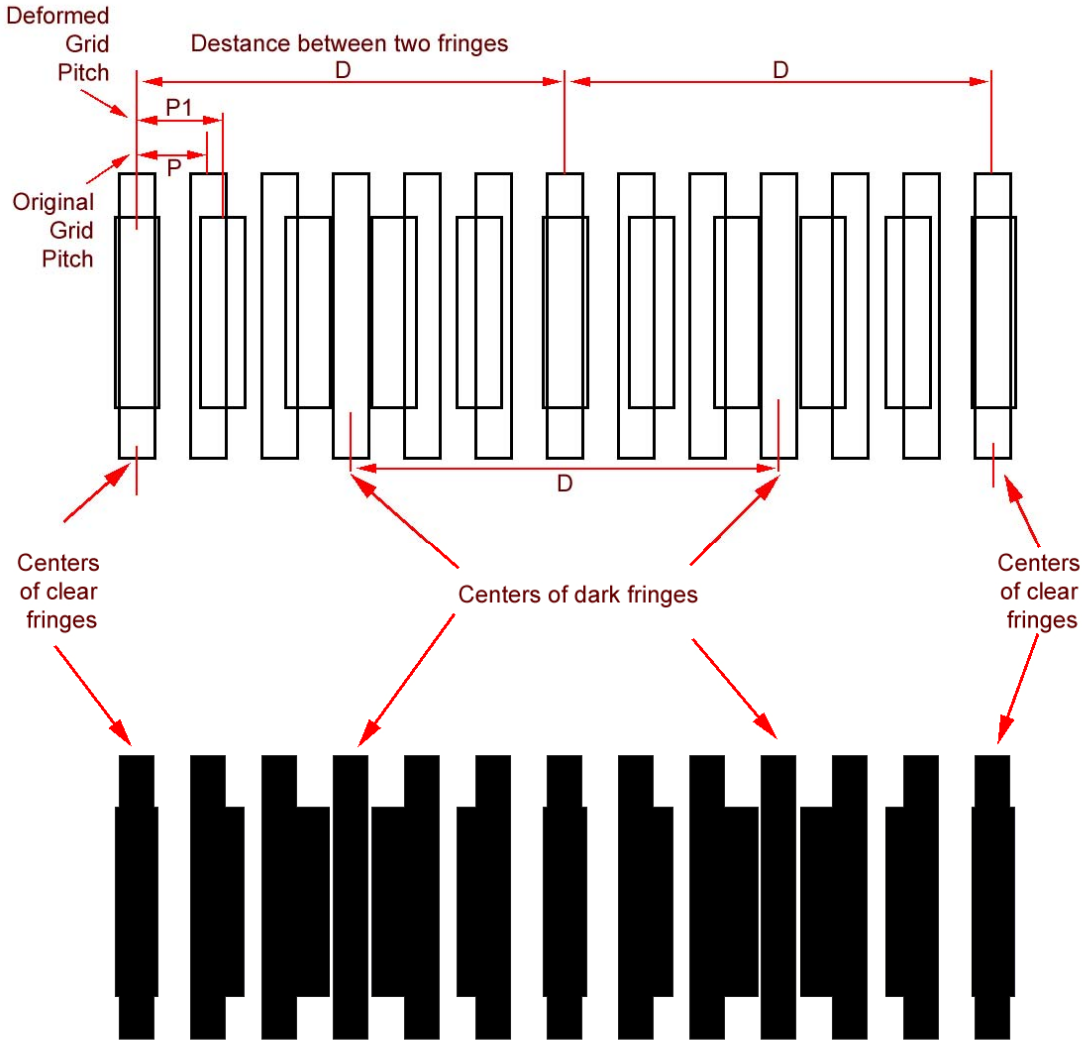

Fig. 3. Moiré topographic fringes formation from lines overlapping.[34]

These two dark fringes reflect the amount of the surface inclination in the form of contour lines. These two contour lines quantify the inclination as two inches for that surface (one pitch unit for each contour).

If the inclination was 30%, the 11 stretched lines will cover 14 reference lines resulting in three fringes indicating 3 inches of inclination and so on. In those cases, the relation with the 45° viewing angle involves the 45° angle tan which results with one unit inclination reflecting each fringe. When changing the viewing angle, the calculation for quantifying the inclination is not one to one but will involve the viewing angle tan, as shown in Fig. 4.

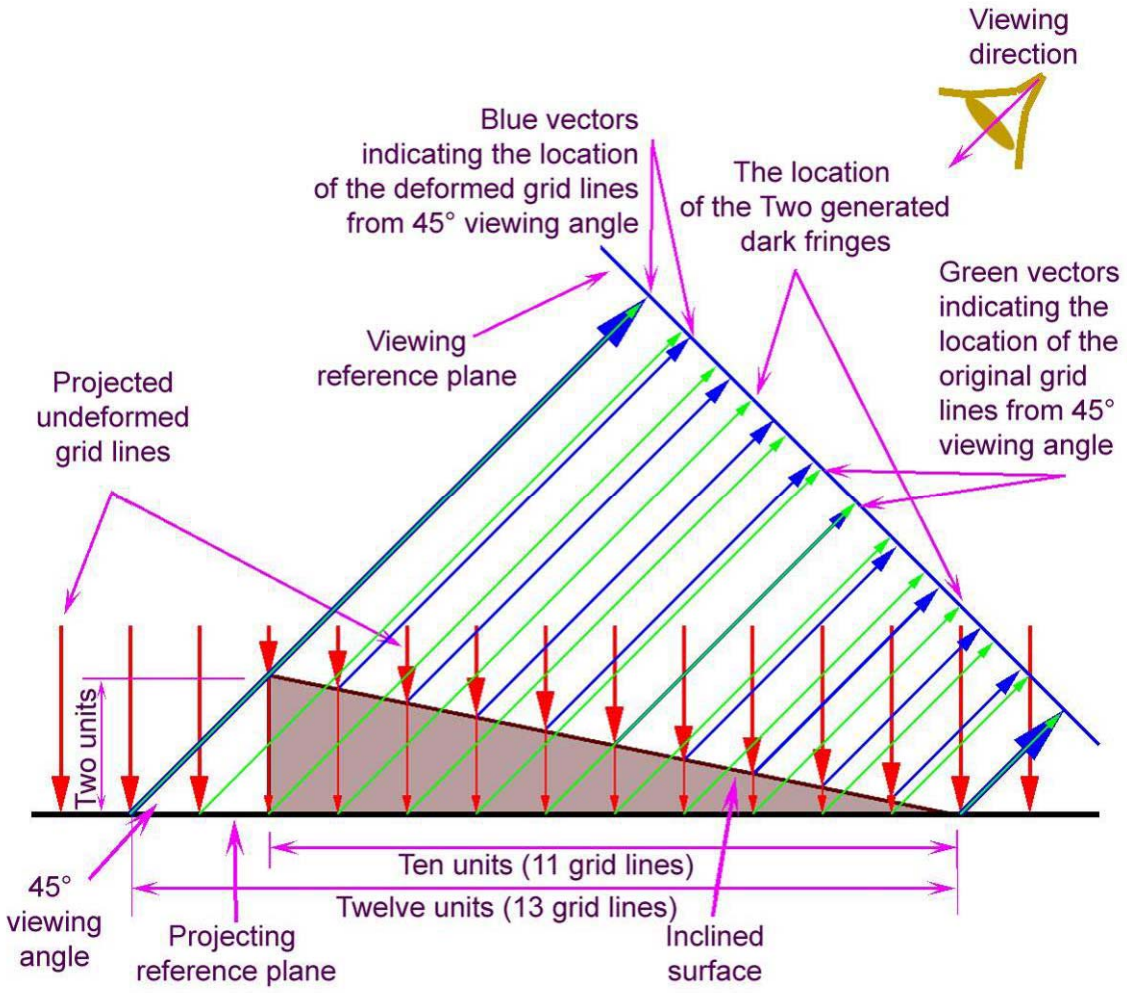

Fig. 4. The physics behind the formation of moiré topographic fringes.

These dark fringes can be straight dark lines if the distances are equal between the adjacent intersections. The variation in distances between the

adjacent intersections of deformed pattern lines and original pattern lines can cause a change in the direction of the resulting dark fringes.

The intersection of a deformed line more than once with a line in the original pattern can cause the resulting fringe to bend back and sometimes to form a closed topographic ring.

In general, moiré topography refers to the three main techniques (shadow, projection, and deformed grating types) commonly applied for the measurement and display of an object's three-dimensional form.[36]

Shadow moiré technique can be produced using a light source and a reference grid placed close to the evaluated surface, as shown in Fig. 5(a). A shadow of the grid is cast on the object surface. As a result of the object surface deformation, the grid shadow is distorted. By arranging the light source and the viewing point at a known distance from the grid, moiré fringes are generated as topographic contours when the distorted shadow is observed through the reference grid, as shown in Fig. 5(b).[35]

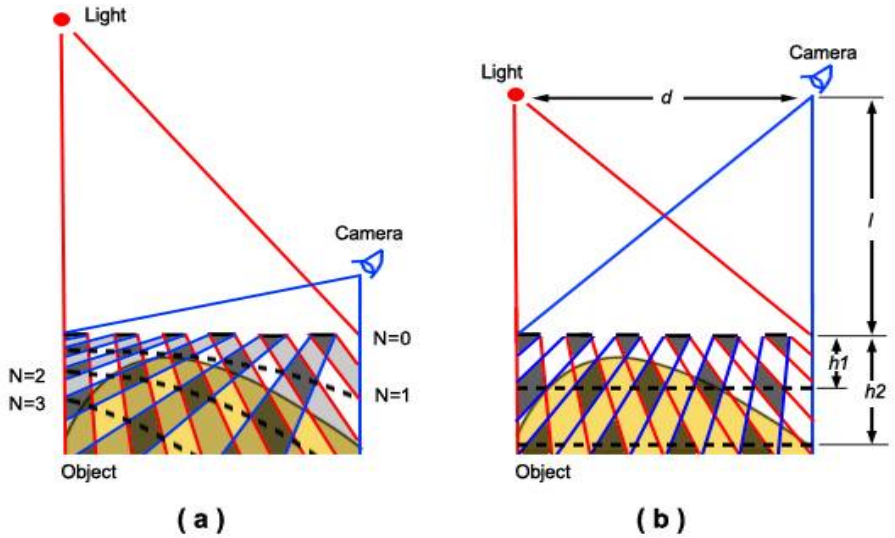

Fig. 5. Shadow moiré technique.[37]

Reflection moiré technique can be produced when projecting a reference grid on the object surface and photographing the result through a separate

reference grid. The formation of moiré fringes will occur on the recording camera image plane as a result of the two grid-images interference, as shown in Fig. 6.

Projecting two images of a reference grid from two positions, the resulting contours observed on the object surface are the additive projection type.[36]

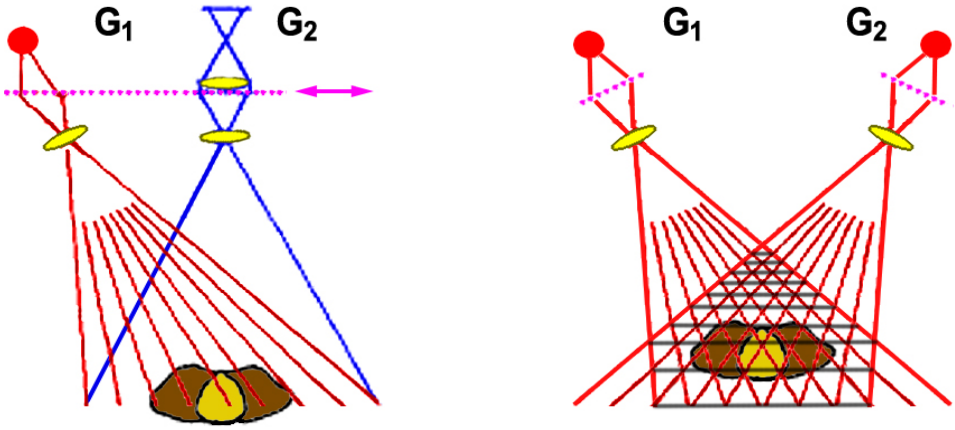

Fig. 6. Projection moiré technique. [36]

Deformed grating technique is the technique that was used in this study. This technique can be produced through photographing the object while projecting a reference grid on its surface, as shown in Fig. 7.

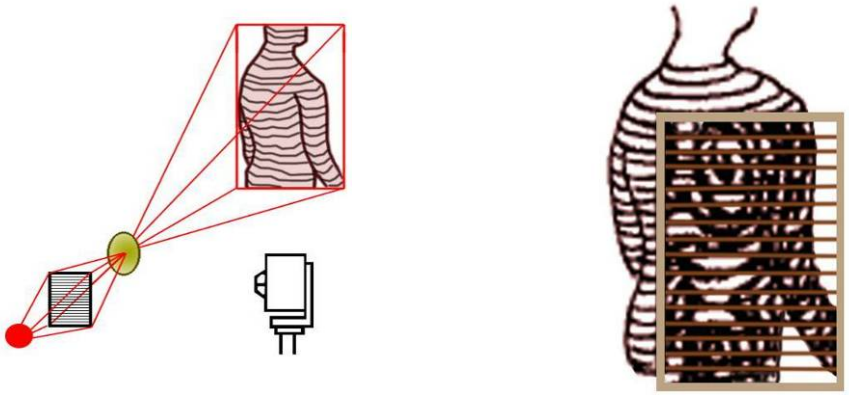

Fig. 7. Deformed grating technique. [36]

The photographed image can then be observed through another image of a reference grating on a reference plane. The result is contour fringes of the object's surface from the reference plane.[36]

Generally, the sensitivity of all moiré techniques depends on the pitch of the grating used in the process. The sensitivity is increasing when the pitch projected on the specimen is reduced. [38]

II.3.4. The mathematics of OMIT for 3D objects

OMIT mathematics refer to the mathematical equations involved in deriving the relative order and location of the dark fringes in space.

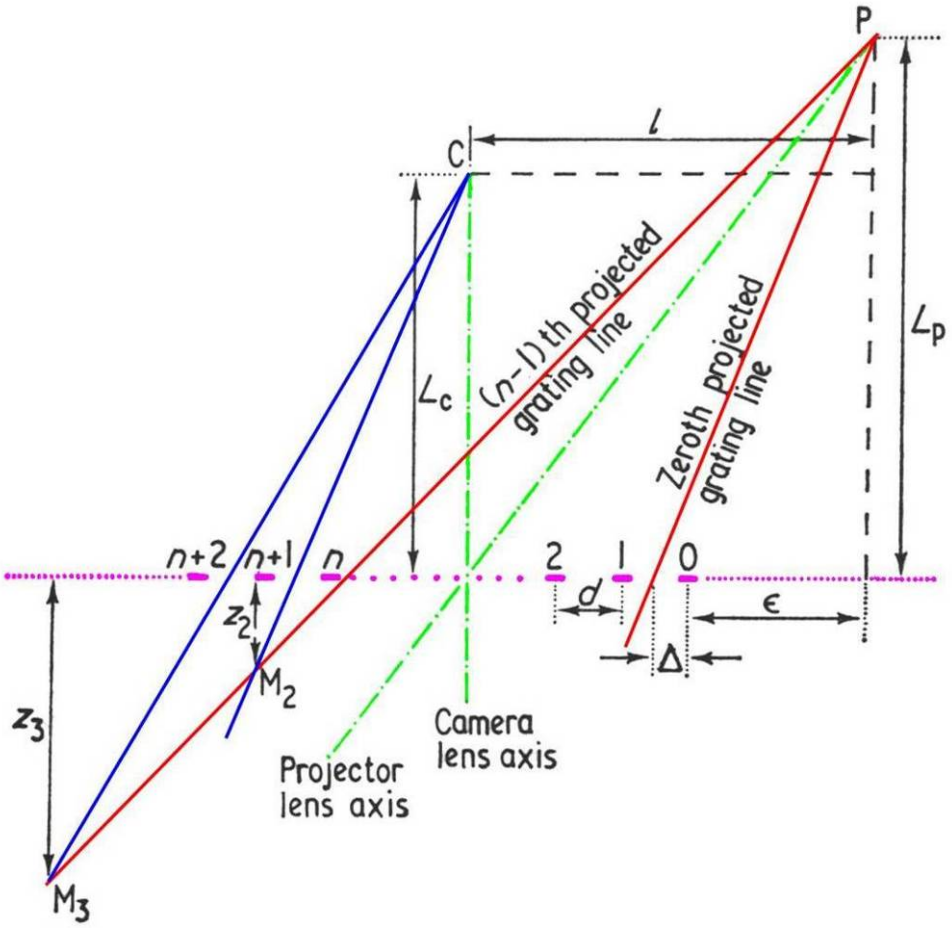

Fig. 8. Diagram for deriving the location of dark fringes. [39]

To derive the expression that gives the location formula of the moiré dark fringes, Miles and Speight in their research titled (Recording the shape of animals by moiré method, 1975) assumed the viewing grating to be located in the same plane with the reference screen.[1,39] They assumed that the viewing grating had the same pitch (d) as the reference screen and was out of phase by an amount (Δ), as shown in Fig. 8.

The researchers stated that dark moiré fringes are observed wherever straight lines connecting the camera lens nodal point with the center of a gap in the viewing grating intersect the straight lines connecting the projector lens nodal point with the center of a solid line in the reference screen, as shown for example at points (M2) and (M3). The numbered dashes from (0) to (n+2) indicate the viewing grating dark lines order. C represents the location of the camera lens nodal point. P represents the projector lens nodal point. Lc and Lp represent respectively the camera and projector distance from the reference plane. The distance between the camera and the projector is referred to as l.

In this arrangement, the researchers derived the distance (Zr) between the (rth fringe) and the reference screen through the following equation (1).

$$Zr = \frac{[(r - ½)\, d - \Delta]\, Lp\, Lc}{[\in + \Delta + (n-1)\, d]\, [Lc - Lp] - Lp[(r - ½)\, d - \Delta - l\,]} \qquad (1)$$

In this situation the fringes were numbered starting from the reference plane and escalating as the distance from the camera increased.

In the case where (Lc) and (Lp) are of equal distances of the value (L), which means that the camera and the projector lenses nodal points are in a plane parallel to the reference screen and at equal distance of (L) from it, the distance between fringe (Zr) is not a function of the line order (n), and it will not

be affected with the value of (n). This means that the location of the fringes will be planes parallel to the reference plane as in the following equation (2).

$$Zr = \frac{[(r - ½)\, d - \Delta]\, L}{l - (r - ½)\, d + \Delta} \qquad (2)$$

The researchers stated that in the special case of equation (2) when [$l >> (r - ½)\, d - \Delta$] the distance between adjacent fringes is approximately independent of the fringe order (r). This would produce an arrangement of dark fringes in approximately equal spaced planes, with a constant distance between adjacent fringes which is given simply by the following equation (3).

$$Z = \frac{L\, d}{l} \qquad (3)$$

Where (Z) refers to the constant distance between the resulting dark fringes and L is the distance from the reference screen to both the camera and the projector, d is the pitch value and l is the distance between the camera and the projector.

From arrangements that vary because of highly complicated variables with high accuracy results to very basic arrangements with minimum variables, equation (3) works as a simple base for arranging any moiré technique settings. The setting can be arranged using three variables; the pitch (d), the distance from the reference grid (L) and the distance between the projector and the camera (l).[40] In the special case when the distance (L) and the distance (l) are equal, the angle between the projector and the camera is 45°, and the distance between adjacent dark fringes (Z) is equal to the pitch (d). This arrangement will be used as the research experiment settings to perform the OMIT measuring method.

II.3.5. Geometry principles of the OMIT for 3D objects

In moiré techniques, the three-dimensional information derived from any used type is defined by projective geometry based on two projection centers in relation to the projection plane. In shadow moiré those centers are the location of the light source and the location of the camera lens in relation to the grid location. In projection moiré and deformed moiré those centers are the location of the projector and the location of the camera lenses in relation to the location of the projection plane.

In that scope, the geometry of moiré techniques is closely related to stereo-photogrammetry. They are related in the sense that both techniques depend on two sets of imaging information produced from two related positions.[37]

In stereo-photogrammetry, the two images included serve as a real representation of the visual characteristics of the object. These two images are employed in extracting the special 3D location of any defined point that can be identified visually on the images of the object's surface.[35]

In the moiré method, the techniques assume that the distorted grid, when viewed from the projector location, will look like the same reference grid with no distortion (according to that viewpoint). The other image from the camera location will record the distortion of the reference grid on the object surface from that location. Based on that assumption, in order to encode three-dimensional information about the object's surface, only one set of imagery information is needed in moiré techniques (the camera image showing grid distortion); the image of the reference grid itself (away from the object or the sitting) serves as the other image set.

As a depth measurement method, the comparison of the two states of almost identical grids is the basis for moiré technique. The first state is the initial state (reference or unloaded grid), and the second state is the modified state (distorted grid associated with surface deformation of the object). Based on that,

the changes in the grid appearance from one state to the other hold the perpendicular displacements experienced by the surfaces with respect to a reference plane. [35]

According to this, the distance in depth between the resulting moiré fringes depends on the distance to the object from the two projection centers as well as their relative distance from each other. Those three distances determine the resolution and accuracy of the depth information derived from moiré images, as they do in stereo-photogrammetry.[35]

The moiré techniques are unique because they include an integral measurement principal that readily displays fringes indicating the topography of the recorded object.[27] This important feature sets moiré apart from stereo-photogrammetry where point-to-point measurements need to be defined and calculated to determine the surface deformation.[35]

II.3.6. Moiré applications

Intentionally created for measurements purposes, the measurement of deflections of thin sheets under loads was an early example of shadow moiré.[35]

An early application was the evaluation of in-plane stress analysis by viewing grid changes printed on the structure surface through a reference grid.[34]

Reflection moiré is another technique used for the same purpose with mirroring surfaces to form a virtual image of the reference grid.[34]

The determination of horizontality, deformation, vibration, refractive index and angular measurement are also applications in the field of metrology and machine vision.[1,35] Deformation measurement of large structural members of aircrafts fuselages is an example of moiré topography use in the aeronautical industry.[1]

The contemporary vast use of moiré interferometry techniques were introduced in many fields of science and engineering. An example is its use in biomechanics science for documenting the effect of changes of moister content

on human teeth.[29] It was used also in electrical engineering for electronic packaging on a microscopic level. In manufacturing, it was used for monitoring residual stresses induced in composite manufacture during the curing process. Other uses utilized video techniques[1] and high speed photography to extract geometric information of a dynamic phenomenon[29] on an object in real time.[41] Some uses in medical applications incorporate measuring the human body form, screening and analysis of spinal deformity for the early detection of scoliosis, facial asymmetry and anterior chest wall deformities.[1]

Other medical applications included the determination of volume and surface area for human body parts, morphometric studies of the feet in clinical diagnosis, the reconstruction of human anatomical parts and determining the corneal configuration of the human eye and monitoring domestic livestock of nonhuman subjects.[1]

Various civil engineering applications utilized moiré topography in structural assessment. One of the many examples is the structural assessment study of a thousand Victorian bridges in England. The process was carried out by stitching hundreds of pasted A3 size sheets of coarsest patterned paper and monitoring the resulting moiré fringes under different loads.[42]

II.3.7. Deficiencies in moiré topography

Most Moiré deficiencies are related to visibility of fringes, imaging method, object form, environment dynamicity, and object location in space.

Some problems related to fringe feasibility are: incoherent noise, fringe contrast, fringe sharpness and surface slope limits.

Incoherent noise refers to the unresolved individual grid lines projected on the object surface. To reduce this problem the physical characteristics of the carrier (the object surface) should reflect the light with coherent noise. This is essential to result resolvable individual grid lines on the objects surface in the

final moiré images.[1] This deficiency was reduced by treating the investigated surface with suitable finishing materials.

Another deficiency is fringe contrast, which is defined optically as the ratio of the difference between the maximum and minimum signals over the sum those signals. This deficiency is associated with the surface reflectivity, the object shape properties, the projector variables like illumination, grid design and imaging optical sensitivity and linearity. Maximum contrast can be achieved when the reference and deformed grid are perfectly resolved by generating images of the projected patterns with darker lines and brighter backgrounds.[1] To reduce this problem in this research, the issues of the projecting equipment resolution and illumination, the imaging equipment resolution and linearity and the projected pattern design, color and contrast were taken into consideration.

Fringe sharpness is another deficiency which refers to the amount of bright and dark fringe boundary differentiation around the fringe center. The low differentiation level results in uncertainty in tracking the center of the fringe. This can be reduced by using binary grids with a square-wave transmittance profile by alternating opaque bars and transparent spaces of equal width.[1] That approach is used in this study to maintain fringe sharpness. The use of software solution for color manipulation to reach higher contrast is also employed in this research to increase fringe sharpness.

Surface slope limit is another deficiency which indicates the amount of surface inclination. Small surface inclinations tend to narrow the projected lines on the surface, increasing its effective spatial frequency. In the large inclinations the low end of the dark line frequencies tends to overlap the dark lines with high frequencies which generate what is called “alias moiré patterns”. Alias moiré pattern can be noticed starting at 30° surface inclinations. With high resolution sharp projections the limits can be pushed up to be noticed at 63° inclinations and in some arrangements can approach the 85° surface inclination.[42-44]

This concern, which was noticed in the pilot study, was overcome in this research by designing the model with inclination lower than the 30° limit.

Problems related to imaging methods are similar to problems with the two and three vanishing points perspective distortion. In the case of a central perspective view, the need for correcting perspective distortion should be considered also. For this case, and for very precise measurement, different in-plane scale factors must apply to the fringes, depending on their distances from the camera.[45] In this research this problem was overcome by targeting relatively low measurement accuracy and relatively small depth range in comparison with the camera distance from the object surface.

Problems related to the object form, such as depth sign determination (hill and valley), can be overcome by extracting the shape-from-shading or involving prior knowledge of the shape.[1] This research used the approach of prior knowledge to overcome this problem. In automated systems there is a need to use special techniques or arrangements to determine depth sign. One example is using double images to produce stereo moiré. In a single image approach, other techniques are used such as raster moiré which refers to projecting thick fiducial lines on to the object along with the pattern to stay visible and encode the depth direction.[1] Other more complex techniques used for that purpose depends on manipulating the relation between the deformed grid and the reference grid and the location of the reference plane in relation to the object surface. Some of those techniques are phase-shifting, phase-difference-scanning, phase-disjoint, and oblique moiré.[1,41,46]

Another problem related to object forms is the difficulty of encoding depth measurements for sharp edges and surfaces stepping. To solve this problem some techniques were developed to generate asymmetric moiré fringes to increase encoding capabilities near edges and steps by increasing the ability to track the unique fringes around edges or steps. Most of those techniques depend on intensity and spectral modulation.[1] In this research, this problem was

eliminated by designing a continuous organic model surface with no edges or steps.

For dynamic environments and for using moiré techniques outside of the controlled lab environments, special arrangement and techniques are needed to overcome occurring deficiencies. Techniques for dynamic moiré fringes were developed to relate deformed grid to a reference grid in dynamic positions. Most of these techniques depend on using movable reference plane located at the position of the original object in special arrangements to generate the reference grid. Some of those techniques are object-and-plate translation which will be used in this research. Other techniques include object-and-plate-rotation and phase lock moiré. More complex techniques use laser light like holographic moiré, holographic phase-lock-moiré and heterodyne moiré. Other techniques use a digitally generated reference grid like detector grid moiré, digital grating moiré, scanning moiré and video-electronic moiré.[1]

Problems related to object location in space are like fringe ordering determination. The problem of non-linearity of the fringe contour interval should be considered for high levels of accuracy and tiny projecting and imaging distances. The corrections can be made based on derived equations. To determine absolute fringe ordering, methods such as the following are incorporated: using a reference plane at a known distance, using a reference line and using a reference plane with control points.[1] This approach was encompassed in this research by marking a reference plane parallel to the fringes by three control points at a known relative position.

CHAPTER III

RESEARCH PROCEDURES

This chapter establishes the research methodology for performing this study. The pilot study is discussed, explaining experimental variables, investigating method instrumentation, experimental samples, and the data treatment method.

III.1. Research methodology

As a first stage, a pilot study is performed to test the validity of employing the OMIT for recording surface relief contours of historic elements based on measurement accuracy and relief measuring potentials. The encountered problems, limitations and difficulties are considered in the second stage.

In the second stage, supported by the pilot study findings, the research examines the feasibility of using the OMIT for contour recording of historic elements with fine-grain surface relief based on time-consumption of the recording process. This time-consumption feasibility for the OMIT is examined against the hand measuring method as the compared traditional recording method.

The examination started by testing the acquired depth data of each sample against the error threshold of one eighth of an inch. This threshold was established based on the smallest unit required by the Historic American Building survey (HABS) guidelines for producing measured drawing for ornamental and construction details and molding profiles.[47] By involving the approved samples against an accuracy measurement threshold, the research compared the processing time for the two methods samples. Based on time-consumption, the methods comparison provided the base for the conclusion about the feasibility of using the OMIT in the heritage recording process.

III.2. Pilot study

The pilot study tested the OMIT method as an effective measurement technique for reducing a major challenge facing traditional technologies.

That major challenge was producing surface relief records for organic shaped objects with irregular fine-grain surfaces.

The pilot study started by testing the applicability of acquiring valid depth data by applying the moiré deformed grating technique using domestic equipment. The investigation targeted the surface relief of a specific object with a surface area of approximately one hundred square inches. The contours of objects with basic-shapes, defined-sizes and fine-grain surface relief were acquired using OMIT. These objects were a manufactured plastic foam sphere of three inches radius, a manufactured plastic foam cone with 6”X3”X1” dimensions, and an assembled cardboard calibration ramp 3.5 inches tall.

Fringe visibility problems such as incoherent noise, fringe contrast, fringe sharpness, and alias moiré patterns in the large inclination portions of the surfaces were noticed. Limitations related to projection size, resolution, pattern colors, and pattern forms were also inspected.

Line and background colors of the projected grid were manipulated digitally and tested to reach the most convenient combination of colors to generate dark fringes with the highest visibility possible.

For generating highly visible dark fringes from superimposing the deformed grid on the reference grid, the main concept was to use the operations offered by Photoshop software to test different layer combination using layer mode change. Some of those combinations are multiply, darken, lighten, and difference modes.

The idea behind identifying the best color combination in the input images is to reduce the number of colors in the final output image resulting from the superimposing procedure. The input contract colors used were the blue color for the lines (R 000, G 000, B 255) and the yellow color for the background (R 255,

G 255, B 000). When using the multiply tool in Photoshop to superimpose the input image layers, three colors were noticed in the output image. Those three colors resulted from overlapping (Red, Green, Blue) color values of the stacked pixels from the three-color combinations. The first resulting color from lines on lines is the blue color (R 000, G 000, B 255). The second resulting color from lines on background is the black color (R 000, G 000, B 000). The third resulting color from background on background is the yellow color (R 255, G 255, B 000). The dark fringes in that situation were hard to spot and follow and the surrounded areas where visible, as shown in Fig. 9.

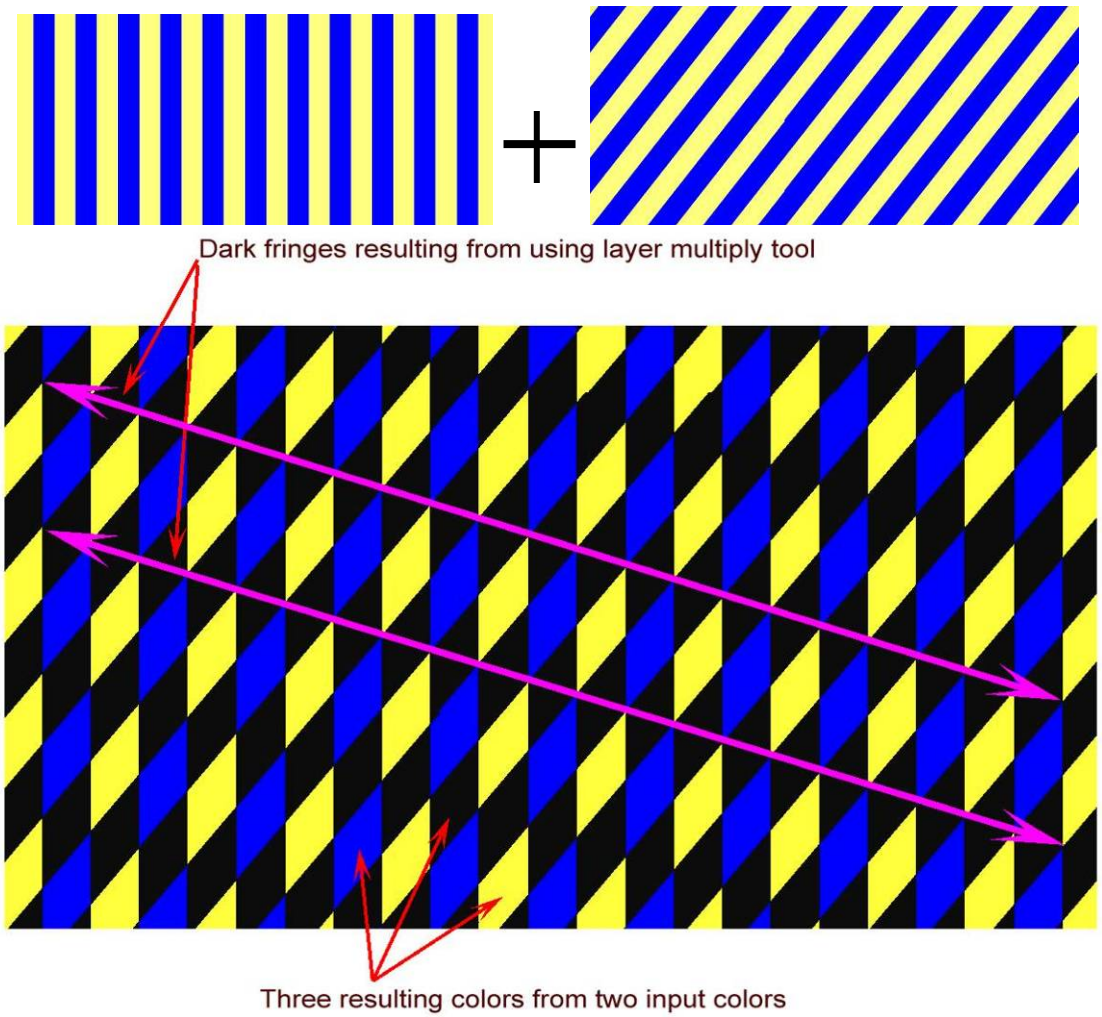

Fig. 9. The input colors and the visibility of the dark fringes using multiply tool.

To reduce the visual effect of color smear on the resulting fringe visibility, the difference tool was used for superimposing layers. This tool subtracts the stacked pixel color values. Two colors resulted from this combination. The first resulting color is the black color (R 000, G 000, B 000) from lines on lines and background on background. The second resulting color from lines on background is the white color (R 255, G 255, B 255). The dark fringes in this situation were one fringe shifted but they were easy to spot and follow and the surrounding areas were neutralized, as shown in Fig. 10.

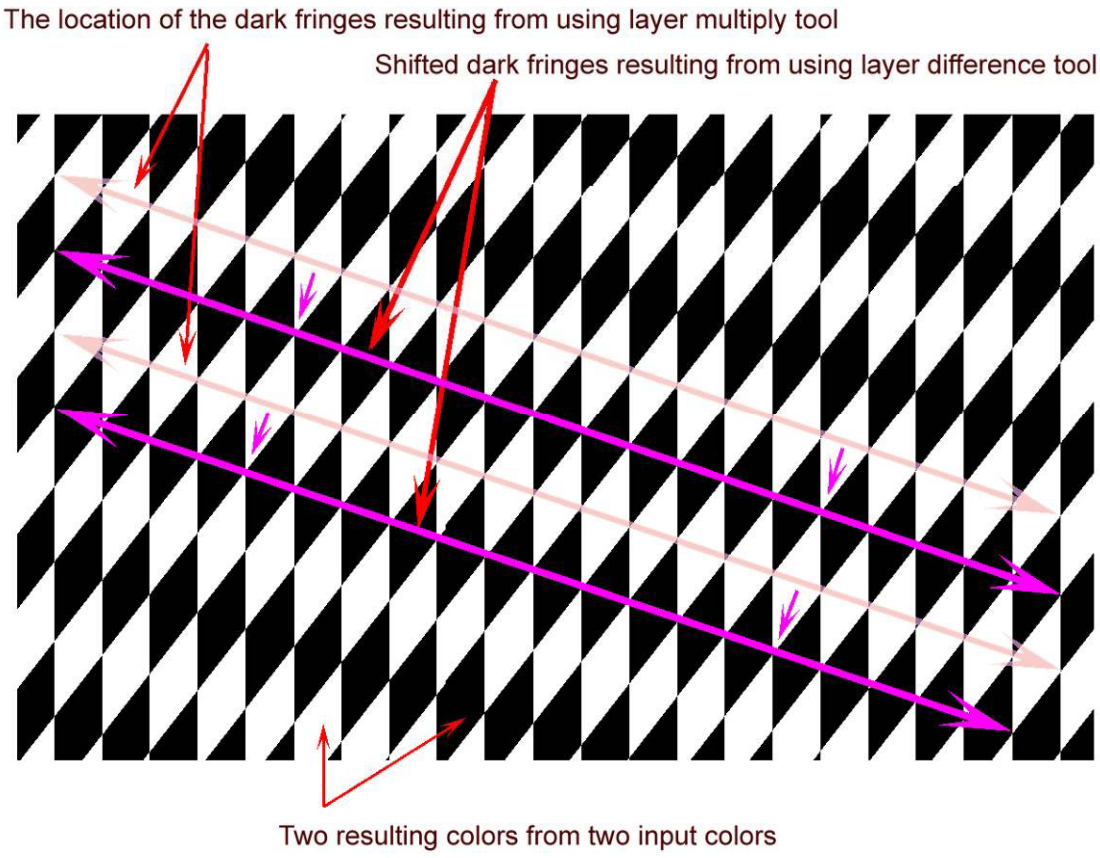

Fig. 10. The input colors and the dark fringe visibility using difference tool.

To isolate the white color resulting from superimposing the white color resulting from light overexposure, the background color was readjusted. The background color used was the light yellow color (R 255, G 255, B 127). In this case, the two colors resulting from difference superimposing were the black color (R 000, G 000, B 000) from lines on lines and background on background and the light yellow color (R 255, G 255, B 127) from lines on background. Using this combination, the overexposure white color was isolated and the resulting dark fringes were easy to spot and follow, as shown in Fig. 11.

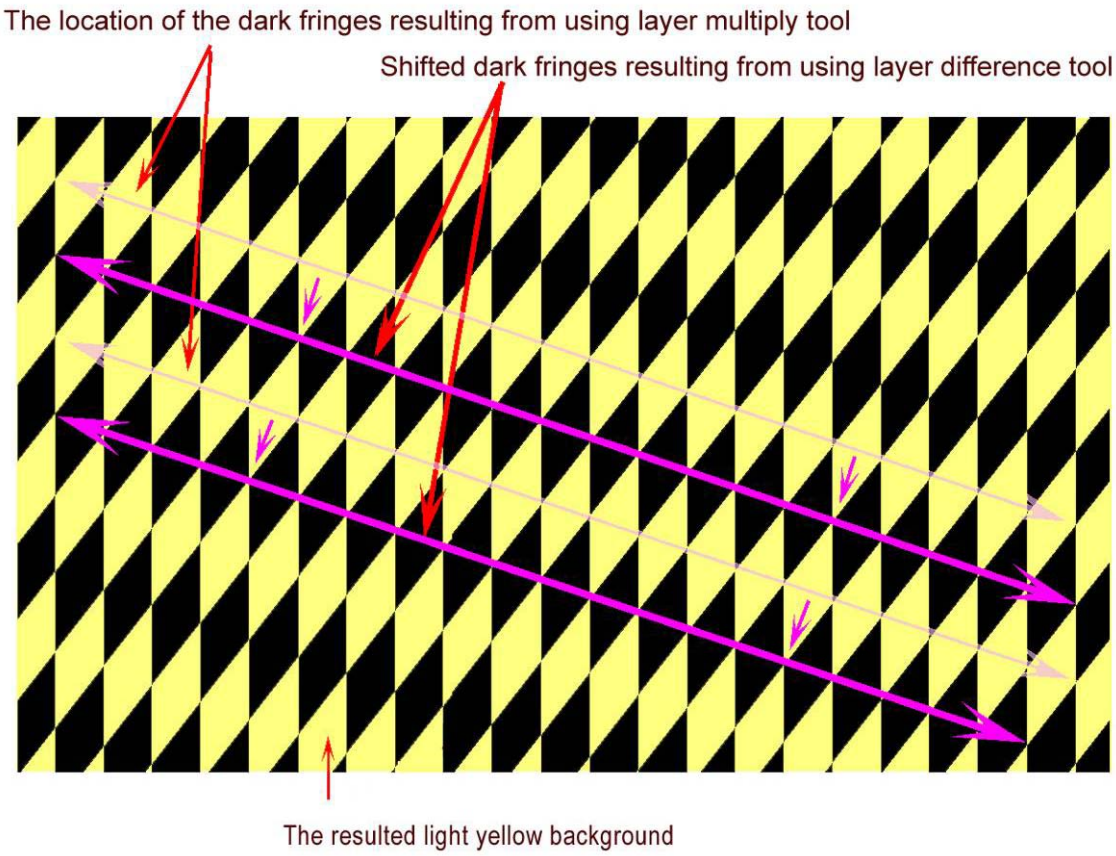

Fig. 11. The visibility of dark fringes using light yellow background.

Using the difference tool and the readjusted color combinations, the visibility enhancement on the resulting dark fringes can be noticed in Fig. 12.

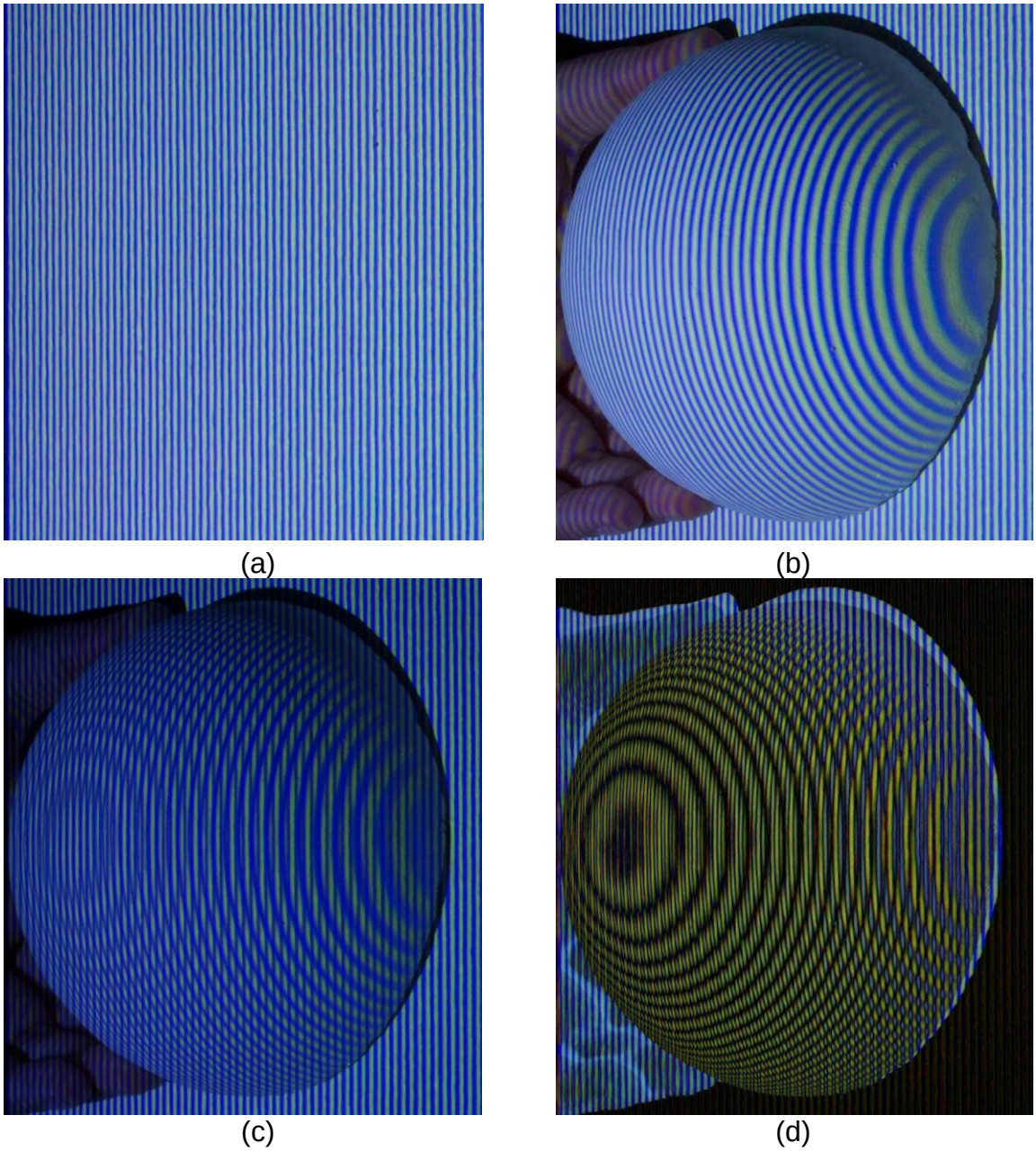

Fig. 12. Visibility enhancement on the resulting dark fringes. (a) The reference pattern with blue and light yellow colors, (b) the deformed pattern, (c) The dark fringes poor visibility using layer multiply tool, (d) The dark fringe visibility enhancement using layer deference tool.

For every object's surface, the accuracy of the resulting moiré contour fringes was examined in relation to the predetermined projected pattern size of 1/8th of an inch. The arrangements of the projector, the camera and the object orientation in relation to the reference plane were also investigated, as shown in Fig. 13.

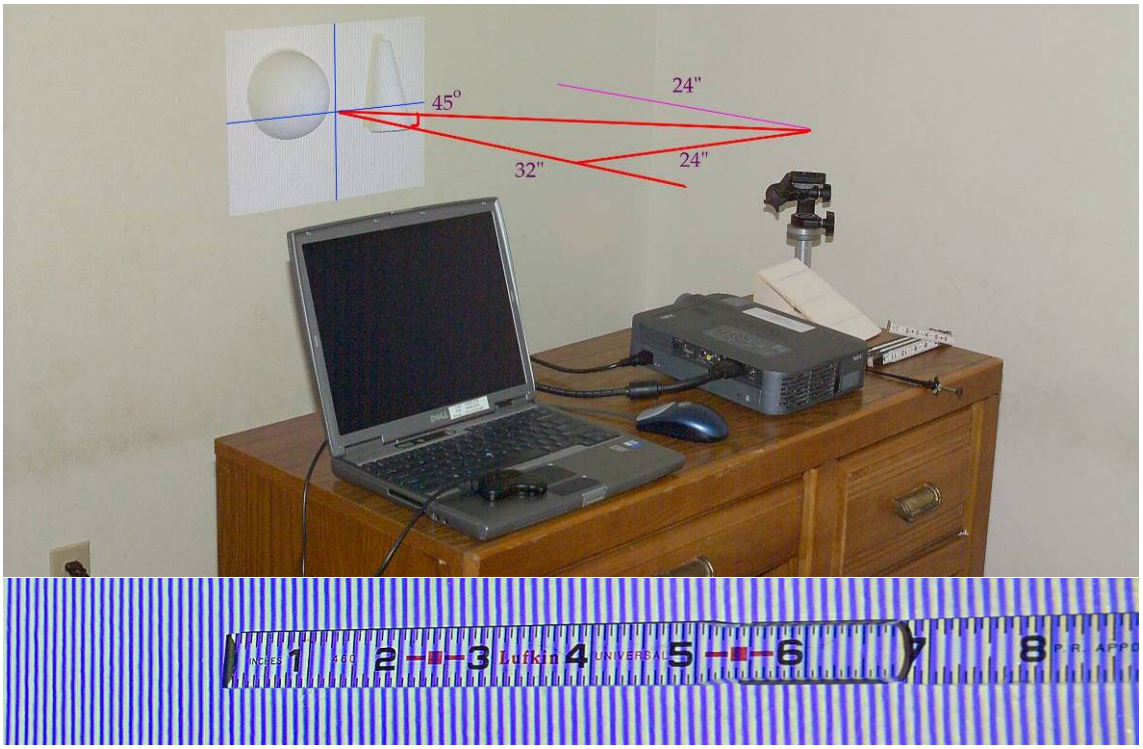

Fig. 13. Pilot study experimental arrangements and projected pattern scale.

Investigation about the maximum projection area offered by the available LCD projector to maintain the highest resolution and the appropriate scale of the projected grid was carried out and tested.

Depth measurement accuracy examination was carried out by utilizing the produced moiré contour data to work as the depth measurement when creating a 3D digital representation of the objects, as shown in Fig. 14.

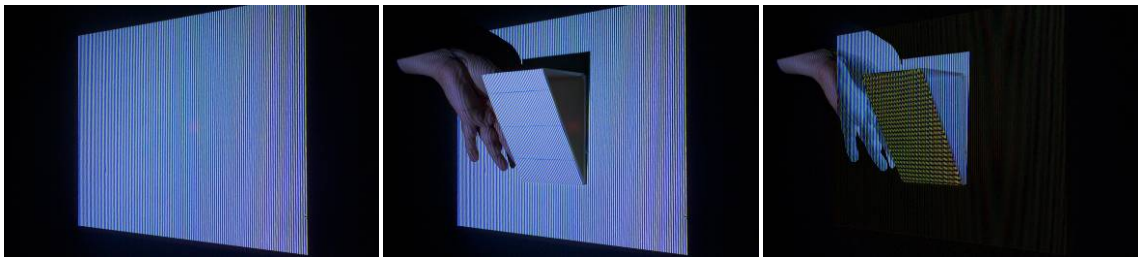

(a)

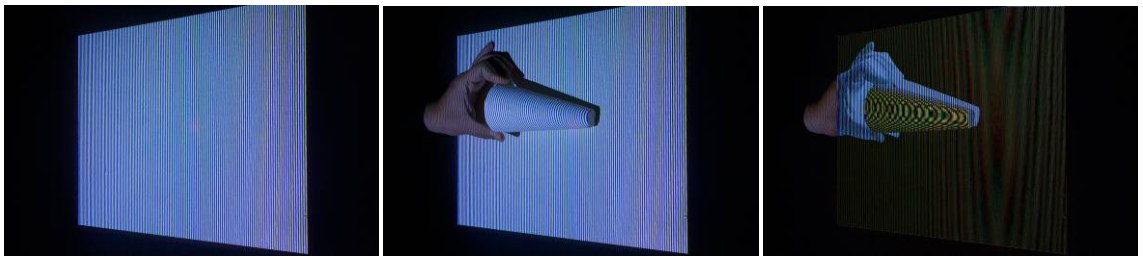

(b)

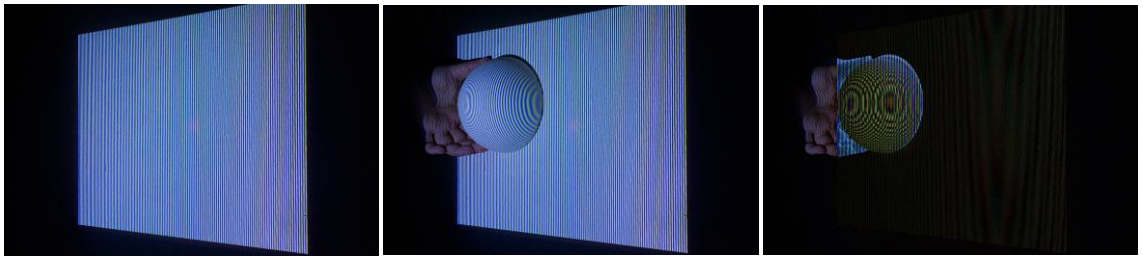

(c)

Fig. 14. Moiré contour data for the targeted objects. (a) Calibration ramp reference projection, deformed projection and the resulting moiré fringes, (b) The cone reference projection, deformed projection and the resulting moiré fringes, (c) The sphere reference projection, deformed projection and the resulting moiré.

For this step, the actual camera and projector arrangements in relation to the location and orientation of the measured object were reversed virtually using 3D studio viz. To accomplish this, the acquired moiré image from the real camera location was projected virtually from the virtual camera to an imaginative surface facing the camera, as shown in Fig. 15.

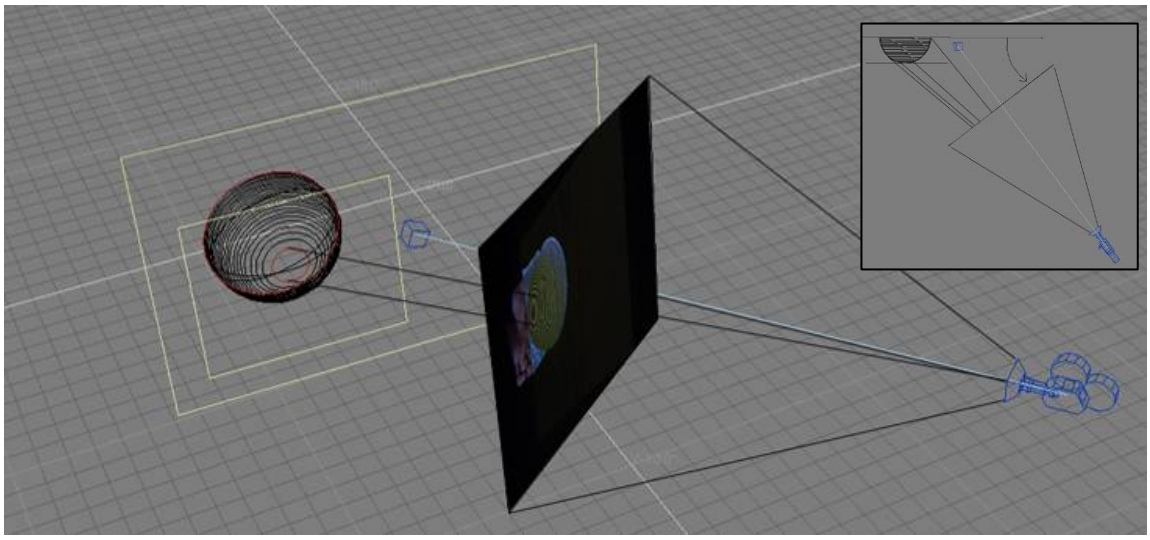

Fig. 15. Virtual reversing of the sphere to create the 3D digital model.

Moiré fringes were traced on that imaginative surface and were virtually projected back to their correspondent assumed depth plane parallel to the original reference plane. By combining the projected traced fringes, the 3D object digital representation was produced, as shown in Fig. 16.

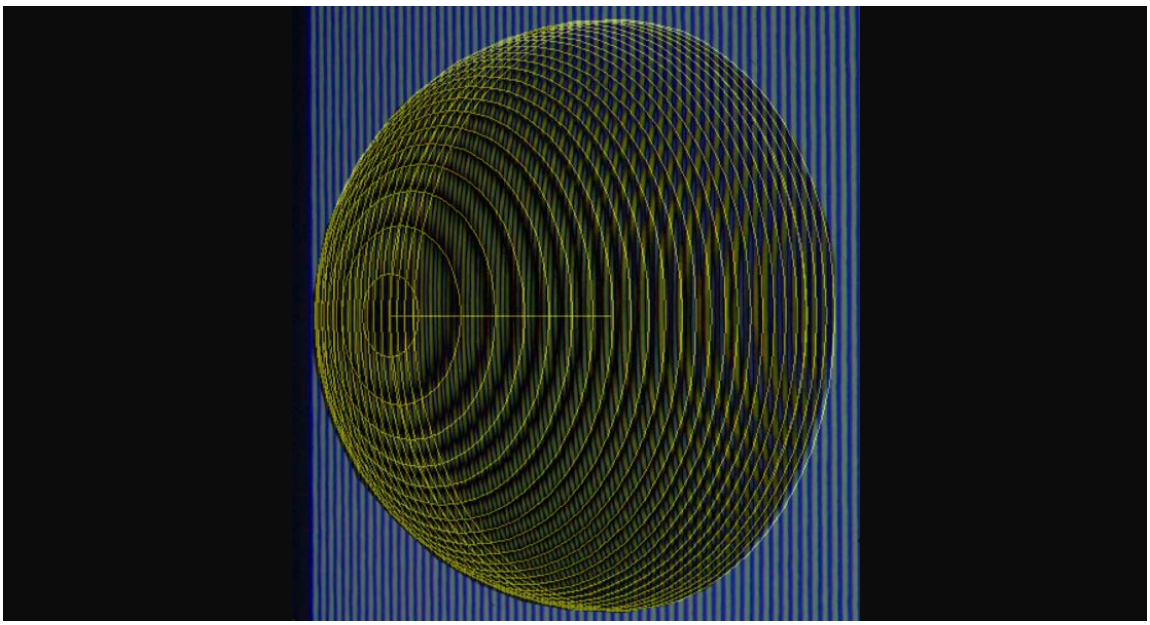

Fig. 16. Virtually tracing and projecting the reversed fringes.

Depth measurement validity of the reversed fringes were tested by comparing the number and location of the virtually reversed moiré fringes with the number and location of the contour lines produced from hand measurements at the targeted accuracy, as shown in Fig. 17.

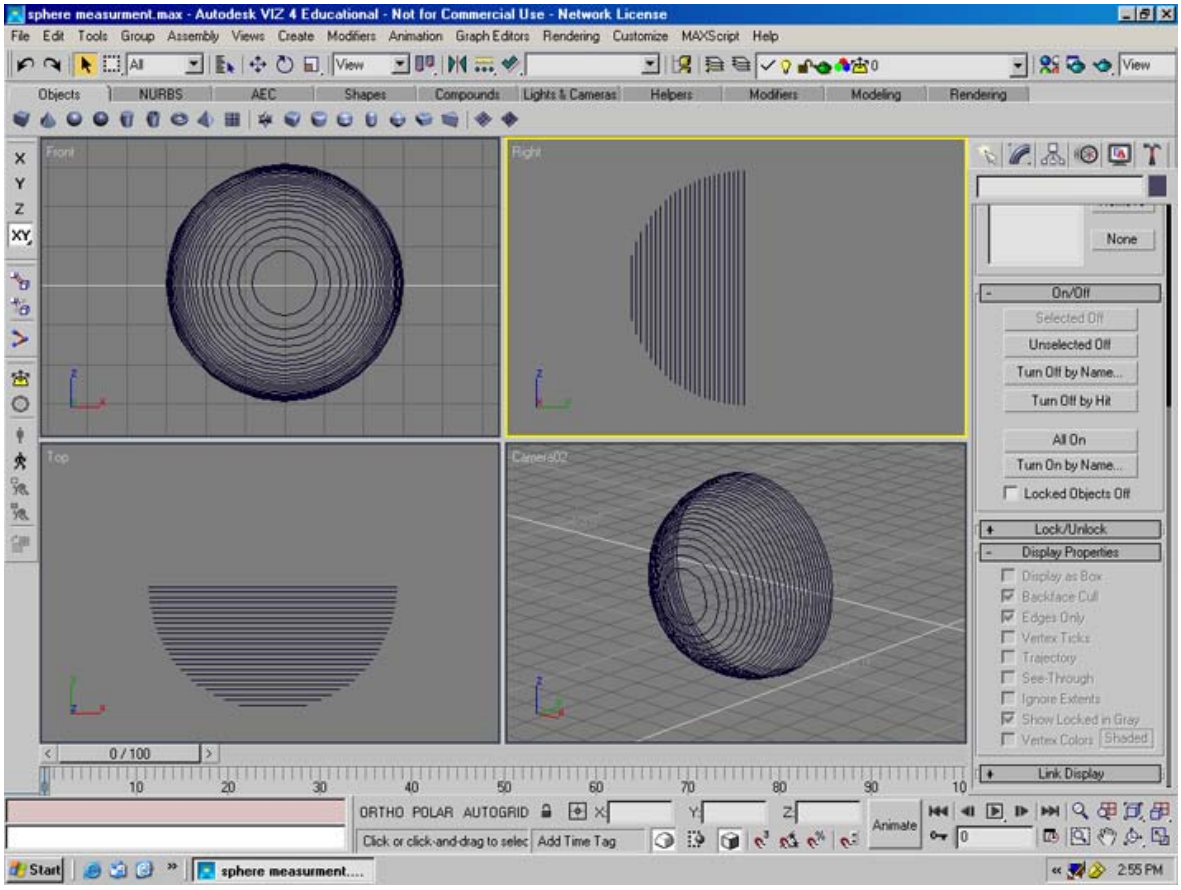

Fig. 17. Testing depth measurement validity of the reversed fringes.

Based on the findings at this stage, the study established the appropriateness of producing the targeted depth measurement using OMIT as a less challenging depth recording method for these kinds of objects, as in Fig. 18.

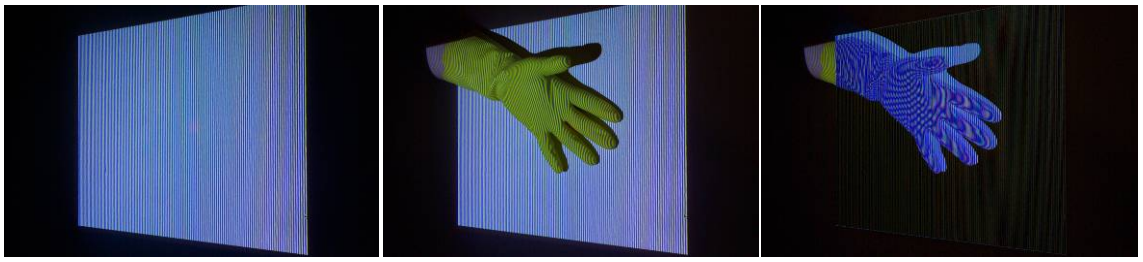

(a) (b) (c)

Fig. 18. Moiré contour of a glove as an example of a complicated object. (a) Organic form reference projection, (b) deformed projection, (c) the resulting moiré fringes.

III.3. Experimental variables

As the previous literature and the pilot study established, the variables in this experimental study were causes or independent variables and effects or dependent variables.

Generally, one way of experimental investigation is to study the impact of specific identifiable variables on the investigated phenomenon.[48]

Based on this approach, this research seeks to investigate the impact of using a tested measuring method on depth measurement accuracy levels and measuring process time-consumption and compare the result against a control method to conclude the feasibility.

In that scope, this study seeks to evaluate time feasibility of using OMIT method for recording surface relief depth measurement. Hand measuring method was identified in this study as a well established traditional measuring method to be used as the control method. On the other hand, OMIT measuring method was identified as the tested method.

In this experimental approach, independent variables are included to generate a change in the dependent variables that are needed to support study objectives. Independent variables (causes) are the variables generating or affecting the results. Dependent variables (effects) are the resulting variables

from manipulating the independent variables. Those dependent variables are the targeted results that form the base for the study conclusions.

To demonstrate the meaning of those variables, here is an arithmetic example: when adding variable (a) as any integer value to variable (b) as any other integer value, the resulting value is the variable (c). In that example the variables (a) and (b) are independent variables as they can be any integer values. The variable (c) is a dependent variable as its value is definite and reliant on the values of the independent variables (a) and (b)

In the research experiment, the independent variables were grouped into four categories: the physical model variables, the true model measuring method variables, the hand measuring method variables and the targeted OMIT measuring method variables. The dependent variables were classified in two categories; depth measurement accuracy level and recording processes time-consumption.

III.4. Instrumentation and variables

The instrumentation in this research refers to the tools and equipment used in the experiments for establishing the true model and generating data from the compared methods.

III.4.1. Physical model instrumentation and variables

The first category in the independent variables is the physical model variables. Those variables are surface formation, surface finish and surface size.

For performing the comparison in an experimental setting, a physical model with fine-grain smooth surface was designed to act as the heritage element under the measuring process. A 10 inch by 10 inch surface area of smooth organic shapes was created with hill and valley portions to simulate the organic nature of an eroded fragile heritage element.

The physical model was created using a base of two-inch-thick plastic foam sheet. The top face of the plastic foam sheet was carved near the middle to form an inch deep recessed portion. Paper sheets saturated with compound filling were layered on top of the surface to create the hilly areas. These paper sheets were also used to cover the entire surface with a smooth homogeneous finish.

The surface formation was determined to produce surface with around 22.5° maximum inclinations (quarter of an inch in Z for one inch in X,Y) to eliminate the deficiency of the surface slope limits discussed earlier in chapter two (section II.3.7). The model surface was covered with layers of off-white sprayed plastic paint to create the fine-grain finish. This finish treatment was determined to minimize the effect of the incoherent noise discussed earlier (section II.3.7) The model surface boundary was defined with a region area of 10 inches height and 10 inches width.

The surface size was determined based on the pilot study investigation about the maximum projection area offered by the available LCD projector to maintain the highest resolution of the projected grid. The maximum depth between the hill and the valley portions of the surface relief was around two inches deep. This relatively small depth range was determined to minimize the imaging method distortion effect of the central perspective view discussed earlier (section II.3.7).

For this investigated deformed grating technique, a flat surface was also prepared on a separate piece of plastic foam to work as the reference surface as discussed earlier (section II.3.3). The same finishing was applied on this surface defining the same boundaries as the physical model, as shown in Fig. 19.

Fig. 19. The physical model made from a plastic foam sheet.

III.4.2. True model measuring method instrumentation and variables

The second category in the independent variables is the true model measuring method variables.

At first, an available total station instrument was evaluated to be included to establish the true model measuring method. To test measurement accuracy limits for the instrument, measurement data of defined points were collected from one hundred measurement samples. The sampling process was performed in the lab setting under controlled conditions. The results indicated an average measurement error of three millimeter (around 0.12 of an inch). This error level was considered high and unsatisfactory for establishing true model measurements for the research purposes.

Based on earlier investigations and evaluations of the accuracy of the extracted measurement, close range digital photogrammetry software (Photomodeler 5.02 pro) was chosen for establishing true model

measurements.[49] The true model measuring process will be discussed in detail in the following section (IV.1).

The independent variables for the true model measuring method are associated with the photogrammetry software variables including the marked targets spacing, location and clarity and the acquired images' number, size and resolution. The method required a digital camera with 3.2M Pixels resolution, Photomodeler 5.02 pro software, a computer station, and marked targets.[49]

For producing the targets needed for the process, the surface was marked with target points placed at the intersections of a one eighth of an inch uniform grid. This grid spacing was based on the study pre-determined accuracy level of one eighth of an inch.

The point's locations were defined by a projected light pattern using an LCD projector. The grid pattern was projected perpendicularly on the model surface, as shown in Fig. 20. The pointes were referenced manually using a pencil and were marked after that with a black china ink using a 0.5 mm head-size pen.

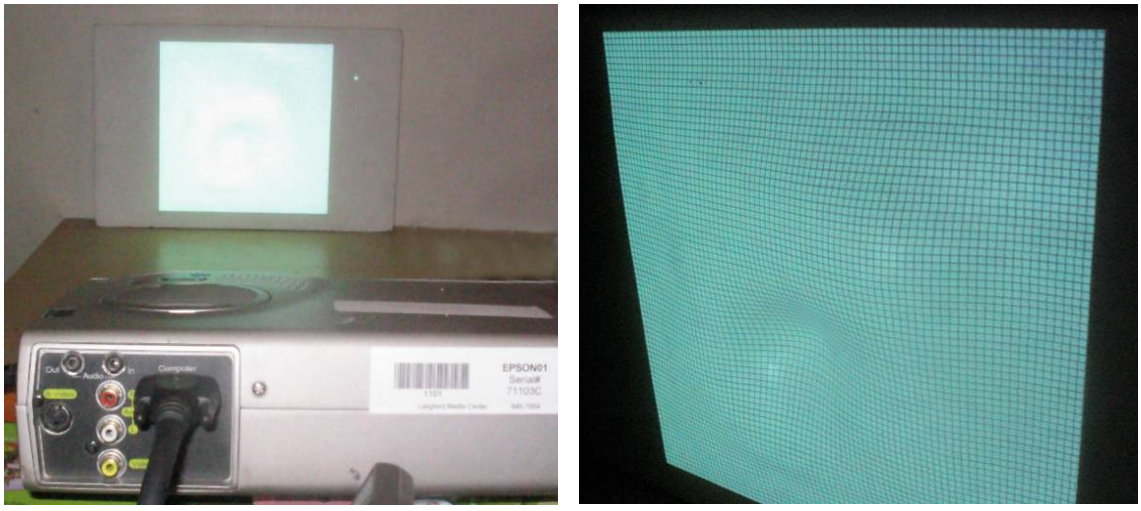

Fig. 20. Grid projecting and targets marking on the model surface.

III.4.3. Hand measuring method instrumentation and variables

The third category of independent variables is the traditional hand-measuring method variables. Those variables were the created instrument leveling mean, scale bar verticality on the vertical sliding part, the horizontal sliding part movement smoothness and horizontality, the spacing and location of the colored targets defined on the model surface.

Special instruments were created for this method using inexpensive hand tools like an angular ruler with a carpenter's spirit level, graph paper, a clipboard, and a pencil.[20,21] The instrument was designed to measure the change in depth for any point on the model surface with relation to a reference plane. The instrument was a horizontal flat frame with a movable cross-shaped part sliding smoothly and horizontally on top of the frame edge in the x-y direction. This cross-shaped part was holding a vertical sliding scaled pointer that can slide in the z direction to indicate on the vertical scale the vertical measurement change of the depth for any point on the surface, as shown in Fig. 21.

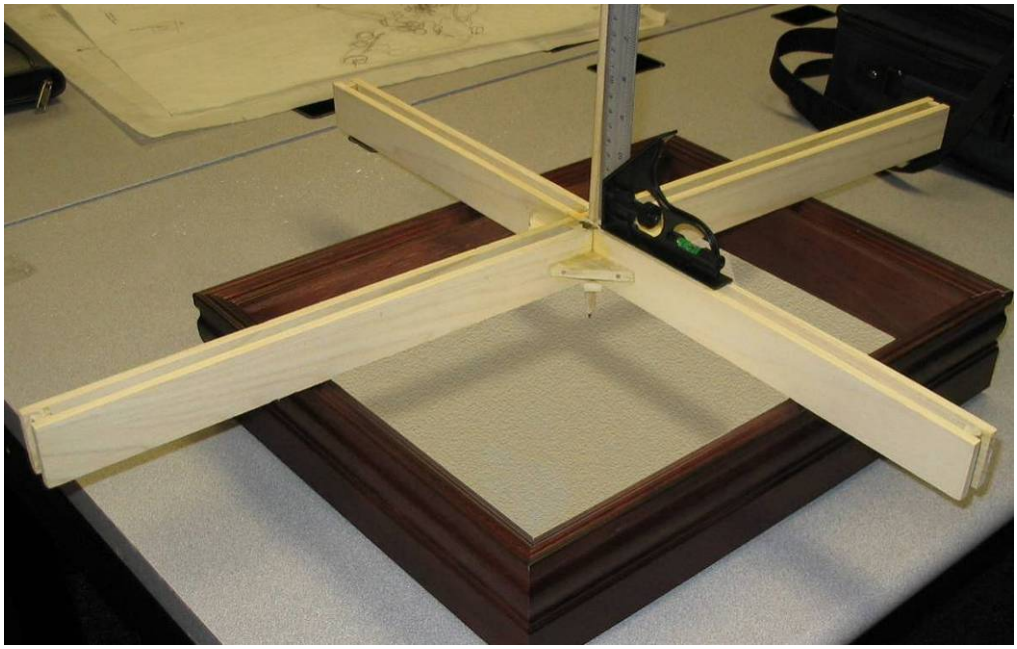

Fig. 21. Hand tool instrument for measuring the change in the relief depth.

For performing the hand measuring method, eight groups of target points were identified to work as eight different measuring samples in order to derive the surface contours. The eight-colored-target groups define the model surface to reveal relief formation. Each group was assigned a different color with uniform grid spacing of one inch in between every two adjacent points in the x-y plane over an area of 100 square inches, as shown in Fig. 22. The one inch space between targets in each group was determined based on the flatness assumption of the in-between area with a quarter of an inch maximum change in depth for the space on the model surface. While assuming that this one inch space will accurately reflect the surface deformation, this space was determined also based on the need to collect one hundred points from each sample to keep measuring time-consumption reasonable for the comparison purposes.

The change in depth information was generated by manually measuring the depth of each point in relation to a reference plane. A stopwatch was used to measure the process time-consumption.

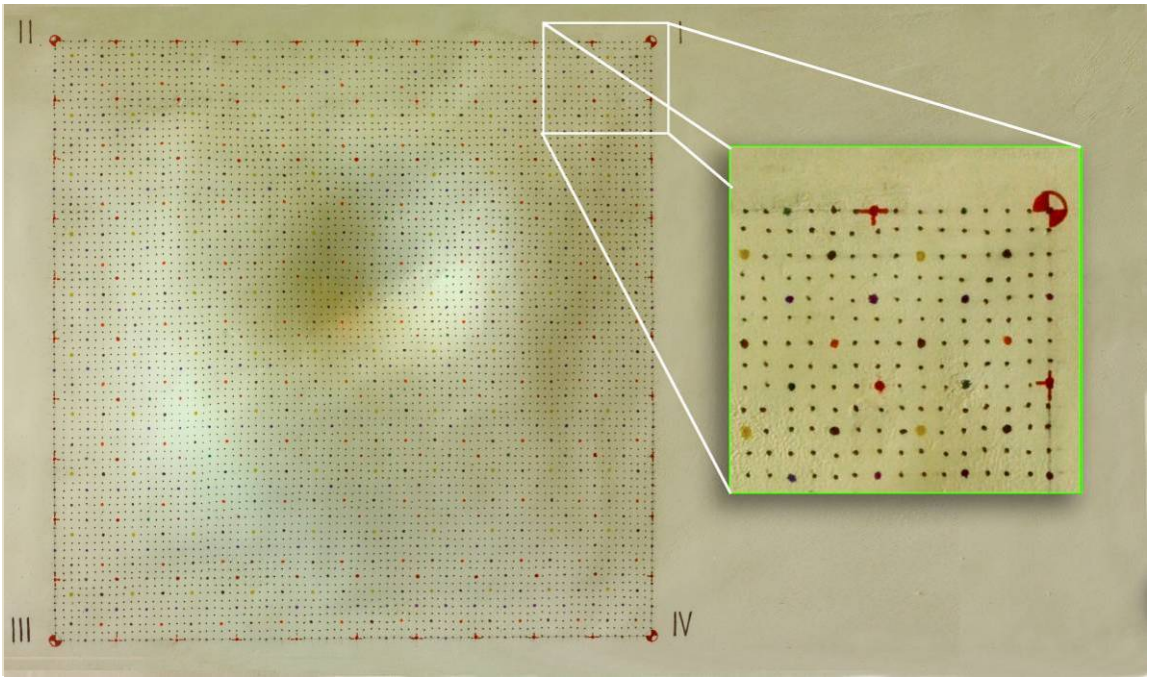

Fig. 22. The marked colored grids for defining the eight samples.

III.4.4. The OMIT measuring method instrumentation and variables

The forth category in the independent variables is the OMIT measuring method variables. Those variables are projected pattern variables (line color, background color, grid design and grid pitch), camera variables (image resolution, lens focal distance and camera location and orientation) and projector variables (image resolution, projecting luminosity and projector location and orientation).

The OMIT method requires a projected pattern in the form of two sets of adjacent straight lines of two contrasting colors with equal line width and separating distances of one eighth of an inch, as shown in Fig. 23.

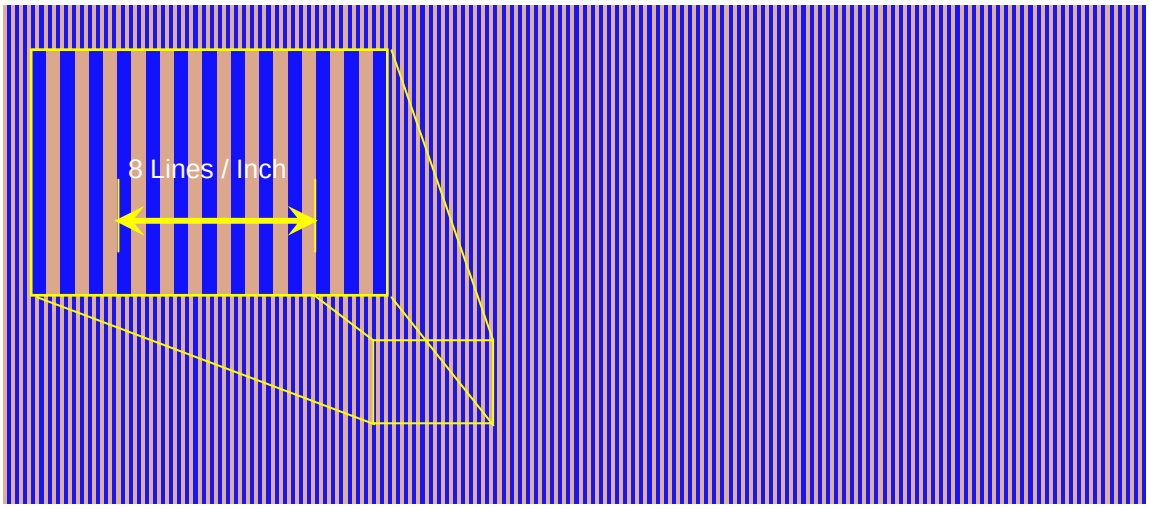

Fig. 23. Moiré projected line pattern.

Lines and background colors were defined using (red, green, blue digital color spectrum). The line color was blue (000 R, 000 G, 255 B). The background color was light yellow (255 R, 255 G, 127 B). These colors were determined based on the grid color manipulation performed in the pilot study as mentioned earlier (section III.2). The manipulation intended to reach the color combination that produces moiré fringes with the highest visibility when superimposed using

the difference mode in Photoshop software, as will be explained later in section IV.2.2. The design of the line pattern used in the projected grid was developed based on increasing fringe sharpness using binary grids with square-wave transmittance profile as mentioned earlier (section II.3.7). This was produced by alternating opaque lines and background spaces of equal width.

The equal width between the lines is the pitch which was determined as one eighth of an inch to generate contour intervals of the same distance as discussed earlier (section II.3.4). This distance was defined to meet the predetermined depth accuracy level of one eighth of an inch for surface relief measurement in the experiments as mentioned earlier (section III.1).

This method requires an LCD digital projector. The available projector was an XGA projector of 1500 lumens with a resolution of 1028px by 768px. This resolution and luminosity limited the projecting area size and the distance; these can be enlarged using a projector with higher specifications as was investigated in the pilot study discussed earlier (section III.2). The projector was positioned on a plane parallel to the model surface with a predetermined distance from the physical model. The distance was measured using measuring tape from the approximate location of the projector lens nodal point to the approximate center of the physical model surface. The projector was oriented to a 45° angle with the physical model surface as established earlier (section II.3.4). The projection angle was controlled using a 45° drafting triangle to adjust the door angle that worked as the background board holding the object base.

A non-metric digital camera with a 50 mm lens and a resolution setting of 3.2Mpx was used as the imaging equipment. The camera had higher image resolution available that was not utilized because of the limited resolution of the projector and the projected grid. The camera was positioned on the parallel plane containing the projector with the same predetermined distance from the model surface. The camera was oriented perpendicularly to the physical model facing its surface as established in section II.3.4.[39] the camera distance from the

object surface was measured from the approximate location of the camera lens nodal point to the approximate center of the physical model surface. The perpendicular location of the camera was controlled using measurement triangulation (12 X 16 X 20 inch triangle method) to approximately approach the 90° angle of the camera axis with the physical model surface.

User friendly software solutions supported by Photoshop, 3Dstudio max and AutoCAD were used for producing the projected pattern imaging and the generated data interpretation. A stopwatch was also used to measure the process time-consumption.

III.5. Experimental samples

The two compared measuring methods were assigned different sampling designs to satisfy each method characteristics. The main concern was to construct measurements validity by measuring different points in different locations each time the experiment was performed. This prevented building a previous knowledge about the data when collecting it. This procedure preserved the credibility and the validity of the gathered measurements.

III.5.1. Hand measuring method samples

For point-to-point approach method (hand-measuring) the measured targets were different for each recording sample. For contour recording, a grid of targets in the x-y plane with approximately one inch separating space was identified and marked with a unique color. For every measured sample, the location of the one inch grid was shifted to give a new set of colored targets, as shown in Fig. 24.

Eight recording samples were performed for the hand measuring method. Two data outcomes were collected from each of those recording samples. The first outcome was the depth (Z Cartesian coordinate) for the 100 previously identified targets on the model surface.

The second outcome was time intervals for carrying out the recording process for each sample starting with the time needed for acquiring point-to-point measurement data, and ending with the time needed for depth measurements interpretation to produce the digital contour output.

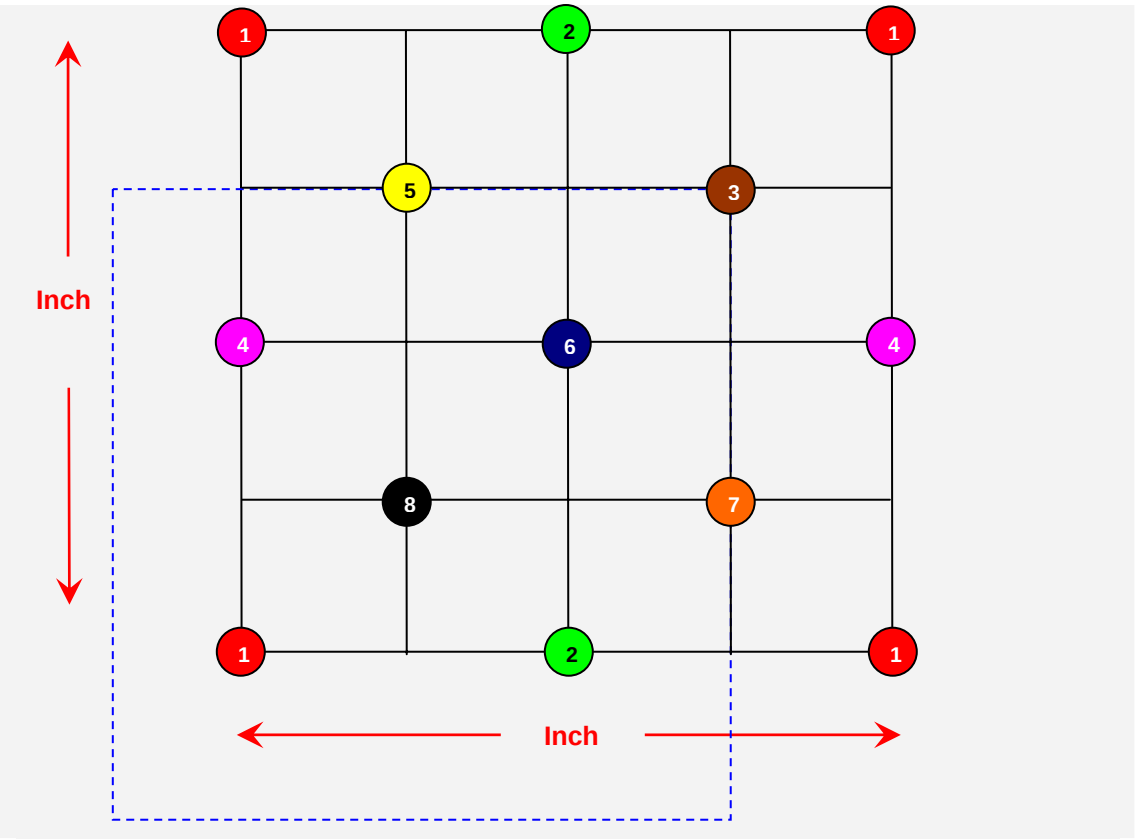

Fig. 24. The shifted one-inch grid used to identify the set of colored targets.

III.5.2. The OMIT measuring method samples

For the integral approach method (the OMIT), eight recording samples were performed. In each sample the model was rotated 45 degrees clockwise in the x-y plane and around the z axes, as shown in Fig. 25. The samples rotation approach was used to generate different sampling data. The shifting procedure that was used in the hand method was not appropriate for the OMIT method

because it didn't change the fringes shape according to the method's integral characteristics.

The first outcome from OMIT method was the contour fields of surface relief from each rotation in the form of dark fringes. Digital representations were created by tracing these contour fields. The second outcome is time intervals for carrying out the recording process for each sample starting with the time needed for producing contour data, and ending with the time needed for contour tracing to produce the digital contour output.

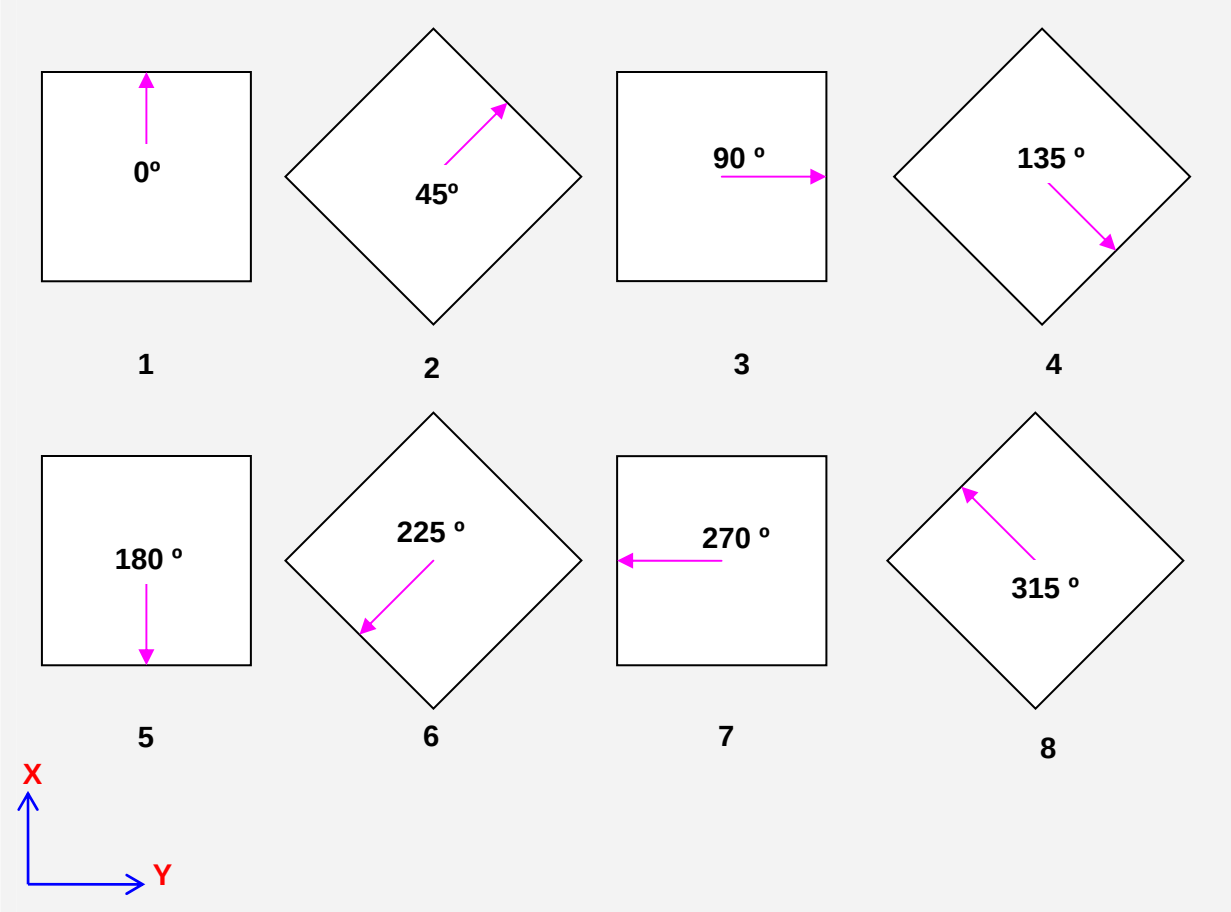

Fig. 25. The 45-degree rotated model in the x-y plane and around the z axes.

III.6. Data treatment

The initial measurement data from the experiment in this study was used to create a contour representation of the physical model for each recording sample obtained from both methods. The created contour diagrams provide the basis for testing the hypotheses.

The measurement accuracy threshold was defined as one-eighth of inch for the depth of every point on the surface. The difference in the resulting contour diagrams between the sample's relief contours and the "true" model were basically compared against this quantity. The resulting contours comparison was extended to higher accuracy tolerance with regions of 3/32nd of an inch, 1/16th of an inch and 1/32 nd of an inch.

By superimposing the measured contour diagrams over the "true" model contour diagram, samples filtration against the targeted accuracy threshold were performed. This filtration was based on verifying the percentage of error between different contour intervals and the tolerance region. Measurement error percentage was the ratio of comparing the magnitude of the area located outside the threshold tolerance regions against the total area of the measured sample surface. This error was tested to determine the accuracy of the created contour diagrams against accurate contour representation of the "true" surface relief of the model. The samples included in the comparison were verified according to the targeted level of accuracy of 1/8th of an inch to determine the targeted accuracy fulfillment.

The hypothesis of measurement accuracy assumes that if the ratio between the measurement error average of the hand measuring method and the measurement error average of the targeted OMIT method is one, then the accuracy level for both methods is the same. The greater the ratio is above one the higher accuracy the OMIT has and the lower the ratio is below one the lower accuracy the OMIT has.

Accuracy verified samples form the basis for the comparison of time-consumption. The hypothesis of time-consumption assumes that if the ratio between time average of the hand measuring method and the time average of the OMIT method is one, then time-consumption for both methods is the same. The greater the ratio is above one the less time-consuming the OMIT is, and the lower the ratio is below one the more time-consuming the OMIT is.

CHAPTER IV

DATA GENERATING AND DISCUSSION

This chapter presents the details of the performed experiments. The true model measurement is established. The relief depth measurement and time-consumption data is generated. The contour generating method and the problems encountered are discussed and analyzed at the end of this chapter.

IV.1. True model measuring implementation

To establish a true measurement for the physical model surface relief, close-range digital-photogrammetry software is incorporated. Photomodeler Pro 5.02 is used to extract an accurate three-dimensional digital representation of the model in the form of a true model virtual surface (TMVS). This software uses a point-to-point information approach in a special numerical algorithm based on advanced mathematical techniques. Those techniques are used to process the input data, to create valid 3D input data while maximizing accuracy and to minimize errors.[24]

As a first step of this process, camera calibration process was performed to determine the characteristics of the camera to be used as a measurement device.[24] KODAK-DCS-Pro14n-50mm/14.2 MP digital camera with 50 mm wide angle lens was used in the process. From identified camera positions, fourteen images were acquired of the printed calibration grid sheet, as shown in Fig. 26. This grid of dots was especially designed by the dealer for this purpose.

Using these images, automatic calibration process was executed using Photomodeler to identify the internal characteristic of the camera. The final total error in calibration processing was less than 0.1 and was accepted according to the software recommendations.[24]

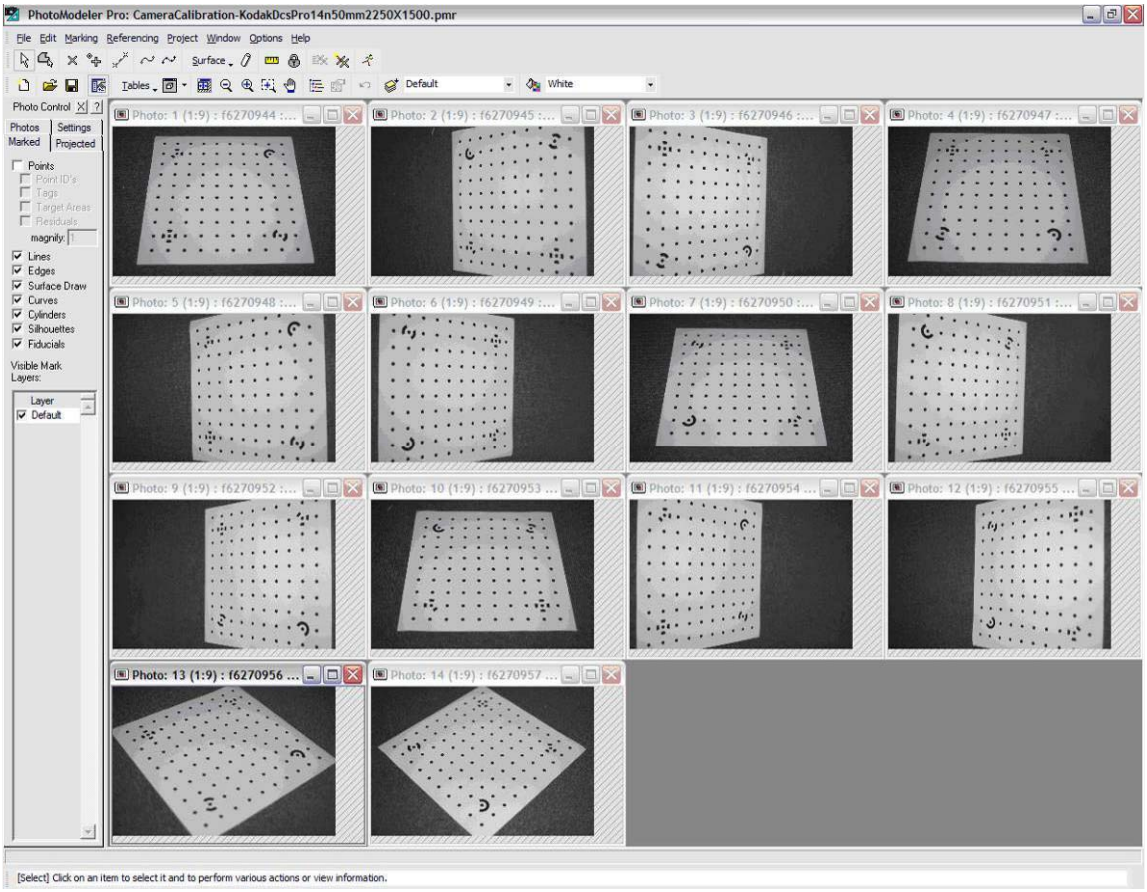

Fig. 26. Photomodeler Pro 5.02 calibration grid images.

The procedure for creating a 3D digital model from acquired images is as follows:

- Creating a new project
- Producing and adding images to the project
- Orienting the images in space
- Marking points and referencing them to corresponding points in all images.
- Auditing the referenced points and correcting errors
- 3D processing and total error evaluating
- Verifying the project results
- Adding scale and rotation

According to these steps, the procedure for building the true model starts with identifying reference points on the model surface to act as marked targets as presented in section III.4.2. To obtain the maximum accuracy[49], nine digital images of the model with a resolution of 6.4 Mpixel were acquired from predefined camera position, as shown in Fig. 27.

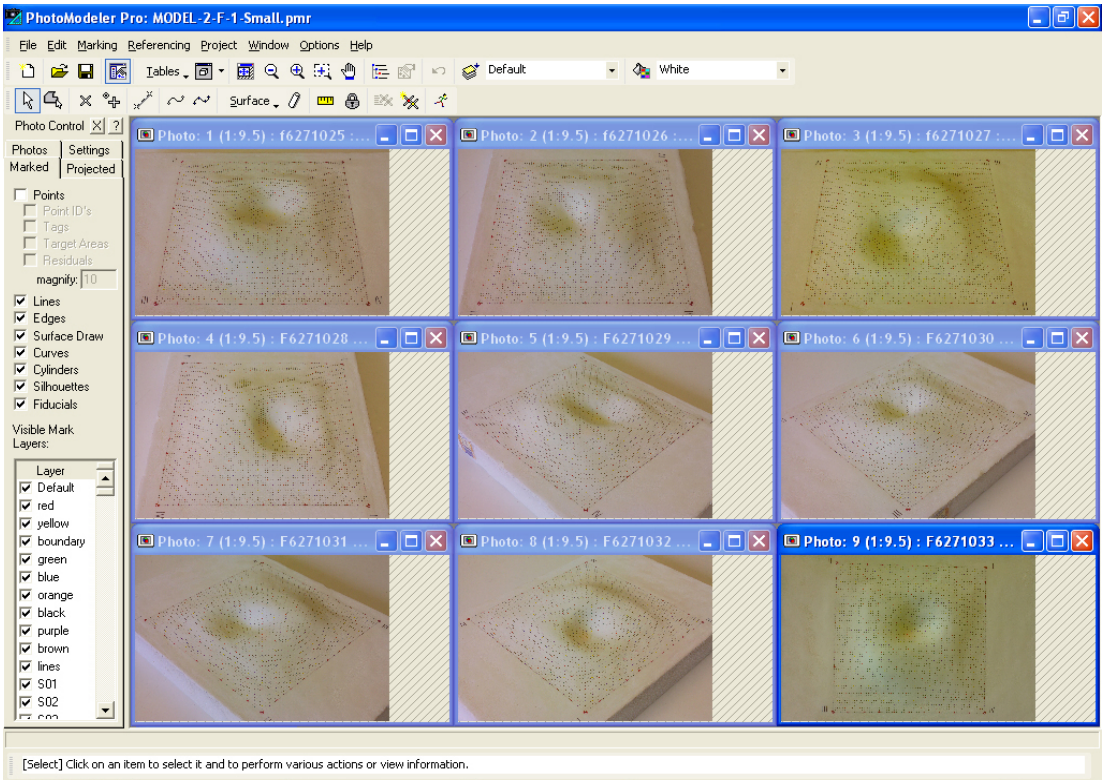

Fig. 27. Photomodeler nine images of the model.

To start building the 3D digital model surface, a new measurement project was initiated by the software and the acquired images were loaded to it. The red grid of 121 marked points was initially referenced to corresponding points on the nine images to define the orientation of those images in space. Automatic target marking was used to mark the 6561 points on the model surface. The marked targets on the model surface were then referenced to corresponding points in all the nine images using auto-drive referencing to form a point-cloud, as in Fig. 28.

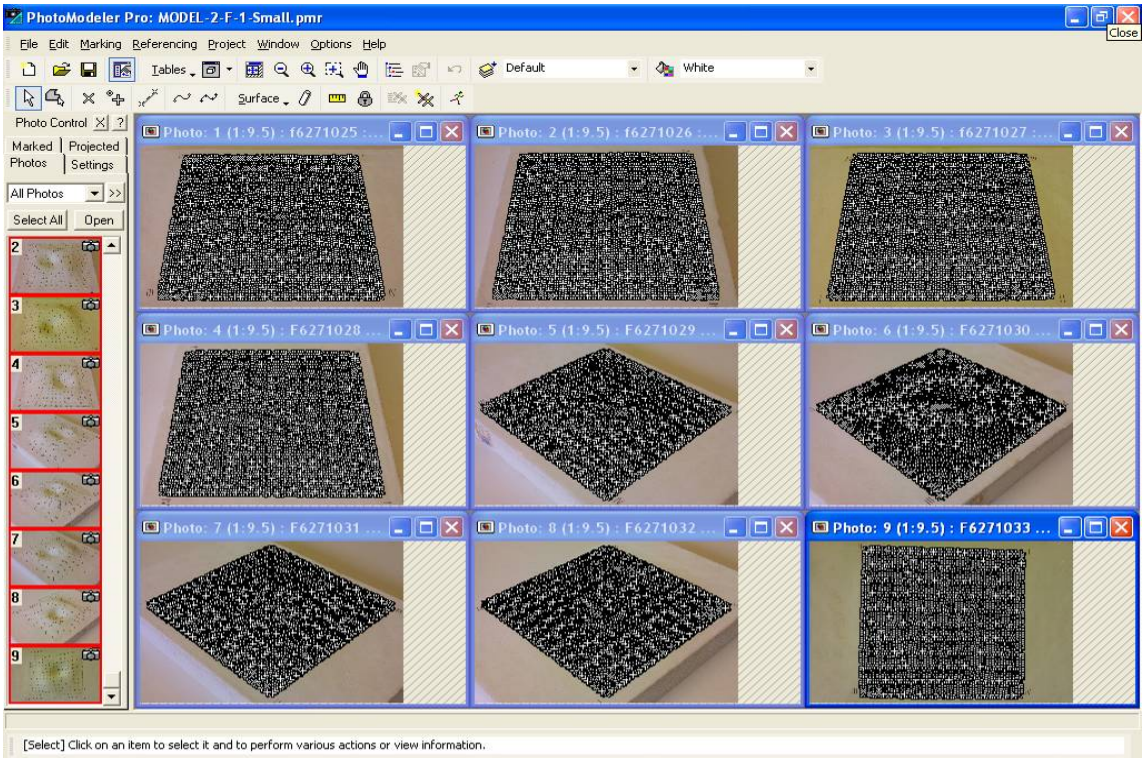

Fig. 28. The 6561 marked targets referencing on the model surface.

To generate the point-cloud from the referencing information, 3D processing was executed and the total error was evaluated.

The process of fine-tuning the referenced points was performed through auditing the points, defining the points with highest error, unreferencing them, referencing them again manually and processing the project again. This procedure was repeated until the total error of (0.036) was accepted, as shown in Fig. 29.

After processing the project properly, the absolute value of the point-cloud proportion was quantified by inserting a known distance between two points on the model surface. The model rotation needed to define the X-Y-Z directions was also assigned by identifying three points located in the X-Y plane. Finally, the 3D point-cloud of the referenced marked points was viewed in the 3D viewer, as shown in Fig. 30.

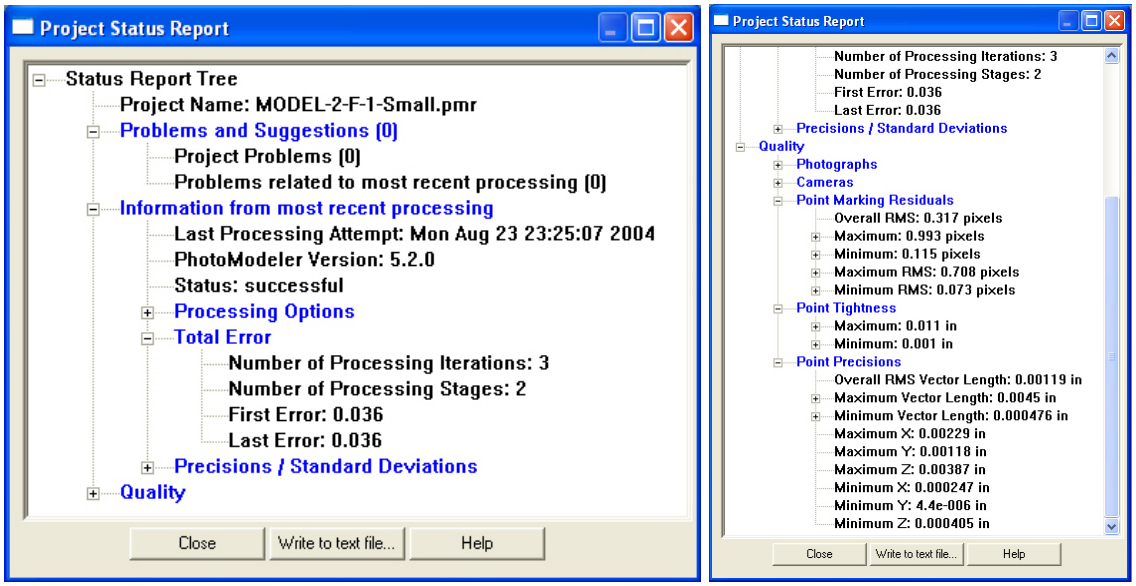

Fig. 29. Project status report.

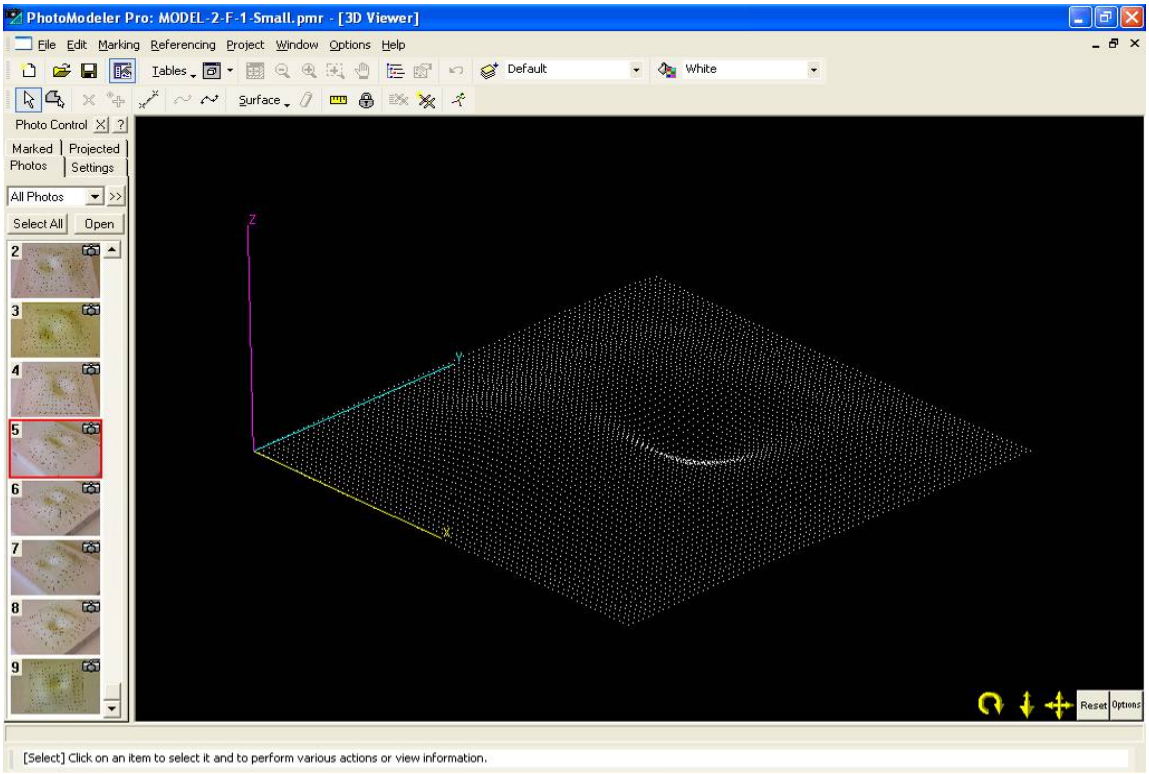

Fig. 30. The 3D model of the Photomodeler points cloud.

After arranging the data in a table following the format of X-Y-Z Cartesian coordinates, the point-cloud data of the 6561 points was exported using data table export. This procedure outputted the data table contents in the form of an ASCII text file to be used in other software.

The (3dmesh) command in Autodesk Architectural Desktop 2004 software was used to form the surface connecting the referenced points. This step required editing the text file exported from Photomodeler in order to create the TMVS as a script file to be used in Architectural Desktop.

The text file exported from Photomodeler needed editing on Microsoft Excel 2003 software. The reference points' coordinates were rearranged in a format accepted by Autodesk Architectural Desktop 2004 software 3dmesh command. The file was in the form of a script file of sequential rows of points.

For rearranging the data in the form of sequential rows, the Y coordinates of all points were sorted in ascending order to group together the points having identical or closely identical Y coordinate value. For these points in each group another sorting for the X coordinate was performed in ascending order. The result was a table of sequential rows of sequential point-groups that were exported to a (.txt) file format for Architectural Desktop use. The exported txt file was edited as a script file to be used by Autodesk Architectural Desktop 2004 software as the following text:

3dmesh	(for the command name)
81	(for size of mesh in M direction)
81	(for size of mesh in N direction)
$X_1\ Y_1\ Z_1$	(first point location)
.	(The rest of the data were inserted as
.	arranged from Excel for all 6561 vertices)
$X_{6561}\ Y_{6561}\ Z_{6561}$	(last point location)

The final result for this process was loading the script file to the Architectural Desktop to create the true model virtual surface (TMVS) as a true representation of the physical model surface, as shown in Fig. 31.

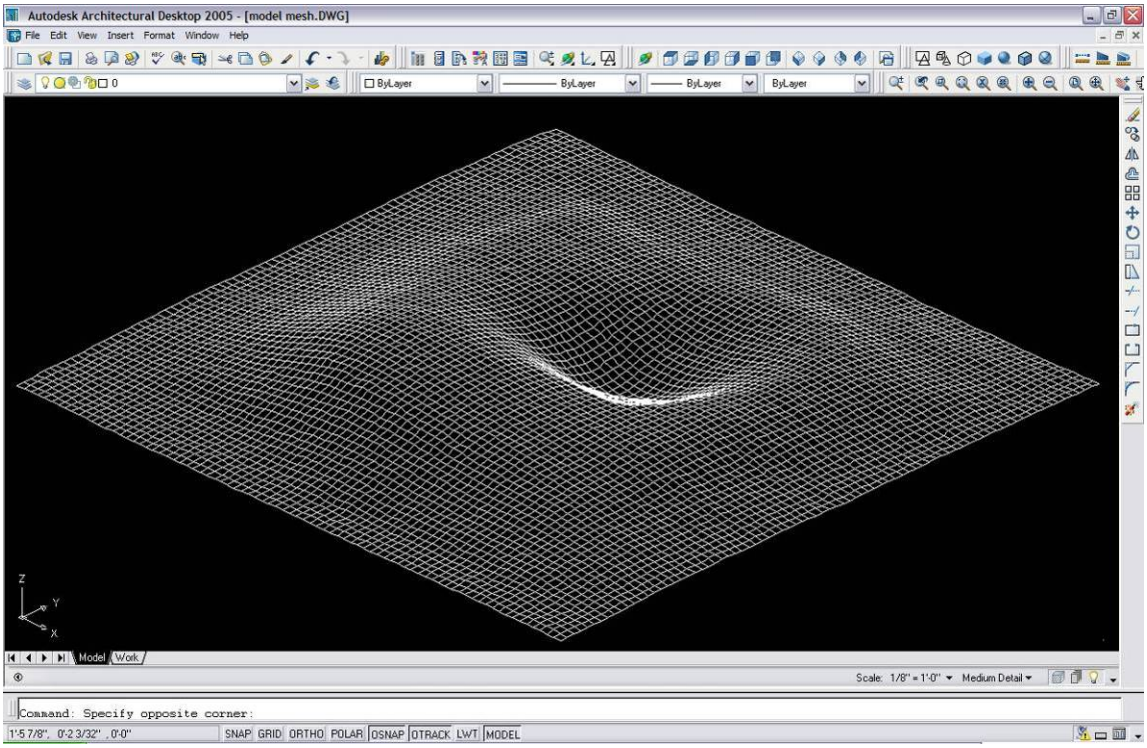

Fig. 31. The generated Desktop virtual true model surface TMVS.

IV.2. Experiments implementation

IV.2.1. Hand measuring implementation

Generally, the hand measuring method uses a point-to-point information approach as discussed earlier. The two collected data outputs from this method used in this study were depth measurement for the predefined points, and time intervals for performing the process. Time intervals were arranged in three categories; measuring process time, model preparing time and the time needed for model editing and producing contours.

To perform this method, the instrument previously explained in section III.4.3 was used for measuring the change in the point's depth on the physical model surface (Z coordinate).

For the hand measuring method, the research experiment consisted of two parts. The first part was measuring the depth and the second part was generating the hand measuring virtual surfaces referred to as (HMVS). The two parts were repeated with the different samples specified in section III.5.1 and time intervals were recorded.

The first part, depth measuring, consisted of the following two steps:

Step 1: Positioning the physical model inside the hand measuring instrument and leveling the sliding plane

Step 2: Collecting depth information in relation to a reference point on the instrument's vertical scale

The second part of the experiment, HMVS generating, consisted of the following two steps:

Step 1: Drawing the points digitally for each sample using X-Y coordinates from the true model surface

Step 2: Creating the HMVS by including the collected depth information (Z coordinates)

The first step of the first part for this method experiment started by inserting the model inside the instrument and leveling the group on a flat surface using the spirit-level attached to the instrument as shown in Fig. 32. The eight samples of point groups consist of four reference points and a group of 100 points of the same color as mentioned earlier (in section III.4.3).

Each of the eight samples was identified by special abbreviation letters. The identified samples start with four reference red-colored points at the surface boundary corners. Those same four points were included in all samples with the abbreviation letters Ref 1, Ref2, Ref3 and Ref4.

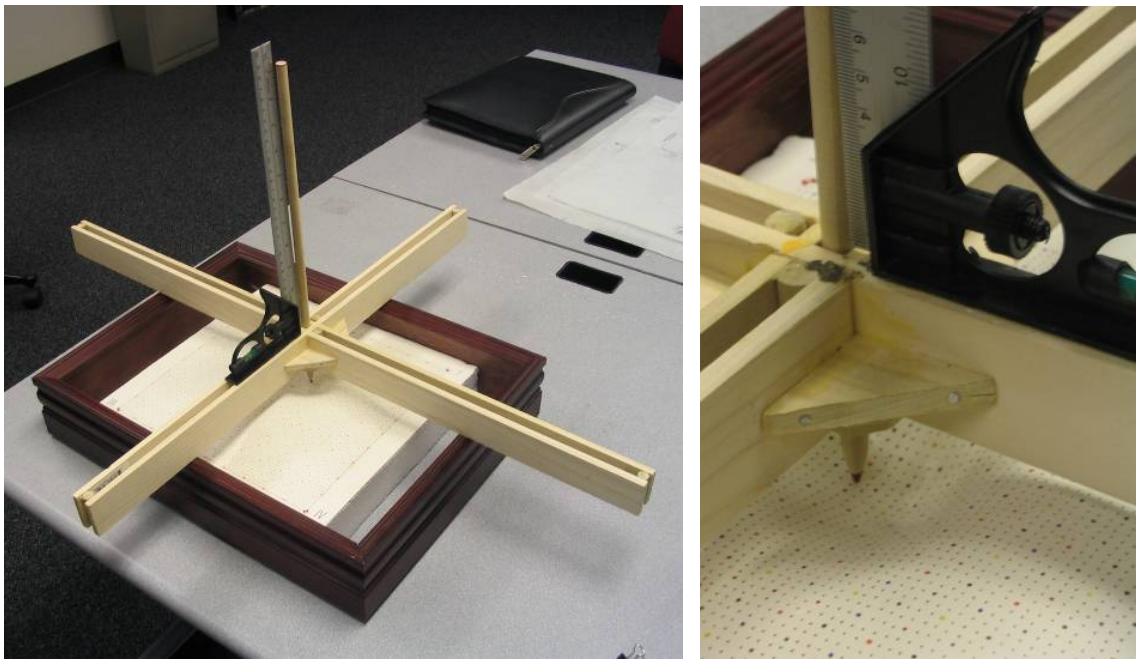

Fig. 32. Hand instrument.

The 100 colored points in each sample are referred to by an abbreviation letter and a sequential number. The abbreviations used in the samples were: R for red in the first sample, K for black in the second sample, Y for yellow in the third sample, B for blue in the fourth sample, O for orange in the fifth sample, M for magenta in the sixth sample, G for green in the seventh sample and BR for brown in the eighth sample. The sequential numbers started with 1, 2, 3 … and ended with 100.

In the second step of this first part, the depth measuring process was carried out by sliding the cross-shaped horizontal part of the instrument on top of the horizontal frame edge. When approaching the targeted point, the vertical pointer piece was lowered to touch the point on the model surface. The reading on the vertical scale indicated the magnitude of that point's depth position (Z coordinates) in relation to the frame top edge as the reference plane.

By referencing all the points in each group to the same plane, the change in the surface relief depth at each point was quantified. This procedure was

repeated for all the eight samples starting with the four reference points and ending with the 100th point with a total of 104 points for each colored sample.

The gathered depth data for each sample were arranged in spreadsheets. The tables included depth magnitude, measuring time for the reference points, and measuring time for every 10 points in each row, as shown in Fig. 33.

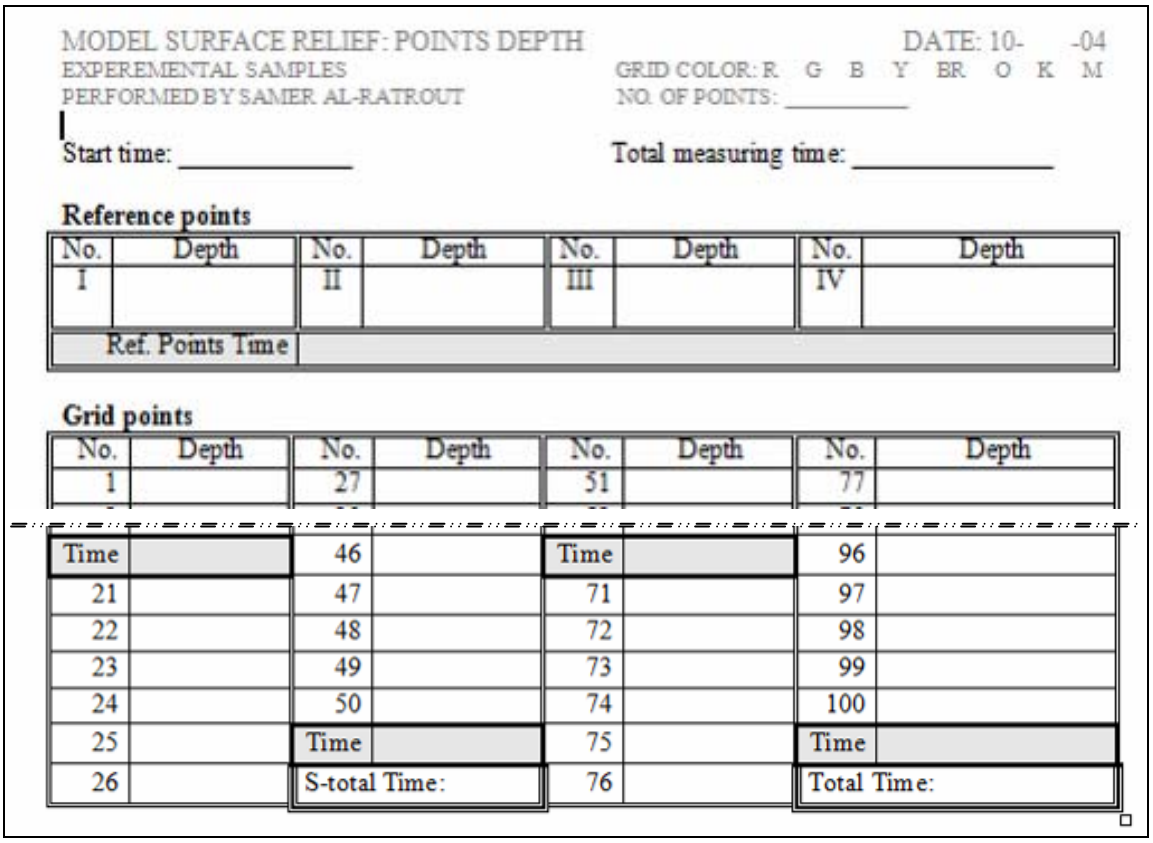

MODEL SURFACE RELIEF: POINTS DEPTH DATE: 10- -04
EXPEREMENTAL SAMPLES GRID COLOR: R G B Y BR O K M
PERFORMED BY SAMER AL-RATROUT NO. OF POINTS: _____

Start time: _____ Total measuring time: _____

Reference points

No.	Depth	No.	Depth	No.	Depth	No.	Depth
I		II		III		IV	
Ref. Points Time							

Grid points

No.	Depth	No.	Depth	No.	Depth	No.	Depth
1		27		51		77	
Time		46		Time		96	
21		47		71		97	
22		48		72		98	
23		49		73		99	
24		50		74		100	
25		Time		75		Time	
26		S-total Time:		76		Total Time:	

Fig. 33. The format of the spreadsheet used for recording depth data.

The second part in the hand measuring experiment included preparing the virtual surfaces for adding depth information. The referenced points collected from Photomodeler formed the basis for creating the HMVS. Autodesk Architectural Desktop 2004 software was used for this step. The points relating to each sample were identified and separated into a different layer. The X-Y coordinates from the TMVS were reserved for all the points in each sample and

given a zero value for the Z coordinate to be replaced later using the acquired hand measuring depth data. The 3dmesh command was used to manually connect the points in the X-Y plane and to establish the projection of the model surface in that plane. The X-Y coordinates for all sample points were treated as known variables imported from the TMVS. The result of this stage was eight 3d-meshes from eight samples based on the known X-Y coordinates of the previously colored points on the model surface, as shown in Fig. 34. The time for this stage was recorded and registered in the tables for each sample.

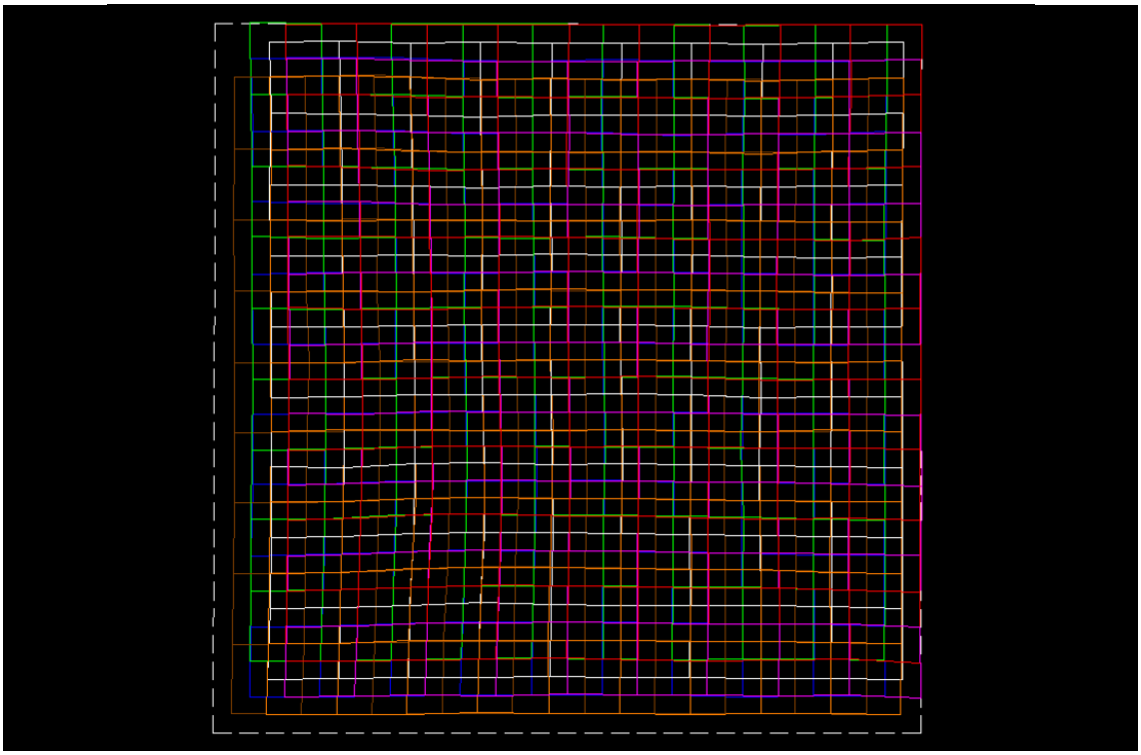

Fig. 34. The meshes based on the colored points known X-Y coordinates.

The second step in part two was assigning the depth measurements collected from the hand measuring process. By inserting the measured depth for each point in each sample as the Z coordinate, eight 3D virtual surfaces were created. Each of those surfaces worked as the 3D representation of the real

model surface relief. The output from the hand measuring method process for each measured sample is referred to as HMVS, as shown in Fig. 35.

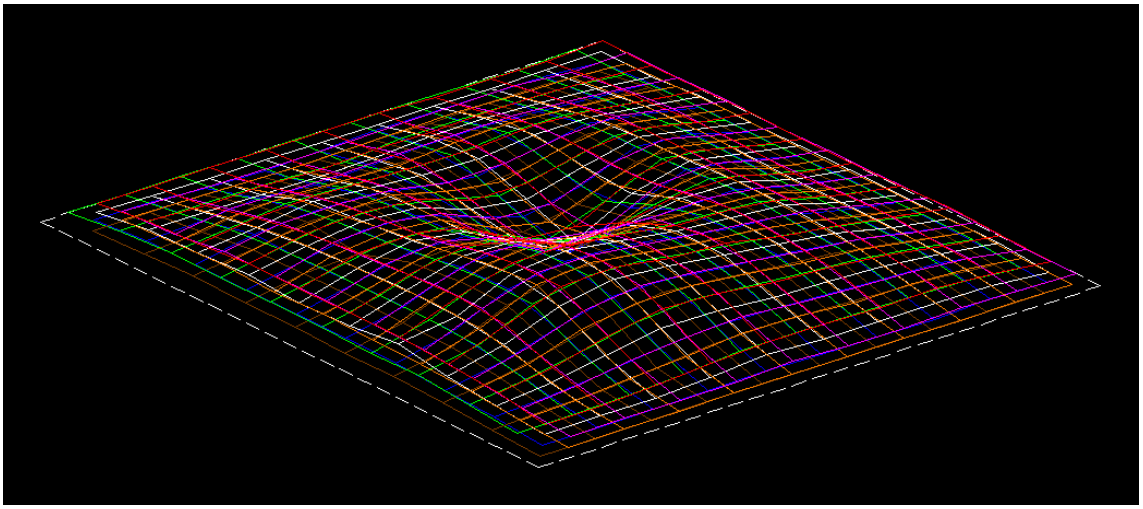

Fig. 35. The eight HMVS resulting from the hand measuring process.

Time-consumption for this stage was recorded and registered to be added to the time intervals for the previous stages to establish the total time-consumption for each sample. By the end of this procedure the hand measuring method experiment was finished and was ready for depth measurement accuracy evaluations which will be discussed later.

IV.2.2. The OMIT measuring implementation

Generally, the targeted method uses an integral information approach. To produce moiré dark fringes, three types of images were included: the reference grating image, the deformed grating image and the model surface image. In this method, the three collected data outputs were moiré dark fringes on the model surface, moiré imaging time-consumption and contour lines generating time-consumption.

To perform the OMIT method, the equipment mentioned earlier (in section III.4.4) is placed in prearranged positions. The targeted time-consumption was

recorded for the two experimental parts of this process. The two parts were repeated with the different sample's rotations as specified earlier (in section III.5.2).

The first part of the experiment is moiré imaging. It consists of the following three steps:

Step 1: Positioning the camera, the projector and the specimen base in the predetermined positions

Step 2: Placing the reference piece on the specimen base and obtaining the reference grating image

Step 3: Placing the physical model on the specimen base and obtaining deformed grating and model surface images

The second part of the experiment was contour lines generating. It consisted of the following two steps:

Step 1: Generating moiré fringes by superimposing the acquired images

Step 2: Producing contour lines from the moiré fringes

The first part of the process for the OMIT measurement method as previously mentioned started with positioning the camera in a perpendicular location facing the surface of the specimen base.[39] From this location the camera was able to produce one vanishing point perspective images with no need for image rectifying to extract orthographic measurements. The LCD projector was also positioned in a location making a 45º angle with the specimen surface.[39] As in Fig. 36, the camera and the projector were located at the same distance from the specimen base as the arrangement discussed in section II.3.4.

The second step was placing the reference surface piece on the specimen base with the predetermined degree rotation of the sample. The pre-designed line pattern grid mentioned in section III.4.4 was then optically projected on the reference piece surface, as shown in Fig. 37.

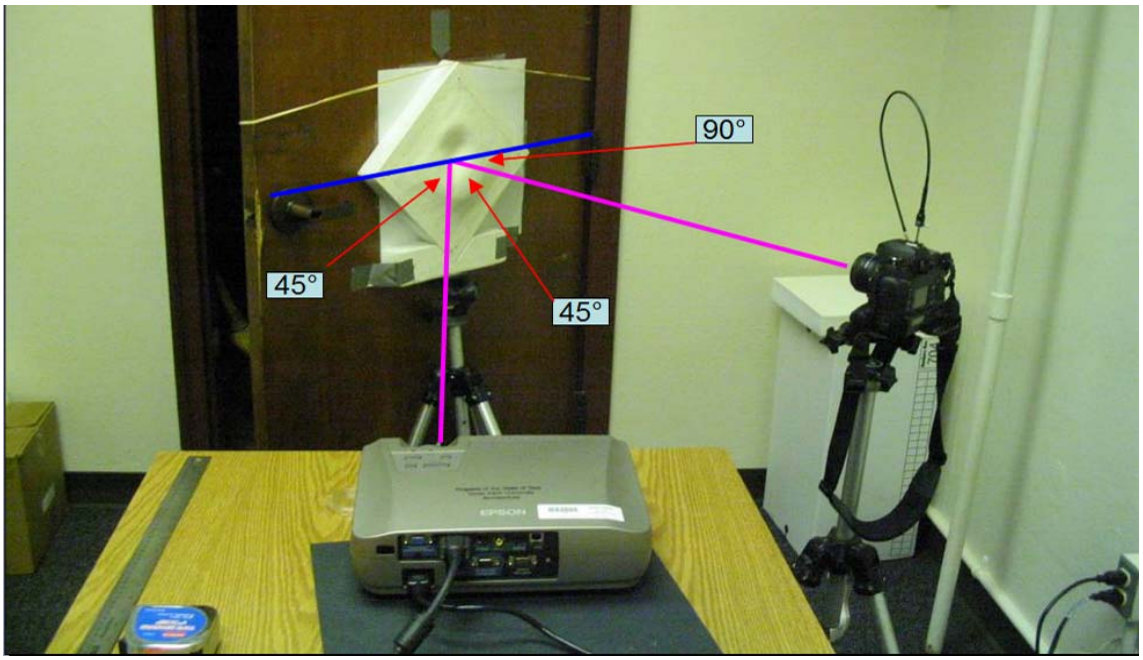

Fig. 36. OMIT measuring method experimental setting.

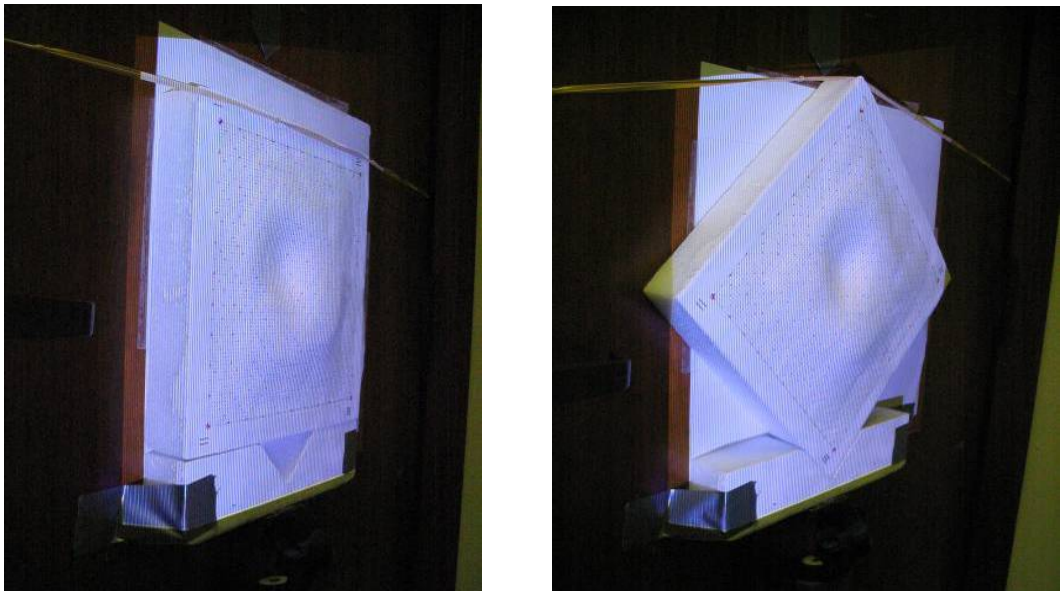

Fig. 37. The line pattern grid projected on the reference piece surface.

This projected grid was manipulated at first to produce a projected image on the reference surface with equal line thicknesses and separation distances of

one eight of an inch from this 45º angle point of projection.[39] This manipulation was performed using Adobe Photoshop CS software by editing the grid using the distort transformation command.

The grid was distorted manually in order to reshape the projection of the original image to give a rectified projection on the 45º projection angle. This rectified projection on the base had the same distances and measurement as the designed squared grid of 16 inches by 16 inches with 128 vertical lines (line every 1/8th of an inch), as shown in Fig. 38. The manipulated grid was checked for accuracy using a prepared sheet of paper of 16 X 16 inch dimensions. This sheet that contains one inch grid lines was placed on the background board under the object. The grid manipulation was performed and checked for accuracy by matching the size and grid scale of the projected grid to the size and grid scale of the prepared sheet.

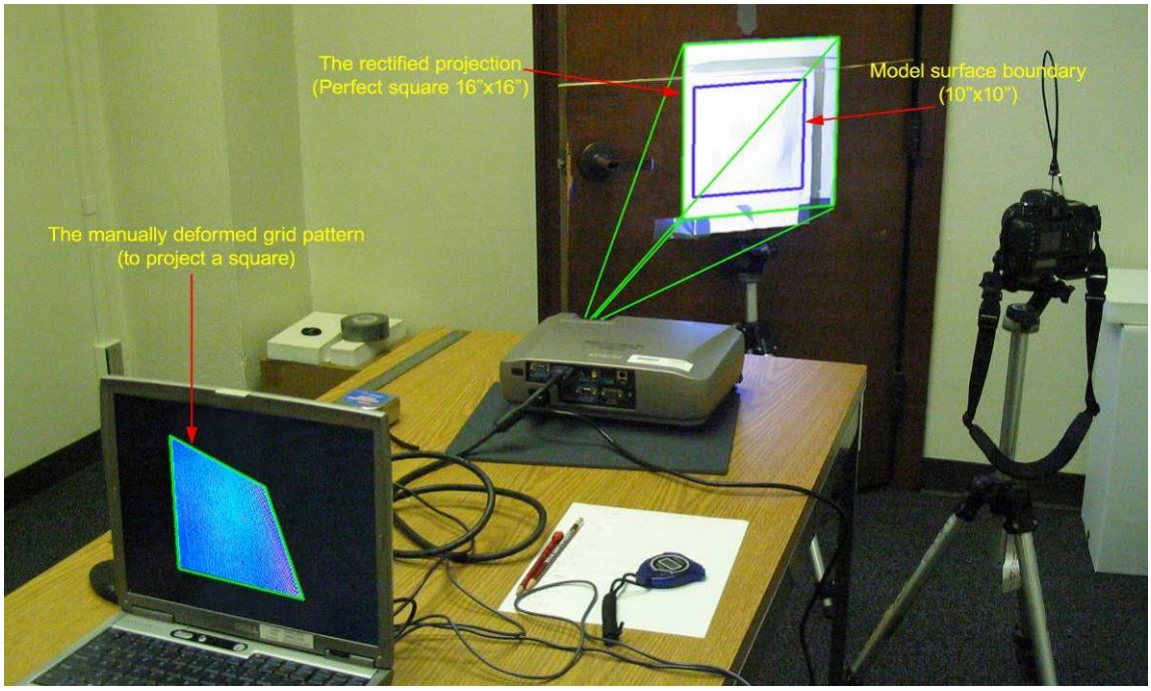

Fig. 38. The projected line pattern grid manipulation.

The generated line pattern was oriented to project vertical lines in relation with the camera-projector axis. Using the camera, the reference grating image of the sample was obtained, as shown in Fig. 39.

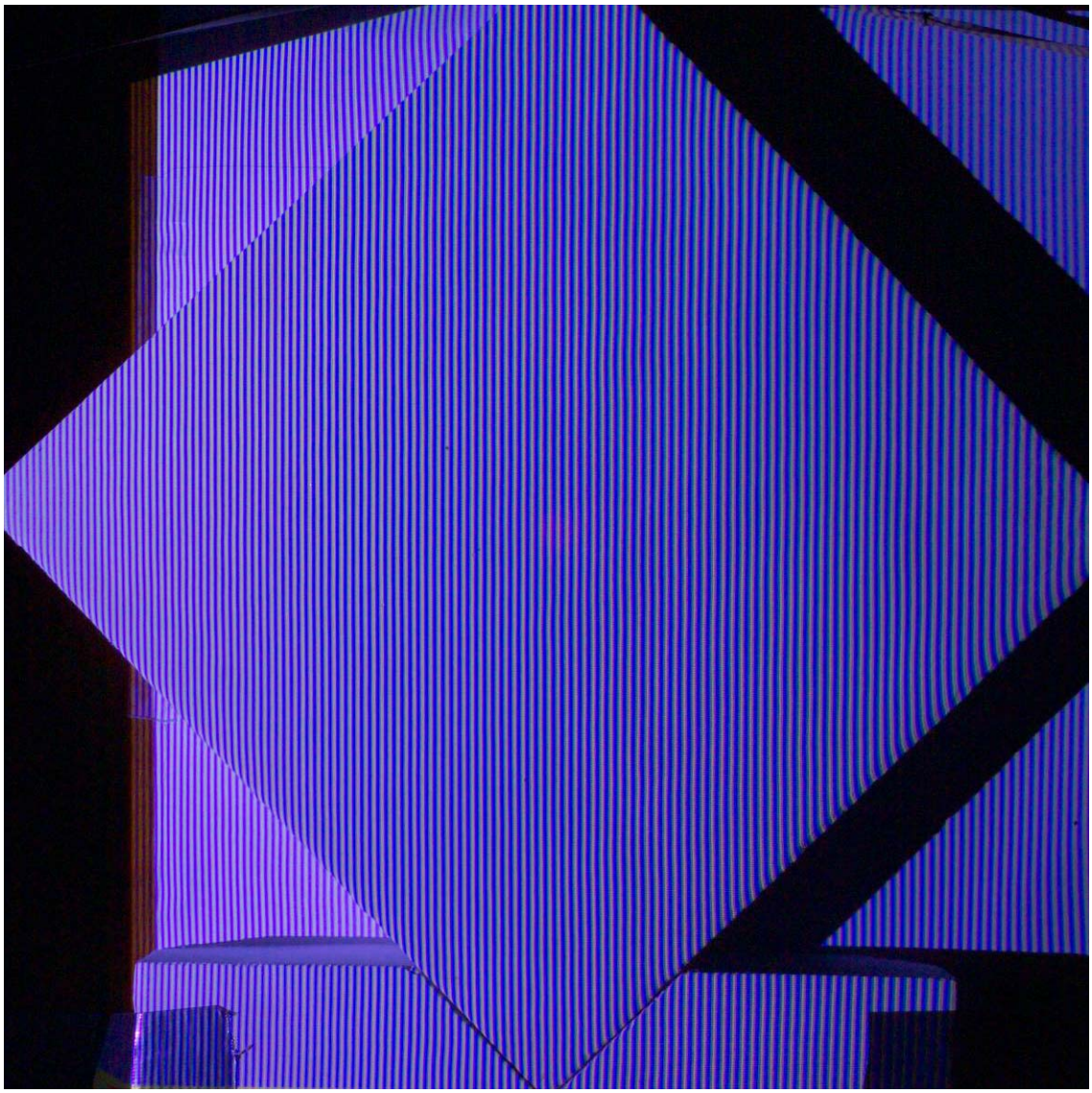

Fig. 39. Reference grating image of the sample.

The third step was placing the physical model on the specimen base with the same predetermined rotation as the reference piece. By projecting the same

rectified line pattern grid on the physical model piece surface, the deformed grating image of the sample was obtained, as shown in Fig. 40.

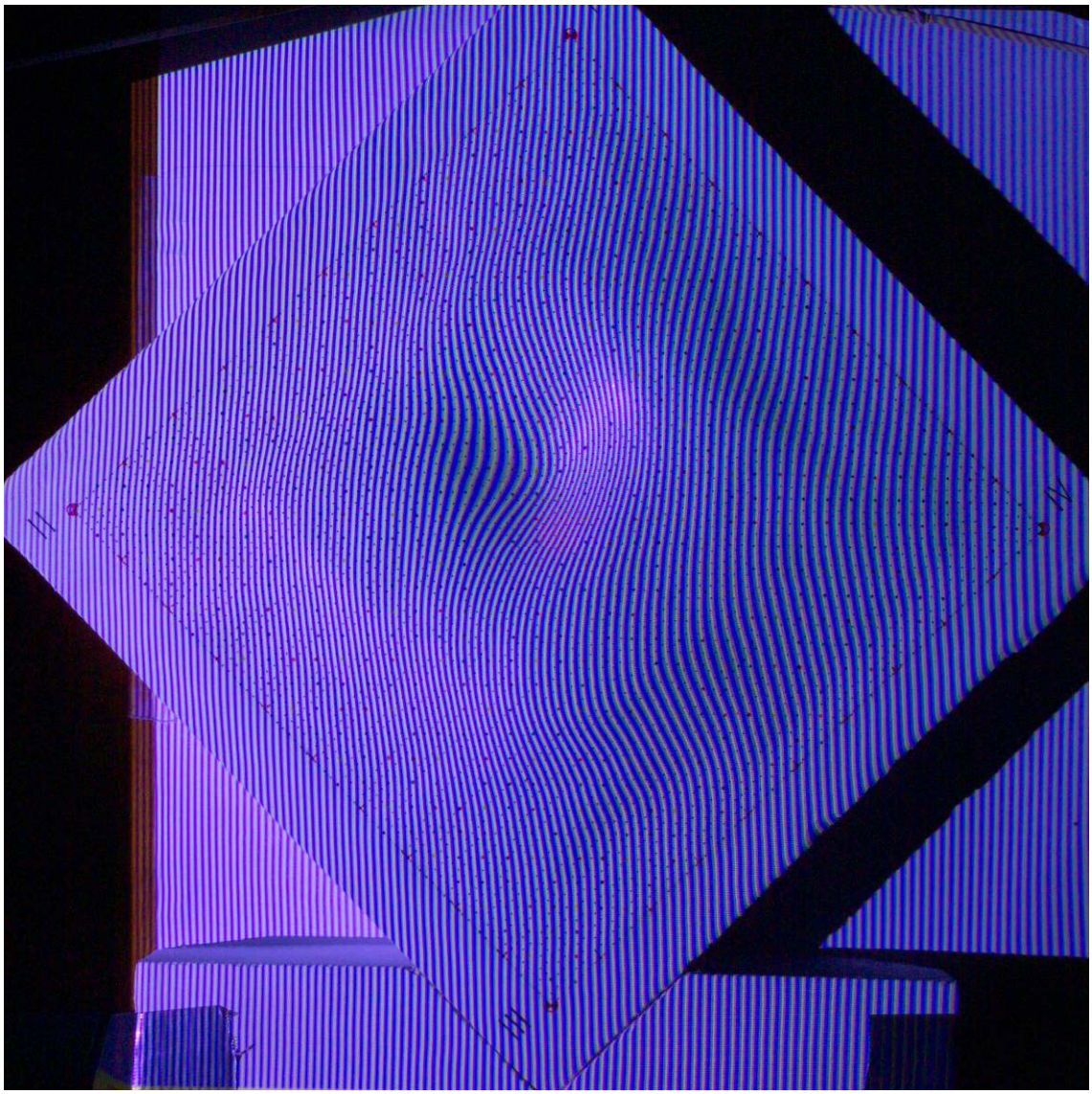

Fig. 40. Deformed grating image of the sample.

Without projecting the pattern, a third image of the model surface at the same rotation and location was obtained showing the location of the marked points on the surface from the same camera location, as shown in Fig. 41.

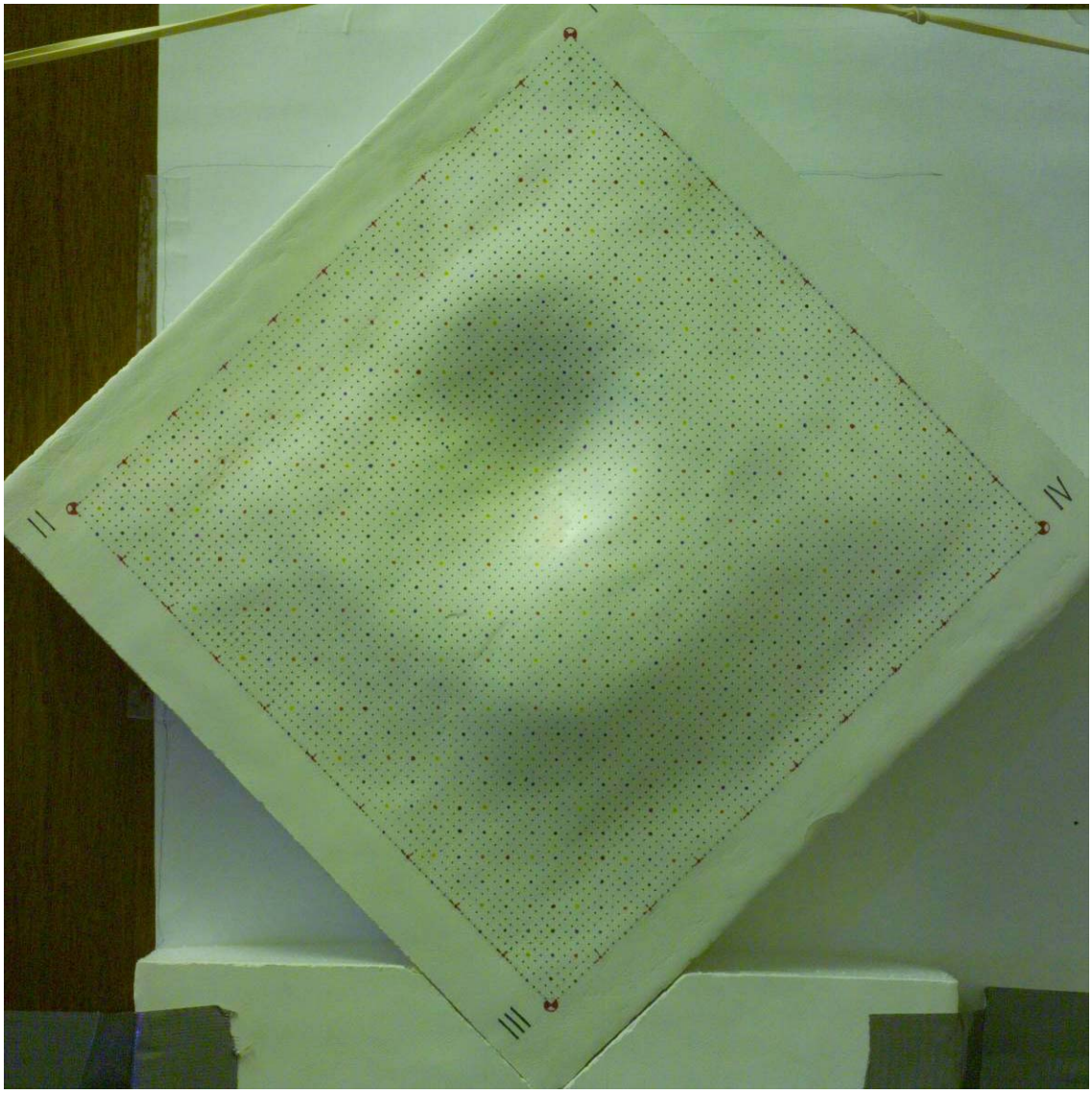

Fig. 41. Real surface image of the sample.

At this stage, time-consumption for the steps of the first part was recorded for each sample.

The second part of this method's experiment started with the first step by generating moiré fringes from superimposing the resulting reference and deformed grating images using Adobe Photoshop CS software. Each image was placed in a separate layer keeping the reference grating image at the top. The two images were aligned exactly on top of each other at the same location. The

blending mode of the layer containing the reference grating image was changed to the difference mode. By doing this, the moiré fringes were generated and the dark contour fields were located on top of the model surface image, as shown in Fig. 42. The image was exported in (jpg) format to make it available in Architectural Desktop software for the next step.

Fig. 42. Moiré dark fringes resulting from images superimposing.

In the second step of this second part, the resulting moiré fringes were traced to produce relief contour lines. Using Architectural Desktop, the process started by inserting the resulting moiré image into the drawing file with the real dimensions of 10” X 10”. Using the SPLINE command, the dark colored fields were traced manually by following the approximate center line of the fringes. The resulting lines represent the surface relief contours, as shown in Fig. 43.

Fig. 43. Moiré traced contours.

At this stage, time-consumption for the second part with these two steps was recorded. The gathered time data were arranged in a separate spreadsheet for each sample. The tables included the sample orientation, time-consumption for moiré imaging, and time-consumption for contour line generating.

By the end of this procedure the OMIT measuring method experiments were finished and were ready for the measurement accuracy test.

IV.3. Encountered problems

While performing the experiments, some problems occurred in relation to the independent variables. Some of those problems were associated with instruments, equipment, the software, model orientation, experimental sitting and experimental environment. The problems noticed have been included in the following sections divided up in relation to the measuring method type.

IV.3.1. True model measuring method problems

The problems encountered while performing the true model measuring method were associated with the Photomodeler software procedures for target points marking and referencing as described below.

IV.3.1.1. Automatic target marking errors problem

When using automatic target marking in Photomodeler for marking target points in the acquired nine images, the software employed parameters to judge the point's existence and identification. Those parameters for target identification and marking are the targeted point's shape, color, contrast, minimum and maximum diameters, fit error, sub pixel marking and coded targets.[24] Those parameters needed some manipulation to reach a satisfying point marking result. The automatic marking result was checked closely for errors for every point of the 6561 points in all the nine images to confirm that each mark referred to a valid point. The final result included some marking errors such as

unmarked points and marking a non-point spot. As recommended by the software,[24] manual re-marking is needed to correct those errors. This was done by deleting incorrect marks and marking the missed points manually, as shown in Fig. 44.

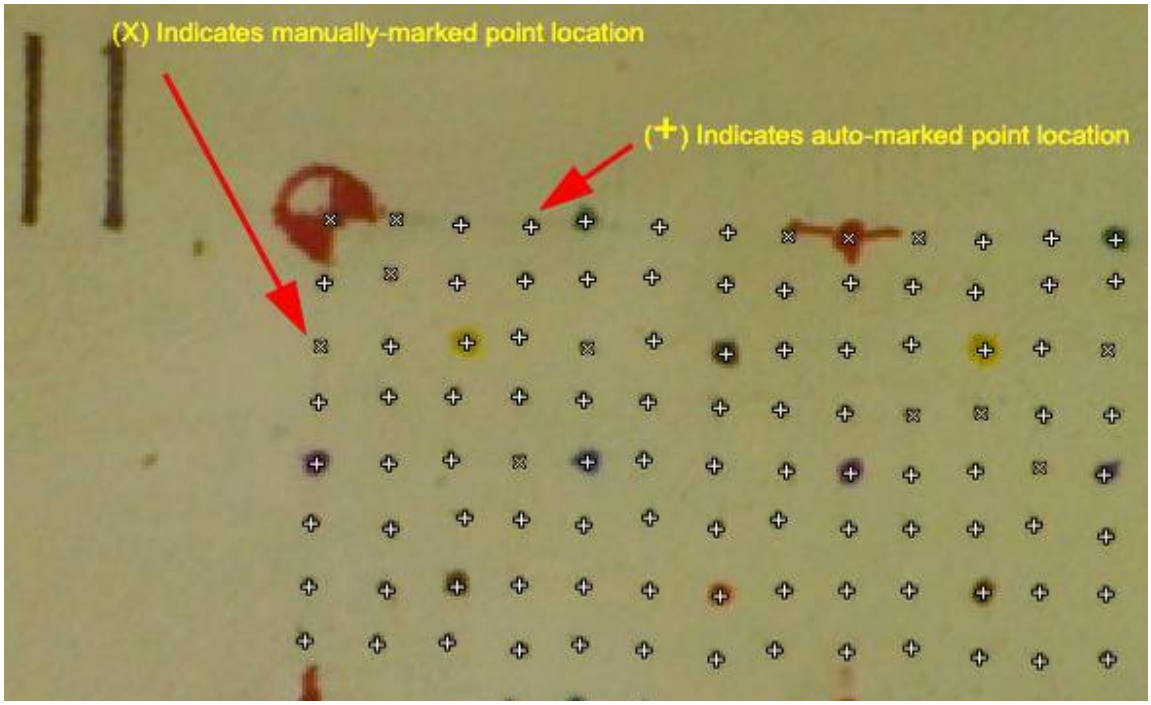

Fig. 44. Marking the missed points manually.

IV.3.1.2. Automatic referencing errors problem

An automatic referencing procedure in Photomodeler was used for referencing the marked points in the acquired nine images. For this procedure, the software uses parameters to link and reference the correct points. Those parameters are search distance, the number of photos, point's selection and the number of iterations.[24] The parameters were manipulated and the process was repeated to achieve acceptable results. The final auto-referencing result was checked closely point by point to confirm that every link referenced to the same point in all the nine photos. Some points were referenced incorrectly and some errors

happened such as linking two different points in the crowded areas in some photos. Correcting referencing errors was performed as recommended in the software[24] by auditing the points, unreferencing inaccurately linked points, and referencing them again manually, as shown in Fig. 45.

Fig. 45 Marked points automatic referencing.

IV.3.2. Hand measuring method problems

The problems encountered while performing the hand measuring method were associated with measurement accuracy and measuring process time.

IV.3.2.1. Measurement accuracy problem

It was noticed that measurement reading accuracy for this method cannot exceed the limit of 1/32nd of an inch according to the scale grading limit. The applicability of the visional reading of the grading was also essential to decide the magnitude. This reading was noticed to be changing according to the position of the measurement pointer location in relation with the scale grading. It

was easy to decide the magnitude when the two lines matched together. And there was an approximation with positive or negative fractions when the two lines didn't mach. This was a source of error in the hand measurement of the depth that didn't exceed 1/32nd of an inch.

IV.3.2.2. Measuring process time problem

It was noticed that the recorded time of the measuring process was affected by the movement magnitude and direction the moving part has to go through to approach the target point. The greater the distance between the sequential point's locations the more that moving part needs vertical and horizontal adjustment.

To make the process faster and smoother that movement was reduced to the minimum by adjusting the numbering system of the targeted points. The numbering system started with point number one at the top right corner and moving to the left. At the end of the first row the numbering continues at the adjacent lower row from the left moving to the right and the next row from the right to the left and so on, reaching the last point number 100 at the lower right corner, as shown in Fig. 46.

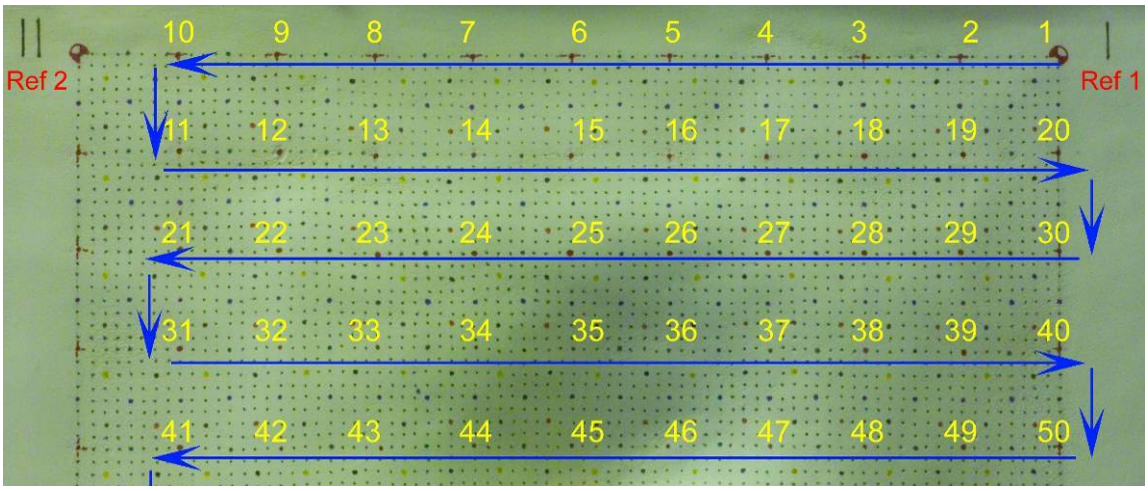

Fig. 46. The numbering system for the point's sequence.

IV.3.3. The OMIT measuring method problems

The problems encountered while performing the OMIT measuring method were associated with images distortion and the resulting moiré dark fringes orientation.

IV.3.3.1. Image distortion problem

The acquired images had a one vanishing point perspective. At the targeted level of accuracy, the main concern was the effect of perspective depth on measurement integrity if the images were used without rectifying. To construct validity for extracting orthographic measurements from images without the need for rectifying, a measurement comparison test was performed.

For this evaluation, the real image of the model surface in each sample was compared with top view of the TMVS. The evaluation was carried out by superimposing the real images on the TMVS top view using Architectural Desktop software. The red colored referenced points were used to indicate the orthographic validity of the images. TMVS red points were assigned a circular mode using the value of (33) on PDMODE command. The size of the circles were assigned the value of $1/8^{th}$ of an inch using the PDSIZE command. For each sample, the locations of the red marked points in the image were visually evaluated to confirm their location within the boundaries of the $1/8^{th}$ of an inch circle of the corresponding referenced points in TMVS top view, as in Fig. 47.

IV.3.3.2. The resulting moiré dark fringes orientation problem

It was noticed that the form of the dark fields differed slightly in each of the eight samples.

These differences were related to the samples' slight differences in the physical model orientation on the specimen base when performing the experiments. The generated contour lines where always parallel to the reference plane (the specimen base).

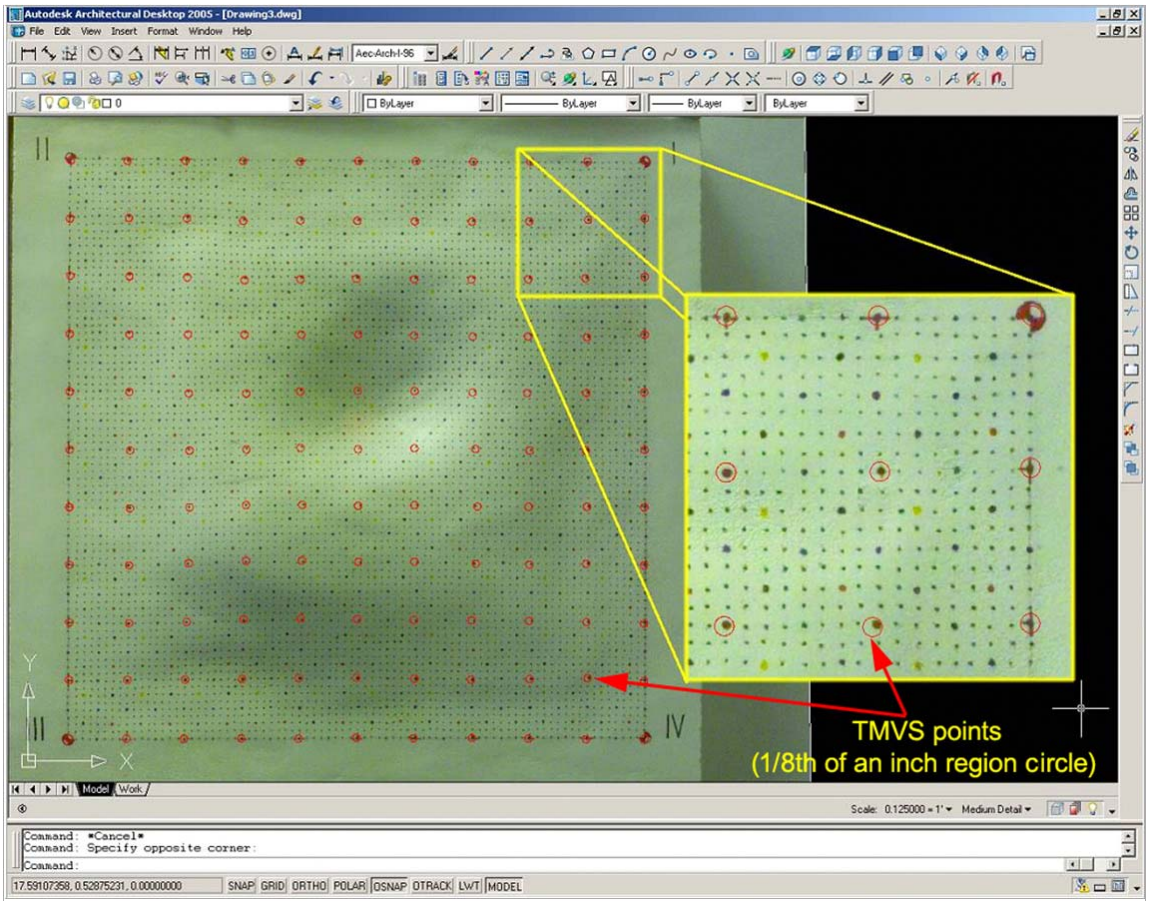

Fig. 47. Evaluating images for orthographic measurements extraction validity.

The small change in model orientation caused the differences in the location of linear dark fields on the model surface. This caused the difference in the fields shapes that were associated with that different orientation. Figure 48 is a demonstration in 3D studio viz showing the changes in the contours shape for four copies of the same model under the same section levels but with different model orientations in space.

For contour accuracy comparison and according to those contour shape differences, there was a need to compare the resulting OMIT contours for each sample with the TMVS contours generated with the same original orientation of the physical model. For referencing the traced contour lines for each sample with a model original orientation, the samples orientations were identified in

relation with a reference plane. For that purpose, the TMVS was reoriented according to the dark field's locations on its surface for each sample.

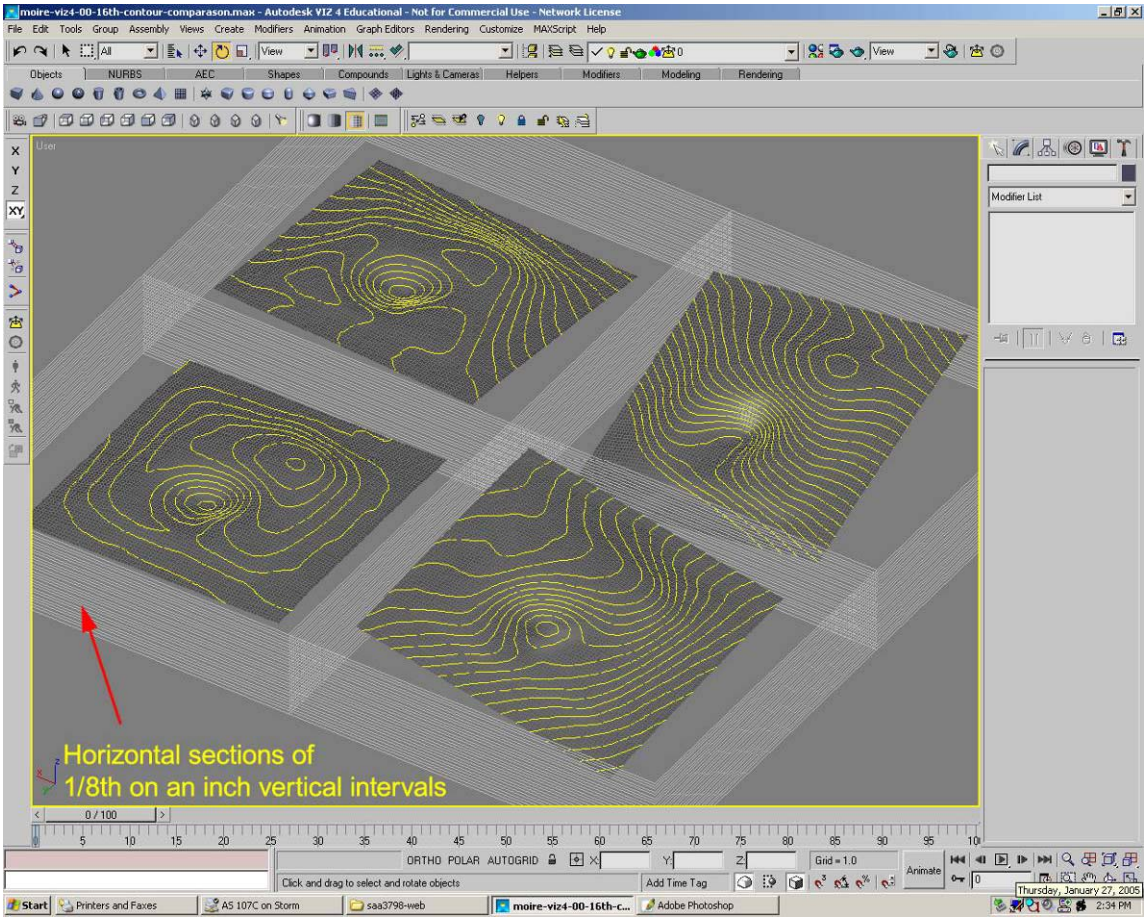

Fig. 48. The change in contours according to orientation in 3D studio viz.

By virtually superimposing the resulting moiré fields on the TMVS, a group of selected vertices were identified on its surface as points located at the same dark field (contour line plane). This means that to orient the TMVS as the physical model in its original location, the plane connecting those points should be parallel to the reference plane. To achieve this, three vertices of this group of vertices (separated as far as possible from each other) were connected with a plane to define the moiré reference plane orientation in space. The TMVS connected with this plane were reoriented to give the selected three vertices on

its surface a parallel location with the X-Y virtual plane (the reference plane of the specimen base). This was performed using align normal command to align the three vertices plane orientation with the X-Y plane orientation, as shown in Fig. 49.

For the eight samples, this procedure was performed to reconstruct the same model orientation of the OMIT experimental setting for each sample.

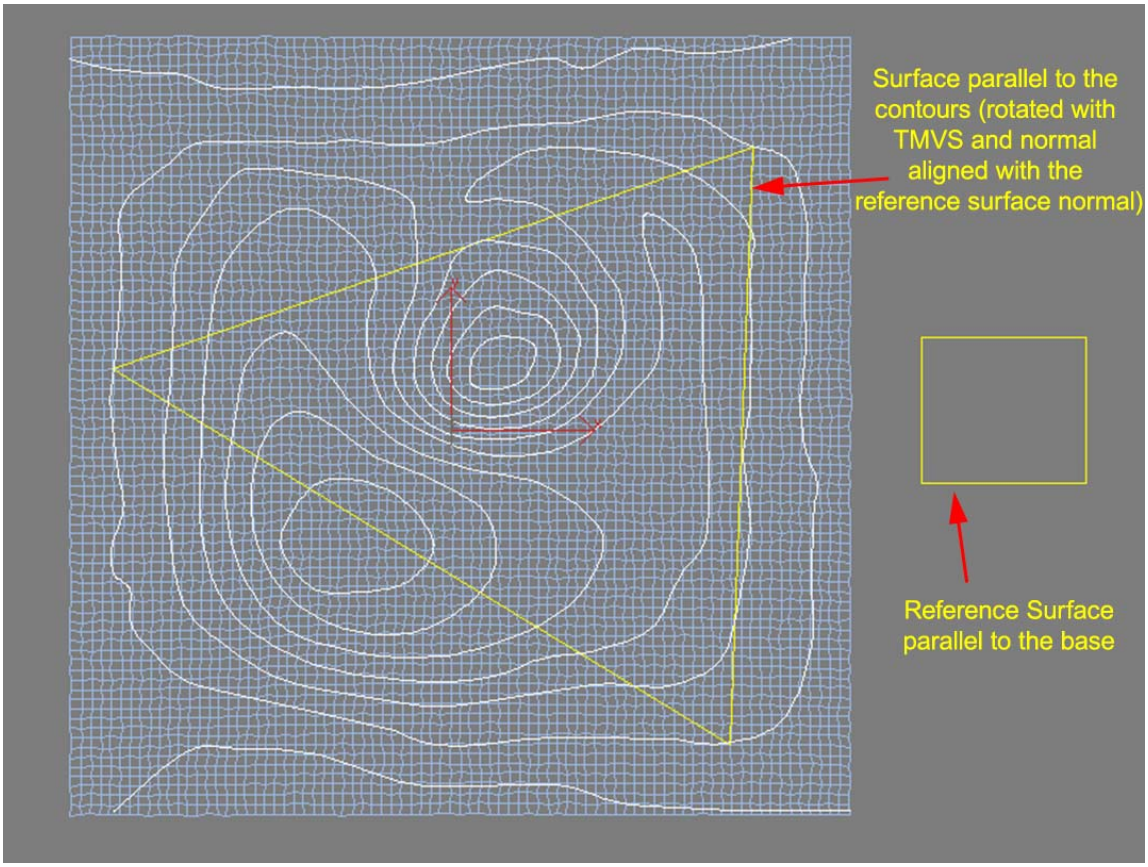

Fig. 49. Moiré field normal alignment in 3D studio viz.

IV.4. Generated data description

Two types of data generated from the experiments were time-consumption data and contour measuring data. The data were associated mainly with pre-defined samples gathered from the two compared measuring methods under

investigation. Contour measuring data generated from the two methods will be discussed in the following sections.

IV.4.1. Contour lines generating method

As the first step toward depth measurement accuracy evaluating, 3D studio viz 2005 software was used for the purpose of generating the contour diagrams.

Contour lines by definition are diagrammatic lines on an object surface connecting points that share the same elevation from a reference level. The section command in the creation panel of 3D studio viz was used to determine the shape of the contour line at a certain level. This command defines (in the form of line) lines of intersection between the section plane and the surface of any 3D object at any inserted level. When changing the section plane level or orientation, the contour line at that level (intersection boundary) was changed accordingly.

To utilize this tool for generating contour lines, a number of section planes were stacked parallel to an imaginary plane connecting the three predefined reference points. These section planes were stacked on top of each other with $1/8^{th}$ of an inch separation between each set of adjacent planes. By this arrangement, each section plane intersected the model surface at that plane elevation. By perceiving all the resulting lines from a view parallel to the reference plane, this process generated section lines that can be considered contour lines for the model surface. Those contour lines are associated with the orientation of the reference plane and the intervals of the distance in-between planes, as shown in Fig. 50.

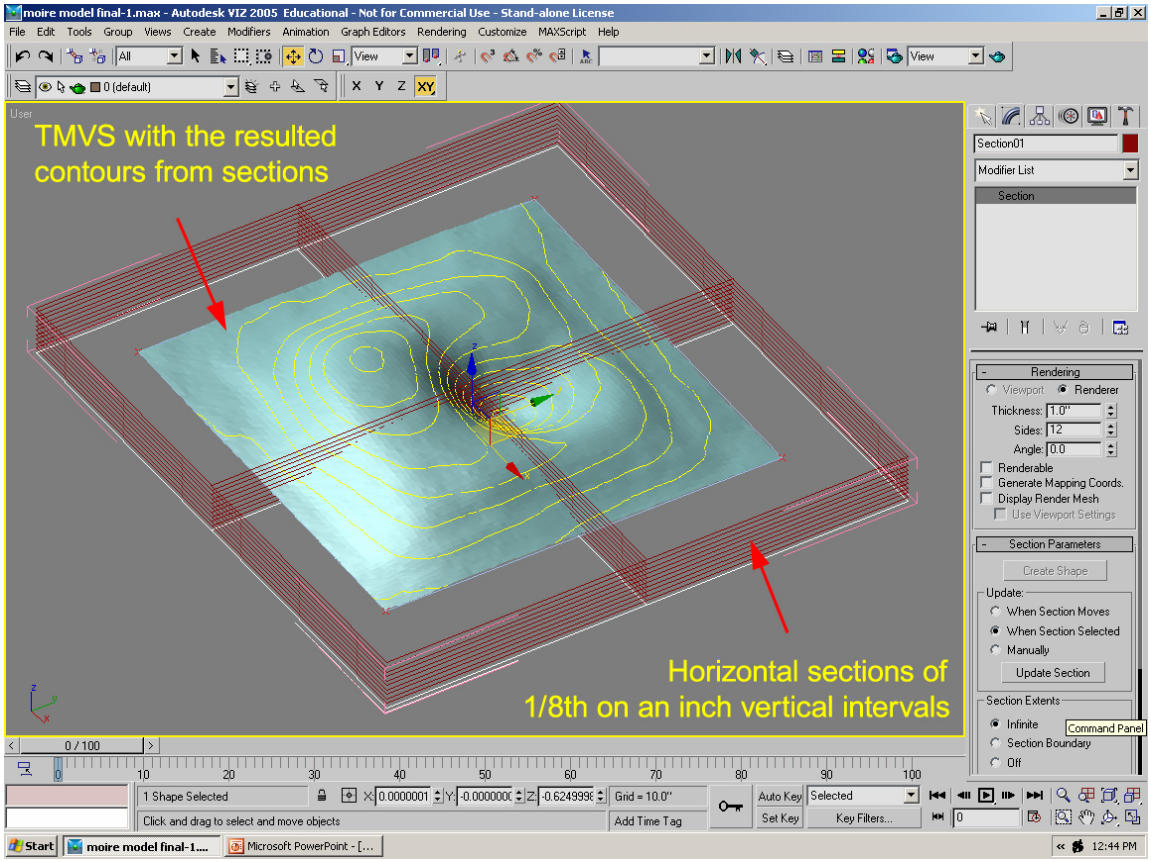

Fig. 50. True model contour lines resulting from sections in 3D studio viz.

IV.4.2. Hand measuring contour data generation

Since it uses a point-to-point information approach, hand measuring method generated a 3D mesh of points forming a virtual surface for each of the eight experimental samples. These hand measuring virtual surfaces (HMVS) worked as digital representations of the measured physical surface and were operated to generate contour diagrams as a 2D representation of the surface relief.

The true model virtual surface (TMVS) and the eight HMVS were imported from AutoCAD to 3D studio viz for contour comparing purposes. For this comparison, the HMVS had to be aligned with the TMVS location and orientation in the virtual space using tools available in 3D studio viz environment. The two virtual surfaces were aligned using the (normal align) command. This

was performed by aligning the normal of a plane connecting three of the four predetermined reference points in the HMVS, with the normal of a plane connecting the corresponding three reference points in the TMVS. By performing this procedure, the HMVS and the TMVS had the same location and orientation in the virtual space. For the eight samples, the two compared virtual surfaces overlapped in the virtual environment, as shown in Fig. 51.

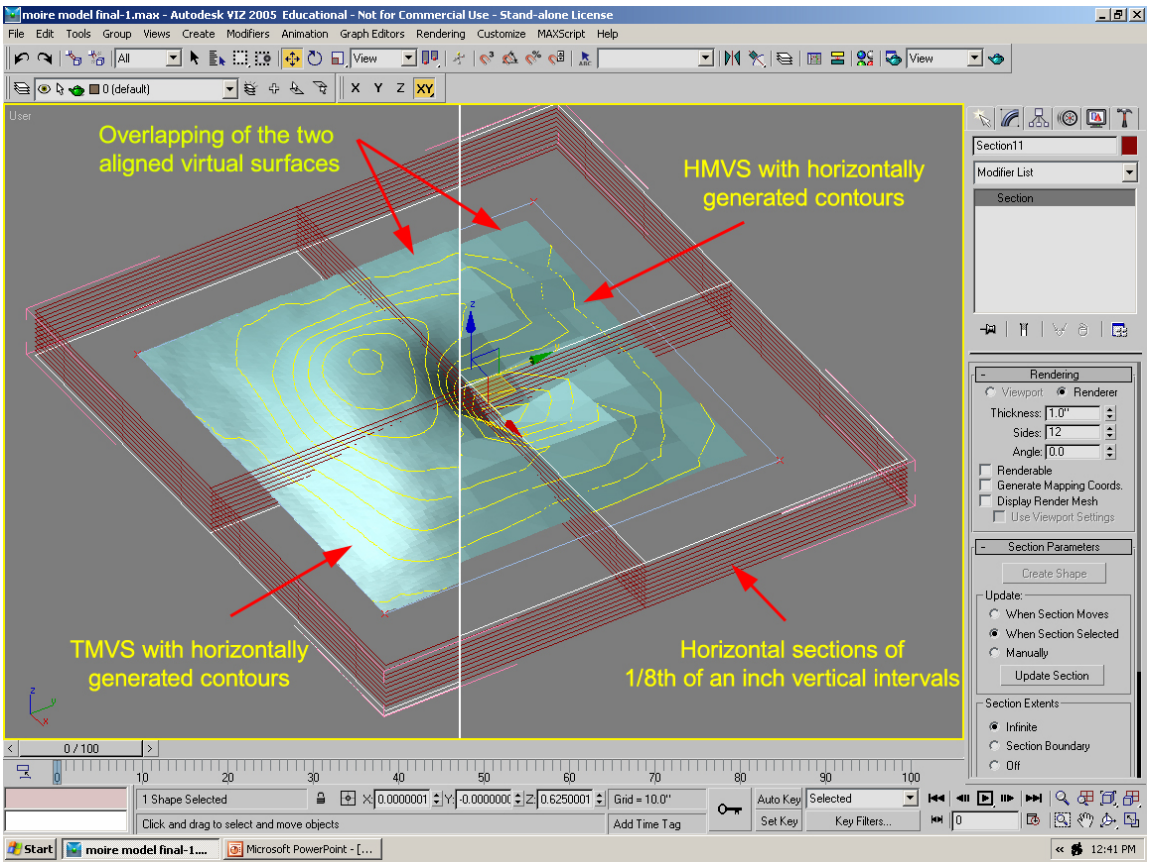

Fig. 51. The TMVS and the HMVS overlapping in 3D studio viz.

By applying the contour lines generating method mentioned earlier in IV.4.1, the contour lines with their error tolerance regions were generated for the TMVS as the basis for testing the measurement accuracy for the hand measurement method, as shown in Fig. 52. The procedure of generating error tolerance regions from the TMVS will be discussed later in Section (IV.5).

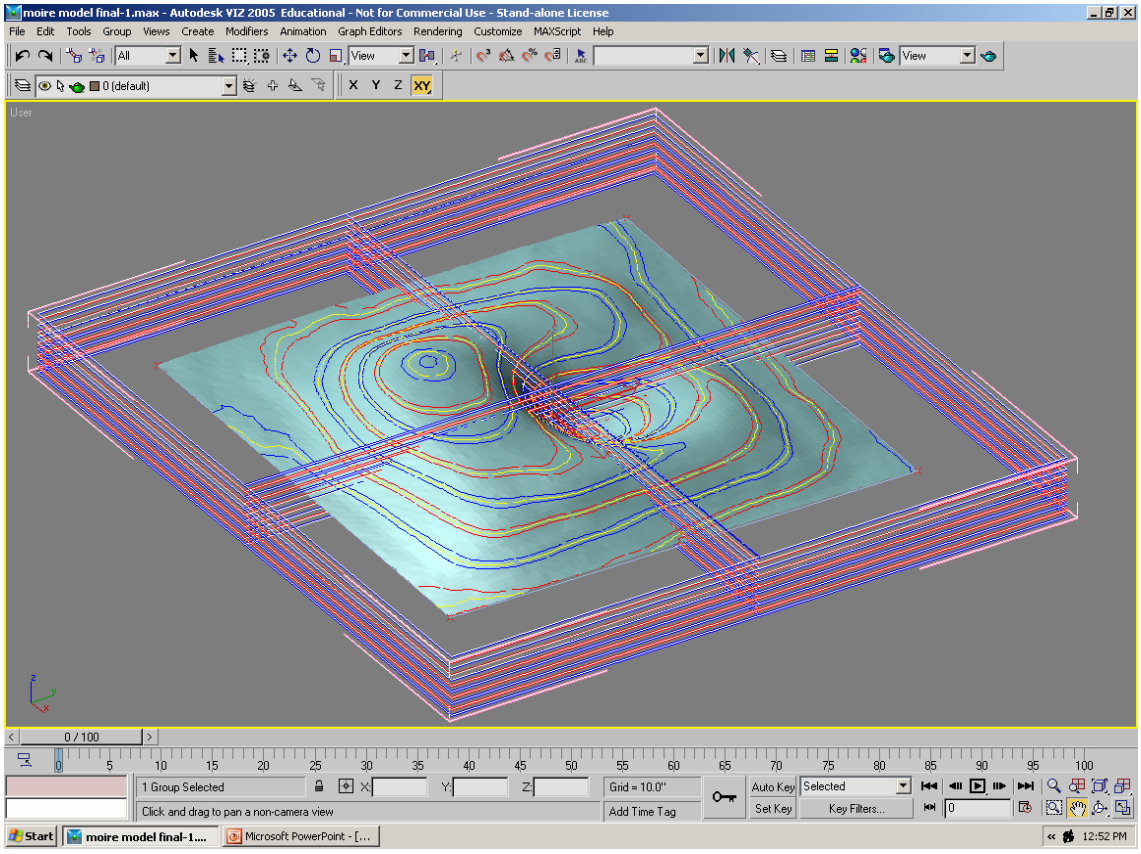

Fig. 52. The contour lines and tolerance region sections for the TMVS.

Using the same contour creating method, the contour lines were generated for the eight virtual surfaces created from the hand measurement method samples, as shown in Fig. 53. After this step, the measurement accuracy test for the resulting contour lines was performed on cad 2D environment. To prepare for exporting the resulting lines to the cad environment, the viewing direction of the 3D studio viz environment was changed to the top view and the document was exported in (DXF) format. The (DXF) file was opened in cad environment and the contour lines drawings were ready for evaluating the depth measurement accuracy.

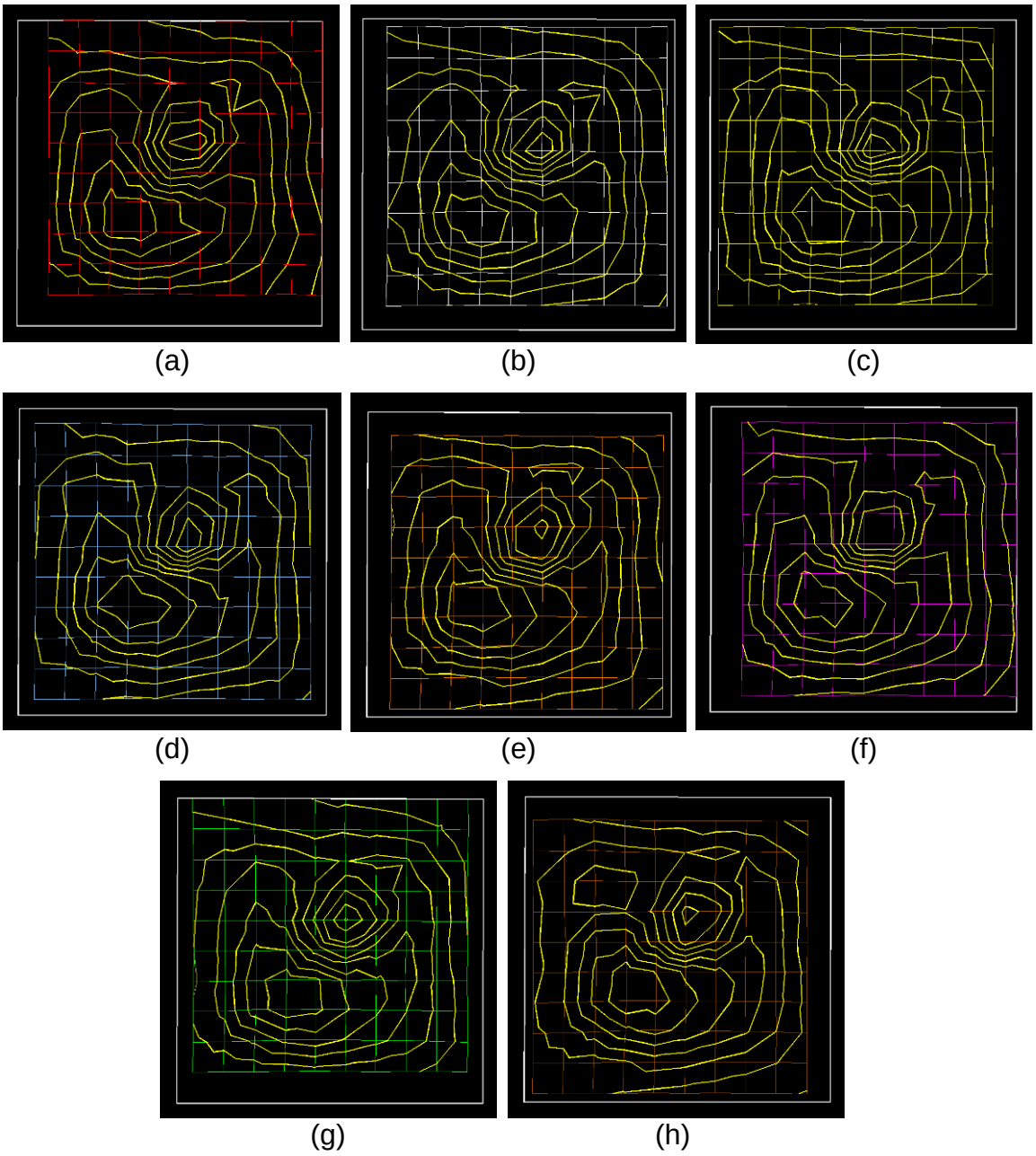

Fig. 53. The contour lines for the eight samples of the HMVS. (a) Red grid sample contours, (c) Black grid sample contours, (d) Yellow grid sample contours, (e) Blue grid sample contours, (f) Orange grid sample contours, (g) Magenta grid sample contours, (h) Green grid sample contours, (j) Brown grid sample contours.

IV.4.3. The OMIT contour data generation

Because of the OMIT potentials as an integral information method, its eight experimental samples instantly produced linear dark fields out of the process of superimposing images. Those fields represented topography contours as a 2D representation of the surface relief. As mentioned earlier, the form of the dark fields differed slightly in each of the eight samples according to model orientation in relation to the reference plane, as shown in Fig. 54.

For each sample, the resulting dark fields from the superimposed images were traced by hand to generate the contour lines as mentioned earlier (in section IV.2.2). The contour drawings resulting from this process worked as the OMIT contour representation of the physical model surface relief, as shown in Fig. 55.

For the eight samples, a special procedure was performed to reconstruct the same model orientation of the OMIT experimental setting for each sample as mentioned in IV.3.3.2. By applying the contour lines generating method mentioned earlier in IV.4.1, contour lines representing the error tolerance regions were generated for the TMVS for each sample. These regions worked as the base for testing the measurement accuracy of the OMIT measuring method. The procedure for generating error tolerance regions will be discussed in the next section (IV.5).

The section tool was used in 3D studio viz for generating contour lines. For measurement accuracy evaluation, Cad 2D environment was used for comparing the contour lines resulting from the OMIT with the TMVS contour lines at the same orientation. To prepare for exporting the resulting lines from the viz environment to the cad environment, the viewing direction of the 3D studio viz environment was changed to top view and the document was exported in (DXF) format. The (DXF) format file was opened in cad environment and the contour line drawings were ready for testing the depth measurement accuracy.

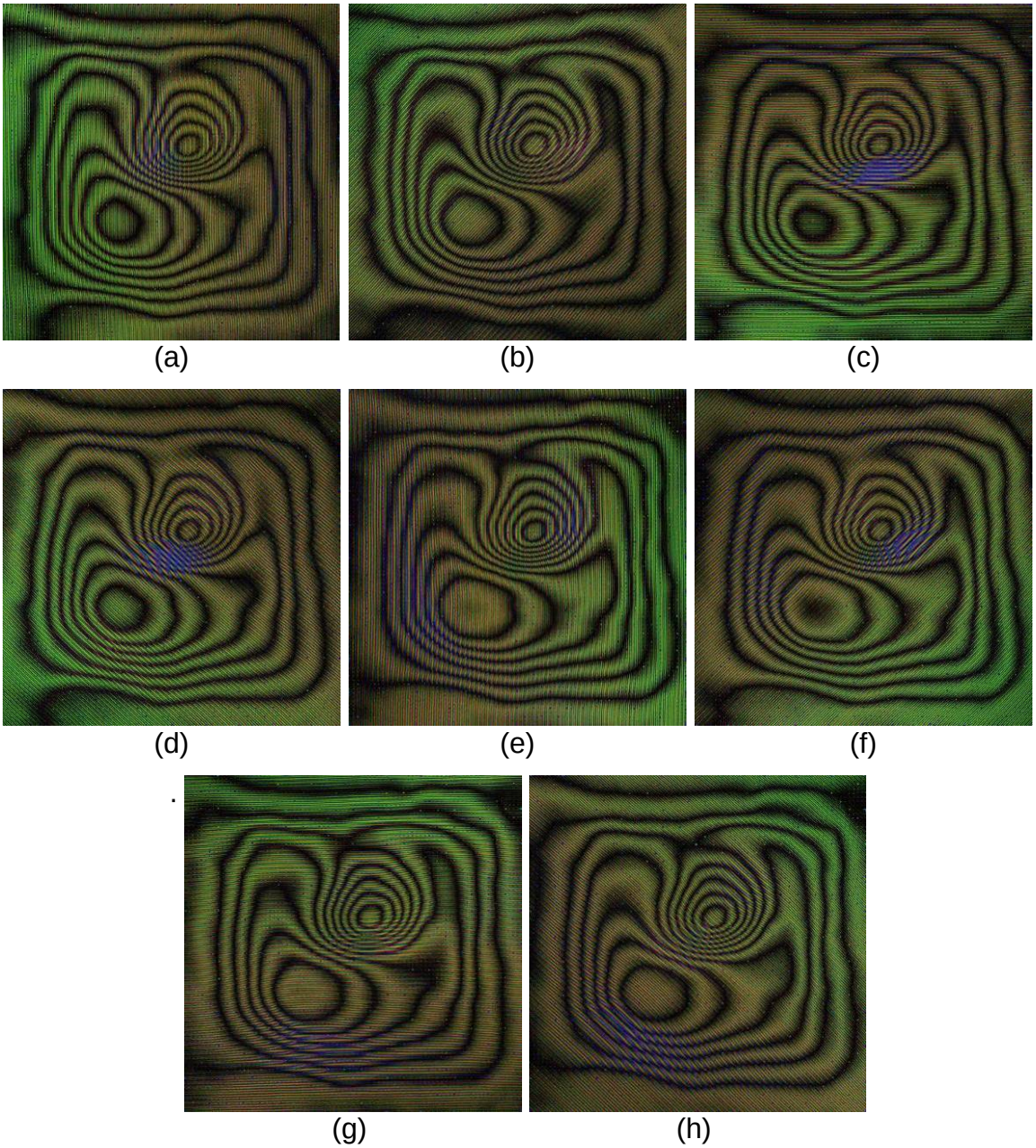

Fig. 54. The resulting dark fringes from the OMIT measuring method samples.
(a) zero degree rotation sample, (b) 45° rotation sample, (c) 90° rotation sample,
(d) 135° rotation sample, (e) 180° rotation sample, (f) 225° rotation sample,
(g) 270° rotation sample, (h) 315° rotation sample.

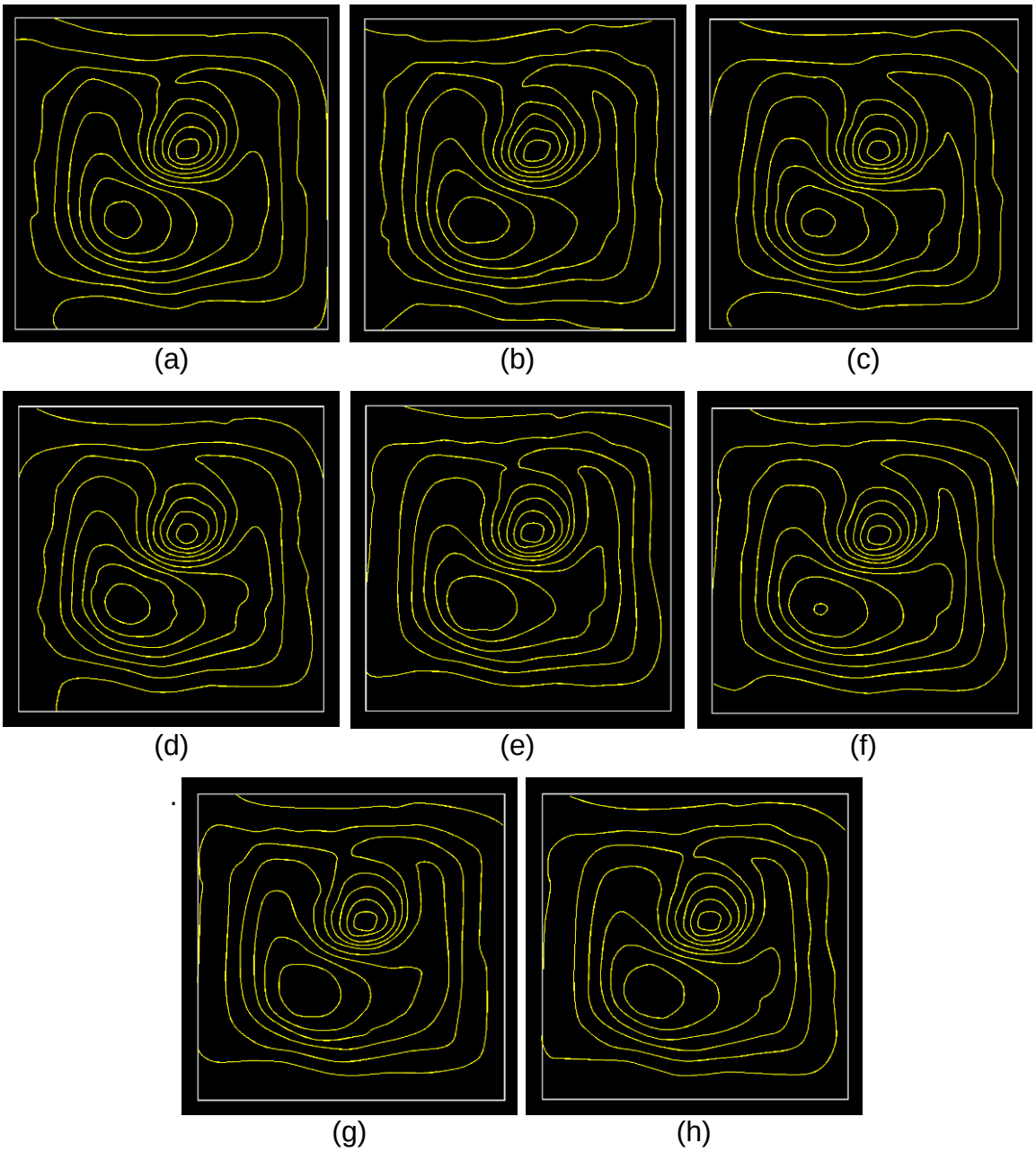

Fig. 55. The resulting contour lines from the OMIT dark fields scanning. (a) zero degree rotation sample, (b) 45° rotation sample, (c) 90° rotation sample, (d) 135° rotation sample, (e) 180° rotation sample, (f) 225° rotation sample, (g) 270° rotation sample, (h) 315° rotation sample.

CHAPTER V

GENERATED DATA ANALYSIS

In this chapter, contour measuring data for each sample was evaluated against the targeted accuracy threshold. This evaluation supports the validity of the accepted individual samples for comparing time-consumption of the processes. Time-comparison results of the methods were examined to conclude feasibility.

V.1. Generated contour drawings analysis

To analyze the resulting contour drawings for the investigated methods, the measurement accuracy is evaluated and discussed in the following sections.

V.1.1. Contour accuracy evaluation procedure

The concept of the contour accuracy evaluation procedure was to find the error magnitude of the contour lines for each sample in comparison with the true contour lines from the true model. This magnitude was quantified by defining error tolerance values surrounding the true contour lines. The tolerance values were associated with a predetermined targeted contour measurement accuracy of 1/8th of an inch, 3/32nd of an inch, 1/16th of an inch and 1/32nd of an inch. The accuracy level of 1/8th of an inch is the targeted level in this study while the other levels were included to explore the methods' measurement accuracy potentials.

By applying the contour lines generating method mentioned earlier (section IV.4.1), it was possible to define the upper tolerance and the lower tolerance of each contour line for each accuracy level.

In 3D studio Viz software, The 1/8th of an inch error tolerance regions were defined by creating new sections located vertically above and below the 1/8th of an inch section lines. This was performed by grouping the original section planes created at a vertical distance of 1/8th of an inch to act as one object. Two copies of that group were cloned. One group was elevated for a

distance of 1/16th of an inch from its original location (50% of the error tolerance value) defining the upper portion of the error tolerance at 1/8th of an inch accuracy level. The other copy was negatively shifted to a distance 1/16th of an inch below its original location (the other 50% of the error tolerance value) defining the lower portion of the error tolerance of the same accuracy level.

By this procedure, these two groups of section levels defined the vertical region of the predetermined error tolerance. This region was placed around the original contour line located at its center, as shown in Fig. 56.

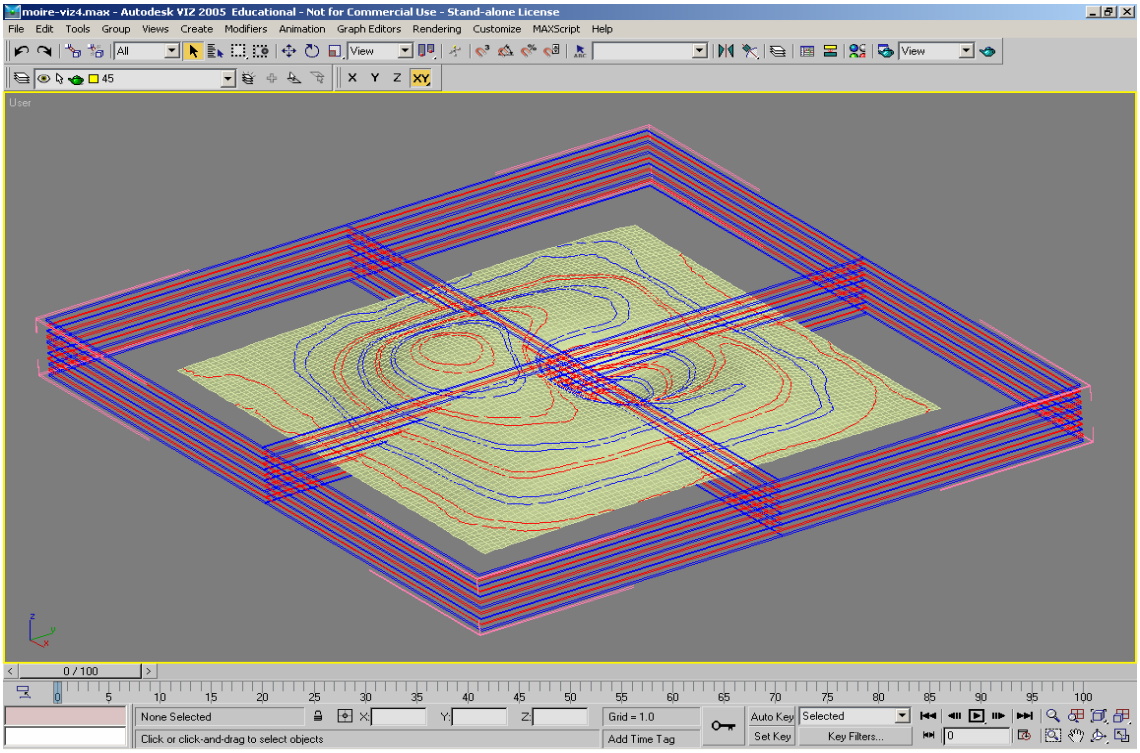

Fig. 56. The OMIT error tolerance region in 3D studio viz for 1/32nd accuracy.

For the two compared methods, this procedure was repeated on the TMVS for the 8 measured samples of each method. Four error tolerance regions of 1/8th of an inch, 3/32nd of an inch, 1/16th of an inch and 1/32nd of an inch were generated for each sample. The total number of error region drawings generated from this procedure for comparison purposes was 64 drawings.

For each predetermined error tolerance, the generated contour lines from the measured samples were evaluated in relation with these defined regions. An error occurred at that accuracy level whenever the measured contour lines left the boundaries of that defined region. The magnitude of the error is quantified by measuring the area enclosed between the measured contour line and the region boundary edge line where the error happened. For each sample and at the predetermined accuracy level, the percentage of error was quantified by the ratio of all the calculated areas to the TMVS total measured area in that sample.

V.1.2. Hand measuring method accuracy evaluation

Each of the eight samples from the hand measuring method was tested for the contour measurement accuracy on the four predetermined levels of accuracy.

For performing the tests, the contour lines resulting from the HMVS were evaluated in relation to the corresponding error tolerance regions resulting from TMVS. The eight hand measuring samples underwent this procedure. The contour lines from the HMVS were superimposed on the error tolerance regions of TMVS for the four accuracy levels as shown in Fig. 57.

AutoCAD Architectural Desktop 2004 software was used for the procedure of isolating and measuring the targeted error areas. For the error percentage calculations, the area enclosed outside the regions between the measured contour line and the region boundary edge line were measured. Using the “trim” and “erase” commands on cad environment, those areas were isolated by excluding all the lines not related to those defined areas. Each group of lines surrounding a targeted area was joined together using the (pedit) command to cause them to act as one object with a measurable area. The error areas were scattered around the regions in both the upper and lower directions as shown in Fig. 58.

To avoid producing false errors resulting from shifting reference planes, it was important to make sure that error areas for each sample did not congregate

in one upper or lower direction. To validate the type of error, the lines defining the areas located below the targeted region were colored in red and the upper ones were colored in blue. By this procedure, the existence of two colored areas in the tested samples is an indication of a real measurement error and not a contour level shifting error.

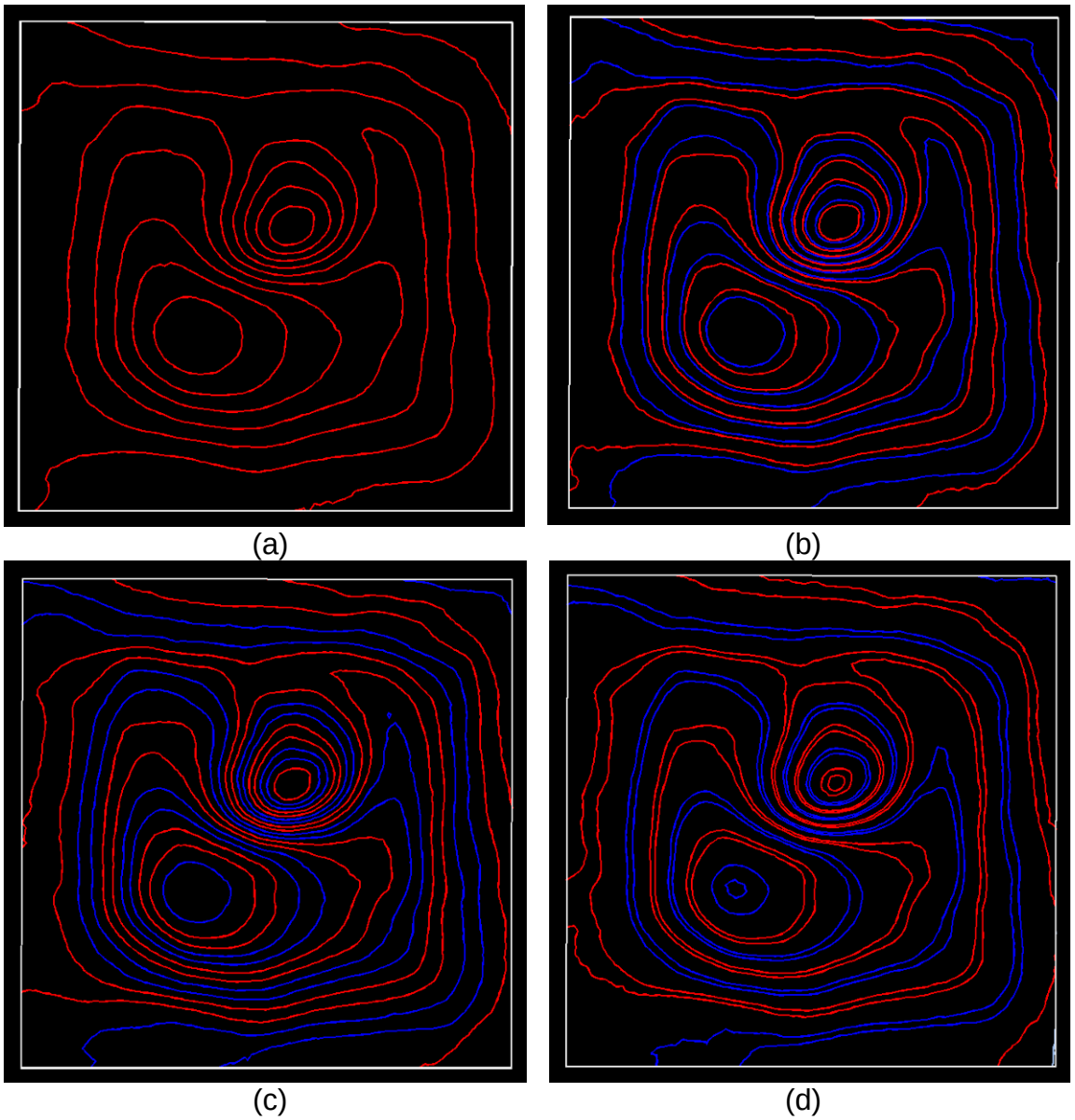

(a) (b)

(c) (d)

Fig. 57. Error region on the four accuracy levels of the TMVS for testing the HMVS. (a) Error region of 1/8th of an inch, (b) error region of 3/32nd of an inch, (c) error region of 1/16th of an inch, (d) error region of 1/32nd of an inch.

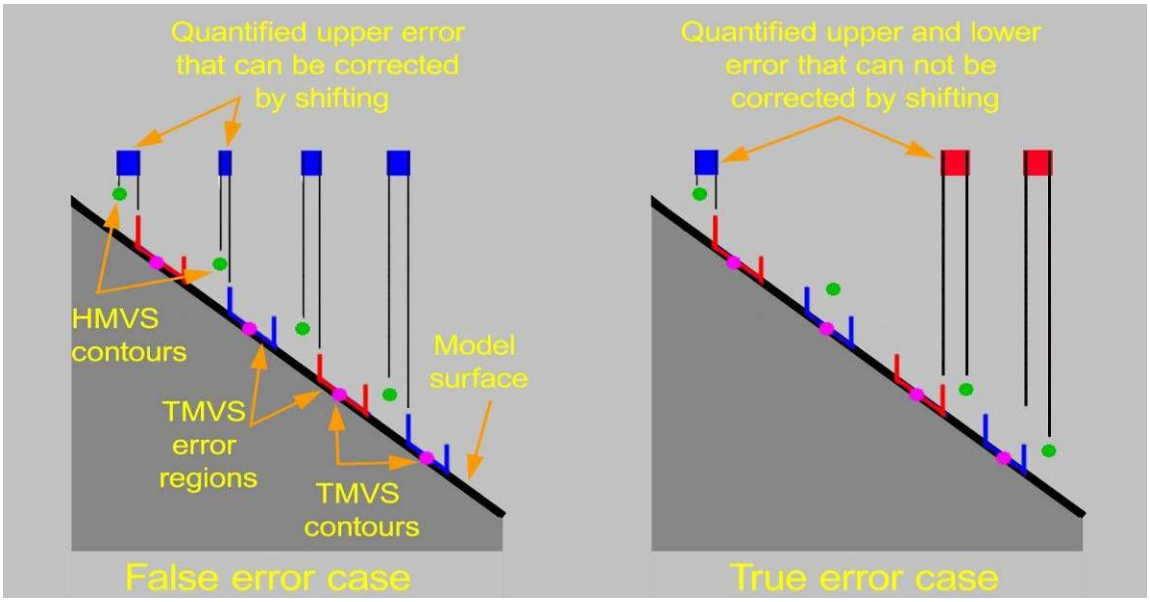

Fig. 58. The concept of quantifying the true error.

The eight colored grid sample errors are shown associated with the four pre-determined accuracy levels in the following Figs. 59 to 90.

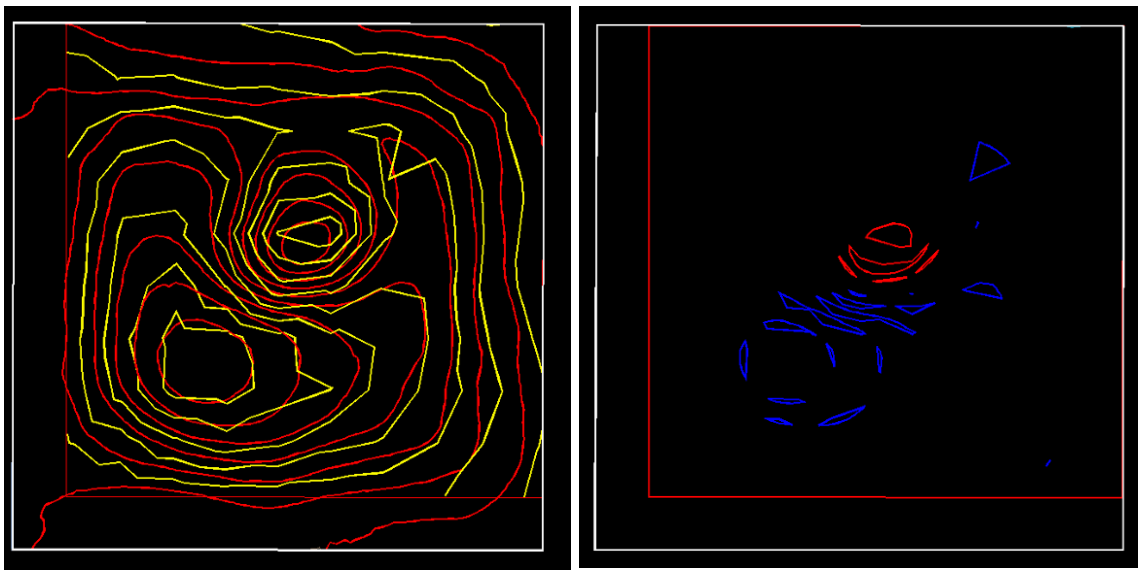

(a) (b)

Fig. 59. The red sample error on 1/8th of an inch accuracy. (a) Contour overlapping, (b) Contour errors: Upper error area = 1.26 in^2, Lower error area = 0.55 in^2 and Total error area = 1.81 in^2.

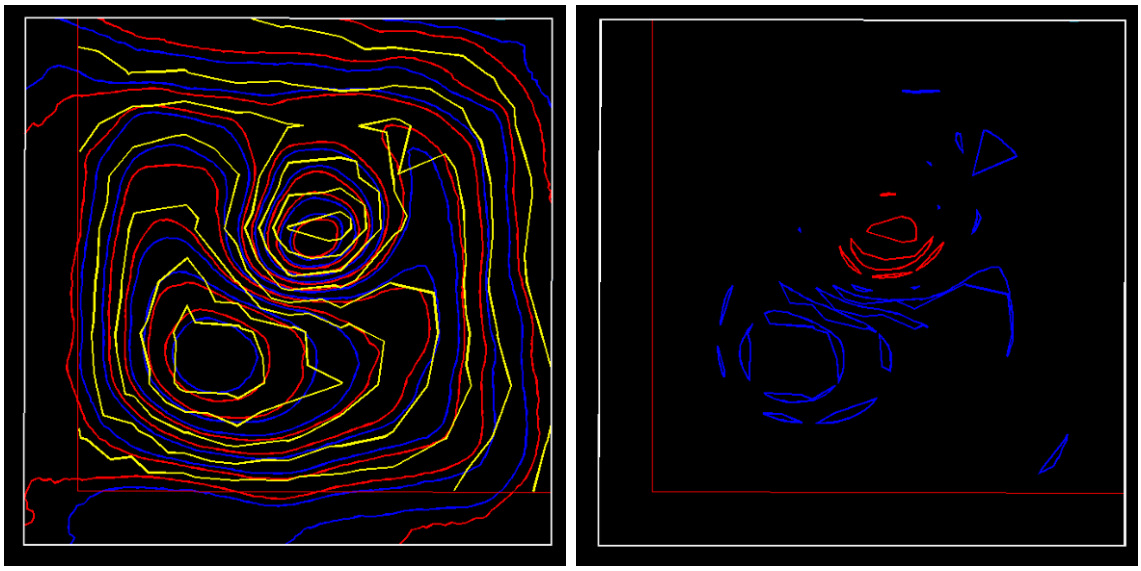

(a) (b)

Fig. 60. The red sample error on 3/32nd of an inch accuracy. (a) Contour overlapping, (b) Contour errors: Upper error area = 2.45 in^2, Lower error area = 0.68 in^2 and Total error area = 3.13 in^2.

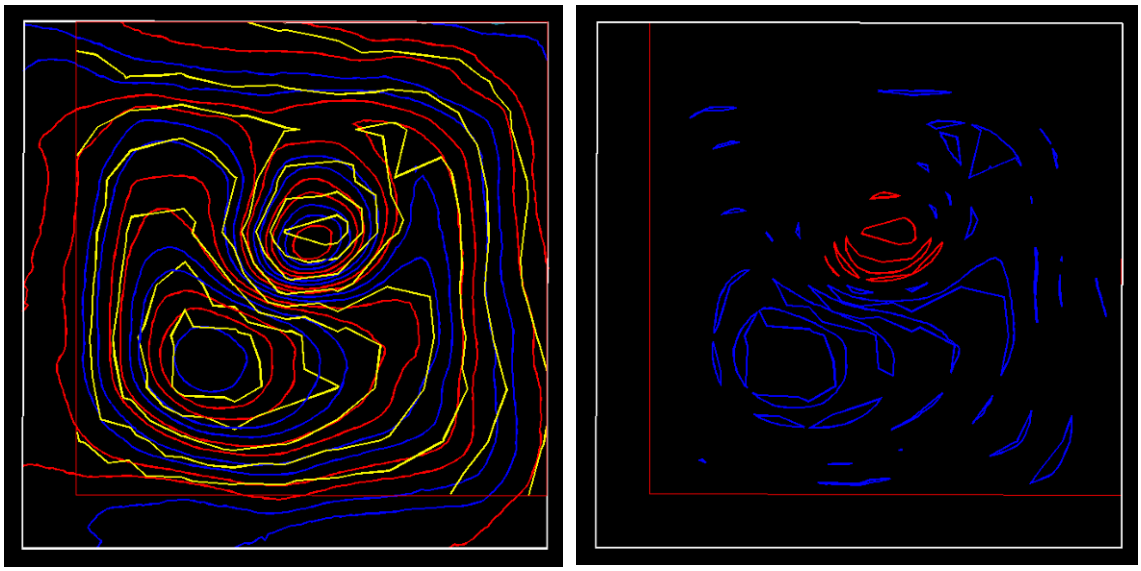

(a) (b)

Fig. 61. The red sample error on 1/16th of an inch accuracy. (a) Contour overlapping, (b) Contour errors: Upper error area = 4.66 in^2, Lower error area = 0.85 in^2 and Total error area = 5.51 in^2.

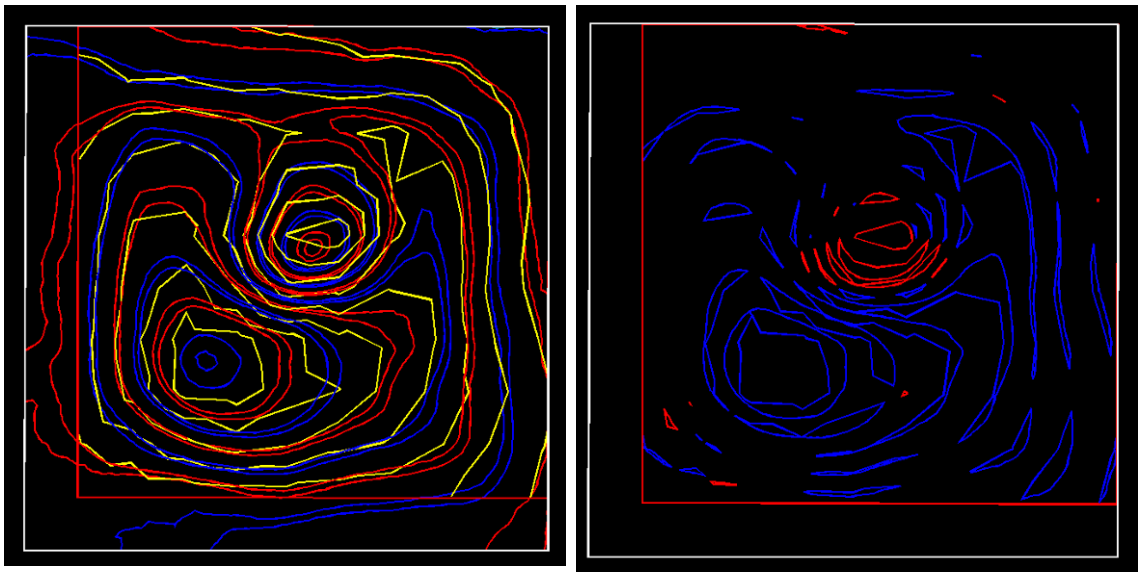

(a) (b)

Fig. 62. The red sample error on 1/32nd of an inch accuracy. (a) Contour overlapping, (b) Contour errors: Upper error area = 9.17 in^2, Lower error area = 1.14 in^2 and Total error area = 10.31 in^2.

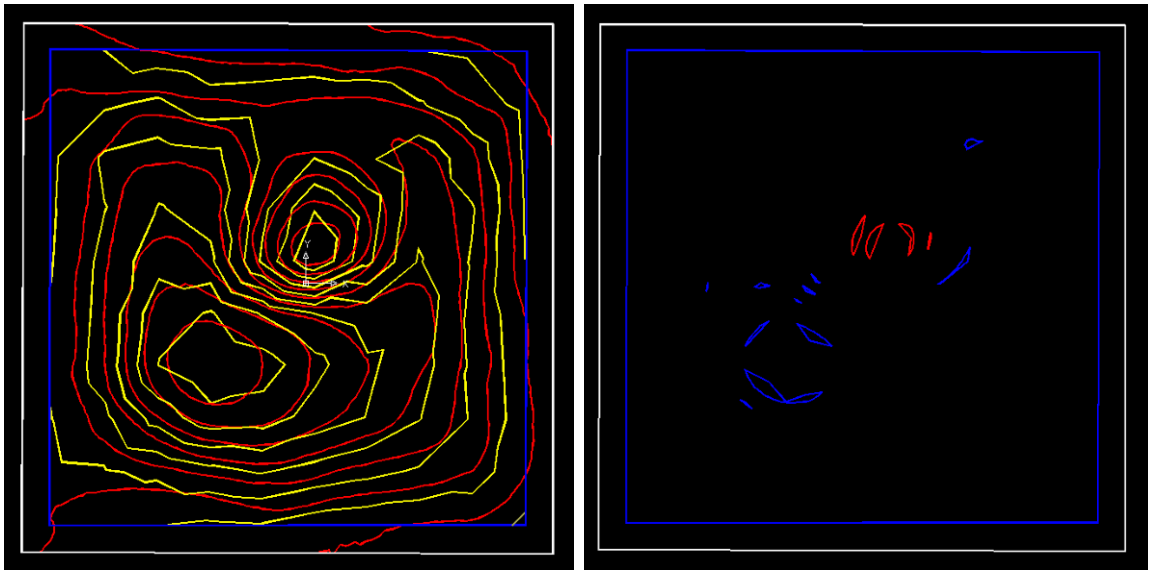

(a) (b)

Fig. 63. The blue sample error on 1/8th of an inch accuracy. (a) Contour overlapping, (b) Contour errors: Upper error area = 0.41 in^2, Lower error area = 0.20 in^2 and Total error area = 0.61 in^2.

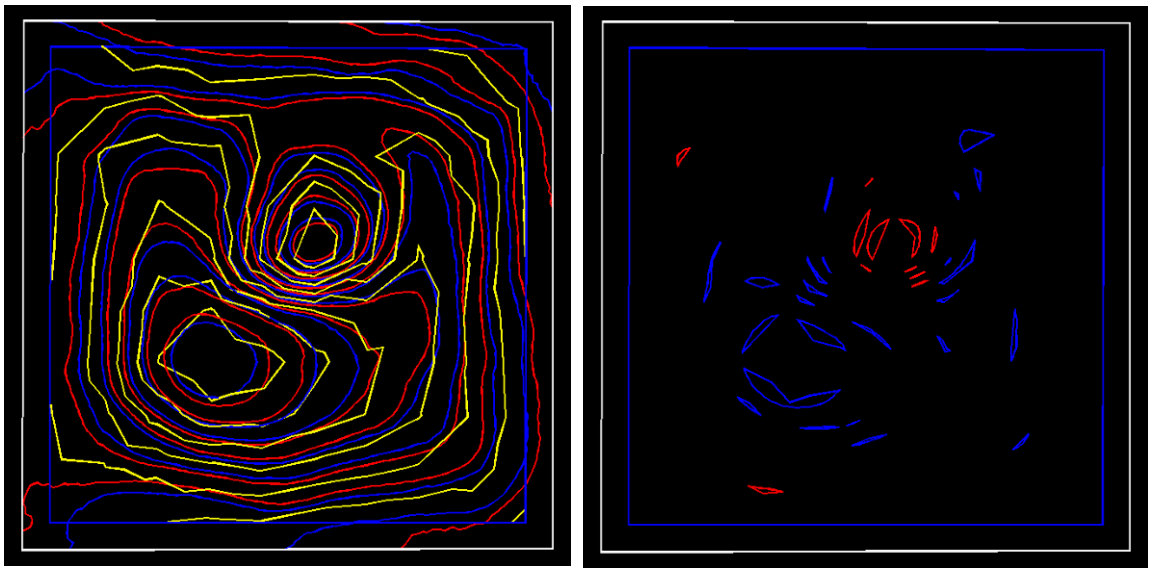

(a) (b)

Fig. 64. The blue sample error on 3/32nd of an inch accuracy. (a) Contour overlapping, (b) Contour errors: Upper error area = 1.22 in^2, Lower error area = 0.38 in^2 and Total error area = 1.60 in^2.

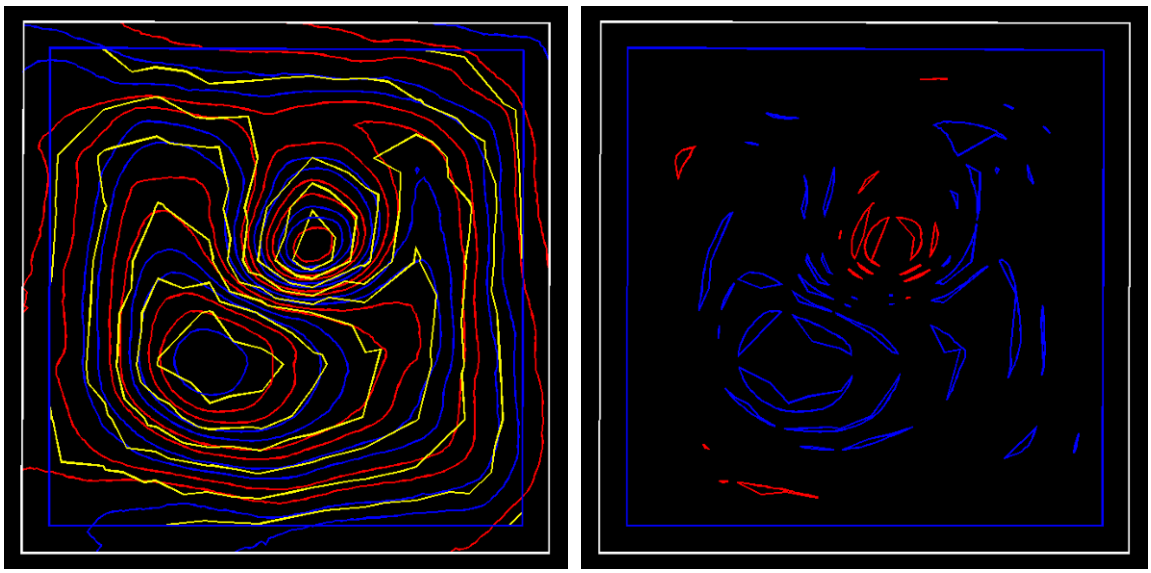

(a) (b)

Fig. 65. The blue sample error on 1/16th of an inch accuracy. (a) Contour overlapping, (b) Contour errors: Upper error area = 3.12 in^2, Lower error area = 0.69 in^2 and Total error area = 3.81 in^2.

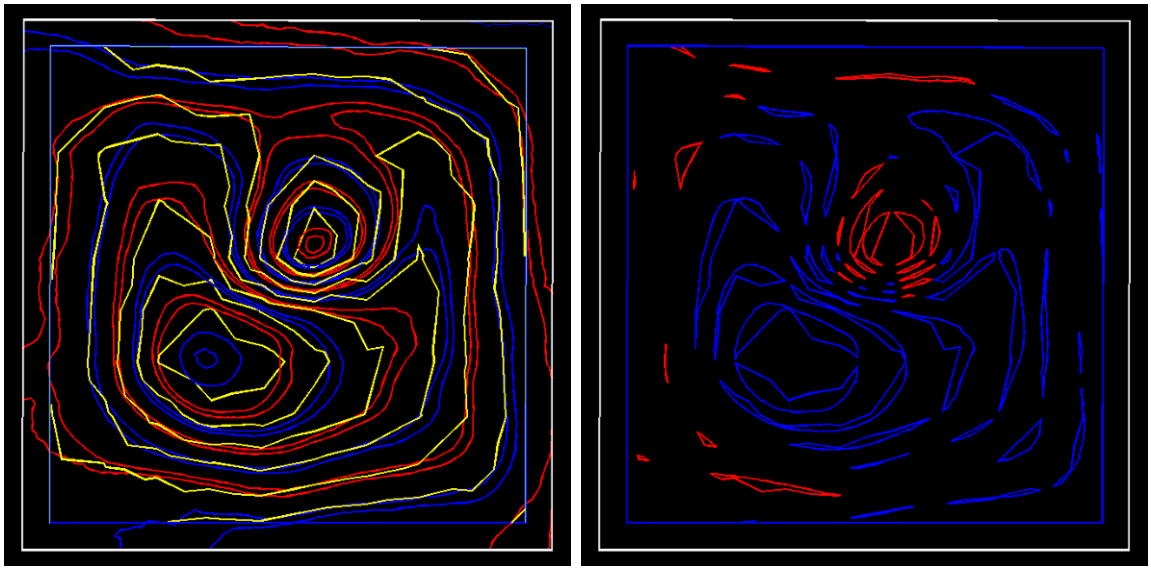

(a) (b)

Fig. 66. The blue sample error on 1/32nd of an inch accuracy. (a) Contour overlapping, (b) Contour errors: Upper error area = 6.88 in^2, Lower error area = 1.41 in^2 and Total error area = 8.29 in^2.

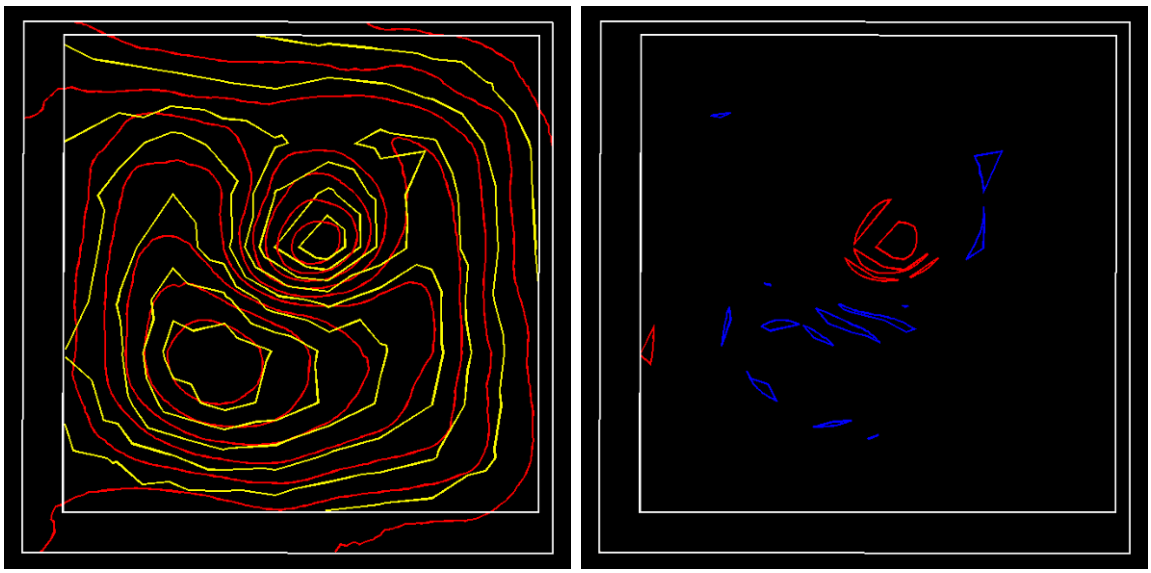

(a) (b)

Fig. 67. The black sample error on 1/8th of an inch accuracy. (a) Contour overlapping, (b) Contour errors: Upper error area = 0.77 in^2, Lower error area = 0.78 in^2 and Total error area = 1.55 in^2.

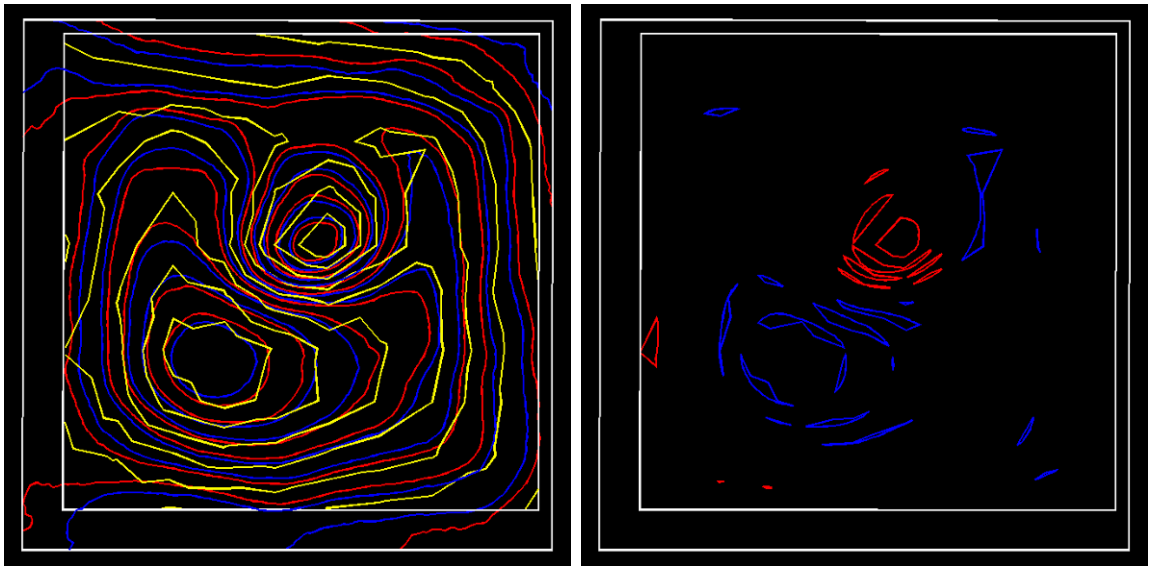

(a) (b)

Fig. 68. The black sample error on 3/32nd of an inch accuracy. (a) Contour overlapping, (b) Contour errors: Upper error area = 1.59 in^2, Lower error area = 1.09 in^2 and Total error area = 2.68 in^2.

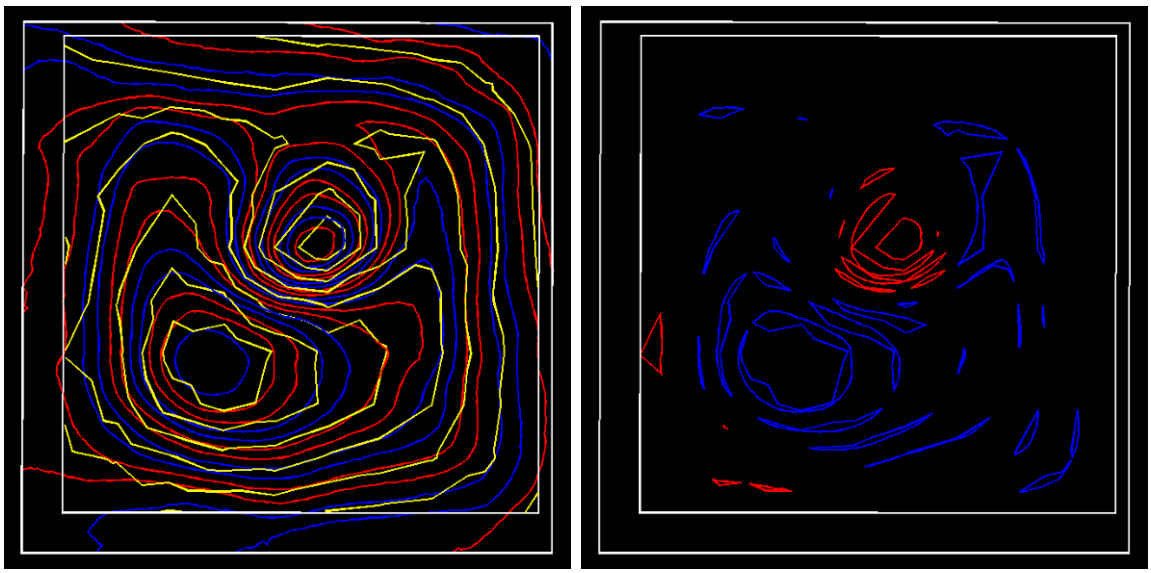

(a) (b)

Fig. 69. The black sample error on 1/16th of an inch accuracy. (a) Contour overlapping, (b) Contour errors: Upper error area = 3.59 in^2, Lower error area = 1.48 in^2 and Total error area = 5.07 in^2.

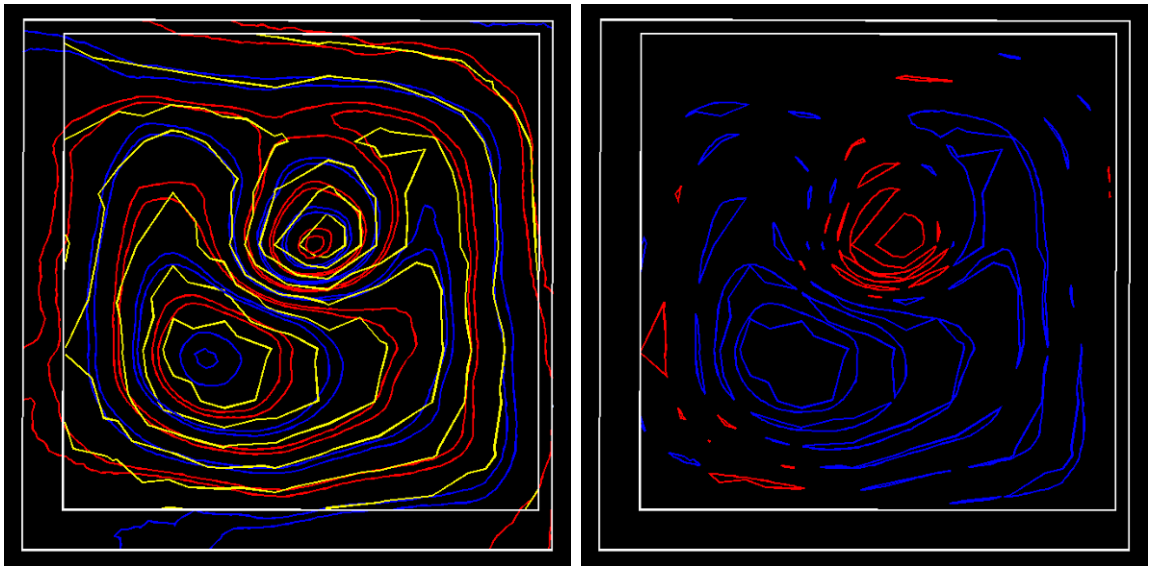

(a) (b)

Fig. 70. The black sample error on 1/32nd of an inch accuracy. (a) Contour overlapping, (b) Contour errors: Upper error area = 7.50 in^2, Lower error area = 2.07 in^2 and Total error area = 9.57 in^2.

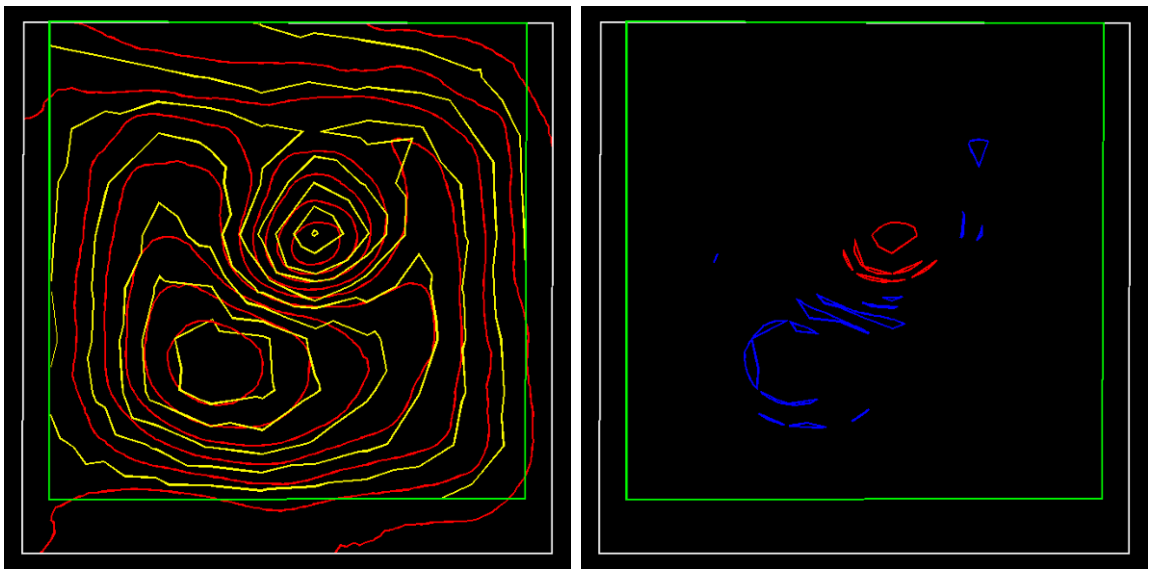

(a) (b)

Fig. 71. The green sample error on 1/8th of an inch accuracy. (a) Contour overlapping, (b) Contour errors: Upper error area = 0.71 in^2, Lower error area = 0.27 in^2 and Total error area = 0.98 in^2.

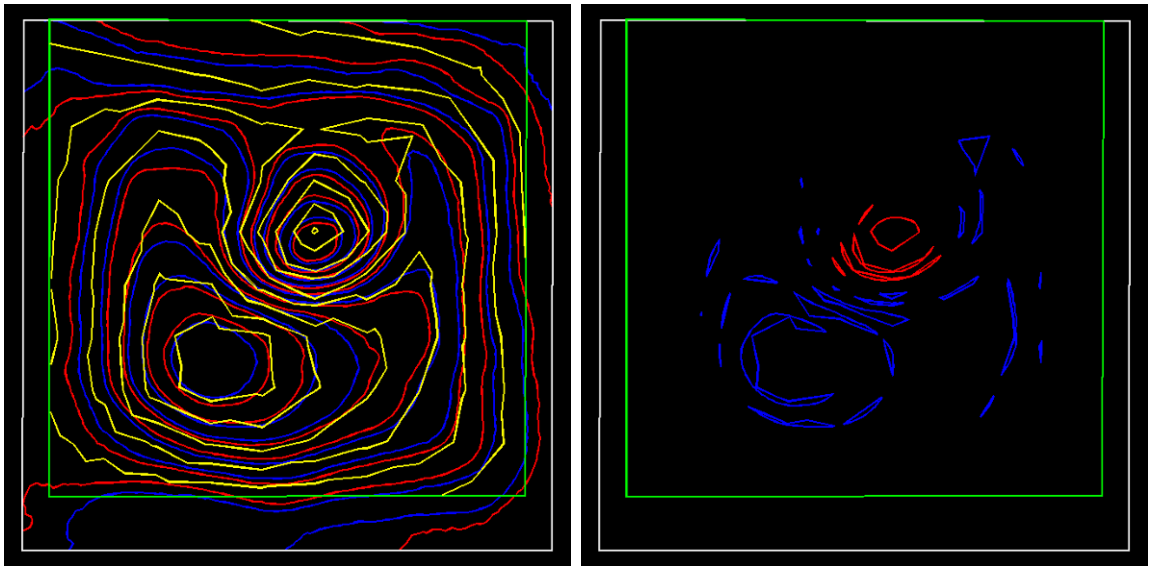

(a) (b)

Fig. 72. The green sample error on 3/32nd of an inch accuracy. (a) Contour overlapping, (b) Contour errors: Upper error area = 1.71 in^2, Lower error area = 0.59 in^2 and Total error area = 2.30 in^2.

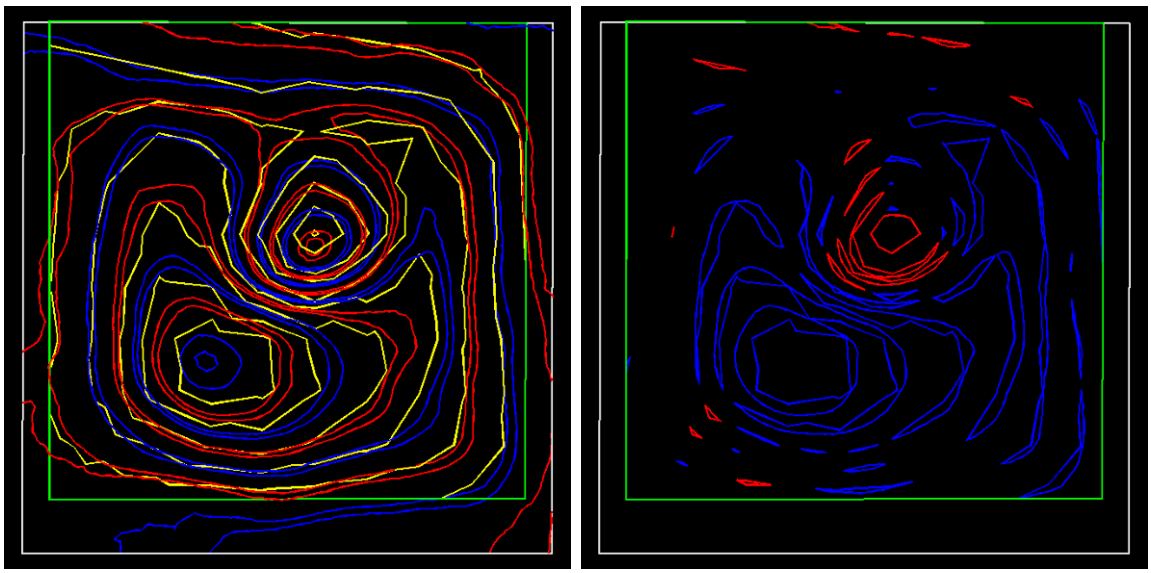

(a) (b)

Fig. 73. The green sample error on 1/16th of an inch accuracy. (a) Contour overlapping, (b) Contour errors: Upper error area = 7.84 in^2, Lower error area = 1.27 in^2 and Total error area = 9.11 in^2.

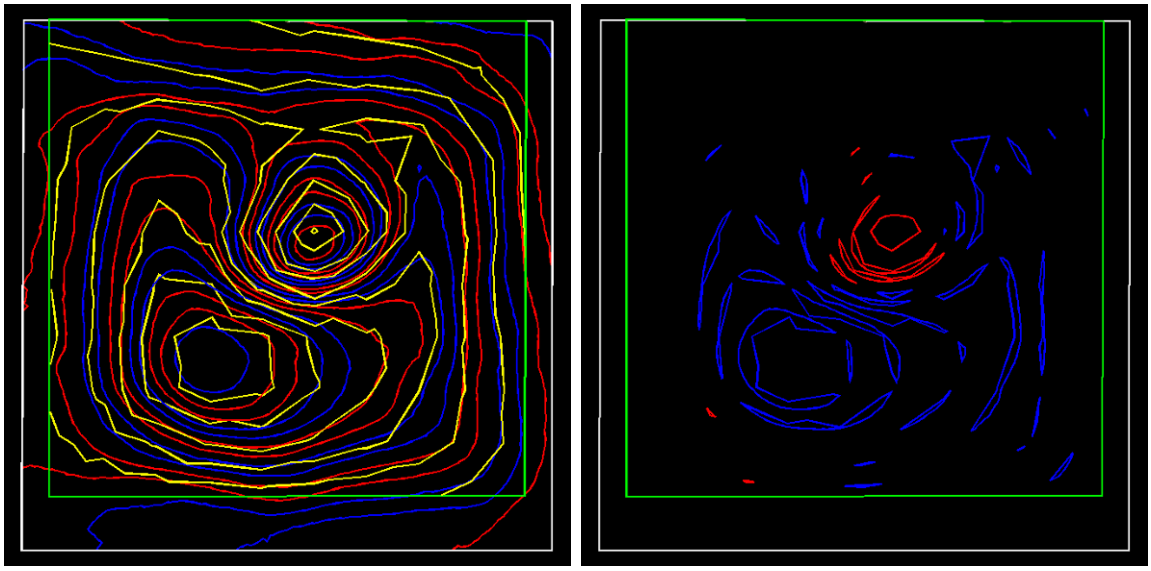

(a) (b)

Fig. 74. The green sample error on 1/32nd of an inch accuracy. (a) Contour overlapping, (b) Contour errors: Upper error area = 3.78 in^2, Lower error area = 0.79 in^2 and Total error area = 4.57 in^2.

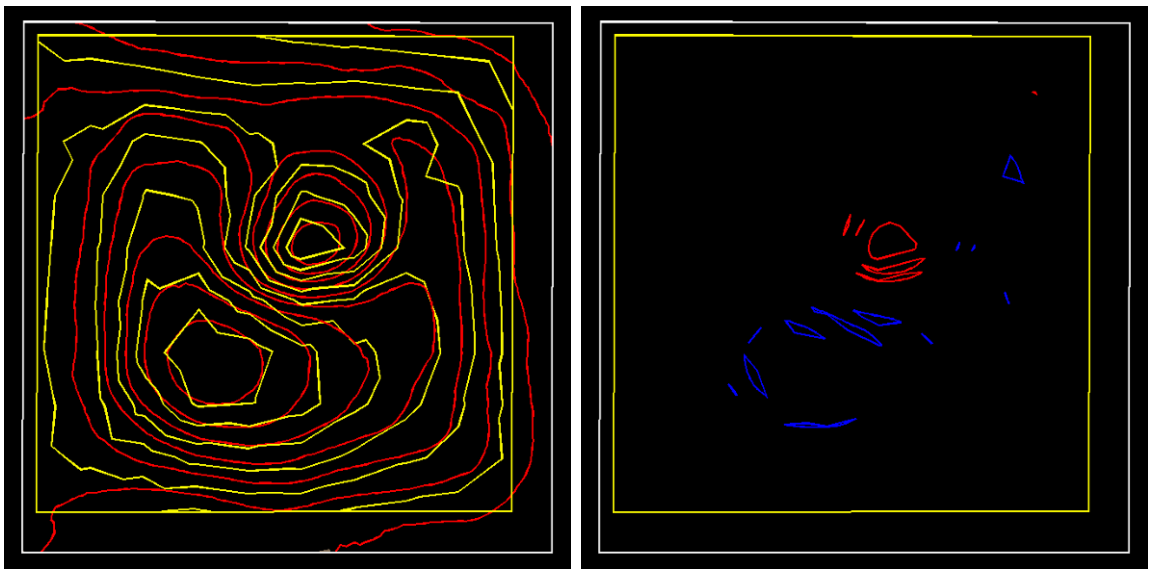

(a) (b)

Fig. 75. The yellow sample error on 1/8th of an inch accuracy. (a) Contour overlapping, (b) Contour errors: Upper error area = 0.54 in^2, Lower error area = 0.61 in^2 and Total error area = 1.15 in^2.

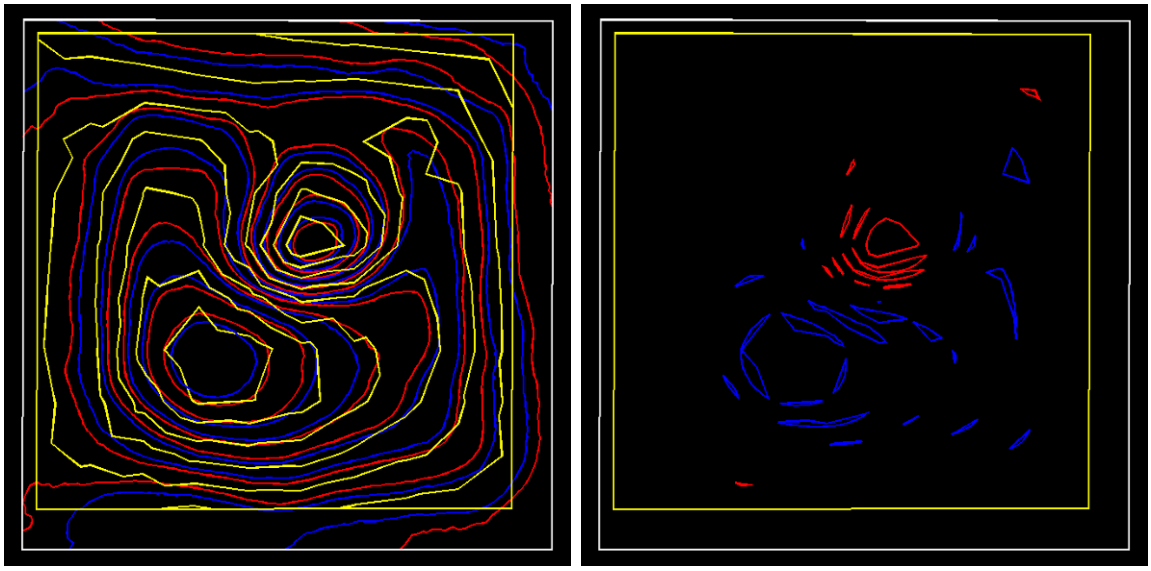

(a) (b)

Fig. 76. The yellow sample error on 3/32nd of an inch accuracy. (a) Contour overlapping, (b) Contour errors: Upper error area = 1.35 in^2, Lower error area = 0.81 in^2 and Total error area = 2.16 in^2.

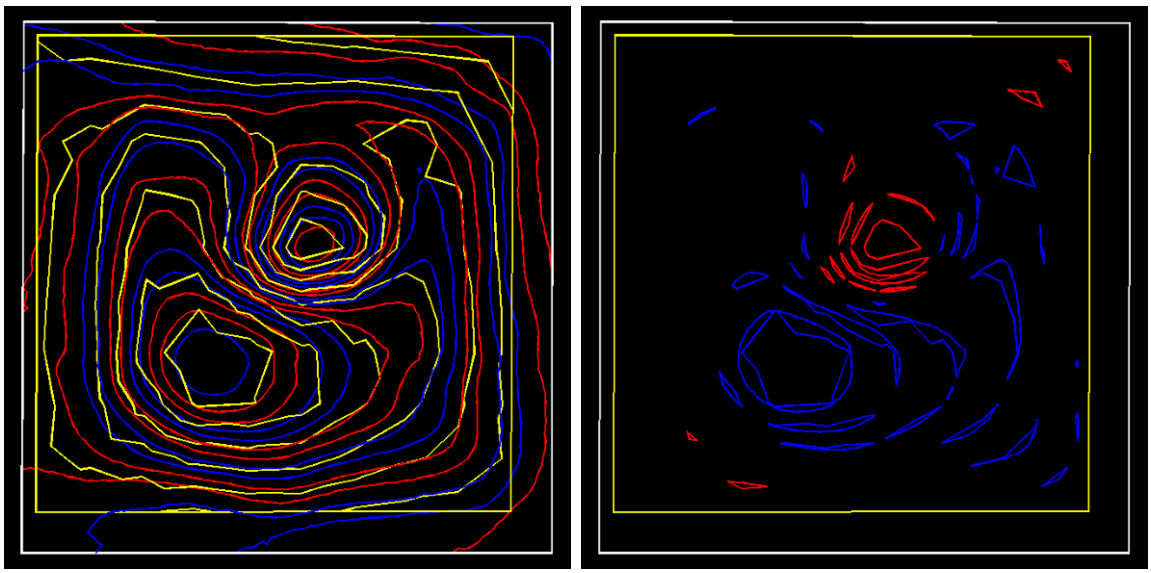

(a) (b)

Fig. 77. The yellow sample error on 1/16th of an inch accuracy. (a) Contour overlapping, (b) Contour errors: Upper error area = 3.26 in^2, Lower error area = 1.15 in^2 and Total error area = 3.41 in^2.

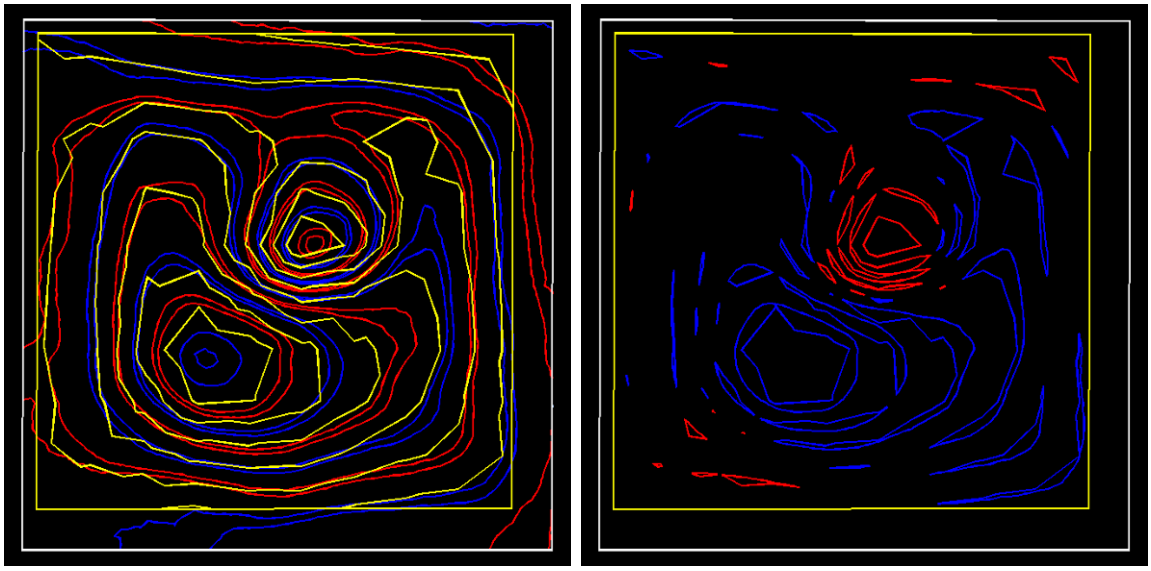

(a) (b)

Fig. 78. The yellow sample error on 1/32nd of an inch accuracy. (a) Contour overlapping, (b) Contour errors: Upper error area = 6.92 in^2, Lower error area = 1.74 in^2 and Total error area = 8.66 in^2.

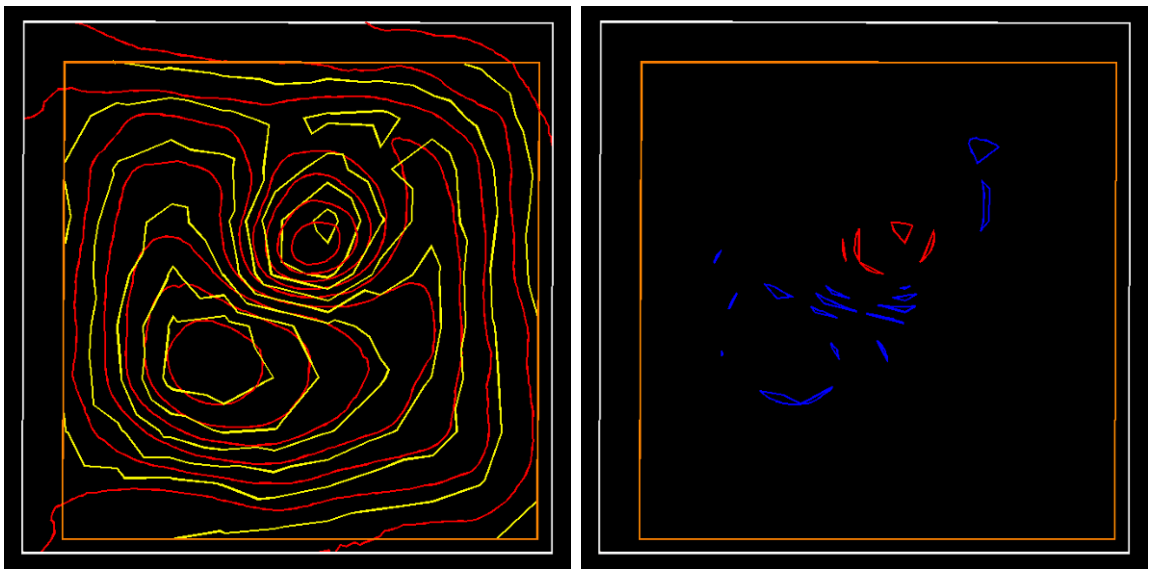

(a) (b)

Fig. 79. The orange sample error on 1/8th of an inch accuracy. (a) Contour overlapping, (b) Contour errors: Upper error area = 0.72 in^2, Lower error area = 0.18 in^2 and Total error area = 0.90 in^2.

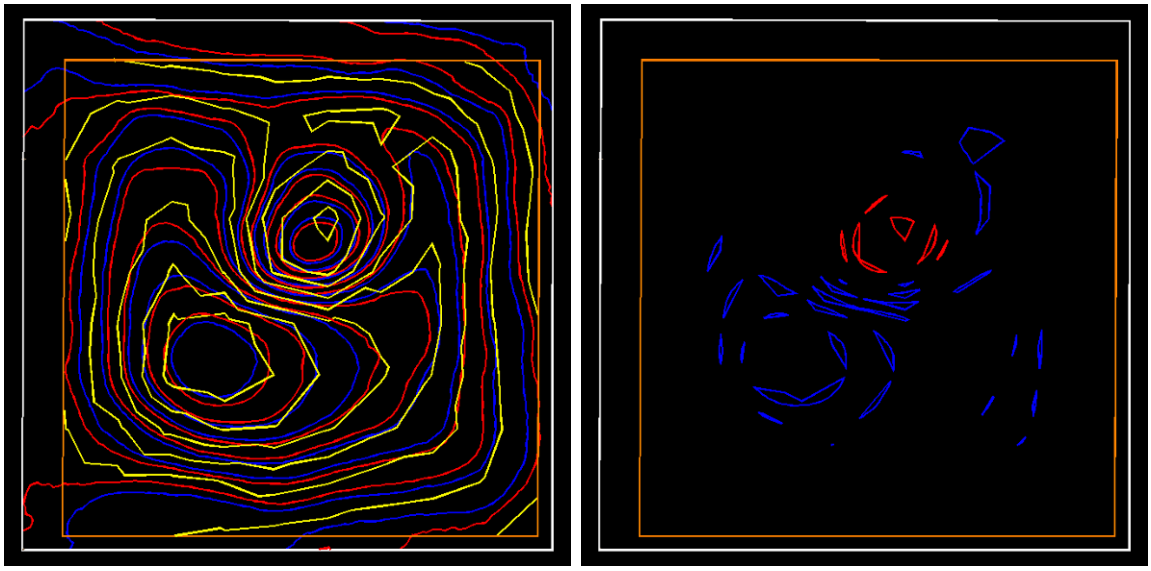

(a) (b)

Fig. 80. The orange sample error on 3/32nd of an inch accuracy. (a) Contour overlapping, (b) Contour errors: Upper error area = 1.55 in^2, Lower error area = 0.28 in^2 and Total error area = 1.83 in^2.

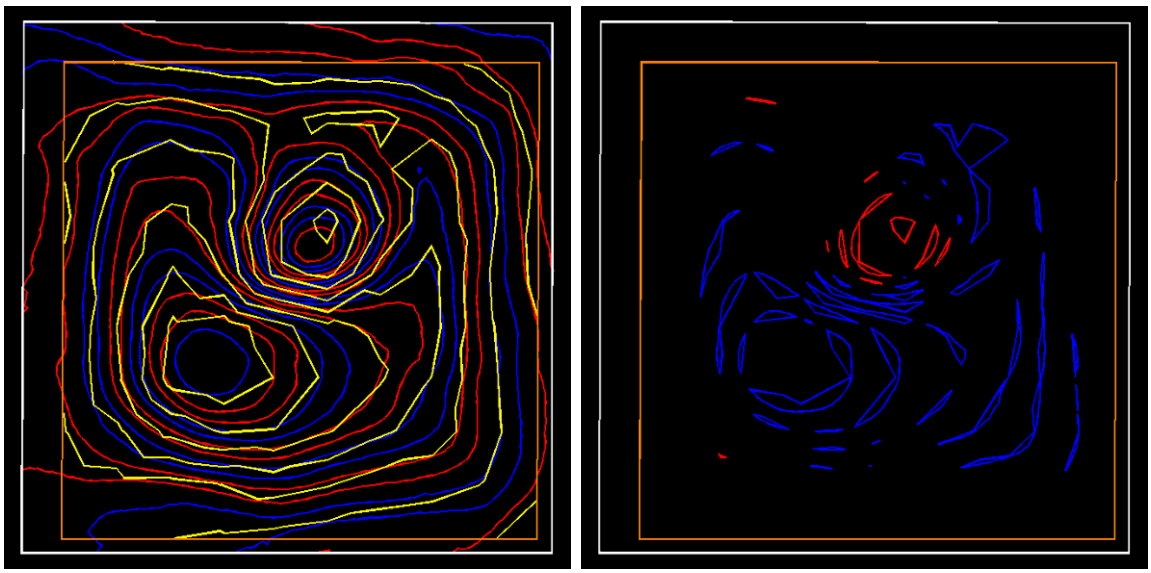

(a) (b)

Fig. 81. The orange sample error on 1/16th of an inch accuracy. (a) Contour overlapping, (b) Contour errors: Upper error area = 3.47 in^2, Lower error area = 0.45 in^2 and Total error area = 3.92 in^2.

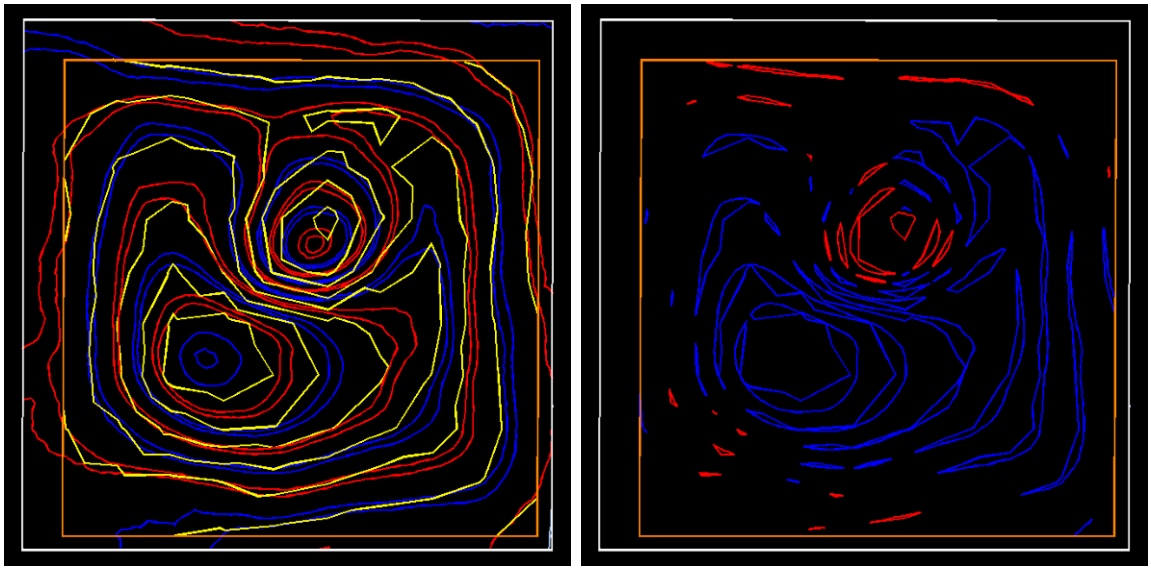

(a) (b)

Fig. 82. The orange sample error on 1/32nd of an inch accuracy. (a) Contour overlapping, (b) Contour errors: Upper error area = 7.71 in^2, Lower error area = 0.99 in^2 and Total error area = 8.70 in^2.

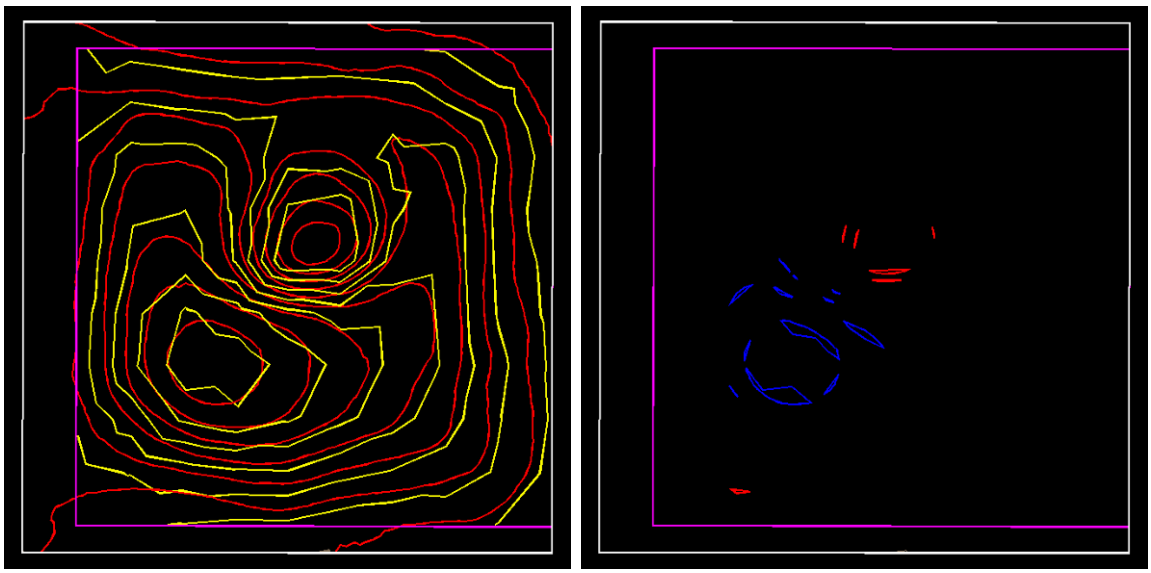

(a) (b)

Fig. 83. The purple sample error on 1/8th of an inch accuracy. (a) Contour overlapping, (b) Contour errors: Upper error area = 0.53 in^2, Lower error area = 0.07 in^2 and Total error area = 0.60 in^2.

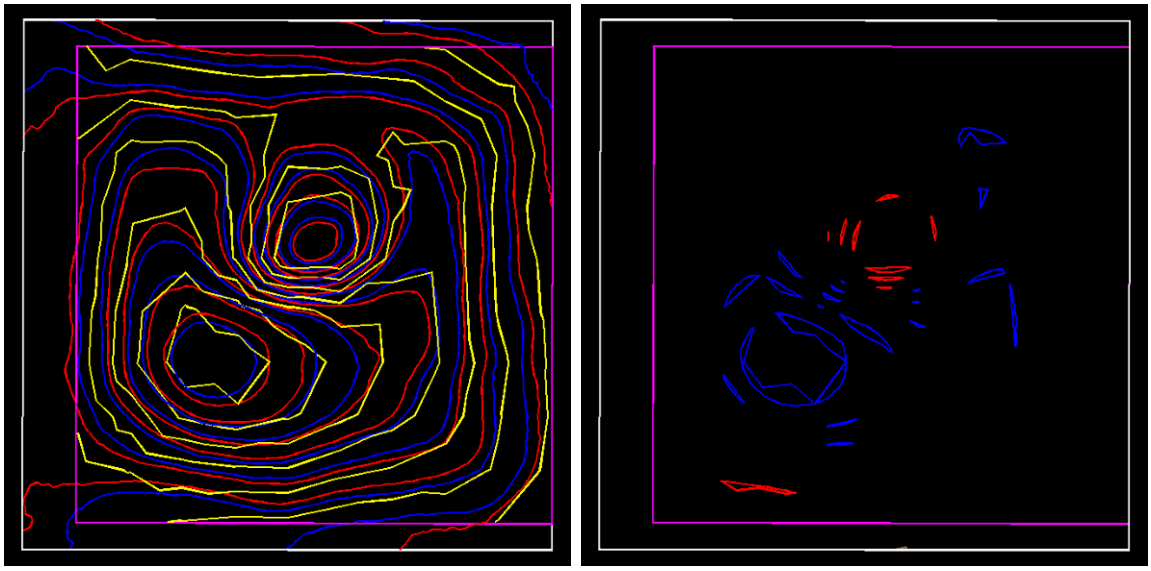

(a) (b)

Fig. 84. The purple sample error on 3/32nd of an inch accuracy. (a) Contour overlapping, (b) Contour errors: Upper error area = 1.29 in^2, Lower error area = 0.23 in^2 and Total error area = 1.52 in^2.

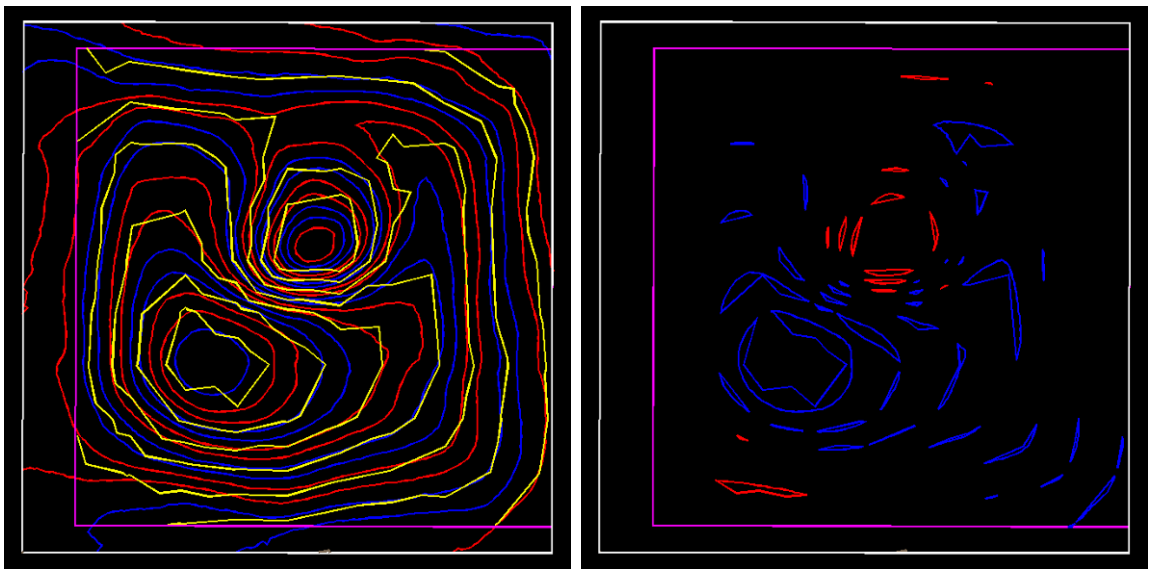

(a) (b)

Fig. 85. The purple sample error on 1/16th of an inch accuracy. (a) Contour overlapping, (b) Contour errors: Upper error area = 1.33 in^2, Lower error area = 0.51 in^2 and Total error area = 3.84 in^2.

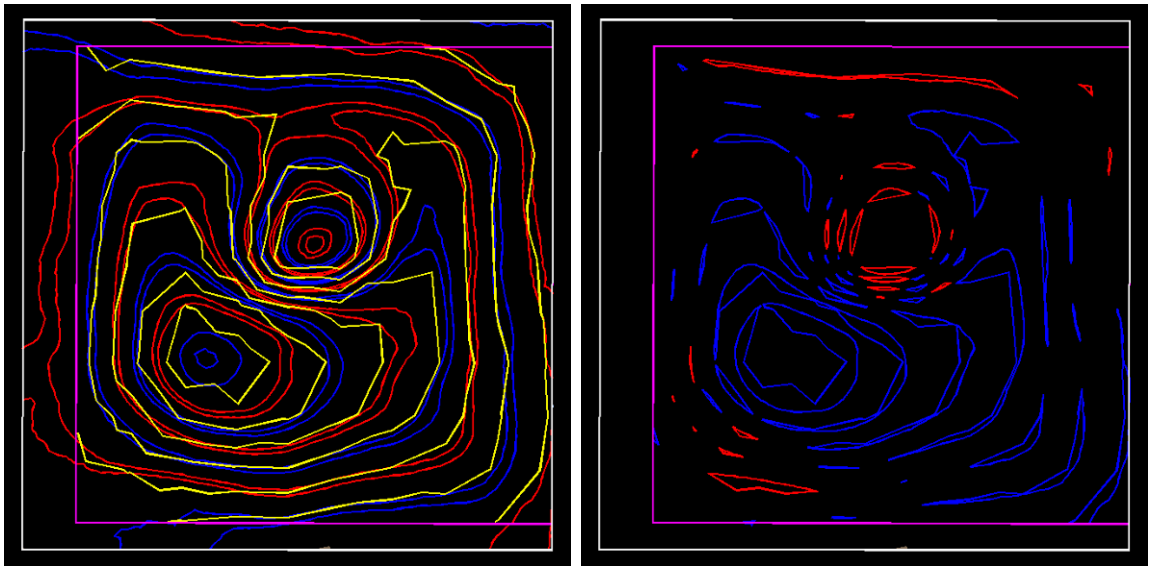

(a) (b)

Fig. 86. The purple sample error on 1/32nd of an inch accuracy. (a) Contour overlapping, (b) Contour errors: Upper error area = 7.36 in^2, Lower error area = 1.23 in^2 and Total error area = 8.59 in^2.

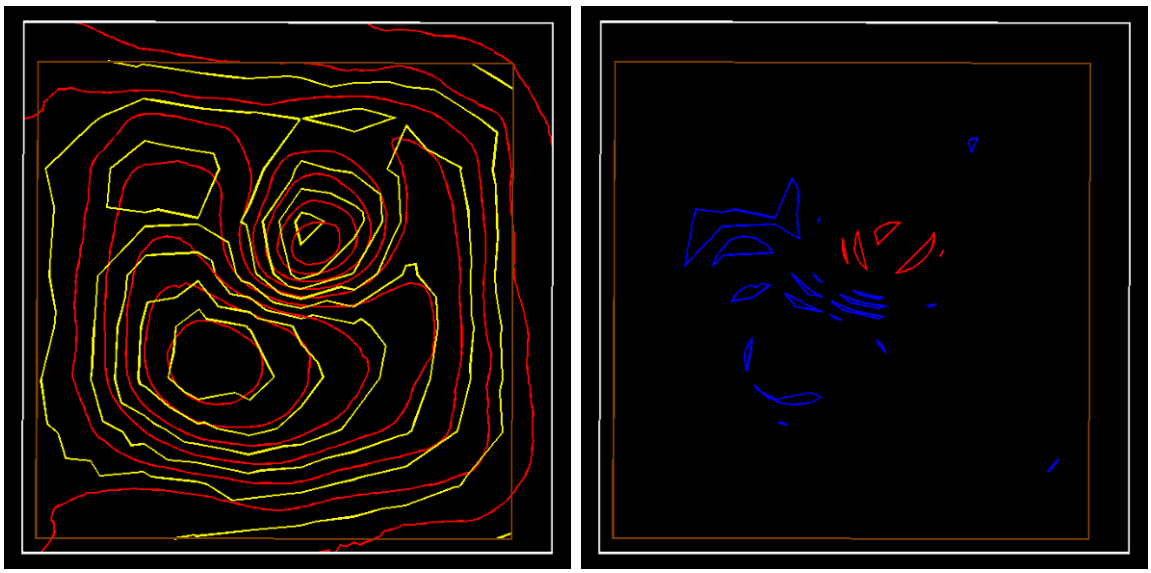

(a) (b)

Fig. 87. The brown sample error on 1/8th of an inch accuracy. (a) Contour overlapping, (b) Contour errors: Upper error area = 1.63 in^2, Lower error area = 0.29 in^2 and Total error area = 1.92 in^2.

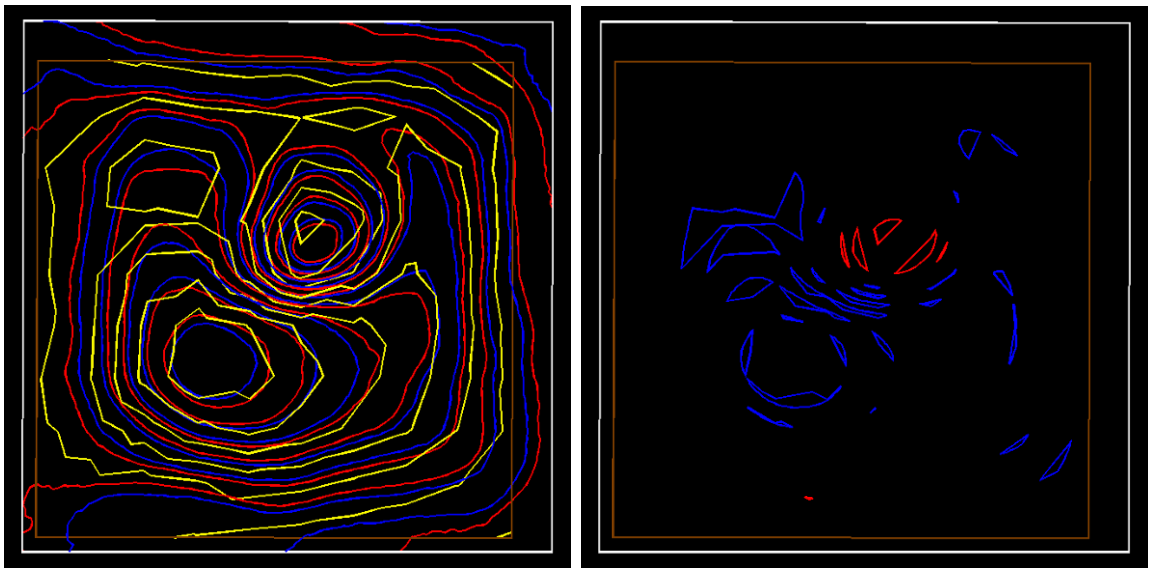

(a) (b)

Fig. 88. The brown sample error on 3/32nd of an inch accuracy. (a) Contour overlapping, (b) Contour errors: Upper error area = 2.85 in^2, Lower error area = 0.39 in^2 and Total error area = 3.24 in^2.

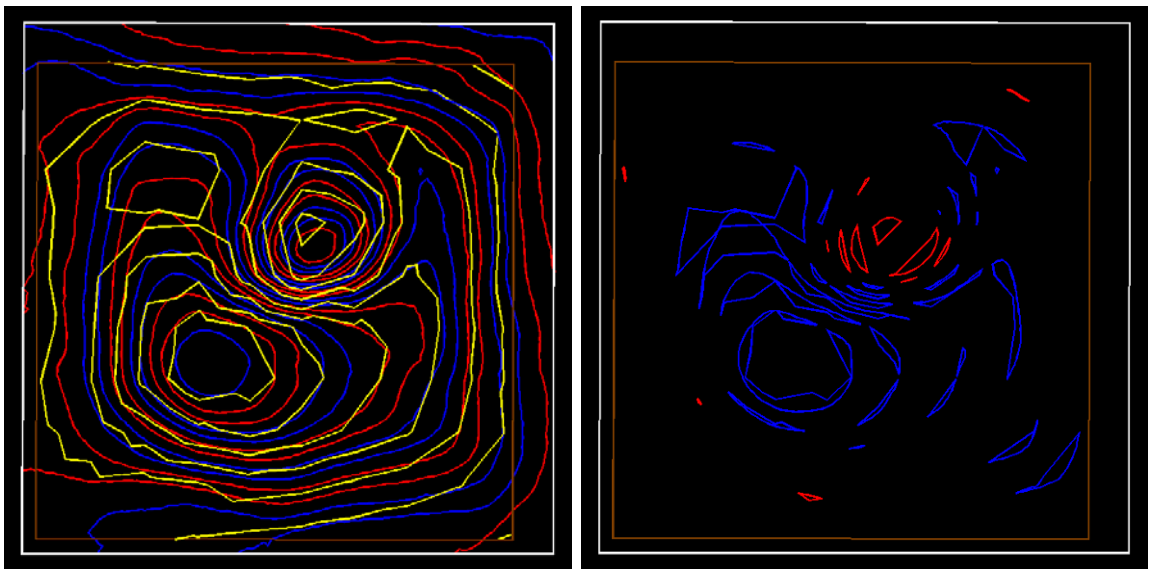

(a) (b)

Fig. 89. The brown sample error on 1/16th of an inch accuracy. (a) Contour overlapping, (b) Contour errors: Upper error area = 5.35 in^2, Lower error area = 0.54 in^2 and Total error area = 5.89 in^2.

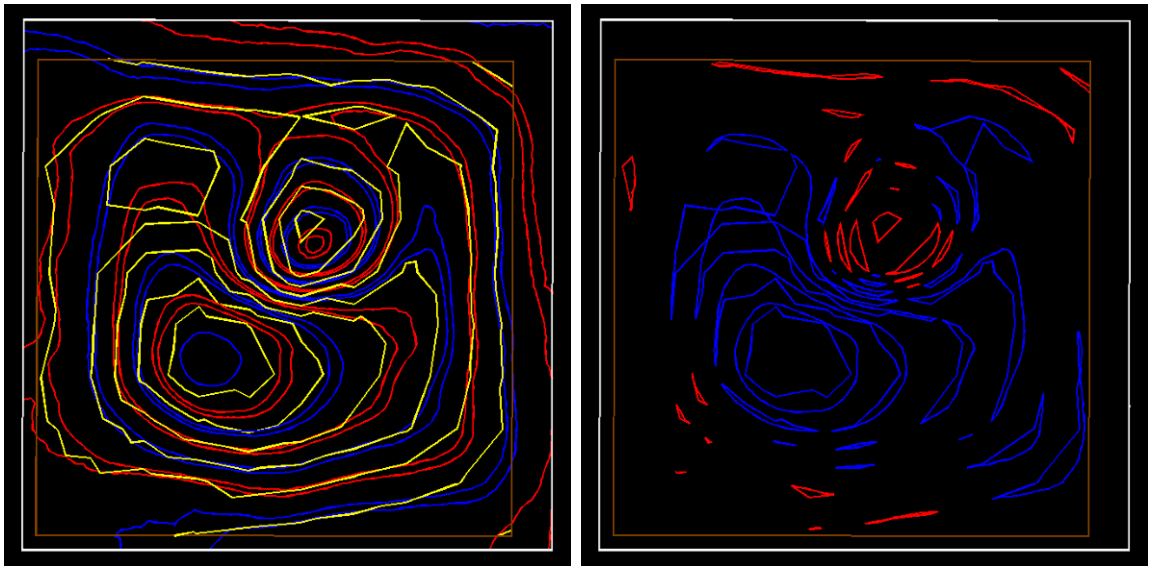

(a) (b)

Fig. 90. The brown sample error on 1/32nd of an inch accuracy. (a) Contour overlapping, (b) Contour errors: Upper error area = 8.73 in^2, Lower error area = 1.32 in^2 and Total error area = 10.05 in^2.

V.1.3. The OMIT measuring method accuracy evaluation

On the four predetermined accuracy levels, the eight samples of the OMIT measuring methods were examined for contour measurement accuracy.

The tests were performed by superimposing the two line drawings resulting from each sample. The first drawing is the contour lines traced from the OMIT measuring result. The other output is the error tolerance region lines generated from the corresponding re-oriented the TMVS at the targeted level of accuracy as aforementioned in section V.1.1.

The eight OMIT measuring samples went through this procedure for the four accuracy levels. Each sample has its unique form of error tolerance regions according to its unique determined orientation. The following Fig. 91 shows an example of the different error tolerance regions generated from the different orientations of the TMVS at an accuracy level of 1/16th of an inch. As mentioned

earlier, these TMVS orientations were the result of the unique orientation of the physical model in each of the eight OMIT samples.

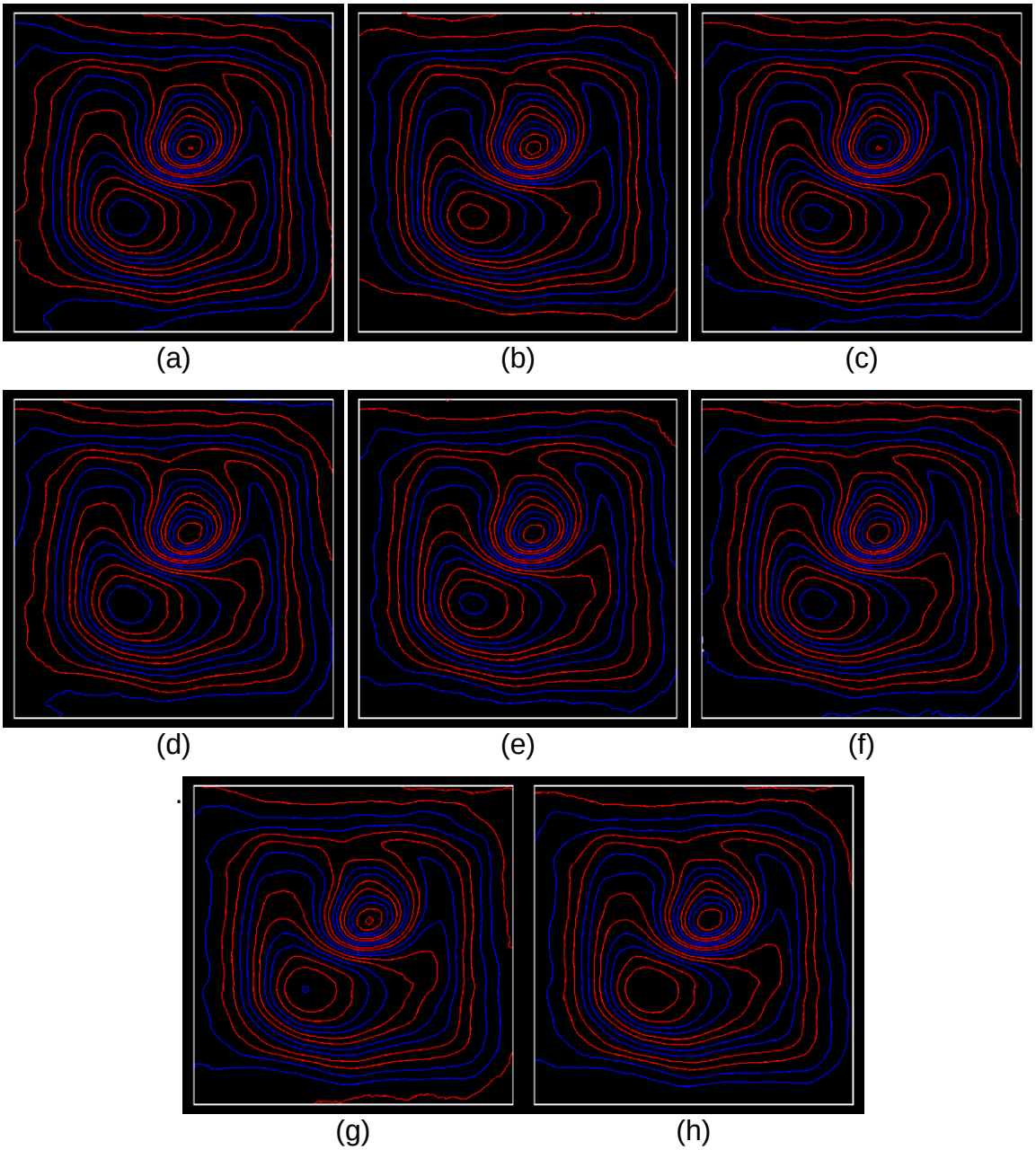

Fig. 91. Error tolerance regions for the OMIT samples on 1/16th of an inch accuracy level. (a) zero degree rotation sample, (b) 45° rotation sample, (c) 90° rotation sample, (d) 135° rotation sample, (e) 180° rotation sample, (f) 225° rotation sample, (g) 270° rotation sample, (h) 315° rotation sample.

For quantifying the error in each sample, the procedure started by defining the areas enclosed by the traced contour lines outside the boundaries of the error tolerance region. As mentioned earlier in the hand measurement method accuracy evaluation (section V.1.2), AutoCAD Architectural Desktop 2004 software was used for this purpose. The defined areas were separated and isolated. The upper error areas were surrounded with blue poly lines and the lower error areas were surrounded by red poly lines. The type of error was validated as a measurement error and not as a contour level shifting error. This was established when the error existed by confirming the existence of areas surrounded by red and blue colored poly lines in each sample.

From the eight investigated samples, the resulting accuracy evaluation drawings are shown in the following Figs. 92 to 123 associated with the four predetermined accuracy levels.

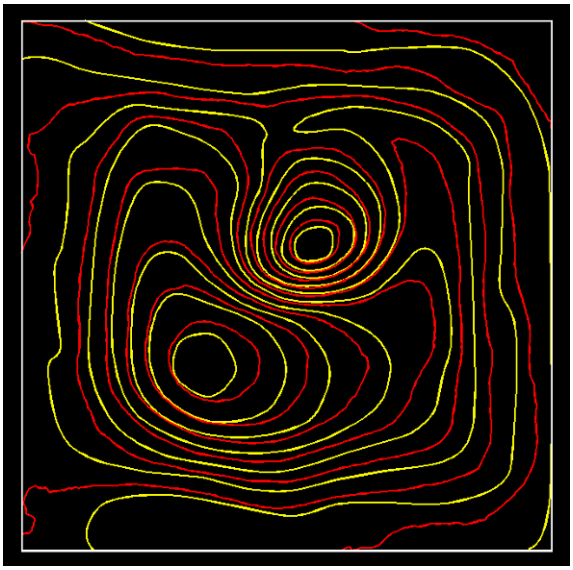

Fig. 92. Contours overlapping of the 0° sample rotation for error on 1/8th of an inch accuracy. Zero errors resulted in this accuracy level.

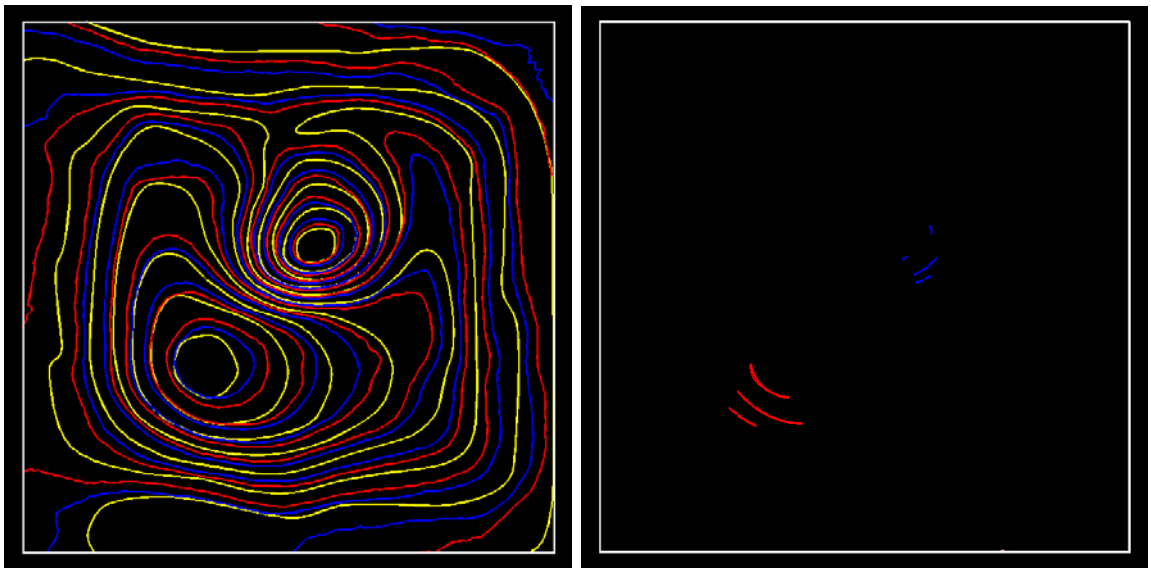

(a) (b)

Fig. 93. The 0° sample rotation for error on 3/32nd of an inch accuracy.
(a) Contour overlapping, (b) Contour errors: Upper error area = 0.01 in^2, Lower error area = 0.03 in^2 and Total error area = 0.04 in^2.

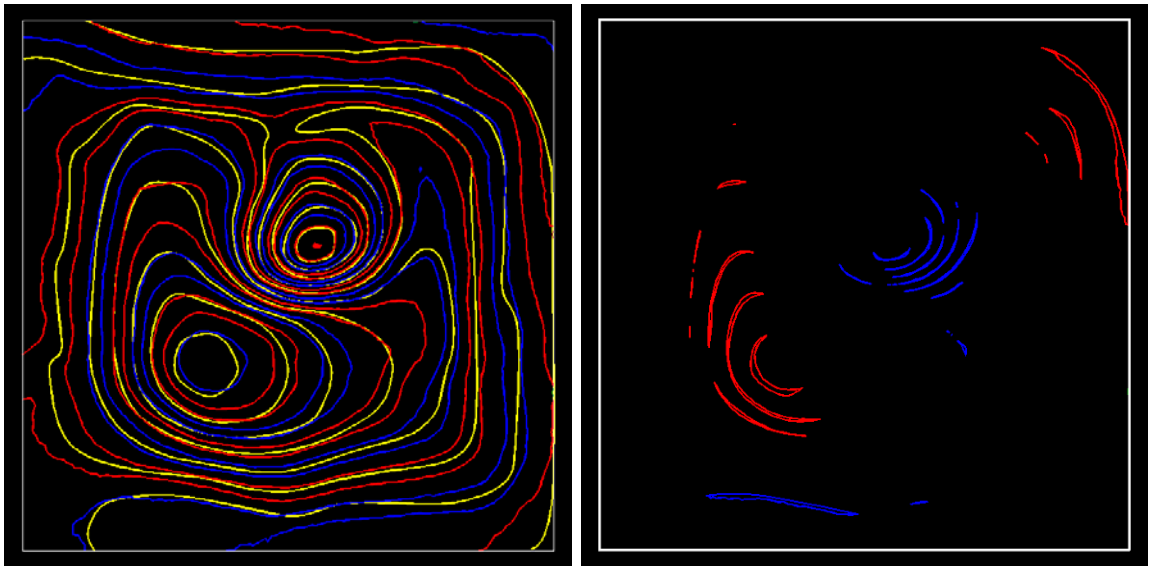

(a) (b)

Fig. 94. The 0° sample rotation for error on 1/16th of an inch accuracy.
(a) Contours overlap, (b) Contour errors: Upper error area = 0.36 in^2, Lower error area = 0.95 in^2 and Total error area = 1.31 in^2.

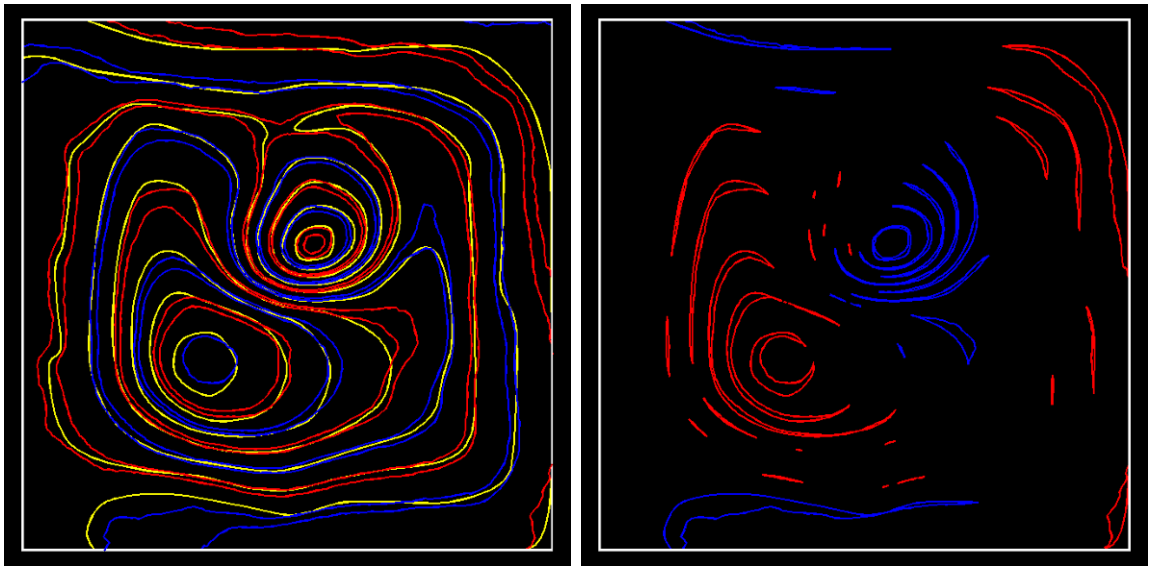

(a) (b)

Fig. 95. The 0° sample rotation for error on 1/32nd of an inch accuracy.
(a) Contours overlap, (b) Contour errors: Upper error area = 2.44 in^2, Lower error area = 3.49 in^2 and Total error area = 5.93 in^2.

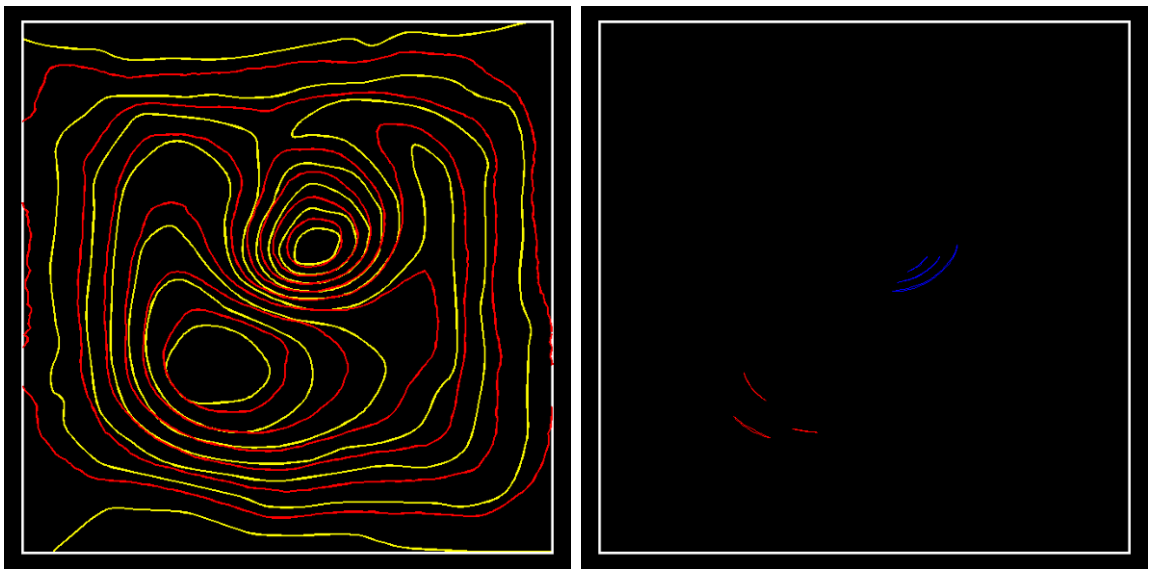

(a) (b)

Fig. 96. The 45° sample rotation for error on 1/8th of an inch accuracy.
(a) Contours overlap, (b) Contour errors: Upper error area = 0.04 in^2, Lower error area = 0.02 in^2 and Total error area = 0.06 in^2

.

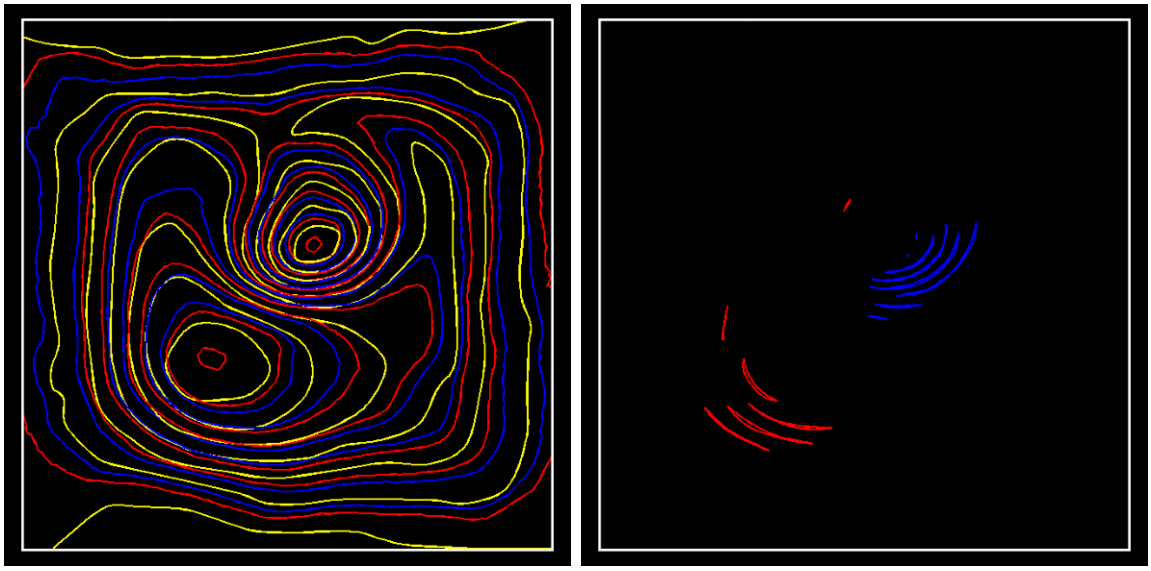

(a) (b)

Fig. 97. The 45° sample rotation for error on 3/32nd of an inch accuracy.
(a) Contours overlap, (b) Contour errors: Upper error area = 0.20 in^2, Lower error area = 0.18 in^2 and Total error area = 0.38 in^2.

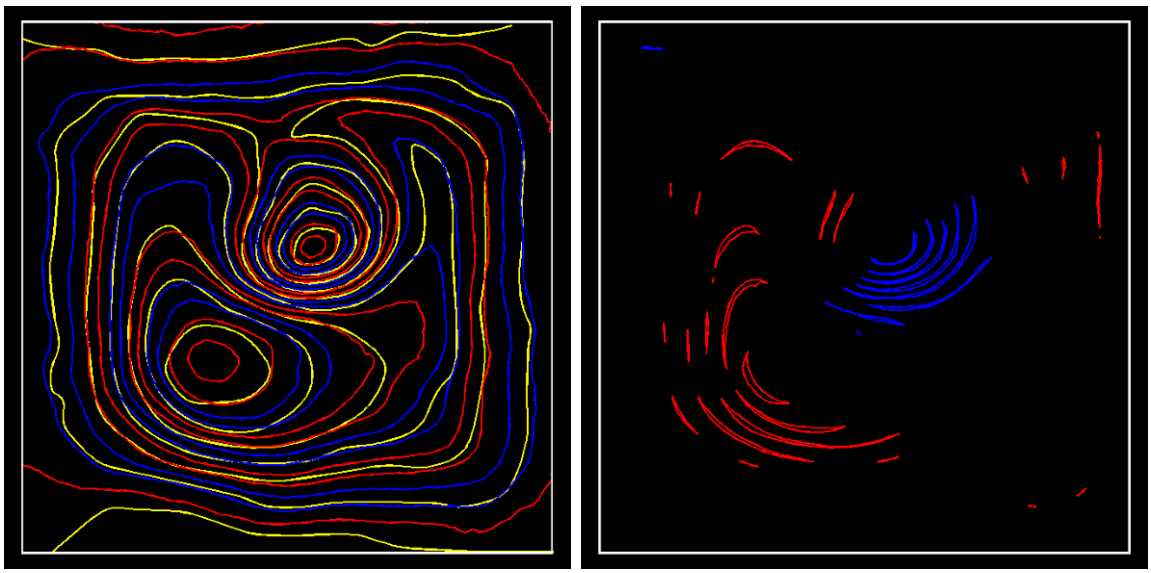

(a) (b)

Fig. 98. The 45° sample rotation for error on 1/16th of an inch accuracy.
(a) Contours overlap, (b) Contour errors: Upper error area = 0.60 in^2, Lower error area = 0.94 in^2 and Total error area = 1.54 in^2.

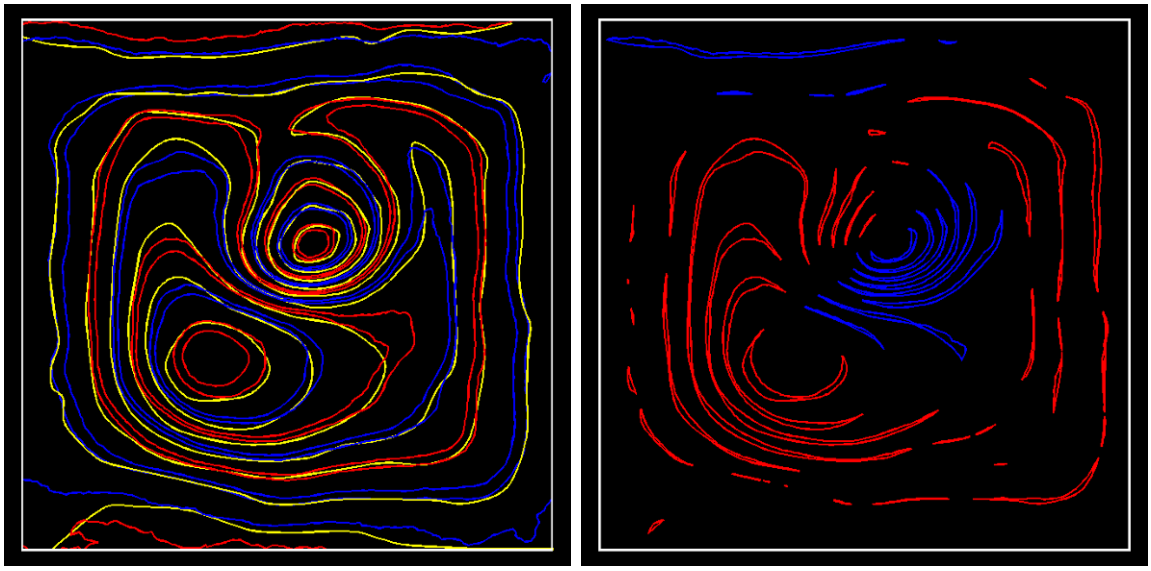

(a) (b)

Fig. 99. The 45° sample rotation for error on 1/32nd of an inch accuracy.
(a) Contours overlap, (b) Contour errors: Upper error area = 1.83 in^2, Lower error area = 4.09 in^2 and Total error area = 5.92 in^2.

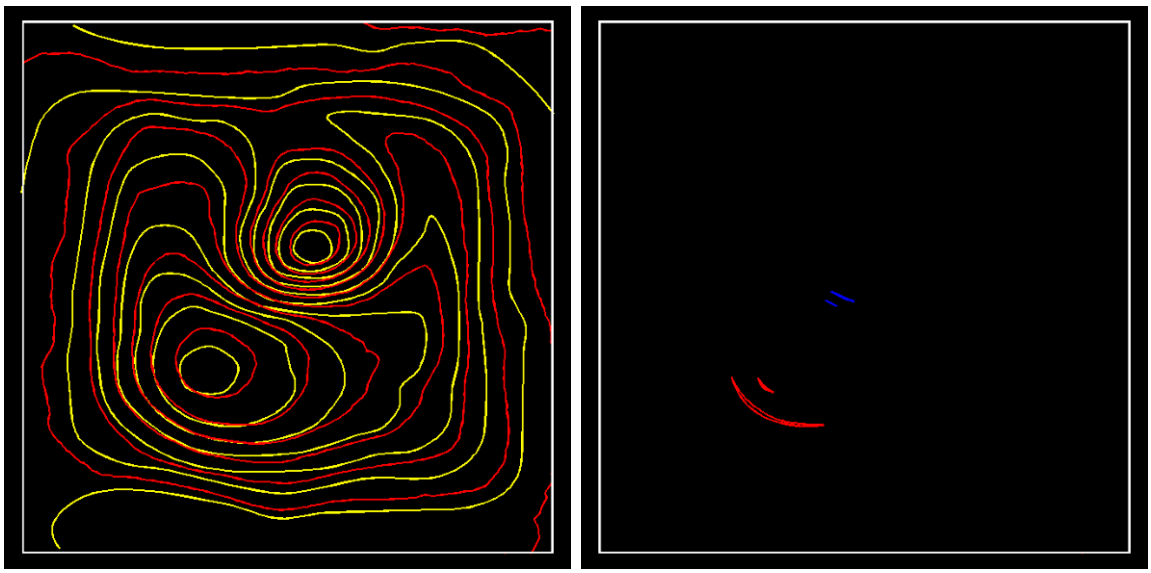

(a) (b)

Fig. 100. The 90° sample rotation for error on 1/8th of an inch accuracy.
(a) Contours overlap, (b) Contour errors: Upper error area = 0.01 in^2, Lower error area = 0.10 in^2 and Total error area = 0.11 in^2.

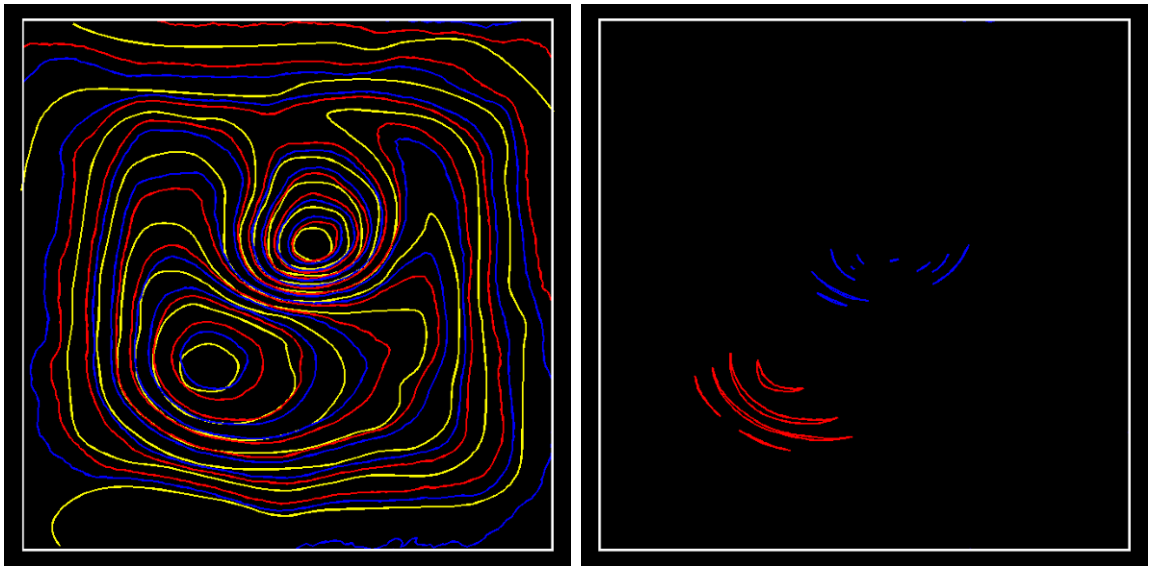

(a) (b)

Fig. 101. The 90° sample rotation for error on 3/32nd of an inch accuracy.
(a) Contours overlap, (b) Contour errors: Upper error area = 0.06 in^2, Lower error area = 0.43 in^2 and Total error area = 0.49 in^2.

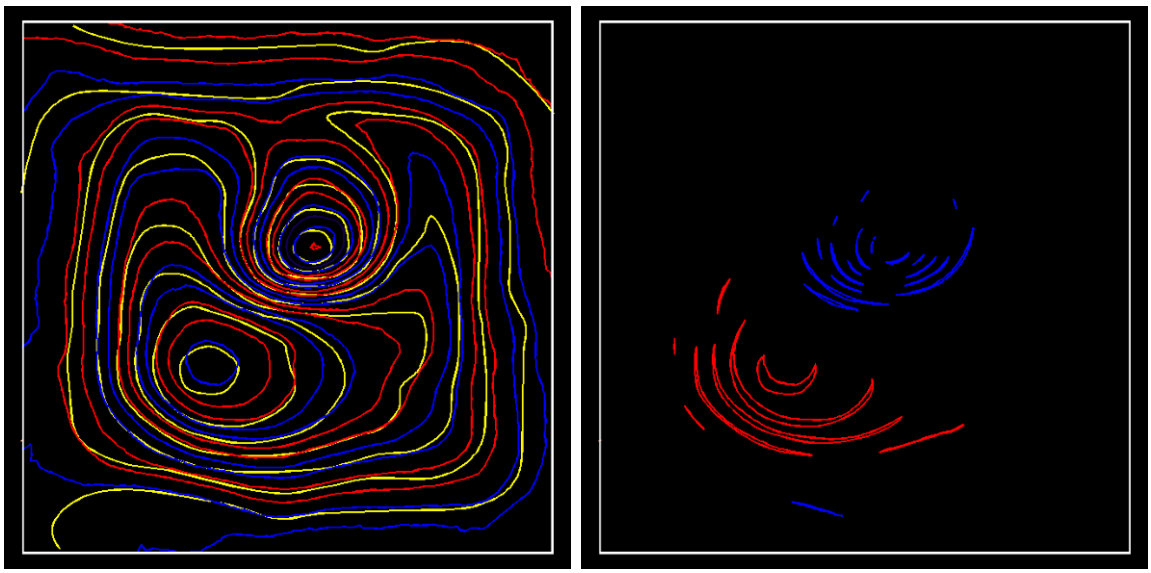

(a) (b)

Fig. 102. The 90° sample rotation for error on 1/16th of an inch accuracy.
(a) Contours overlap, (b) Contour errors: Upper error area = 0.28 in^2, Lower error area = 1.17 in^2 and Total error area = 1.45 in^2.

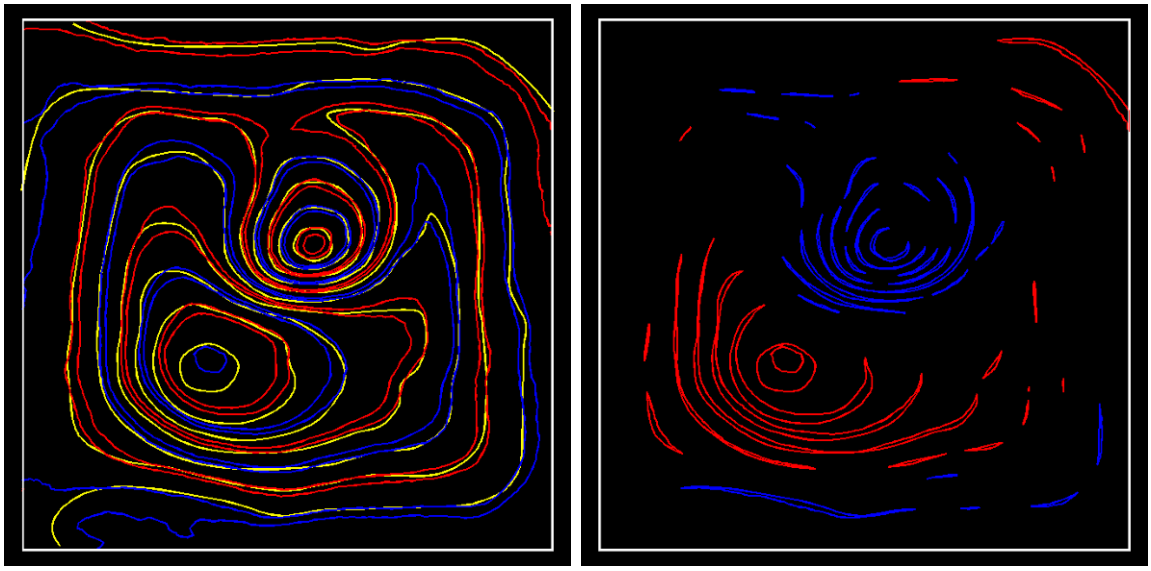

(a) (b)

Fig. 103. The 90° sample rotation for error on 1/32nd of an inch accuracy.
(a) Contours overlap, (b) Contour errors: Upper error area = 1.26 in^2, Lower error area = 3.23 in^2 and Total error area = 4.49 in^2.

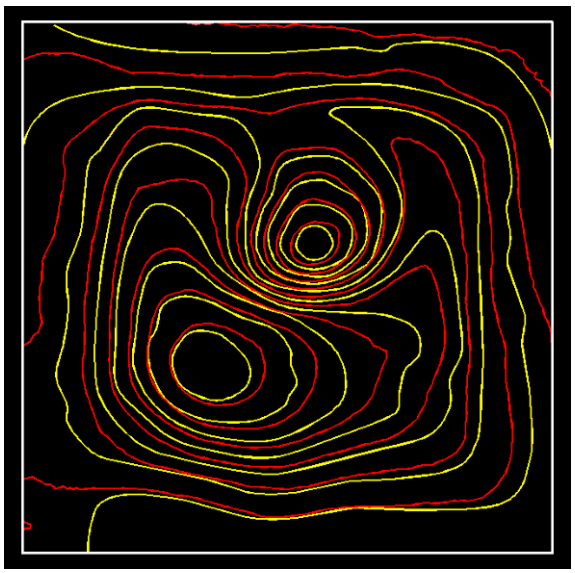

Fig. 104. Contours overlapping of the 135° sample rotation for error on 1/8th of an inch accuracy. Zero errors resulted in this accuracy level.

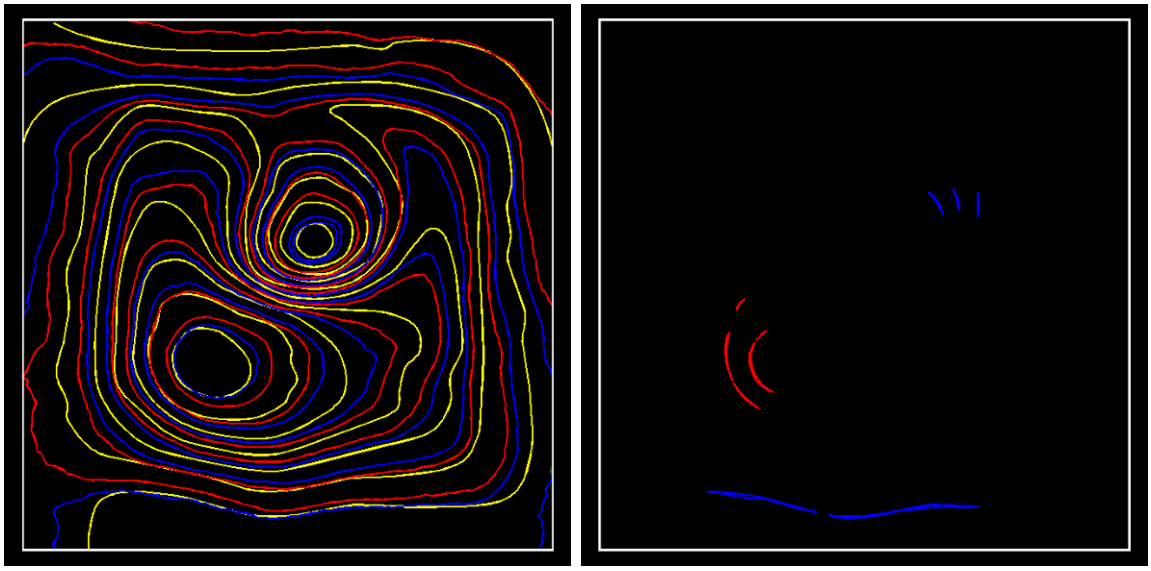

(a) (b)

Fig. 105. The 135° sample rotation for error on 3/32nd of an inch accuracy.
(a) Contours overlap, (b) Contour errors: Upper error area = 0.15 in^2, Lower error area = 0.06 in^2 and Total error area = 0.21 in^2.

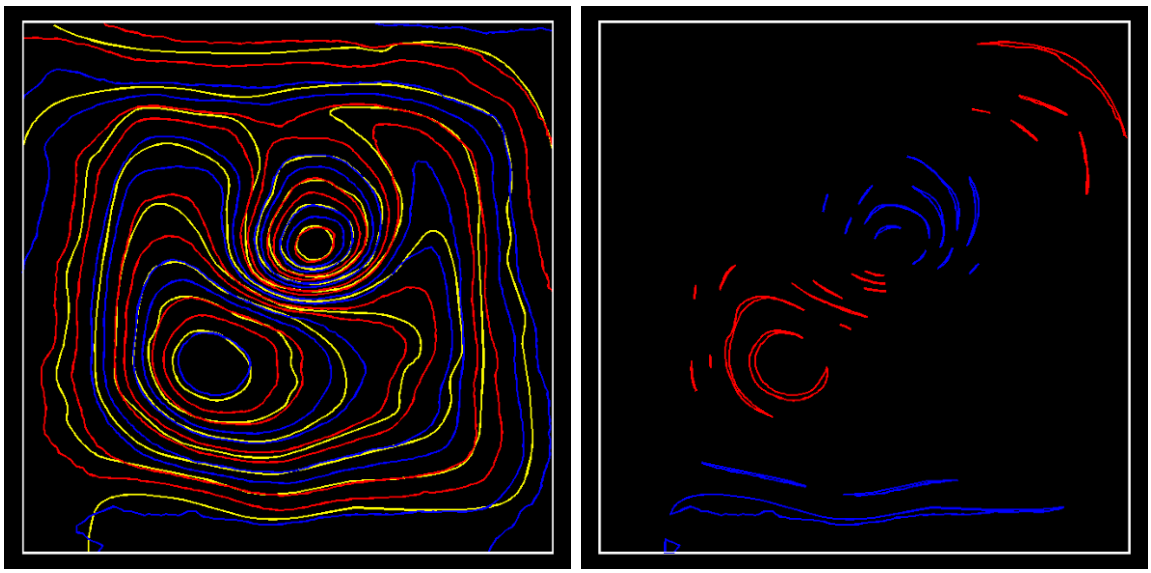

(a) (b)

Fig. 106. The 135° sample rotation for error on 1/16th of an inch accuracy.
(a) Contours overlap, (b) Contour errors: Upper error area = 1.44 in^2, Lower error area = 0.85 in^2 and Total error area = 2.29 in^2.

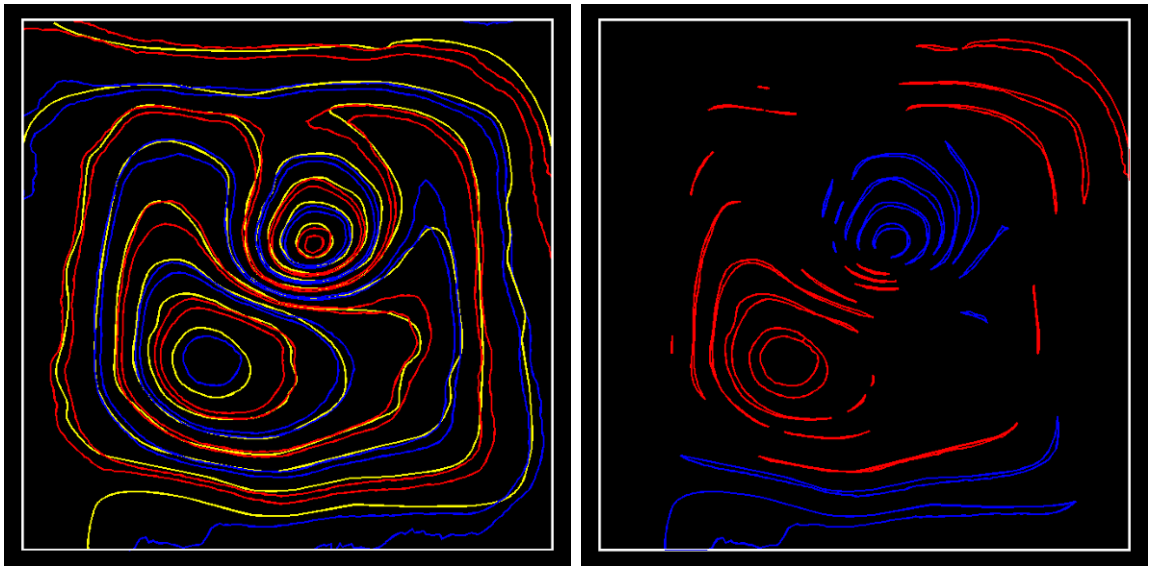

(a) (b)

Fig. 107. The 135° sample rotation for error on 1/32nd of an inch accuracy.
(a) Contours overlap, (b) Contour errors: Upper error area = 4.57 in^2, Lower error area = 3.16 in^2 and Total error area = 7.73 in^2.

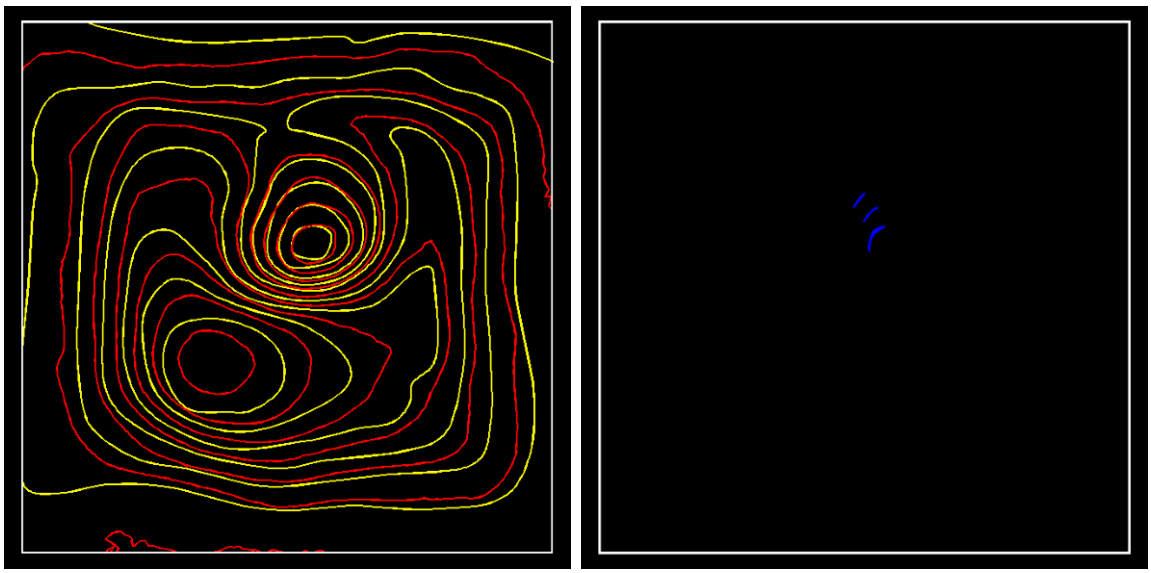

(a) (b)

Fig. 108. The 180° sample rotation for error on 1/8th of an inch accuracy.
(a) Contours overlap, (b) Contour errors: Upper error area = 0.02 in^2, Lower error area = 0.00 in^2 and Total error area = 0.02 in^2.

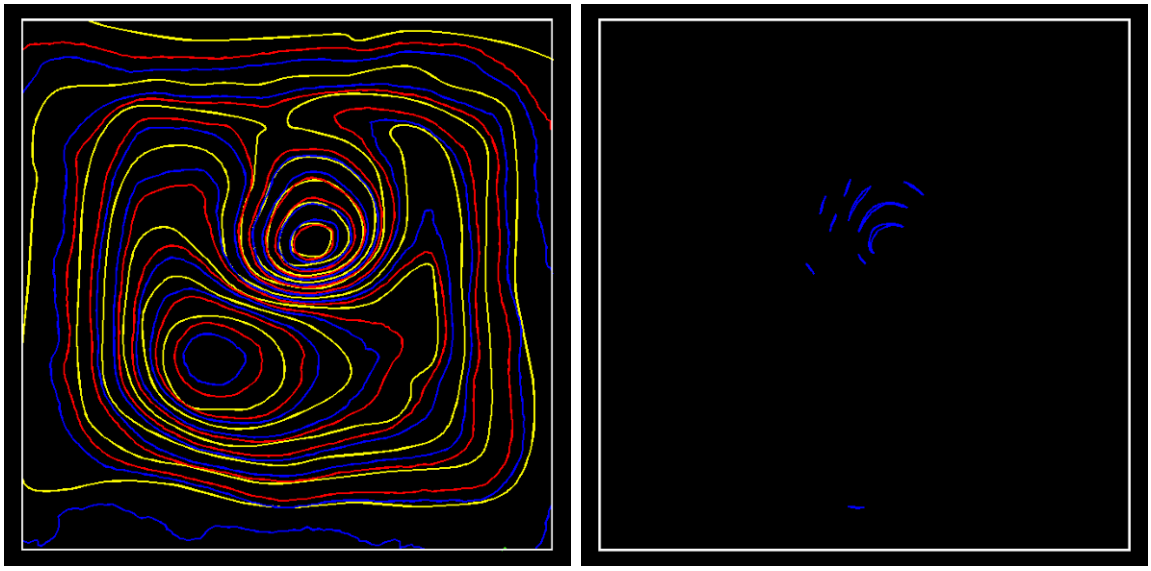

(a) (b)

Fig. 109. The 180° sample rotation for error on 3/32nd of an inch accuracy.
(a) Contours overlap, (b) Contour errors: Upper error area = 0.13 in^2, Lower error area = 0.00 in^2 and Total error area = 0.13 in^2.

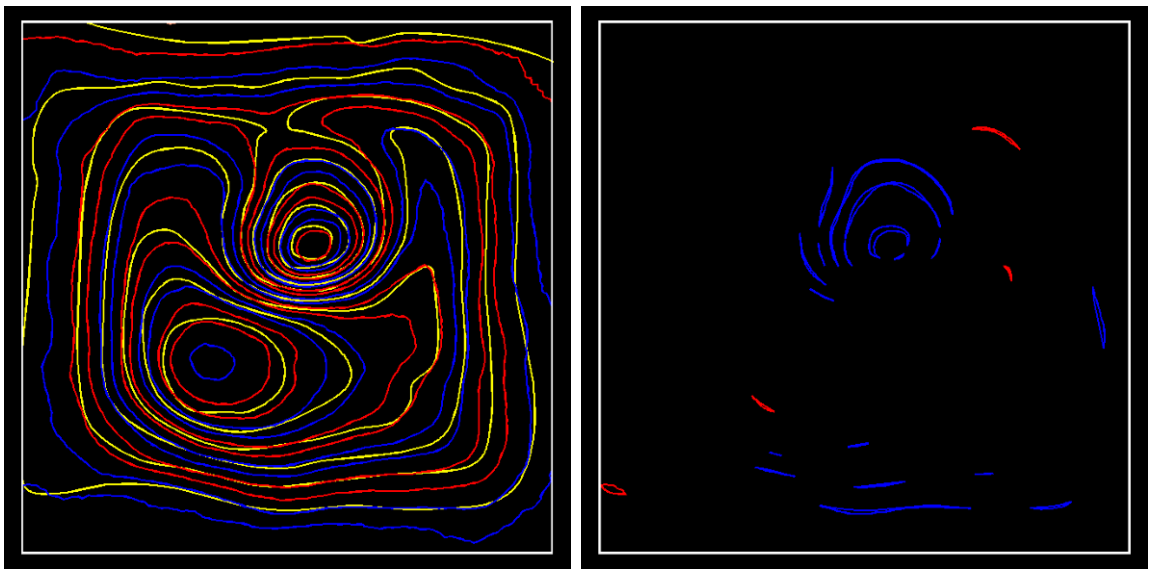

(a) (b)

Fig. 110. The 180° sample rotation for error on 1/16th of an inch accuracy.
(a) Contours overlap, (b) Contour errors: Upper error area = 0.63 in^2, Lower error area = 0.09 in^2 and Total error area = 0.72 in^2.

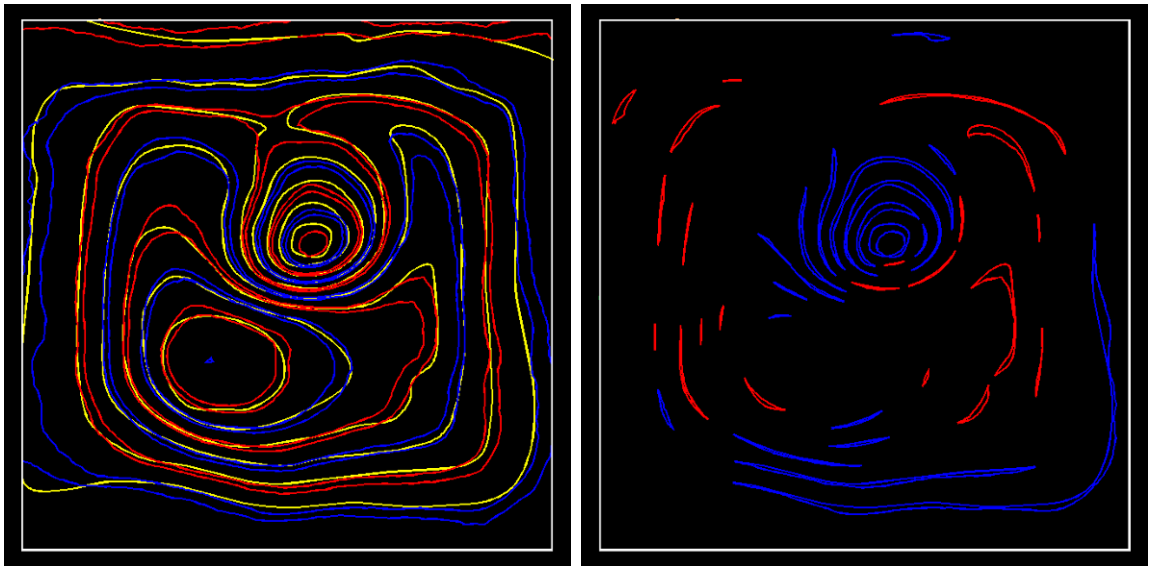

(a) (b)

Fig. 111. The 180° sample rotation for error on 1/32nd of an inch accuracy. (a) Contours overlap, (b) Contour errors: Upper error area = 2.80 in^2, Lower error area = 0.98 in^2 and Total error area = 2.78 in^2.

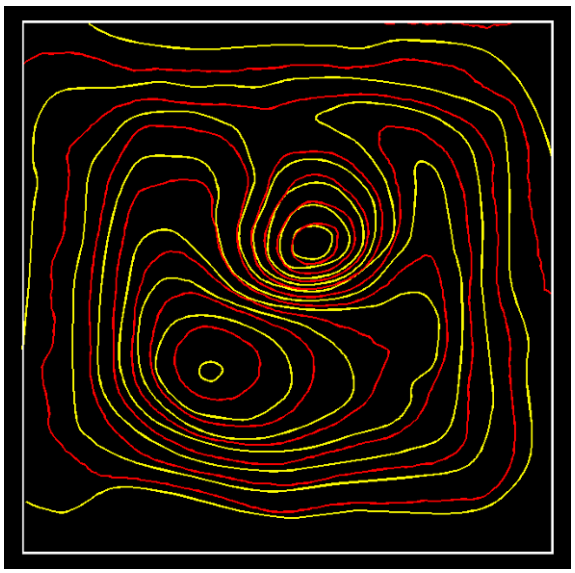

Fig. 112. Contours overlapping of the 225° sample rotation for error on 1/8th of an inch accuracy. Zero errors resulted in this accuracy level.

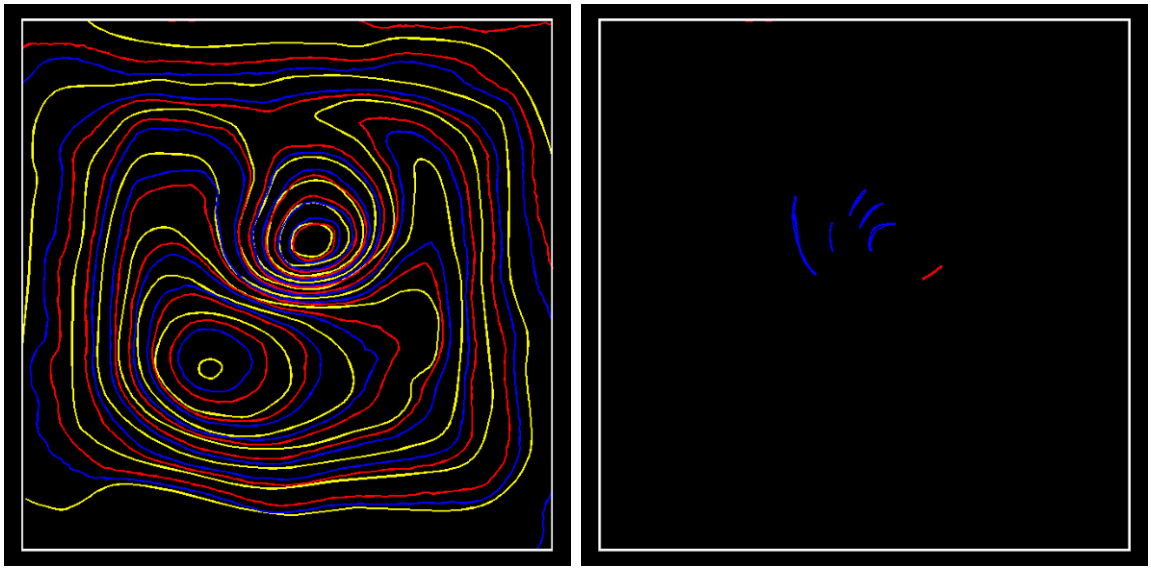

(a) (b)

Fig. 113. The 225° sample rotation for error on 3/32nd of an inch accuracy.
(a) Contours overlap, (b) Contour errors: Upper error area = 0.27 in^2, Lower error area = 0.01 in^2 and Total error area = 0.28 in^2.

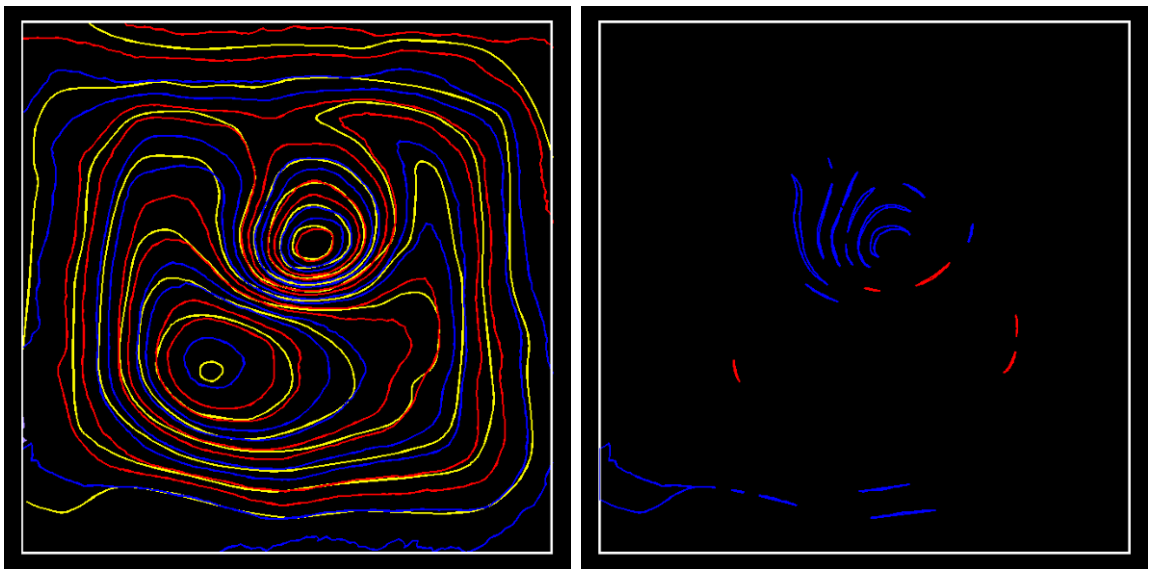

(a) (b)

Fig. 114. The 225° sample rotation for error on 1/16th of an inch accuracy.
(a) Contours overlap, (b) Contour errors: Upper error area = 1.43 in^2, Lower error area = 0.03 in^2 and Total error area = 1.46 in^2.

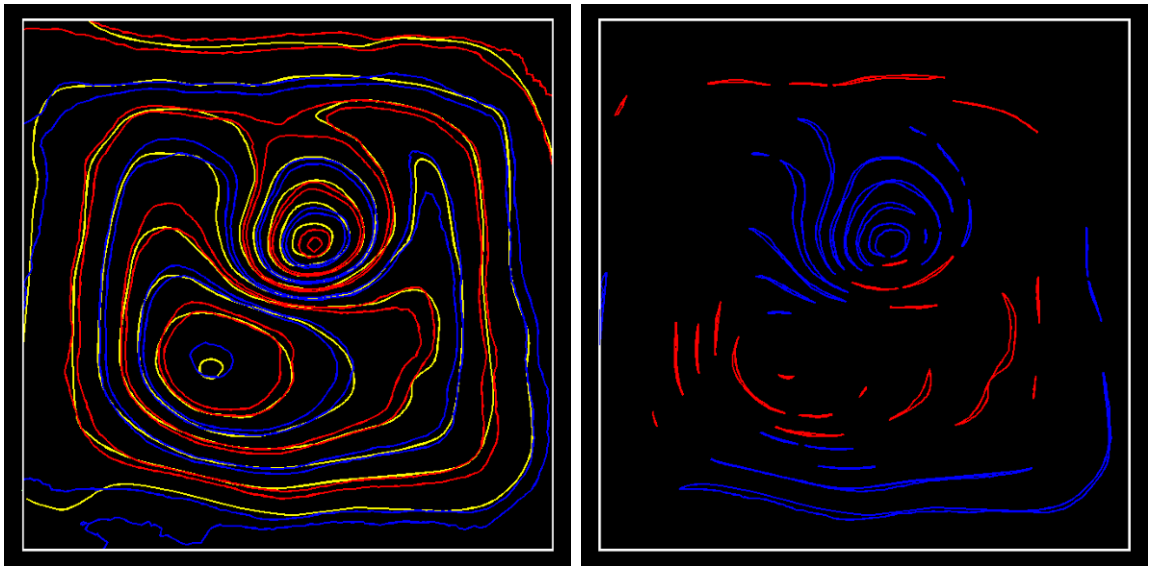

(a) (b)

Fig. 115. The 225° sample rotation for error on 1/32nd of an inch accuracy. (a) Contours overlap, (b) Contour errors: Upper error area = 3.03 in^2, Lower error area = 0.74 in^2 and Total error area = 3.77 in^2.

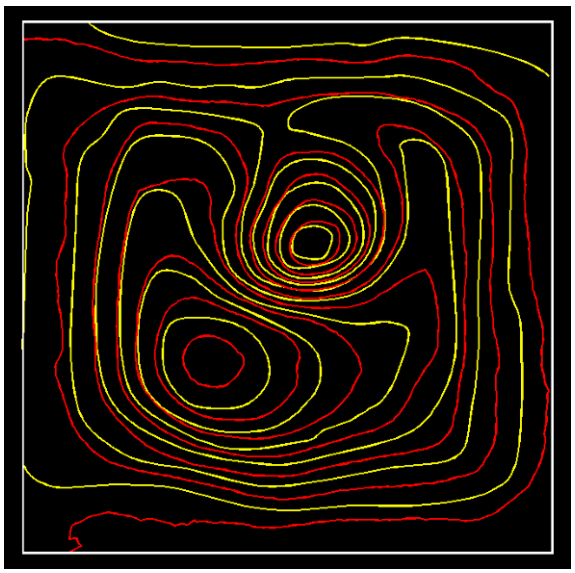

Fig. 116. Contours overlapping of the 270° sample rotation for error on 1/8th of an inch accuracy. Zero errors resulted in this accuracy level.

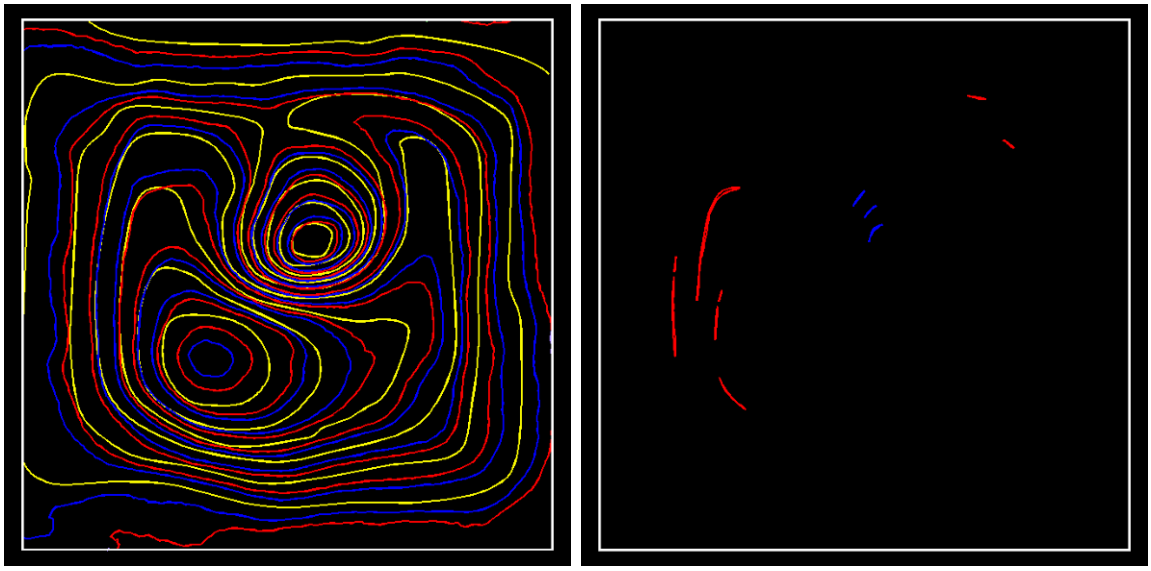

(a) (b)

Fig. 117. The 270° sample rotation for error on 3/32nd of an inch accuracy.
(a) Contours overlap, (b) Contour errors: Upper error area = 0.01 in^2, Lower error area = 0.11 in^2 and Total error area = 0.12 in^2.

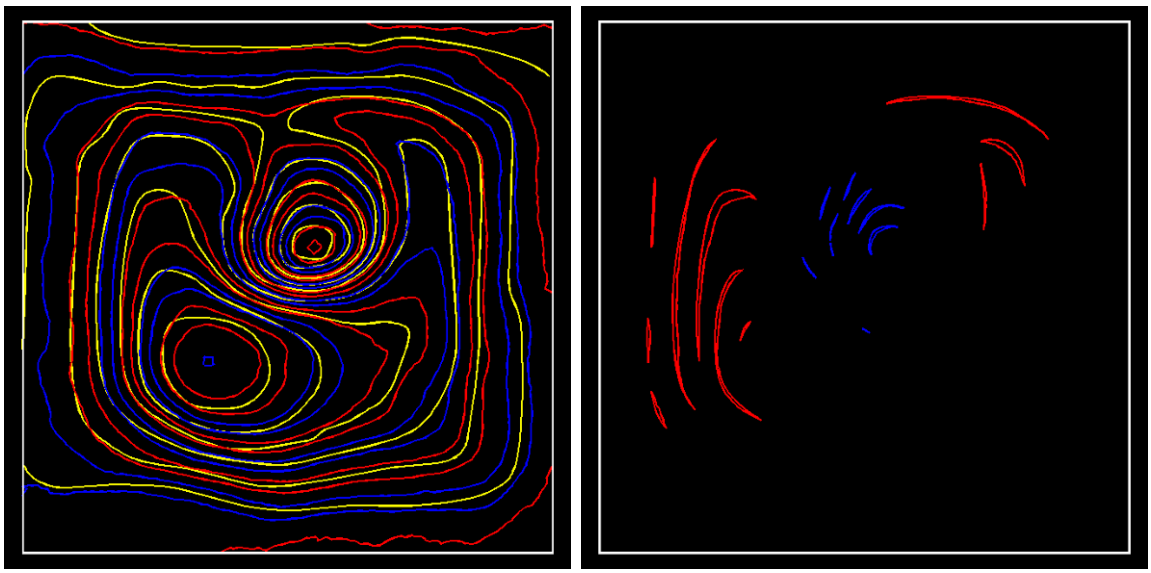

(a) (b)

Fig. 118. The 270° sample rotation for error on 1/16th of an inch accuracy.
(a) Contours overlap, (b) Contour errors: Upper error area = 0.12 in^2, Lower error area = 1.08 in^2 and Total error area = 1.20 in^2.

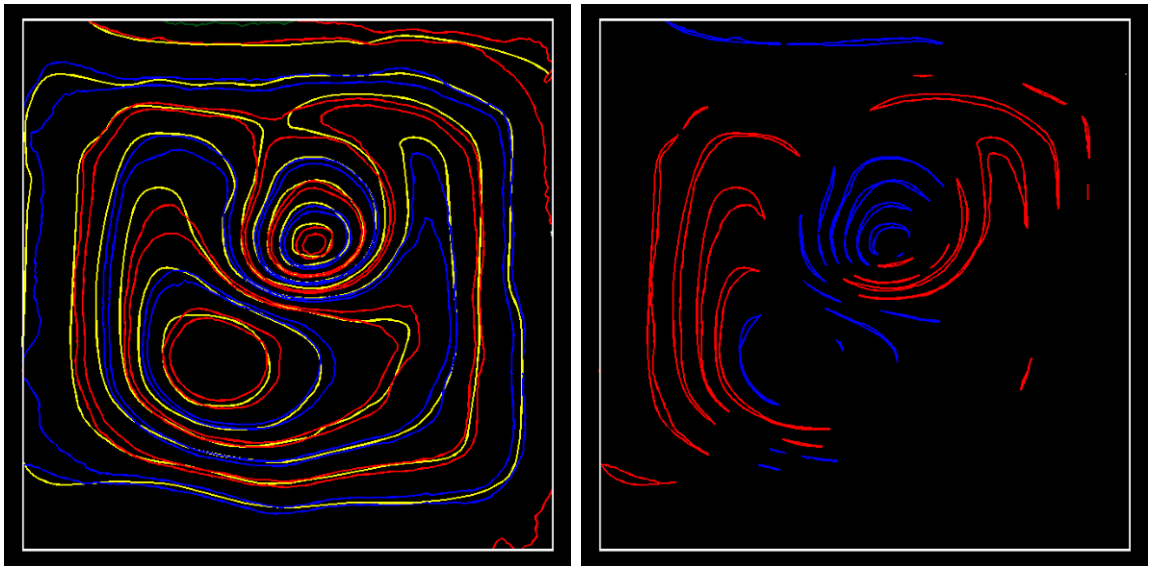

(a) (b)

Figure 119. The 270° sample rotation for error on 1/32nd of an inch accuracy. (a) Contours overlap, (b) Contour errors. Upper error area = 0.91 in^2, Lower error area = 3.80 in^2 and Total error area = 4.71 in^2.

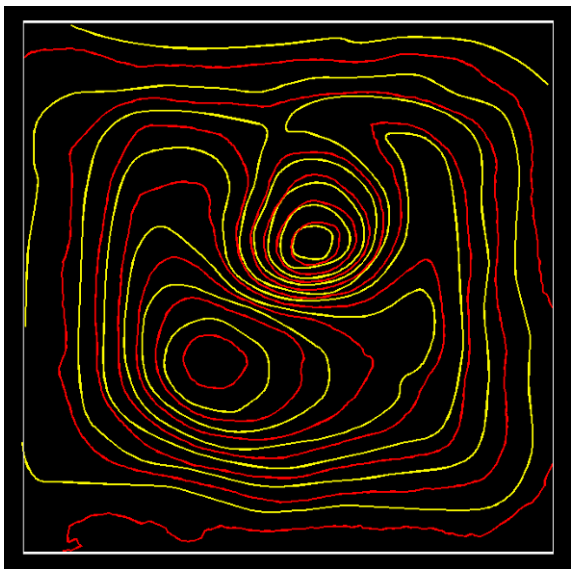

Fig. 120. Contours overlapping of the 315° sample rotation for error on 1/8th of an inch accuracy. Zero errors resulted in this accuracy level.

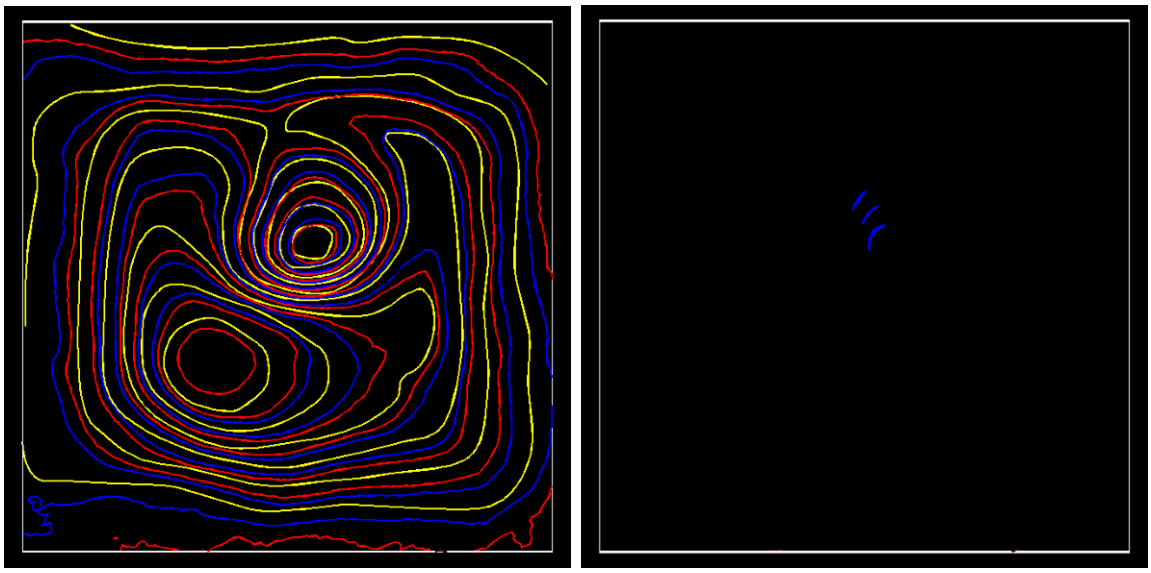

(a) (b)

Fig. 121. The 315° sample rotation for error on 3/32nd of an inch accuracy.
(a) Contours overlap, (b) Contour errors: Upper error area = 0.03 in^2, Lower error area = 0.00 in^2 and Total error area = 0.03 in^2.

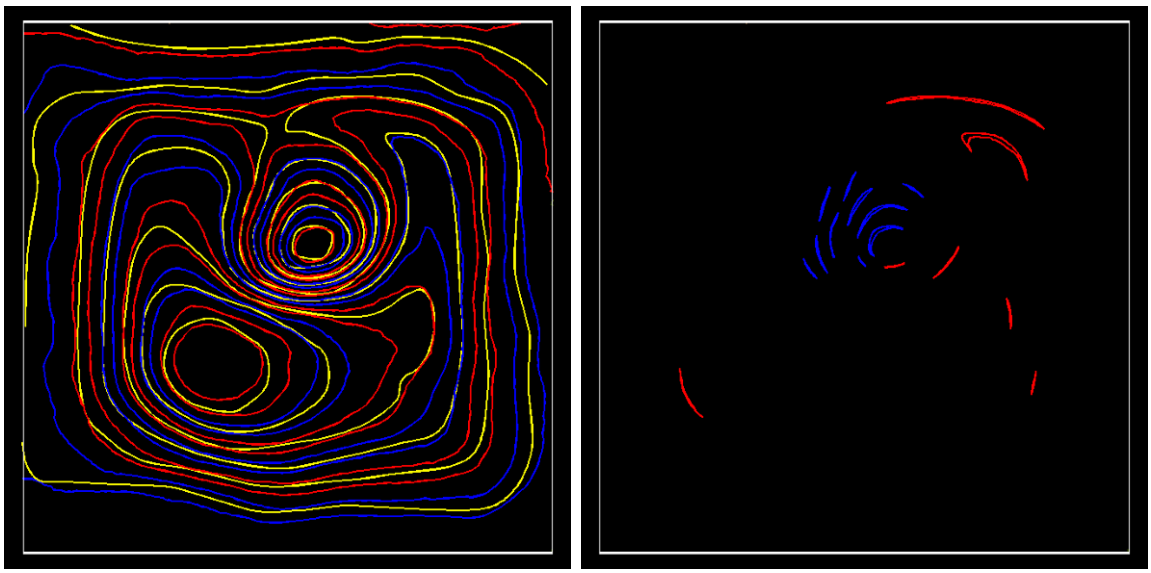

(a) (b)

Fig. 122. The 315° sample rotation for error on 1/16th of an inch accuracy.
(a) Contours overlap, (b) Contour errors: Upper error area = 0.18 in^2, Lower error area = 0.25 in^2 and Total error area = 0.43 in^2.

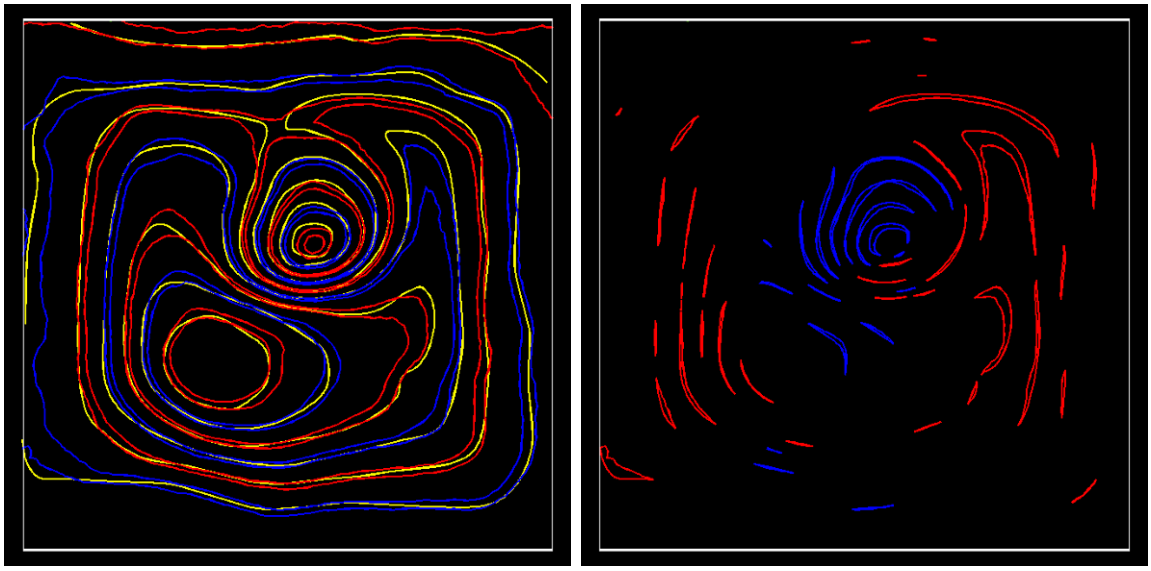

(a) (b)

Fig. 123. The 315° sample rotation for error on 1/32nd of an inch accuracy. (a) Contours overlap, (b) Contour errors: Upper error area = 0.77 in^2, Lower error area = 1.98 in^2 and Total error area = 2.75 in^2.

V.1.4. Accuracy interpretation and analysis

Measurement accuracies resulting from the previous evaluation worked as the basis for measurement validity in this study. This validity supported the inclusion of samples to evaluate time-consumption feasibility. The error percentage generated from the previous phase will be presented in the following sections.

V.1.4.1. Accuracy level of 1/8th of an inch

For the targeted accuracy level of 1/8th of an inch, the hand measurement samples showed an average area error of 1.45% of the total TMVS area of 82.151 squared inches for all the samples, as shown in Table 1.

The largest error percentage occurred in the brown grid sample. The error was 2.34% with 23 incidences. The lowest error percentage occurred in the magenta grid sample. The error was 0.73% with 18 incidents.

Table 1. The hand measuring method error on 1/8th of an inch accuracy

	Number of Incidences	Model Surface Area	Upper Error Area	Lower Error Area	Total Error Area	Error Percentage
Sample 1 (R)	22	82.16	1.26	0.55	1.81	2.20%
Sample 2 (K)	19	81.97	0.77	0.78	1.55	1.89%
Sample 3 (Y)	18	82.18	0.54	0.61	1.15	1.40%
Sample 4 (B)	15	82.36	0.41	0.2	0.61	0.74%
Sample 5 (O)	21	82.02	0.72	0.18	0.9	1.10%
Sample 6 (P)	18	82.13	0.53	0.07	0.6	0.73%
Sample 7 (G)	22	82.24	0.71	0.27	0.98	1.19%
Sample 8 (BR)	23	82.15	1.63	0.29	1.92	2.34%

Two samples were spotted in the (2.0% - 2.5%) error range, the brown and the red samples. In the error range of (1.5% - 2.0%) there was the black sample. In the error range of (1.0% - 1.5%) three samples were spotted there, green, orange and yellow. The purple and the blue samples were in the error range of (0.5% - 1.0%), as shown in Fig. 124.

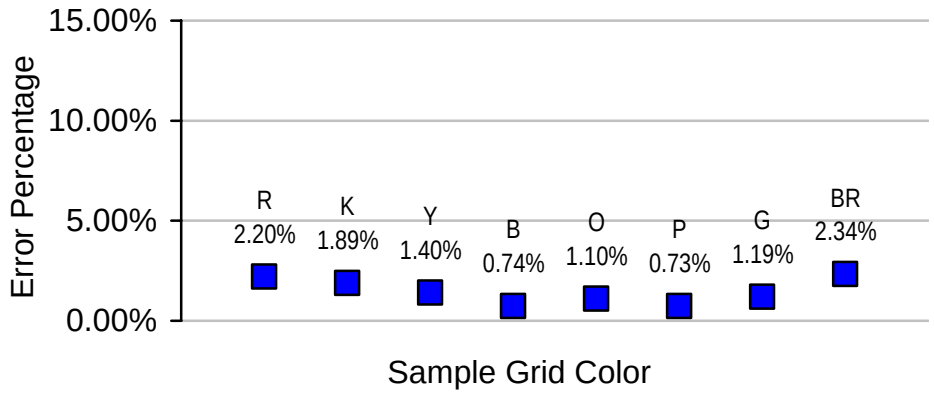

Fig. 124. The hand measuring method error on 1/8th of an inch accuracy.

For the same targeted accuracy of 1/8th of an inch, the OMIT measurement samples showed an average area error of 0.02% of the total TMVS area of 102.24 squared inches for all the samples, as shown in Table 2.

Table 2. The OMIT measuring method error on 1/8th of an inch accuracy

	Number of Incidences	Model Surface Area	Upper Error Area	Lower Error Area	Total Error Area	Error Percentage
Sample 1 (00)	0	102.24	0.00	0.00	0.00	0.00%
Sample 2 (45)	6	102.24	0.04	0.02	0.06	0.06%
Sample 3 (90)	4	102.24	0.01	0.10	0.11	0.11%
Sample 4 (135)	0	102.24	0.00	0.00	0.00	0.00%
Sample 5 (180)	3	102.24	0.02	0.00	0.02	0.02%
Sample 6 (225)	0	102.24	0.00	0.00	0.00	0.00%
Sample 7 (270)	0	102.24	0.00	0.00	0.00	0.00%
Sample 8 (315)	0	102.24	0.00	0.00	0.00	0.00%

The largest error percentage occurred in the 90º rotation sample. The error was 0.11% with 4 incidences. The lowest error percentage occurred in five samples with the rotation of 0º, 135 º, 225 º, 270 º and 315 º. The error was 0.00% with no incidences.

One sample was in the (0.10% - 0.15%) error range, the 90° rotation sample. In the error range of (0.05% - 0.10%) there was the 45° rotation samples. In the error range of (0.00% - 0.05%) six samples, 0°, 135°, 180°, 225°, 270° and 315° rotation samples, were spotted there, as shown in Fig. 125.

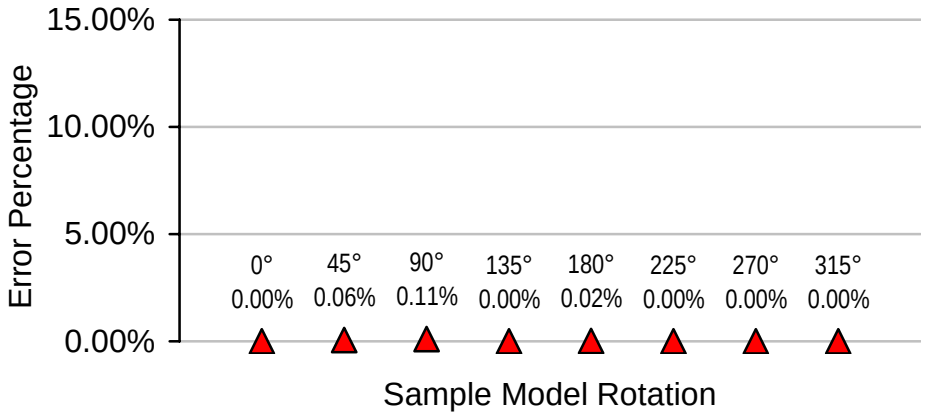

Fig. 125. The OMIT measuring method error on 1/8th of an inch accuracy.

V.1.4.2. Accuracy level of 3/32nd of an inch

For the accuracy level of 3/32nd of an inch, the hand measurement samples showed an average area error of 2.81% of the total average TMVS average area of 82.151 squared inches for all the samples, as shown in Table 3.

The largest error percentage occurred in the brown grid sample. The error was 3.94% with 32 incidences. The lowest error percentage occurred in the purple grid sample. The error was 1.85% with 29 incidences.

Table 3. The hand measuring method error on 3/32nd of an inch accuracy

	Number of Incidences	Model Surface Area	Upper Error Area	Lower Error Area	Total Error Area	Error Percentage
Sample 1 (R)	27	82.16	2.45	0.68	3.13	3.81%
Sample 2 (K)	29	81.97	1.59	1.09	2.68	3.27%
Sample 3 (Y)	33	82.18	1.35	0.81	2.16	2.63%
Sample 4 (B)	35	82.36	1.22	0.38	1.6	1.94%
Sample 5 (O)	34	82.02	1.55	0.28	1.83	2.23%
Sample 6 (P)	29	82.13	1.29	0.23	1.52	1.85%
Sample 7 (G)	32	82.24	1.71	0.59	2.3	2.80%
Sample 8 (BR)	32	82.15	2.85	0.39	3.24	3.94%

Three samples were spotted in the (3.0% - 4.0%) error range, the red, the black, and the brown samples. In the error range of (2.0% - 3.0%), there were also three samples: yellow, orange, and green. In the error range of (1.0% - 2.0%) two samples, blue and purple, were spotted, as shown in Fig. 126.

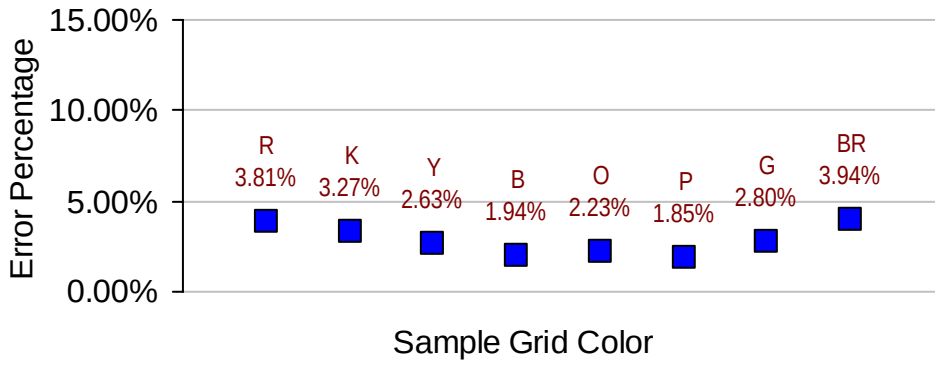

Fig. 126. The hand measuring method error on 3/32nd of an inch accuracy.

For the same targeted accuracy of 3/32nd of an inch, the OMIT measurement samples showed an average area error of 0.21% of the total TMVS area of 102.24 squared inches for all the samples, as shown in Table 4.

Table 4. The OMIT measuring method error on 3/32nd of an inch accuracy

	Number of Incidences	Model Surface Area	Upper Error Area	Lower Error Area	Total Error Area	Error Percentage
Sample 1 (00)	8	102.24	0.01	0.03	0.04	0.04%
Sample 2 (45)	14	102.24	0.20	0.18	0.38	0.38%
Sample 3 (90)	14	102.24	0.06	0.43	0.49	0.48%
Sample 4 (135)	11	102.24	0.15	0.06	0.21	0.21%
Sample 5 (180)	10	102.24	0.13	0.00	0.13	0.13%
Sample 6 (225)	6	102.24	0.27	0.01	0.28	0.27%
Sample 7 (270)	11	102.24	0.01	0.11	0.12	0.12%
Sample 8 (315)	3	102.24	0.03	0.00	0.03	0.03%

The largest error percentage occurred in the 90º rotation sample. The error was 0.48% with 14 incidences. The lowest error percentage occurred in the 315 º rotation samples. The error was 0.03% with three incidences.

One sample was in the (0.40% - 0.50%) error range, the 90° rotation sample. In the error range of (0.30% - 0.40%) there was the 45° rotation sample.

In the error range of (0.02% - 0.03%) two samples were spotted, the 135° and 225° rotation samples. In the error range of (0.01% - 0.02%) two samples were found, the 180° and 270° rotation samples. The 0° and 315° rotation samples were found,in the error range of (0.01% - 0.02%), as shown in Fig. 127.

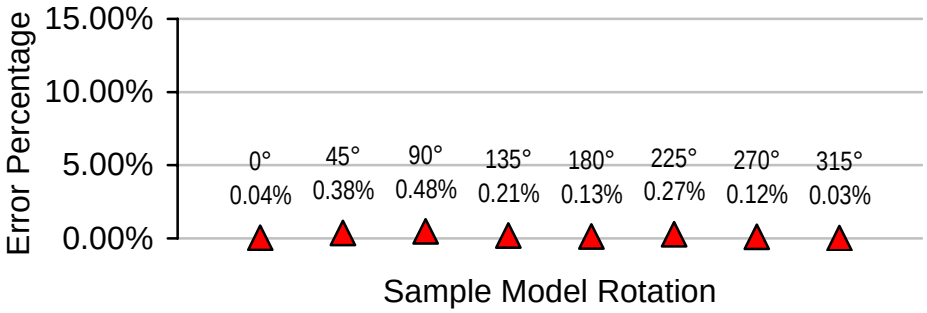

Fig. 127. The OMIT measuring method error on 3/32nd of an inch accuracy.

V.1.4.3. Accuracy level of 1/16th of an inch

On the accuracy level of 1/16th of an inch, the hand measurement samples showed an average area error of 5.63% of the total average TMVS area of 82.151 squared inches for all the samples, as shown in Table 5.

Table 5. The hand measuring method error on 1/16th of an inch accuracy

	Number of Incidences	Model Surface Area	Upper Error Area	Lower Error Area	Total Error Area	Error Percentage
sample 1 (R)	46	82.16	4.66	0.85	5.51	6.71%
sample 2 (K)	38	81.97	3.59	1.48	5.07	6.19%
sample 3 (Y)	48	82.18	3.26	1.15	4.41	5.37%
sample 4 (B)	55	82.36	3.69	0.12	3.81	4.63%
sample 5 (O)	50	82.02	3.47	0.45	3.92	4.78%
sample 6 (P)	52	82.13	3.33	0.51	3.84	4.68%
sample 7 (G)	42	82.24	3.78	0.79	4.57	5.56%
sample 8 (BR)	42	82.15	5.35	0.54	5.89	7.17%

The largest error percentage occurred in the brown grid sample. The error was 7.17% with 42 incidences. The lowest error percentage occurred in the blue grid sample. The error was 4.63% with 55 incidences.

One sample was spotted in the (7.0% - 8.0%) error range, the brown sample. In the error range of (6.0% - 7.0%) there were two samples, red and black. In the error range of (5.0% - 6.0%) there were two samples, yellow and green. The last three samples—blue, orange and purple—were spotted in the error range of (4.0% - 5.0%), as shown in Fig. 128.

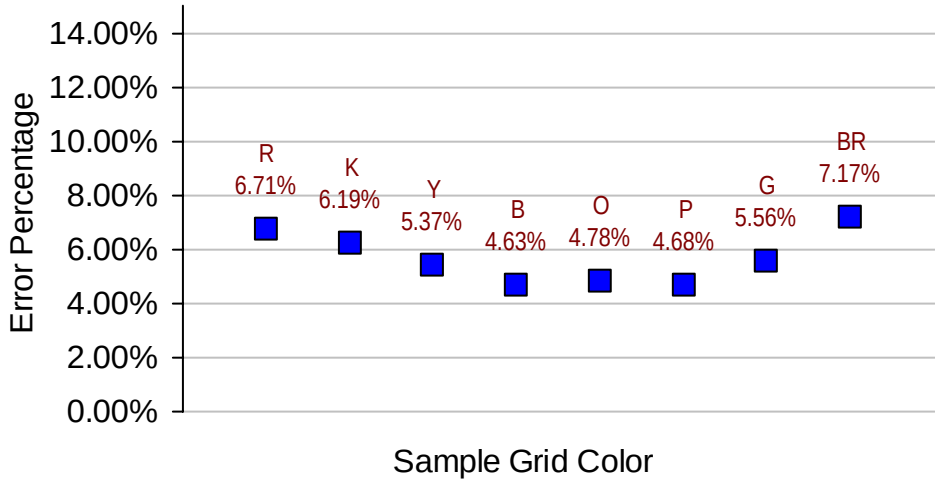

Fig. 128. The hand measuring method error on 1/16th of an inch accuracy.

For the same targeted accuracy of 1/16th of an inch, the OMIT measurement samples showed an average area error of 1.27% of the total TMVS area of 102.24 squared inches for all the samples, as shown in Table 6.

The largest error percentage occurred in the 135º rotation sample. The error was 2.24% with 32 incidences. The lowest error percentage occurred in the 315 º rotation sample. The error was 0.42% with 17 incidences.

Table 6. The OMIT measuring method error on 1/16th of an inch accuracy

	Number of Incidences	Model Surface Area	Upper Error Area	Lower Error Area	Total Error Area	Error Percentage
sample 1 (00)	33	102.25	0.36	0.95	1.31	1.28%
sample 2 (45)	36	102.25	0.60	0.94	1.54	1.51%
sample 3 (90)	26	102.25	0.28	1.17	1.45	1.42%
sample 4 (135)	32	102.25	1.44	0.85	2.29	2.24%
sample 5 (180)	22	102.25	0.63	0.09	0.72	0.70%
sample 6 (225)	24	102.25	1.43	0.03	1.46	1.43%
sample 7 (270)	19	102.25	0.12	1.08	1.20	1.17%
sample 8 (315)	17	102.25	0.18	0.25	0.43	0.42%

One sample was in the (2.0% - 2.5%) error range, the 135° rotation sample. In the error range of (1.5% - 2.0%) there was the 45° rotation sample. In the error range of (1.0% - 1.5%) four samples were spotted: the 0°, 90°, 225° and 270° rotation samples. In the error range of (0.5% - 1.0%) one sample was spotted, the 180° rotation sample. The last rotation sample, 315°, was spotted in the error range of (0.0% - 0.5%), as shown in Fig. 129.

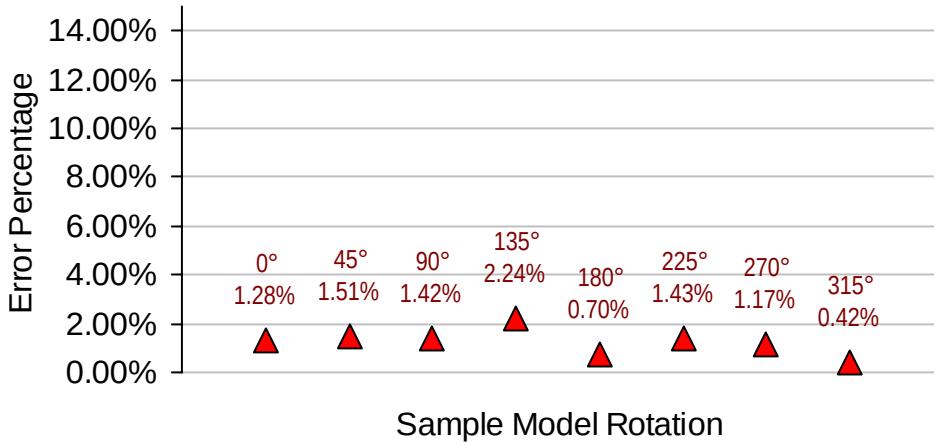

Fig. 129. The OMIT measuring method error on 1/16th of an inch accuracy.

V.1.4.4. Accuracy of 1/32nd of an inch

For the accuracy level of 1/32nd of an inch, the hand measurement samples showed an average area error of 11.15% of the total TMVS average area of 82.151 squared inches for all the samples as shown in Table 7.

Table 7. The hand measuring method error on 1/32nd of an inch accuracy

	Number of Incidences	Model Surface Area	Upper Error Area	Lower Error Area	Total Error Area	Error Percentage
sample 1 (R)	56	82.16	9.17	1.14	10.31	12.55%
sample 2 (K)	59	81.97	7.5	2.07	9.57	11.68%
sample 3 (Y)	55	82.18	6.92	1.74	8.66	10.54%
sample 4 (B)	64	82.36	6.88	1.41	8.29	10.07%
sample 5 (O)	60	82.02	7.71	0.99	8.7	10.61%
sample 6 (P)	69	82.13	7.36	1.23	8.59	10.46%
sample 7 (G)	55	82.24	7.84	1.27	9.11	11.08%
sample 8 (BR)	48	82.15	8.73	1.32	10.05	12.23%

The largest error percentage occurred in the red grid sample. The error was 12.55% with 56 incidences. The lowest error percentage occurred in the blue grid sample. The error was 10.07% with 64 incidences.

Two samples were spotted in the (12.0% - 13.0%) error range, red and brown samples. In the error range of (11.0% - 12.0%) there were two samples, black and green. In the error range of (10.0% - 11.0%) the last four samples, yellow, blue, orange and purple, were spotted there, as shown in Fig 130.

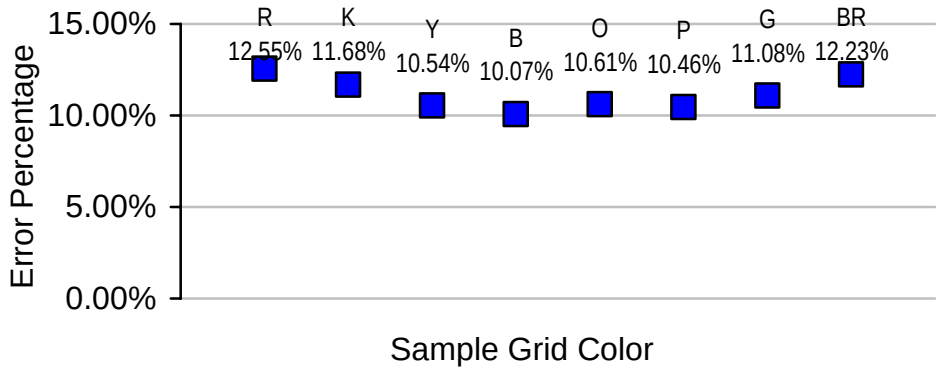

Fig. 130. The hand measuring method error on 1/32nd of an inch accuracy.

For the same targeted accuracy level of 1/32nd of an inch, the OMIT measurement samples showed an average area error of 4.78% of the total TMVS area of 102.24 squared inches for all the samples as shown in Table 8.

Table 8. The OMIT measuring method error on 1/32nd of an inch accuracy

	Number of Incidences	Model Surface Area	Upper Error Area	Lower Error Area	Total Error Area	Error Percentage
sample 1 (00)	40	102.24	2.43	3.49	5.93	5.80%
sample 2 (45)	49	102.24	1.83	4.09	5.92	5.79%
sample 3 (90)	51	102.24	1.26	3.23	4.49	4.39%
sample 4 (135)	38	102.24	4.57	3.16	7.73	7.56%
sample 5 (180)	39	102.24	2.80	0.98	3.78	3.70%
sample 6 (225)	50	102.24	3.03	0.74	3.77	3.69%
sample 7 (270)	38	102.24	0.91	3.80	4.71	4.61%
sample 8 (315)	51	102.24	0.77	1.98	2.75	2.69%

The largest error percentage occurred in the 135º rotation sample. The error was 7.56% with 38 incidences. The lowest error percentage occurred in the 315 º rotation sample. The error was 2.69% with 51 incidences.

One sample was in the (7.0% - 8.0%) error range, the 135° rotation sample. In the error range of (5.0% - 6.0%) there were the 45°and the 0° rotation samples. In the error range of (4.0% - 5.0%) two samples were spotted, the 90° and 270° rotation samples. In the error range of (3.0% - 4.0%) two samples were spotted, the 180° and 225° rotation samples. The last sample, 315° rotation sample, was spotted in the error range of (2.0% - 3.0%) as shown in Fig. 131.

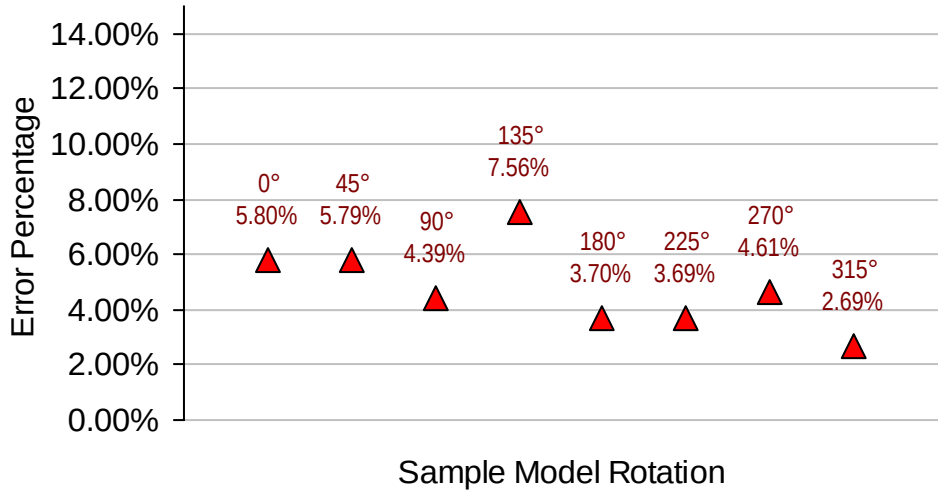

Fig. 131. The OMIT measuring method error on 1/32nd of an inch accuracy.

V.1.4.5. Measurement errors on all accuracy levels

For the hand measuring method, Table 9 shows the error percentage for all the samples on the four accuracy levels.

Table 9. The hand measuring error for all samples on all accuracy levels

	1/8th	3/32nd	1/16th	1/32nd	Average
sample 1 (R)	2.20%	3.81%	6.71%	12.55%	6.32%
sample 2 (K)	1.89%	3.27%	6.19%	11.68%	5.76%
sample 3 (Y)	1.40%	2.63%	5.37%	10.54%	4.98%
sample 4 (B)	0.74%	1.94%	4.63%	10.07%	4.34%
sample 5 (O)	1.10%	2.23%	4.78%	10.61%	4.68%
sample 6 (P)	0.73%	1.85%	4.68%	10.46%	4.43%
sample 7 (G)	1.19%	2.80%	5.56%	11.08%	5.16%
sample 8 (BR)	2.34%	3.94%	7.17%	12.23%	6.42%

Figure 132 shows graphically the relation between error percentages of all the samples.

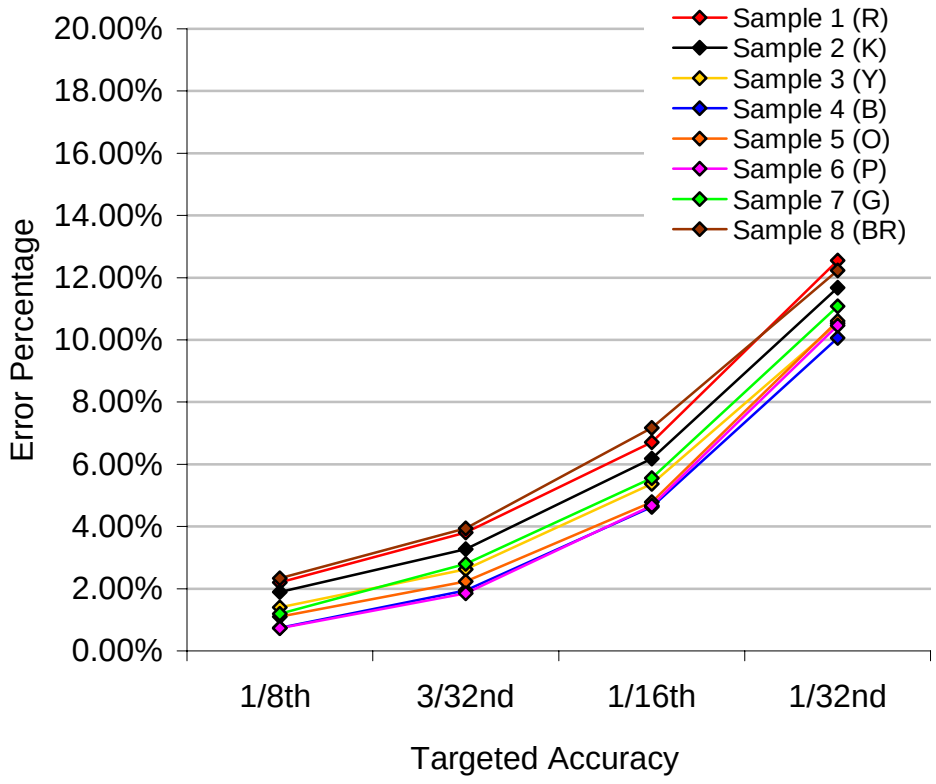

Fig. 132. The hand measuring error percentage in relation to accuracy levels.

For the hand measuring method, the most accurate sample measurement on the four accuracy levels was the blue grid sample with an average percentage error of 4.34%. The least accurate sample measurement on the four accuracy levels was the brown grid sample with an average percentage error of 6.42%, as shown in Fig. 133.

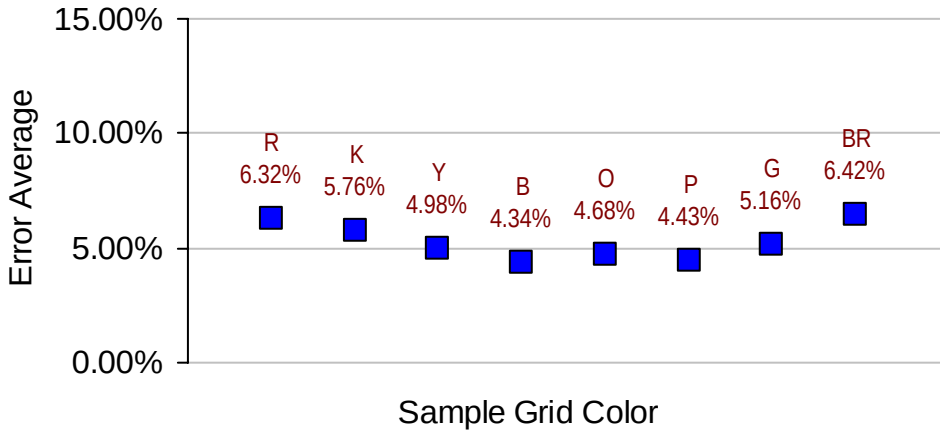

Fig. 133. The hand measuring error percentage in relation to sample grid color.

For the OMIT measuring method, Table 10 shows the error percentage for all the samples on the four accuracy levels.

Table 10. The OMIT measuring error for all samples on all accuracy levels

	1/8th	3/32nd	1/16th	1/32nd	Average
Sample 1 (00)	0.00%	0.04%	1.28%	5.80%	1.78%
Sample 2 (45)	0.35%	0.38%	1.51%	5.47%	1.93%
Sample 3 (90)	0.11%	0.48%	1.42%	4.39%	1.60%
Sample 4 (135)	0.00%	0.21%	2.24%	7.56%	2.50%
Sample 5 (180)	0.02%	0.13%	0.70%	3.68%	1.13%
Sample 6 (225)	0.00%	0.27%	1.43%	3.69%	1.35%
Sample 7 (270)	0.00%	0.12%	1.17%	4.61%	1.47%
Sample 8 (315)	0.00%	0.03%	0.42%	2.69%	0.78%

The following Fig. 134 shows graphically the relation between error percentages of all the samples.

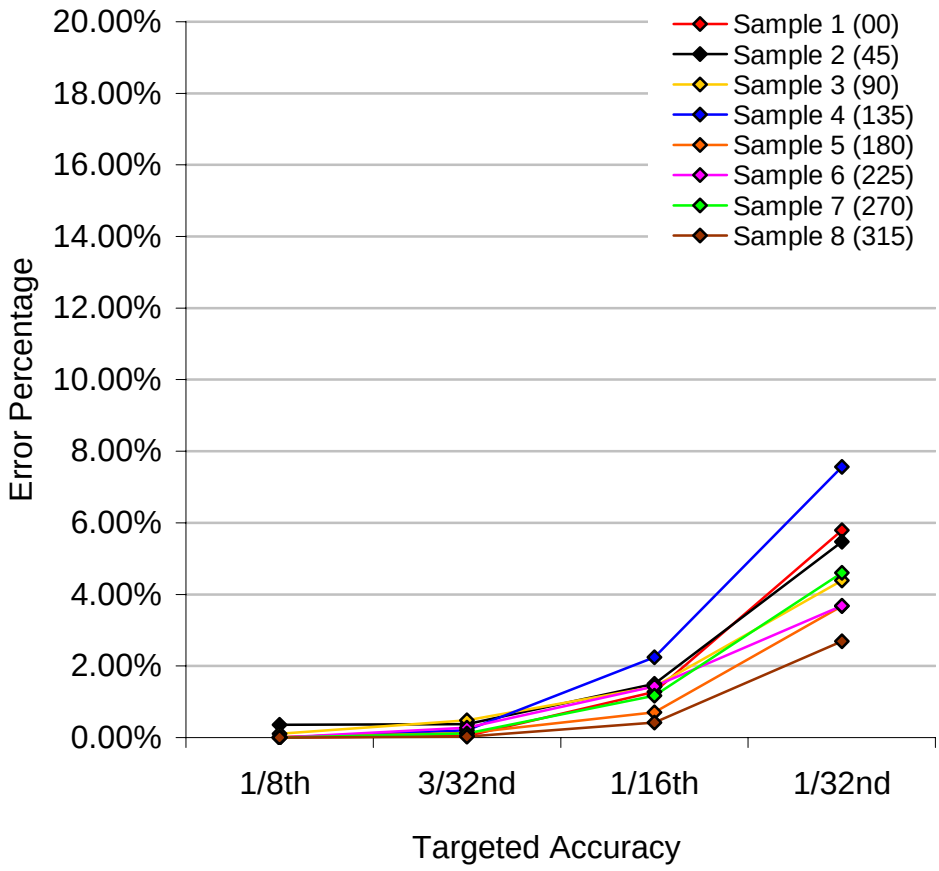

Fig. 134. The OMIT measuring error percentage in relation to accuracy levels.

For the OMIT measuring method, the most accurate sample measurement on the four accuracy levels was the 315° rotation sample with an average percentage error of 0.785%. The least accurate sample measurement on the four accuracy levels was the 135° rotation sample with an average percentage error of 2.50%, as shown in Fig. 135.

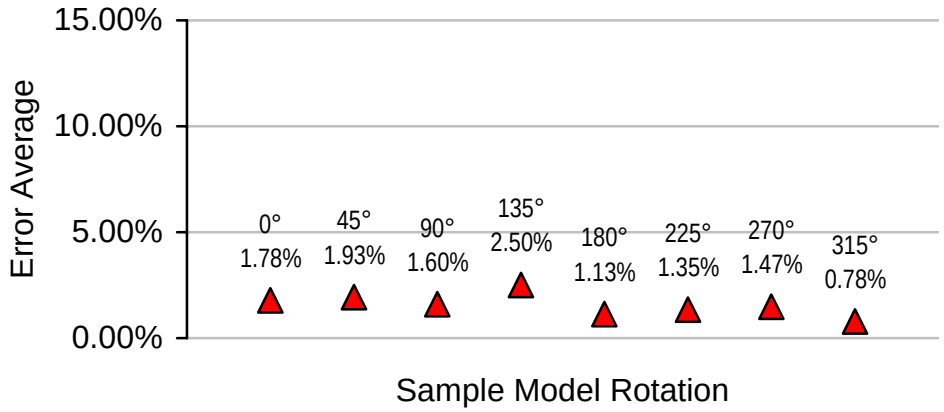

Fig. 135. The OMIT measuring error percentage in relation to sample rotation.

V.1.4.6. Accuracy comparison of the two methods

The ratio of measurement errors between all the samples of the hand measuring method and the OMIT method for the targeted accuracy of 1/8th of an inch is shown in Fig. 136.

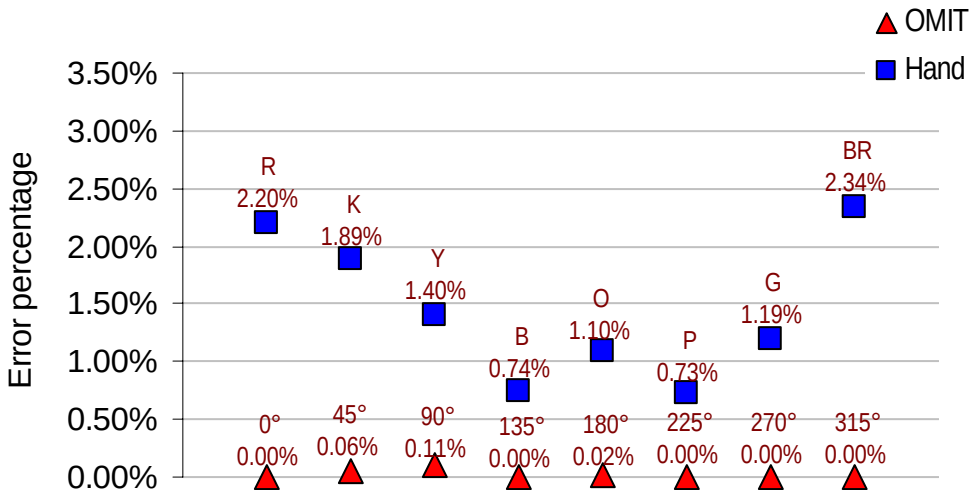

Fig. 136. The two methods error comparison on 1/8th of an inch accuracy.

Measurement average error ratio between the two methods was around 62.5:1 for the targeted accuracy of 1/8th of an inch, as shown in Fig. 137.

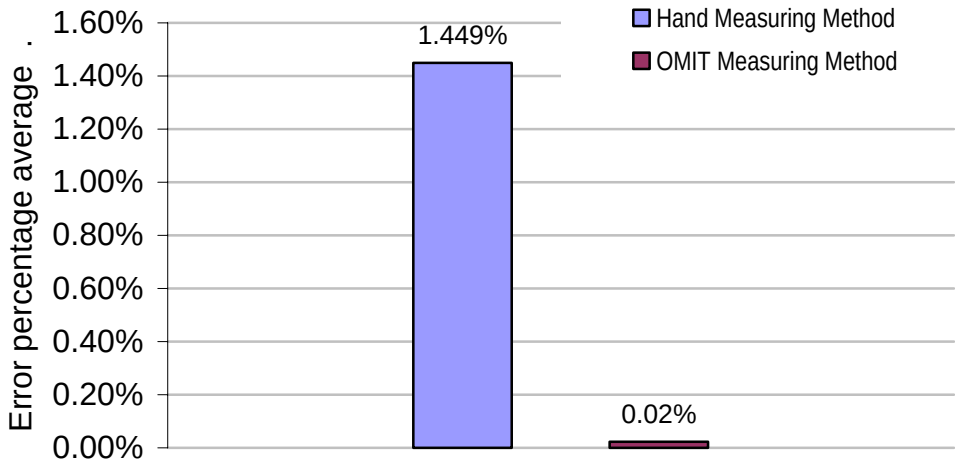

Fig. 137. The methods average error comparison on 1/8th of an inch accuracy.

The ratio of measurement errors between all the samples of the hand measuring method and the OMIT method for the investigated accuracy of 3/32nd of an inch is shown in Fig. 138.

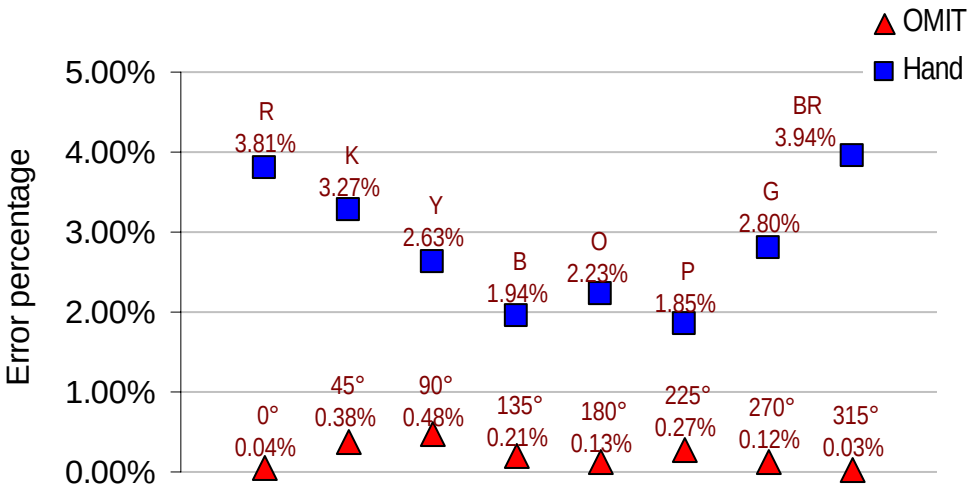

Fig. 138. The two methods error comparison on 3/32nd of an inch accuracy.

Measurement average error ratio between the two methods was 13.6:1 for the investigated accuracy of 3/32nd of an inch, as shown in Fig. 139.

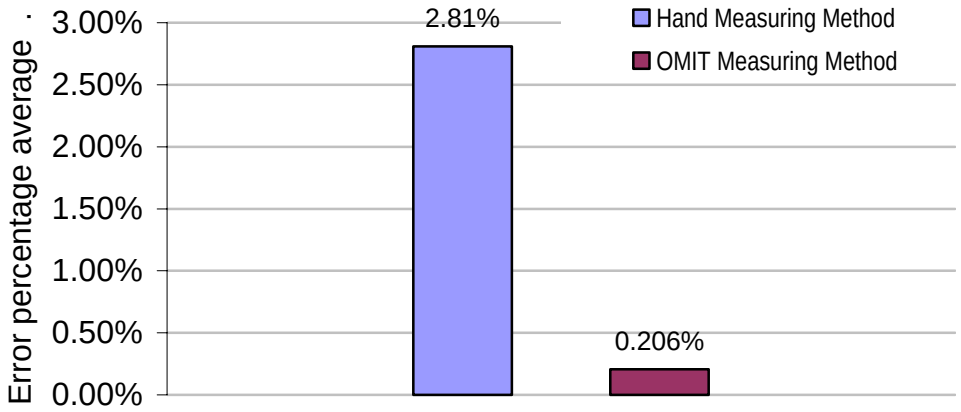

Fig. 139. The methods average error comparison on 3/32nd of an inch accuracy.

The ratio of measurement errors between all the samples of the hand measuring method and the OMIT method for the investigated accuracy of 1/16th of an inch is shown in Fig. 140.

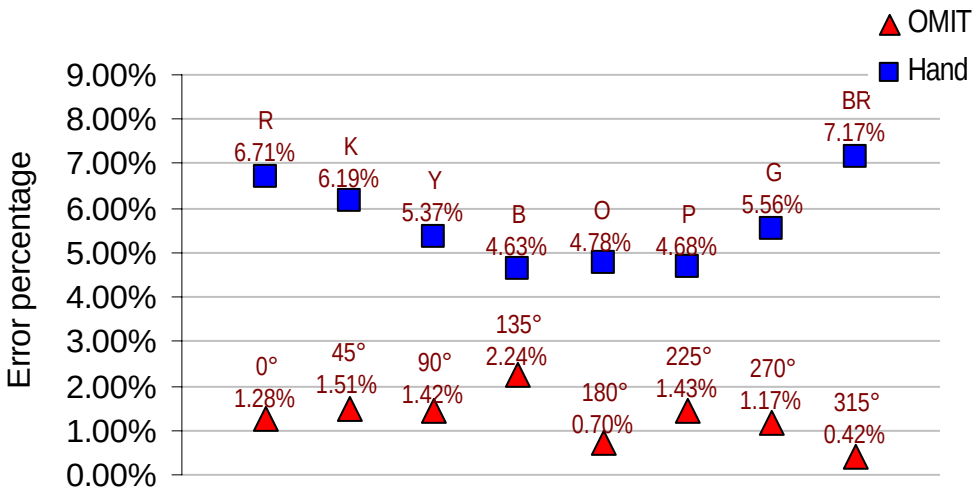

Fig. 140. The two methods error comparison on 1/16th of an inch accuracy.

Measurement average error ratio between the two methods was 4.4:1 for the investigated accuracy of 1/16th of an inch, as shown in Fig. 141.

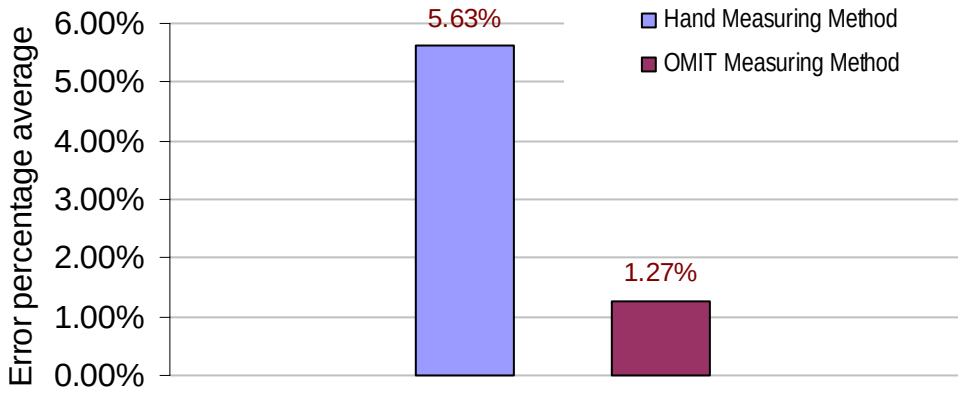

Fig. 141. The methods average error comparison on 1/16th of an inch accuracy.

The measurement errors ratio between all the samples of the hand measuring method and the OMIT measuring method for the investigated accuracy of 1/32nd of an inch is shown in Fig. 142.

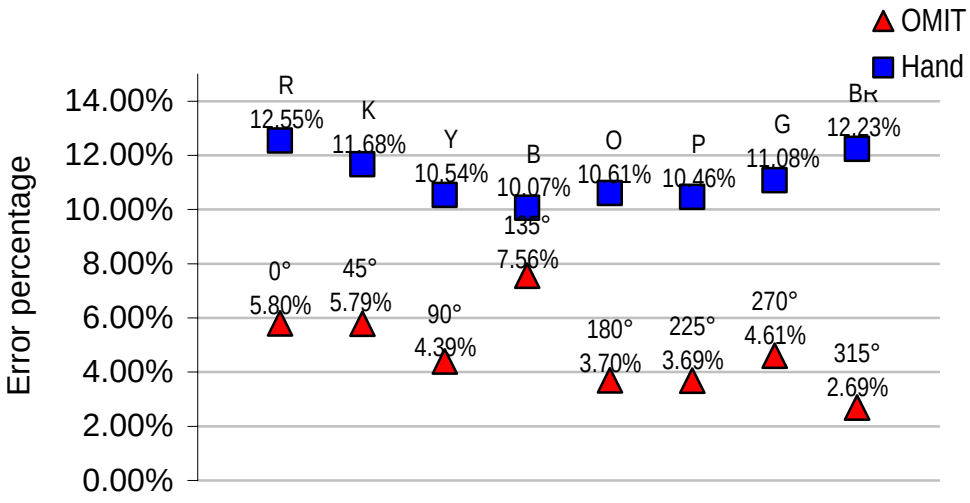

Fig. 142. The two methods error comparison on 1/32nd of an inch accuracy.

Measurement average error ratio between the two methods was 2.3:1 for the investigated accuracy of 1/32nd of an inch, as shown in Fig. 143.

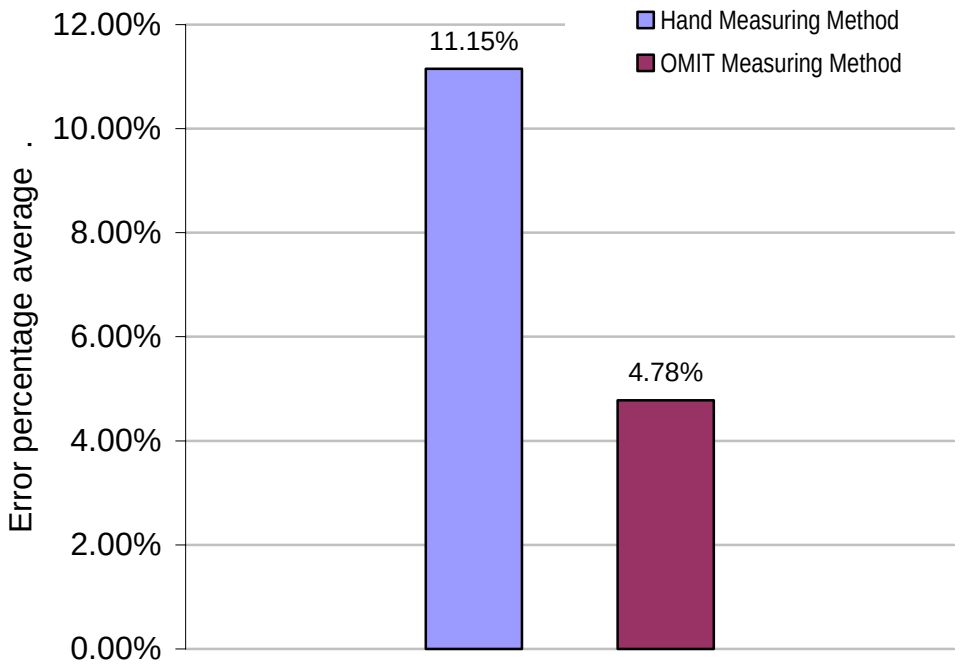

Fig. 143. The methods average error comparison on 1/32nd of an inch accuracy.

The following Table 11 and Fig. 144 show measurement average error comparison for the two investigated measuring methods on the four accuracy levels.

Table 11. The methods average error comparison on all accuracy levels

	1/8th	3/32nd	1/16th	1/32nd
Hand measuring method	1.449%	2.81%	5.63%	11.15%
OMIT measuring method	0.02%	0.206%	1.27%	4.78%

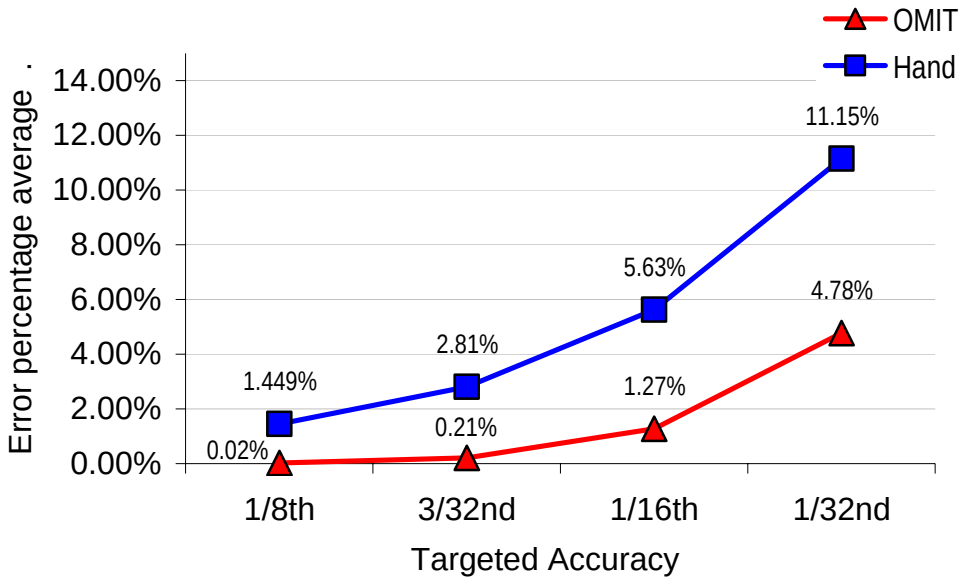

Fig. 144. The two methods average error comparison on all accuracy levels.

V.2. Time-consumption interpretation and comparison

The two methods processes were monitored for their time-consumption. In the experiments, the measuring process in each method as mentioned in section IV.2 consisted of two major parts: data collection and data treatment.

The time spent setting up equipment was not included in the investigation of time-consumption. The reason for this exclusion is the experimental nature of the involved arrangements and instruments. The non-standard equipment and the investigational arrangements were considered as an independent phase in this study. The different use of equipment such as the instrument created for the hand measuring method and the camera-projector arrangement for the OMIT measuring method consumed incomparable time according to that experimental nature. For this, the procedures for that part were recorded without referring to time-consumption because there was no justification for comparing time-consumption for two different measuring approaches on that level.

The targeted parts of the process were the parts concerned with data collection and data treatment.

V.2.1. Hand measuring method time-consumption result interpretation

The monitored parts of the hand measuring process were divided into three main phases. The first phase was the measurement collection phase referred to as the measuring phase. The second phase was the virtual model preparation phase referred to as the model preparing phase. The third phase was digital data insertion and contour generating phase referred to as the drawing phase.

Table 12 shows time intervals for collecting measurements from samples in the first phase. In order to trace the location of any occurrence of error in the recorded time-consumption the recording process was divided into segments for each sample. The collected time was based on recording time segments for measuring the four reference points and point groups of ten points each. The considered time-consumption for the entire phase was the total measuring time.

Table 12. Measuring phase time for the hand measuring method

Measured Sample Grid Color	Ref M.T.	1-10 M.T.	11-20 M.T.	21-30 M.T.	31-40 M.T.	41-50 M.T.	51-60 M.T.	61-70 M.T.	71-80 M.T.	81-90 M.T.	91-100 M.T.	Total M.T.
Sample (1) R	1.62	1.73	1.90	1.70	1.98	2.07	2.07	1.98	2.10	1.87	1.63	20.65
Sample (2) K	0.93	1.38	1.65	2.03	1.73	1.92	1.88	2.53	2.22	1.93	1.92	20.13
Sample (3) Y	0.87	1.63	1.67	1.85	1.82	2.02	1.83	2.18	2.05	1.42	2.25	19.58
Sample (4) B	0.78	1.90	1.68	1.58	1.95	1.88	1.95	2.00	2.08	1.82	1.95	19.58
Sample (5) O	0.82	1.80	1.73	1.70	1.75	2.22	2.10	1.88	2.25	1.98	1.32	19.55
Sample (6) M	0.67	1.92	1.63	1.67	2.02	1.92	2.35	2.38	2.08	2.00	1.80	20.43
Sample (7) G	0.67	1.67	2.02	1.57	1.95	2.15	1.85	1.97	1.97	1.80	2.13	19.73
Sample (8) BR	0.70	1.93	1.77	1.67	1.53	2.15	1.85	2.03	2.17	1.95	1.52	19.27

In the second phase, time intervals were recorded for preparing the virtual model for inserting the collected data.

In the third phase, time intervals were collected for the same segments used in the first phase. The recorded time was for generating contours by inserting digital data using point coordinates resulting from the collected measurements as shown in Table 13.

Table 13. Drawing phase time for the hand measuring method

Measured Sample Grid Color	Ref M.T.	1-10 M.T.	11-20 M.T.	21-30 M.T.	31-40 M.T.	41-50 M.T.	51-60 M.T.	61-70 M.T.	71-80 M.T.	81-90 M.T.	91-100 M.T.	Total M.T.
Sample (1) R	0.68	1.90	2.37	2.05	2.12	2.20	1.85	2.65	2.07	2.18	1.68	21.75
Sample (2) K	0.70	3.58	3.23	2.73	4.10	2.75	2.37	3.07	2.25	2.32	2.43	29.53
Sample (3) Y	1.05	2.27	2.08	2.15	2.55	3.18	2.72	2.53	2.45	2.30	2.60	25.88
Sample (4) B	0.97	2.38	2.27	2.23	2.35	2.48	2.18	2.08	2.02	2.28	2.37	23.62
Sample (5) O	1.53	2.65	3.50	2.63	4.63	3.50	2.80	2.87	3.10	2.82	2.77	32.80
Sample (6) M	0.88	2.05	2.03	2.25	2.48	2.10	2.48	2.60	2.13	2.30	2.45	23.77
Sample (7) G	1.02	2.18	2.23	2.45	2.30	2.50	2.45	2.55	2.58	2.72	2.22	25.20
Sample (8) BR	0.85	2.23	2.20	2.13	2.30	2.32	2.40	2.08	1.97	2.02	2.10	22.60

For the hand measuring method, Table 14 shows the total time-consumption resulting from each phase and the total processing time for each sample.

Table 14. Measuring process time for the hand measuring method

Measured Sample Grid Color	Total Measuring Time	Model Preparing Time	Total Drawing Time	Total Processing Time
Sample 1 (R)	20.65	10.38	21.75	52.78
Sample 2 (K)	20.13	9.20	29.53	58.87
Sample 3 (Y)	19.58	9.62	25.88	55.08
Sample 4 (B)	19.58	10.28	23.62	53.48
Sample 5 (O)	19.55	9.62	32.80	61.97
Sample 6 (P)	20.43	10.25	23.77	54.45
Sample 7 (G)	19.73	10.25	25.20	55.18
Sample 8 (BR)	19.27	10.32	22.60	52.18
Average	19.87	9.99	25.64	55.50

The chart in Fig. 145 shows the cumulative time-consumption for all the three phases of all hand measuring process samples. It also shows the time ratio between each of the three phases in relation with the recorded process's time-consumption.

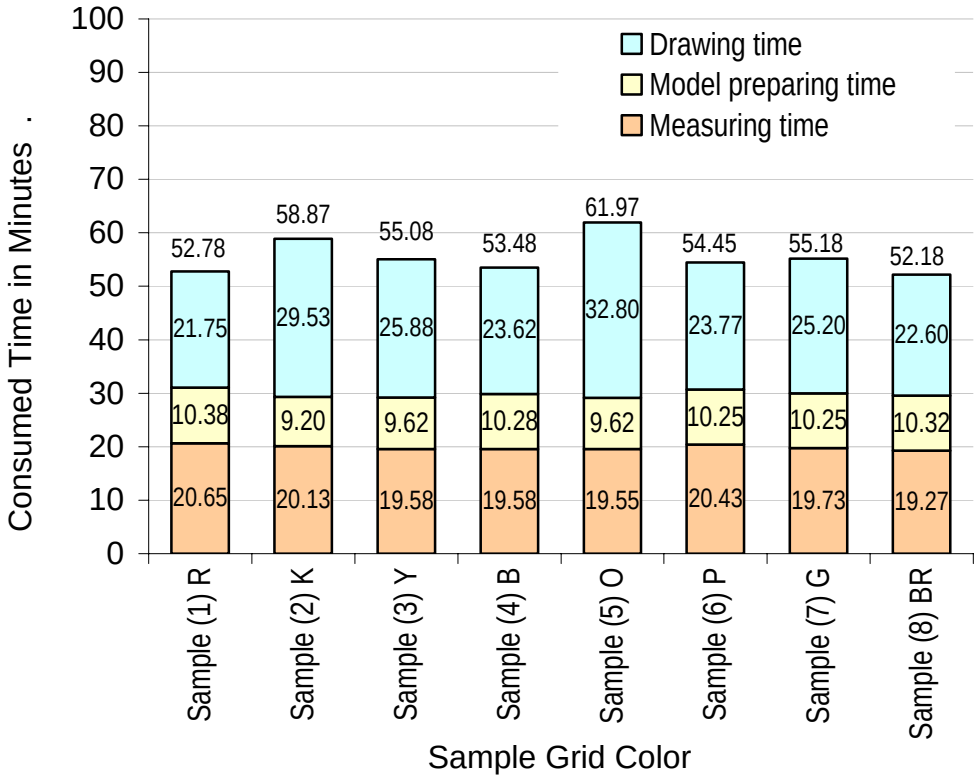

Fig. 145. Total time-consumption for the hand measuring method process.

The chart shows that the least time-consumption occurred when measuring the brown grid color sample with total time of 52.18 minutes. This recorded time was about 94% of the time average for all samples which was 55.50 minutes.

The chart shows also that the most time-consumption occurred when measuring the orange grid color sample with total time of 61.97 minutes. This recorded time was about 112% of the time average for all the samples.

V.2.2. OMIT measuring method time-consumption result interpretation

The measuring part of the OMIT measuring process was divided into two main phases. The first phase was the phase of pattern projection and moiré image acquisition. This phase was referred to as the OMIT measuring phase. The second phase was the dark fringes tracing phase referred to as the contour tracing phase.

Table 15 shows the collected time-consumption data for the OMIT measuring method process from the rotated samples in the two phases. The collected time-consumption in the first phase was based on recording time for placing the model on the base and taking a photo, projecting the light pattern and taking the second photo, and finally placing the reference piece on the base under the projected pattern and taking the third photo.

In the second phase, the recorded time-consumption was for superimposing the acquired photos to produce moiré fringes and tracing these resulting dark fringes to generate contour drawings.

Table 15. Measuring process time for the OMIT measuring method

Measured Sample Model Rotation	OMIT Measuring Time	Contour Tracing Time	Total Processing Time
Sample (1) 0°	1.77	3.10	4.87
Sample (2) 45°	1.45	2.25	3.70
Sample (3) 90°	1.43	2.82	4.25
Sample (4) 135°	1.48	2.75	4.23
Sample (5) 180°	1.65	2.38	4.03
Sample (6) 225°	1.45	2.53	3.98
Sample (7) 270°	1.47	2.58	4.05
Sample (8) 315°	1.60	2.87	4.47
Average	1.54	2.66	4.20

The chart in Fig. 146 shows the cumulative time-consumption for the two phases of all samples in the OMIT measuring process. It also shows the time

ratio between the two phases in relation with the recorded process's total time-consumption.

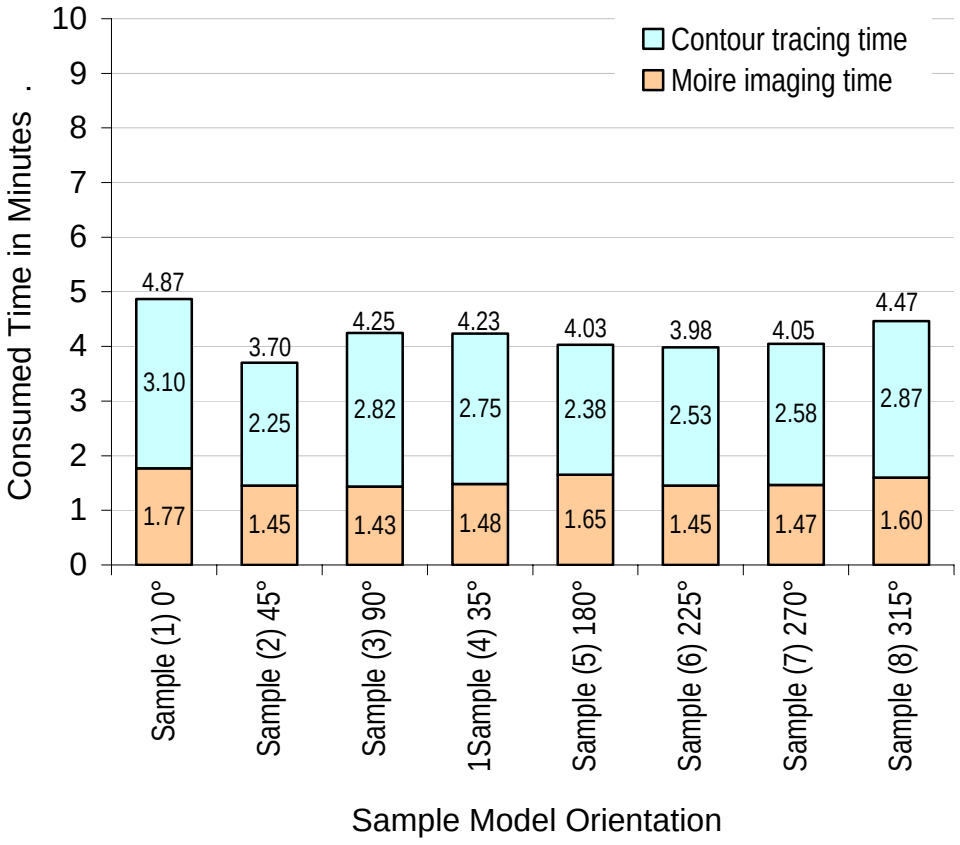

Fig. 146. Total time-consumption for the OMIT measuring method process.

The chart shows that the least time-consumption occurred when measuring the 45° rotation sample with total time of 3.70 minutes. This recorded time was about 88% of the time average for all samples which was 4.20 minutes.

The chart shows also that the most time-consumption occurred when measuring the 0° rotation sample with total time of 4.87 minutes. This recorded time was about 116% of the time average for all the samples.

V.2.3. Time-consumption comparison

To establish the feasibility of using the OMIT as a measuring method, comparing time-consumption was an objective in this investigation.

The ratio of process time-consumption between all the samples of the hand measuring method and the OMIT method is shown in Fig. 147.

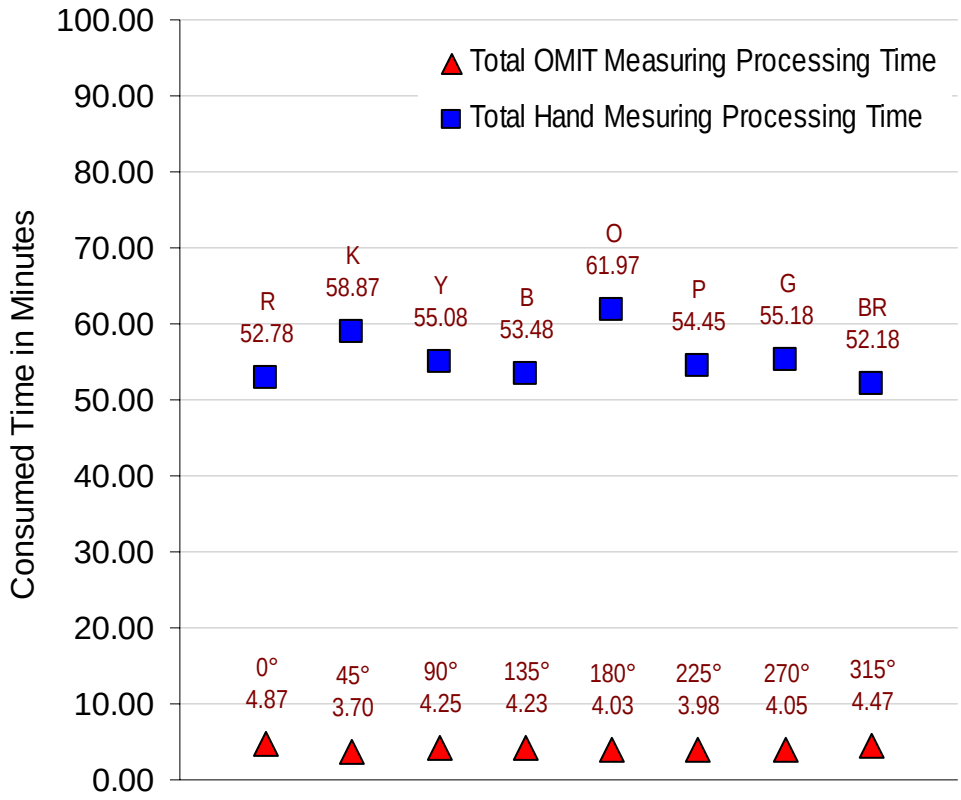

Fig. 147. Time-consumption average for the two methods processes.

The ratio of the collected time-consumption average between the two measuring methods was around 13:1, as shown in Fig. 148.

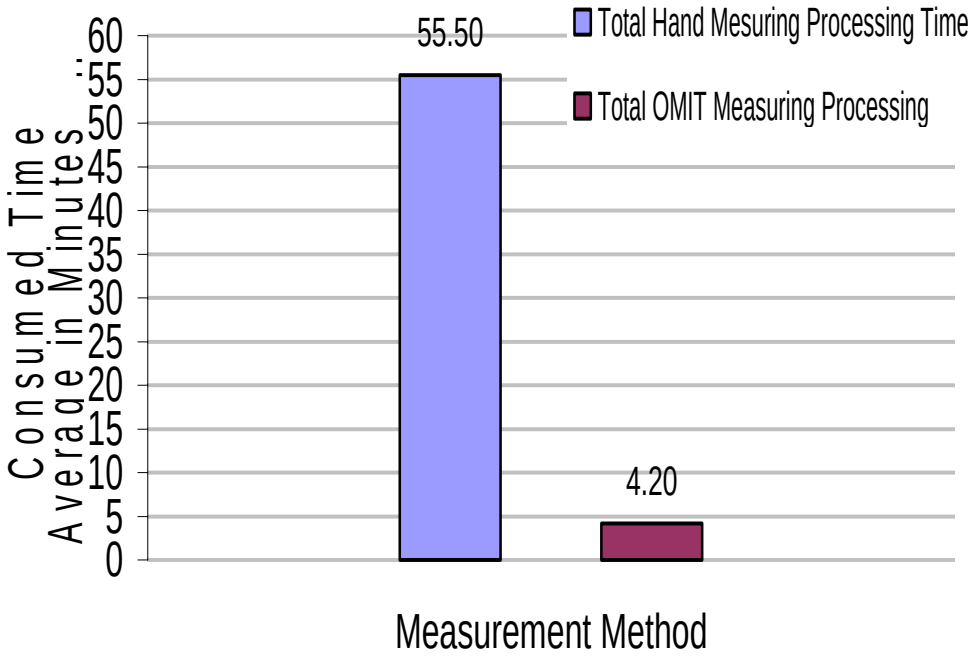

Fig. 148. Time-consumption average comparison for measuring processes.

V.3. Data analysis conclusions

From section V.1.4.6, the accuracy comparison results of the two methods indicated that the measurement error average ratio of hand method to the OMIT method was (62.5 to 1) for the targeted accuracy of 1/8th of an inch. According to the research measurement accuracy hypothesis explained earlier (section 1.3), this resulting ratio is above one on the targeted accuracy. This indicates that for depth measurement, the accuracy of the OMIT is 62.5 times higher than the accuracy of the compared hand measuring method under the same experimental conditions.

Although the OMIT experimental setting was designed to target the 1/8th of an inch accuracy threshold, and hand measurements were collected using a 1/32nd of an inch measuring unit (which gives measurement precision advantage

for hand measuring method), the generated depth measurements were tested on higher accuracy levels to grow confidence in the results. To accomplish that, multiple accuracy levels of 3/32nd of an inch, 1/16th of an inch and 1/32nd of an inch were targeted for increasing confidence in the conclusion.

On the 3/32nd of an inch accuracy level, the comparison showed that the accuracy of the OMIT is 13.6 times higher than the accuracy of the compared hand measuring method. On the 1/16th of an inch accuracy the comparison showed that the accuracy of the OMIT is 4.4 times higher than the accuracy of the compared hand measuring method. On the 1/32nd of an inch accuracy the comparison showed that the accuracy of the OMIT is 2.3 times higher than the accuracy of the compared hand measuring method.

In measurement accuracy conclusion, by testing the resulting measurements on the targeted accuracy of 1/8th of an inch and on three higher levels of accuracies, the results maintained the superiority of the OMIT method over the hand measuring method under the same experimental conditions. Another indication was that the integral information principal approach used by the OMIT added additional depth information which maintained acceptable accuracy on higher non-targeted levels.

From section V.2.3, time-consumption comparison results of the two methods indicated that the collected time-consumption average ratio of the hand method to the OMIT was (13 to 1). According to the research time-consumption hypothesis explained in section 1.3, the fact that the resulting ratio is above one indicates that for the depth measurement process, the hand measurement method consumed 13 times the time consumed by the OMIT under the same experimental conditions.

In the research time-consumption conclusion, the OMIT process time-consumption results are superior to the hand method process time-consumption results under the same experimental conditions.

CHAPTER VI

CONCLUSIONS AND RECOMMENDATIONS

The following sections establish the outcome of this study comparison based on the data analysis results of the previous chapter. The concluded feasibility of the OMIT as a measuring method is presented. Advantages of the OMIT method are identified and limitations are also encountered. Finally, the research recommendations and suggested future studies are pointed out and put forward.

VI.1. The OMIT feasibility conclusions

Based on the conclusion of the data analysis in this research investigation, the OMIT method shows superiority over the hand method in reducing process time-consumption when acquiring depth measurement. This superiority was established on a significant level of confidence. This confidence level was based on the considerable time-consumption difference between the two methods with a ratio of 13 to 1 to the advantage of the OMIT method.

The concern about depth measurement accuracy was also satisfied on a significant level of confidence. This level of confidence was based on considerable difference in measurement error between the two methods with a ratio of 62.5 to 1 to the advantage of the OMIT method.

This indicates that for acquiring depth measurements on a one eighth of an inch accuracy level under the same experimental conditions, the OMIT measurement method process consumed 7.7% of the time consumed by the control hand measuring method while achieving 6250% of the accuracy reached by the hand measuring method.

In conclusion, the OMIT as a measuring method in this study showed noticeable time-consumption feasibility that can be utilized for fine-grain surface relief for heritage recording purposes. Observed advantages of the OMIT

method were pointed out to establish future development potentials for future use and investigation. Observed limitations of the method were also pointed out in the study to establish enhancement potentials for further studies.

VI.2. The OMIT observed advantages and limitations

For heritage recording of objects with fine-grain surface relief, the hand measuring method was considered in this study as a well established conventional method with limitations of time-money consumption, intrusiveness, accuracy assumption, and efficiency.

For the same purpose, the OMIT was also considered as a well established conventional method in other disciplines with the potential of being a fast, accurate, non-intrusive and relatively inexpensive way to reveal surface relief measurements in one set of information.

The two methods were performed for recording the change in surface relief depth in a physical model with fine-grain surface relief under controlled conditions.

Associated with these considerations and the performed experiments, the conclusion of data analysis in this study indicates that the OMIT depth measuring method had high superiority over the hand depth measuring method concerning measurement accuracy and process time-consumption.

This concluded superiority demonstrated the advantages of OMIT and shows the merits of including it as a measuring method in historic recording work. These advantages were based on accuracy level and time-consumption as concluded in this study.

In that scope, this involvement of the OMIT in historic recording of objects surface relief can reduce the limitations associated with time-money consumption and accuracy assumptions encountered by the contemporary historic recording practices.

The results suggest the potential of this method to also fulfill the need for a remote-non-intrusive technique to prevent the deterioration of fragile heritage.

The advantage of incorporating an integral information principal approach (used by the OMIT) is reflected in the resulting high efficiency when utilized for recording surface relief. This full field technique enables extracting quantitative measurement data throughout the inspected surface from a single image. The efficiency can be noticed when utilizing the capability of the records to reveal additional depth measurement information beyond the targeted level.

The spatial resolution of this technique provides flexibility to control the amount of information that is revealed. Employing low special grid resolution enables gathering information in large areas, while employing high spatial grid resolution enables gathering measurements in tiny areas. The technique can work with large range object sizes and orientations using the same arrangements by employing image stitching procedures.

Since the physical characteristics of the OMIT are easy to generate using basic portable instruments with simple arrangements, the OMIT provides an advantage in difficult and challenging site situations outside of the lab environment, such as surface fragility, high relief irregularity and limited time accessibility.

Another advantage afforded by OMIT is that the compact instruments it uses can be sent and adjusted remotely—this is particularly useful in inapproachable places with direct visual accessibility and places that don’t have human operator accessibility or direct visual accessibility.

The high sensitivity of the method along with its low control needs and simple geometry principles offer the possibility to correct errors digitally after acquiring images which can allow for less complicated training and less procedure controls.

The digital technologies involvement in projection, superimposing and mathematical calculations can augment the capability of on-site control of the

dark fringes performance to have high sensitivity, high contrast and good visibility. The fringes can be generated using real time technique which enables the viewing of resulting fields as they are applied on the investigated surfaces.

On the other hand, the main noticed limitation of the OMIT as a depth measuring method in this study was the need to minimize the ambient light level. This method uses light projection to reveal relief information. The more the light projection is dominant, the more the information is clear and sharp. This limitation can be critical in the places with high levels of ambient light such as objects located outside under direct daylight. Although these cases can be solved using shadow moiré for objects with limited sizes.

The other limitation is the need for involving perspective distortion corrections for extracting very precise measurements. This limitation can be reduced using the one point perspective images and rectified photogrammetry.

The difficulty to determine the depth signs is also a serious limitation when previous knowledge of the surface is not possible if complicated surfaces are encountered. This limitation can be reduced by involving fiducial lines (thick lines with different colors and defined direction) impeded in the projected patterns.

Limitations of fringe visibility—like noise, contrast and sharpness—can be confronted if high accuracy levels are targeted outside of a controlled lab environment.

Surface slope limits and cavity existence is critical when targeting surfaces with high relief slopes or if portions of the surface are located in the shadow of other portion. The surface can prevent the capturing of projected light if the surface is located in a plane parallel to or hidden from the projected light direction. In this situation, the projecting direction needs to be adjusted or measurements need to be performed using other supporting projecting positions.

The advantage of the OMIT's high sensitivity to orientation can be considered a limitation in some cases. The sensitivity makes this method produce different forms of contour fringes for the same surface if, in relation to a reference plane, a small change occurs in the orientation of the projected light. This can make the image stitching procedure or identifying repeated data harder if the contour forms are the main source of data without identifying the reference plane. Usually identifying the projection reference plane requires another instrument like a total station to identify the location in space of three reference points located on the reference plane.

As in this study, in the case of building a 3D model in relation to an identified reference plane out of the resulting contours, this limitation can be reduced based on the form of the model in space and not on the OMIT generated contour shapes. In this situation, the reference for stitching or comparing will be the form of the model in relation to the position and orientation of its reference plane in space.

VI.3. Recommendations and future studies

According to the discussion that was established in this research, OMIT as a measuring method shows potential to be developed for heritage recording purposes. The following recommendations are introduced based on this potential.

The OMIT, as an optical method that was traditionally developed in relation with traditional optical tools and physical instruments, should be directed to be developed in complete dependent on computer aided means and digital technologies. This will reduce the amount of transitional steps needed and the physical material required.

The method can be developed toward involvement in historic recording, toward developing the method's components, and toward developing instruments for these purposes.

After the initial step of involving OMIT in historic recording established in this research, the door is wide open to investigate OMIT in the larger heritage recording context.

Investigations should be made for recording larger surface areas with more complex components and irregularity to simulate heritage elements with its wider physical situations, forms, locations and conditions.

Investigation should be made into utilize the long range capability of this method by performing studies involving recording surfaces in far locations using concentrated light projections and lasers that can reach far objects and retrieve the far projected deformed patterns using closing lens cameras.

Investigation should also be made to utilize the remote capability of this method by performing studies involving recording surfaces in distant locations using tools operated remotely using radio controls or through the internet.

For the OMIT method components, future studies are needed for investigating and developing light projecting instruments, the projected patterns, the imaging tools, the referencing procedures and measurement extracting encoding solutions.

Studies can be performed involving the development of line patterns to be treated as a profile encoding source to extract surface deformation in the form of a series of referenced sectional profiles of surface relief.

Studies can be performed on projected patterns through manipulating resolutions, forms, sizes and colors to reveal as much as possible of the measurement data using simpler procedures and less site variables.

Studies can be performed involving a new generation of LCD projectors with higher illumination and resolution with different light quality, light intensity

and light distribution to enhance the quality of the projected pattern which will be reflected on the fringe visibility limitations.

Studies can be performed to utilize higher camera resolutions and sensitivity with different lens combinations to enhance the image quality of the retrieved deformed patterns.

Studies can be performed to develop software solutions to automate the encoding procedures for extracting the measurements from the deformed patterns directly by involving virtually calculated reference patterns.

For the OMIT instrumentation, future studies are needed for investigating and developing instruments to reach higher levels of performance with less site variables.

Instruments can be developed to involve projected laser patterns to reach distant locations resulting in sharper projections.

Instruments can be developed to join the projecting and the imaging equipment in one tool that can be adjusted, directed and rotated to handle a wider range of situations with minimal adjustments.

Instruments can also be developed to identify the reference plane using laser sensors or three pointer sticks to automate recording the reference plane location in relation to OMIT projecting and imaging equipment.

Instruments can be developed to minimize the involved projecting and imaging equipment sizes by directing the technical development toward the specific needs of the method.

Finally, newly emerging technologies can push instrumentation to the extreme limit in regards to creating portable state-of-the-art equipment in the form of a helmet projector and polarized eyeglasses with an impeded camera to produce optical and virtual images to investigate and record surface deformations in real time.

REFERENCES

1. H. Karara, *Non-Topographic Photogrammetry, 2nd ed.* (American Society for Photogrammetry and Remote Sensing, Falls Church, Virginia, 1989).

2. C. Sciammarella, "Moiré in science and engineering," in *Trends in Optical Non-Destructive Testing and Inspection*, P. Rastogi and D. Inaudi, eds. (Elsevier Science Ltd, New York, 2000), pp. 345-373.

3. J. Mauch and J. Birch, *Guide to Successful Thesis and Dissertation* (Marcel Dekker, Inc, New York, 1998).

4. M. A. Notturno, *Knowledge and the Body-Mind Problem, in Defense of Interaction* (Routledge, New York, 1994).

5. K. Popper, *In Search of a Better World* (Routledge, New York, 1992).

6. K. Rogers, *Toward a Postpositivist World* (Peter Lang, New York, 1996).

7. K. Popper*, Conjectures and Refutations; the Growth of Scientific Knowledge* (Routledge, New York, 2002).

8. K. Popper, *All Life Is Problem Solving* (Routledge, New York, 1999).

9. W. L. Reese, *Dictionary of Philosophy and Religion* (Humanities Press, Atlantic Highlands, New Jersey, 1980).

10. Y. Lincoln and E. Guba, "Paradigmatic controversies, contradictions, and emerging conflicts", in *Handbook of Qualitative Research 2nd ed.,* N. K. Denzin and Y. S. Lincoln, eds. (Sage Publications, Thousand Oaks, California, 2000), pp. 163-188.

11. P. D. Leedy, *Practical Research, Planning and Design, 3rd ed.* (Macmillan Publishing Company, New York, 1985).

12. I. Newman and C. Benz, *Qualitative-Quantitative Research Methodology* (Southern Illinois University Press, Carbondale, 1998).

13. J. W. Creswell, *Research Design, Qualitative, Quantitative, and Mixed Method Approaches, 2nd ed.* (Sage Publications, Thousands Oaks, California, 2003).

14. E. Mikhail, J. Bethel and J. McGlone, *Introduction to Modern Photogrammetry* (John Wiley & Sons, Inc, New York, 2001).

15. R. Dallas, “Architectural and archaeological recording,” in *Development in Close Range Photogrammetry*, K. Atkinson ed., (Applied Science Publishers Ltd, London, 1980), pp. 81-116.

16. K. B, Atkinson, *Development in Close Range Photogrammetry 1st ed.* (Applied Science Publisher Ltd, London, 1980).

17. S. McPherron and H. Dibble, *Using Computer in Archaeology* (McGraw-Hill Companies Inc., Boston, 2002).

18. J. Avern, “A new technique for recording archaeological excavations: research progress report,” in *Proceedings of Computing Archaeology for Understanding the Past*, Z. Stancic and T. Veljanovski, eds. (Archaeopress, Oxford, 2001), pp. 3-7.

19. R. Fontana, M. Gambino, M. Greco, E. Pampaloni, L. Pezzati, and R. Scopigno, “High-resolution 3D digital models of arteorks,” in *Optical Metrology for Arts and Multimedia*, R. Salimbeni, ed. Proc. SPIE **5146**, 34-43 (2003).

20. ICOMOS *Guide to Recording Historic Buildings* (Butterworth Architecture, London, 1990).

21. J. A. Burns, *Recording Historic Structures 2nd ed*. (John Wiley & Sons, Inc, Hoboken, New Jersey, 2004).

22. J. Roberts, *Construction Surveying: Layout and Dimension Control* (Delmar Publishers Inc, New York, 1995).

23. E. Reali, “Computerized techniques for field data acquisition,” in *Proceedings of Computing Archaeology for Understanding the Past*, Z. Stancic and T. Veljanovski, eds. (Archaeopress, Oxford, 2001), pp. 13-17.

24. Eos Systems Inc. *PhotoModeler Pro User Manual, 25th ed.* (Eos Systems Inc, Vancouver, 2003).

25. R. Scopigno, P. Cignoni, M. Callieri, F. Ganovelli, G. Impoco, P. Pingi, and F. Ponchio, “Using optically scanned 3D data in the restoration of Michelangelo’s David,” in *Optical Metrology for Arts and Multimedia*, R. Salimbeni, ed. Proc. SPIE **5146**, 44-53 (2003).

26. R. Ricci, R. Fantoni, M. Ferri De Collibus, G. Fornetti, M. Guarneri, and C. Poggi, “High resolution laser radar for 3D imaging in artwork cataloguing, reproduction and restoration,” in *Optical Metrology for Arts and Multimedia*, R. Salimbeni, ed. Proc. SPIE **5146**, 62-73 (2003).

27. A. Wegdam, “Topographical measuring based on the shadow and projection moiré method”, Ph.D. Dissertation, (Twente University, Netherlands, 1991)

28. O. Kafri and I. Glatt, *The Physics of Moiré Metrology* (John Wiley & Sons, New York, 1990).

29. D. Post, B. Han, and P. Ifju, “Moiré interferometer,” in *Trends in Optical Non-Destructive Testing and Inspection*, P. Rastogi and D. Inaudi, eds. (Elsevier Science Ltd, New York, 2000), pp. 375-389.

30. K. Patorski, *Handbook of the Moiré Fringe Technique* (Elsevier, Amsterdam, 1993).

31. D. Laboury, Y. Renotte, B. Tilkens, M. Dominique, R. Billen, and Y. Cornet, “The Osiris Project (Optical systems for interferometric - photogrammetric relief investigation and scanning). Development of a device for 3D numerical recording of archeological and epigraphic documents by optoelectronic processes,” in *Proceedings of Scanning for Cultural Heritage Recording,* W. Boehler, ed. (Corfu, Greece, 2002), pp. 139-142, http://www.isprs.org/commission5/workshop/ part6.pdf

32. I. Amidror, *The Theory of the Moiré Phenomenon* (Kluwer Academic Publisher, Netherlands, 2000).

33. O. Bryngdahi, “Moire: Formation and interpretation”, in *Optical Moiré and Applications,* G. Indebetouw and R. Czarnek, eds. (SPIE Optical Engineering Press, Washington D.C., 1992), pp. 70-77.

34. C. Sciammarella, “Theoretical and experimental study on moiré fringes”, Ph.D. Dissertation, (Illinois University, Chicago, 1960).

35. J. Perkelsky and M. Wijk, “Moire topography: Systems and applications”, in *Non-Topographic Photogrammetry* 2nd ed*.,* H. M. Karara ed., (American Society for Photogrammetry and Remote Sensing, Falls Church, Virginia, 1989), pp. 231-263.

36. H. Takasaki, “Moiré application from its birth to practical application,” J. Opt. Las. Eng. A **3**, 3-14 (1981).

37. H. Liu, “Automated phase-measuring profilometry of 3-D diffuse object”, Ph.D. Dissertation, (State University of New York, Stony Brook, 1985)

38. A. Asundi, “Digital moiré for deformation analysis”, in *Trends in Optical Non-Destructive Testing and Inspection*, P. Rastogi and D. Inaudi, eds. (Elsevier Science Ltd, New York, 2000), pp. 391-399.

39. C. Miles and B. Speight, “Recording the shape of animals by a moiré method”, in *Optical Moiré and Applications,* G. Indebetouw and R. Czarnek, eds. (SPIE Optical Engineering Press, Washington D.C., 1992), pp. 401-404.

40. H. Kurz and O, Leder, “Pc-based moiré for field studies on human body surface,” in *Close-Range Photogrammetry Meets Machine Vision*, A. Gruen, E. Baltsavias, eds. Proc. SPIE **1395**, 1066-1073 (1990).

41. Y. Morimoto and M. Fujigaki, “Real-time phase distribution analysis in moiré”, in *Trends in Optical Non-Destructive Testing and Inspection*, P. Rastogi and D. Inaudi, eds. (Elsevier Science Ltd, New York, 2000), pp. 415-432.

42. C. Forno, “Deformation measurement in civil engineering using high-resolution moiré”, in *Trends in Optical Non-Destructive Testing and Inspection*, P. Rastogi and D. Inaudi, eds. (Elsevier Science Ltd, England, 2000), pp. 401-414.

43. J. Hooker, “Video applications to moiré metrology”, PhD. Dissertation, (Florida Institute of Technology, Melbourne, 1991).

44. Y. Yoshino, “Enhancement of visibility of fringes and exposure time for moiré topography,” J. Opt. Las. Eng. A **3**, 53-58 (1981).

45. E. M Mikhail, *Modern Photogrammetry, 1st ed.* (John Wiley & Sons, Inc, New York, 2001)

46. E. Childes, “Non-contact topographic measurements using a phase shifting algorithm of moiré interferometry, Master Thesis,” (University of North Carolina at Charlotte, 1999).

47. J. Balachowski, *The Handbook for Recording Structures with Measured Drawings* (HABS/HAER, Washington, D.C, 1993).

48. L. Groat and D. Wang, *Architectural Research Methods* (John Wiley & Sons, Inc, New York, 2002).

49. R. Burt, “An investigation into the factors affecting the accuracy of close range digital photogrammetry for the measurement of historic adobe wall ruins”, PhD. Dissertation, (Texas A&M University, College Station, 2000).

VITA

Samer Al-Ratrout, of Amman, Jordan, received the degree of Bachelor of Science in architectural engineering in 1988 from the University of Jordan and a Master of Science degree in architecture, with concentration on urban design from the University of Jordan in 1994.

In 2002 he received a Fulbright Scholarship for two years to pursue a Ph.D. degree in architecture at Texas A&M University where he worked as a lecturer in that department.

He is certified as a consulting architect in Jordan where he practiced architectural design for 14 years with extensive experience in computer mediated design solutions.

Al-Ratrout's research interests include architectural and urban design, 3D visualization, virtual recording of historic structures, and close-range digital photogrammetry. He is currently focused on employing structured light projections for extracting object depth measurements from digital images. He also applies optical moiré interferometry techniques to problems in the area of historic recording, including improvements to surface relief remote measuring and recording.

He can be reached at:

SAMER AL-RATROUT
Western Al-Hussein P.O. Box 622546
Amman, Jordan, 11192